Fall 2019

# Establishing the Role of the Mississippi-Alabama Barrier Islands in Mississippi Sound and Bight Circulation Using Observational Data Analysis and a Coastal Model

Laura Hode
*University of Southern Mississippi*

## Recommended Citation

Hode, Laura, "Establishing the Role of the Mississippi-Alabama Barrier Islands in Mississippi Sound and Bight Circulation Using Observational Data Analysis and a Coastal Model" (2019). *Dissertations*. 1737.
https://aquila.usm.edu/dissertations/1737

# ESTABLISHING THE ROLE OF THE MISSISSIPPI-ALABAMA BARRIER ISLANDS IN MISSISSIPPI SOUND AND BIGHT CIRCULATION USING OBSERVATIONAL DATA ANALYSIS AND A COASTAL MODEL

by

Laura Elizabeth Hode

A Dissertation
Submitted to the Graduate School,
the College of Arts and Sciences
and the School of Ocean Science and Engineering
at The University of Southern Mississippi
in Partial Fulfillment of the Requirements
for the Degree of Doctor of Philosophy

Approved by:

Dr. Stephan D. Howden, Committee Chair
Dr. Dmitri A. Nechaev
Dr. Jeremy D. Wiggert
Dr. Patrick J. Fitzpatrick
Dr. Davin J. Wallace

| | | |
|---|---|---|
| Dr. Stephan D. Howden<br>Committee Chair | Dr. Jeremy D. Wiggert<br>Associate Director of School | Dr. Karen S. Coats<br>Dean of the Graduate School |

December 2019

***Published by the Graduate School***

THE UNIVERSITY OF
SOUTHERN
MISSISSIPPI

# ABSTRACT

The Mississippi-Alabama barrier islands restrict exchange between the Mississippi Sound and Mississippi Bight in the northern Gulf of Mexico. The islands also act as storm breaks for tropical cyclones, so their continued existence sustains marine ecosystems and protects coastal communities. However, the chain has undergone extensive segmentation, erosion, and westward migration in the past two hundred years. The islands are now more susceptible to further erosion (Pendleton et al., 2013; Morton, 2007). Additional reduction in island subaerial land extent would alter circulation in the Mississippi Sound and Bight.

Consequently, this study targeted the two most vulnerable barrier islands in the chain for removal in an ocean model to understand how circulation might change in an island loss scenario. A multiplatform data analysis assessed patterns in existing circulation over a four year period. Circulation varied both seasonally and on short time scales ranging from hours to days. Additionally, storm-induced changes to circulation were examined for the hurricane seasons of the same four year period to gauge how non-periodic events impacted the Mississippi Sound and Bight. Circulation response to tropical cyclones that entered the Gulf of Mexico varied storm to storm. Prior to initiating the island removal scenarios, validation of the oceanic and atmospheric models was completed to deduce model skill using the observational data.

Finally, the response of Mississippi Sound and Bight circulation to island loss was examined under time-invariant and time-variant conditions. Analysis of model output found island removal weakened currents in existing island passes but created new water exchange pathways where the islands had been removed. The new pathways increased salinity within the Mississippi Sound by as much as 2 near the removed islands. However, the island chosen for removal dictated the extent of circulation changes and which half of the Sound saw larger salinity increases. Seasonality played a role in how the Mississippi Sound and Bight responded to island loss. Results suggest permanent changes to circulation which would impact the resiliency of the remaining barrier islands and substantially shift distributions of hydrographic properties. These changes would have ecological and economic consequences throughout the Mississippi Sound.

# ACKNOWLEDGMENTS

This research was made possible in part by a grant from the Gulf of Mexico Research Initiative. High frequency radar data are publicly available through the Gulf of Mexico Research Initiative Information & Data Cooperative (GRIIDC) at https://data.gulfresearchinitiative.org (https://doi.org/ 10.7266/N77D2SJ5D5RBW). Funding was also provided by the Shelf-Slope Interactions and Carbon Transformation and Transport in the Northern Gulf of Mexico: Platform Proof of Concept for the Ocean Observing System in the Northern Gulf of Mexico project as part of the Northern Gulf Institute and the National Oceanic and Atmospheric Administration.

The design and implementation of this project would not have been possible without the assistance and dedication of multiple individuals. I would like to acknowledge the exemplary efforts of Dr. Stephan Howden, Dr. Arne Diercks, Kevin Martin, James Davis, and Richard Slaughter in establishing and maintaining the Central Gulf of Mexico Ocean Observing System high frequency radar network. The support staff at CODAR Ocean Sensors also deserve thanks. The coastal ocean model used in the study was created as part of the CONsortium for oil spill exposure pathways in COastal River-Dominated Ecosystems efforts. Model development was led by Dr. Jeremy Wiggert. Many thanks are due to Dr. Wiggert as well as to current and former members of the modeling group including Mike Dinniman, Dr. Kemal Cambazoglu, Dr. Stephan O'Brien, and Dr. Chudong Pan for their efforts in the creation and development of the coastal ocean model. Additionally, Dr. Patrick Fitzpatrick and Yee Lau developed a Mississippi Bight region-specific atmospheric product for use in the model. Thank you.

Several persons provided invaluable input on the study region's dynamics and on equipment that supplied data used in this study.  I would like to thank Dr. Ervin Otvos and Dr. Gregory Carter for discussions on the history of the Mississippi-Alabama barrier islands.  I would especially like to thank Dr. Davin Wallace for insights into the barrier islands' vulnerability.  Thanks are due as well to Dr. Dmitri Nechaev for discussion on model skill assessment and output analysis.  Robert Moss Jr. and Mike Runner supplied details on the Mississippi Department of Marine Resource-US Geological Survey hydrological stations needed for model validation.  Thank you.

Several current and former graduate students aided in the research and troubleshooting of this project.  Thank you to Robert Hollis, Dr. Stephan O'Brien, Dr. Sarah Epps, Uchenna Nwankwo, Shara Gremillion, and Courtney Bouchard.  Thank you as well to Samuel Wright for his ArcGIS assistance.

I am grateful to the University of Southern Mississippi for the opportunity to conduct this research.  Finally, I would like to thank the members of my committee: Dr. Stephan Howden, Dr. Dmitri Nechaev, Dr. Jeremy Wiggert, Dr. Davin Wallace, and Dr. Patrick Fitzpatrick.  Thank you for your assistance and dedication.

# DEDICATION

I would like to dedicate this work to my grandfather, Emil Handzel, and my father, Phillip Handzel. Growing up, my father told stories about how my grandfather immigrated to the United States as a child. He never finished high school, so his dream for his children was that they graduate high school. They all received their diplomas. My father carried that dream forward. He wanted my brother and me to attend and finish college. We both have bachelor's degrees, and I have had the pleasure and opportunity to move forward onto graduate studies. To both of them, I owe a heartfelt thanks for dreaming of more for the generations that come after. My grandfather and father instilled a dream of higher achievements in me, and this work would not have been possible without their vision and the support of my friends and family.

## TABLE OF CONTENTS

# LIST OF TABLES

# LIST OF ILLUSTRATIONS

# LIST OF ABBREVIATIONS

| | |
|---|---|
| CenGOOS | Central Gulf of Mexico Ocean Observing System |
| *COAWST* | Coupled Ocean-Atmosphere-Waves-Sediment Transport |
| *CODAR* | Coastal Ocean Dynamics Applications Radar |
| *CONCORDE* | CONsortium for oil exposure pathways in COastal River-Dominated Ecosystems |
| *HFR* | High Frequency Radar |
| *MDMR* | Mississippi Department of Marine Resources |
| *NCEI* | National Centers for Environmental Information |
| *NEGOFS* | Northeast Gulf of Mexico Operational Forecast System |
| *NOAA* | National Oceanic and Atmospheric Administration |
| *ROMS* | Regional Ocean Modeling System |
| *ROMSmsb* | ROMS Mississippi Sound and Bight |
| *USGS* | United States Geological Survey |
| *USM* | The University of Southern Mississippi |

# CHAPTER I - INTRODUCTION

The northern Gulf of Mexico hosts a number of high-value industries. As of August 2018, there were more than 1,400 active oil and gas leases in the Gulf of Mexico, and several hundred million cargo tons are transported through the ports at Plaquemines, Terrebonne, New Orleans, Gulfport, Biloxi, Pascagoula, and Mobile annually (BSEE 2018; USACE, 2016). Shrimping vessels in Louisiana, Mississippi, and Alabama caught more than 100 million pounds of shrimp in the last five years, and Mississippi reported a quarter-million sacks of oysters harvested in the same period (MDMR 2018; NOAA Fisheries, 2018). Historic sites also draw tourists, and multiple military branches have bases in the area. Economic growth in the region is tightly aligned with these industries, but the coastline, barrier islands, and coastal water bodies are highly dynamic. Rising sea levels, subsidence, marsh disappearance, and barrier island evolution mean the northern Gulf of Mexico undergoes measurable changes in terms of sediment resources, island resiliency, and the region's industries. Additionally, the northern Gulf is susceptible to hurricanes, oil spills, hypoxic conditions, and harmful algal blooms.

Understanding the physics that govern circulation in the northern Gulf of Mexico and potential sub-decadal and decadal changes to that circulation can be vital to keeping coastal communities safe and industries in operation. To that end, this study endeavors to pair observations with a series of model simulations from a coastal model to constrain patterns of variability in circulation of the northern Gulf of Mexico, both for the region as it is now and under barrier island removal scenarios.

This dissertation is organized as follows. Chapter I gives specifics on the layout and history of the northern Gulf of Mexico and explores the physical forcing mechanisms that mediate circulation in the region. Results from previous studies are also considered, as are efforts by agencies to bolster the barrier islands. Chapter II uses data from a collection of observing platforms to ascertain variability in circulation caused by cyclical forcing to gain an overview of circulation patterns across a 12-month cycle. In contrast, Chapter III investigates isolated forcing events in the form of tropical storm and hurricane impacts on the study region since storms are punctuated events. Chapter IV highlights a coastal model used to mimic dynamics in the study region and how well that model captures circulation variability measured by the observational data. Chapter IV also examines changes in circulation brought about by island removal in model simulations. Chapter V finishes the study with overall conclusions and a note on potential future work.

### 1.1 Study Area

Stretching from the bird foot delta of the Mississippi River to Cape San Blas, Florida, the Mississippi Bight encompasses the coastal ocean east of Louisiana and south of Mississippi, Alabama, and a portion of the Florida panhandle. Figure 1.1 shows the layout of the region. Two groups of barrier islands border the Bight along the northern Gulf of Mexico coastline. To the west lie the Chandeleur Islands, Chandeleur Sound, and the present Mississippi River bird foot delta. To the north, the Mississippi-Alabama barrier islands run mostly parallel to the coast. The Bight extends south of these islands. Much of the northern Mississippi Bight has depths shallower than 100 m, but the De Soto Canyon cuts through the southern portion, and depths in that area exceed 1,000 m.

Six islands comprise the Mississippi-Alabama barrier chain. Lying northeast of the St. Bernard Delta, Cat Island is the westernmost island. West and East Ship Island, Horn Island, Petit Bois Island, and Dauphin Island lie east of Cat Island. Smaller islands, such as Round Island and Deer Island, fall much closer to the coast, and Pelican Island, south of Dauphin, sees an intermittent connection with Dauphin. Notably, a small dumping site for dredging spoils exists west of Petit Bois Island on the western side of the Pascagoula shipping channel; it surfaced above the water line in the 1980s. Sand Island (Western Dauphin Island) exists within the chain, but it was an unintentional consequence of dredging that has since developed its own ecosystem. Its sediment accretion and erosional patterns now make it part of the chain.

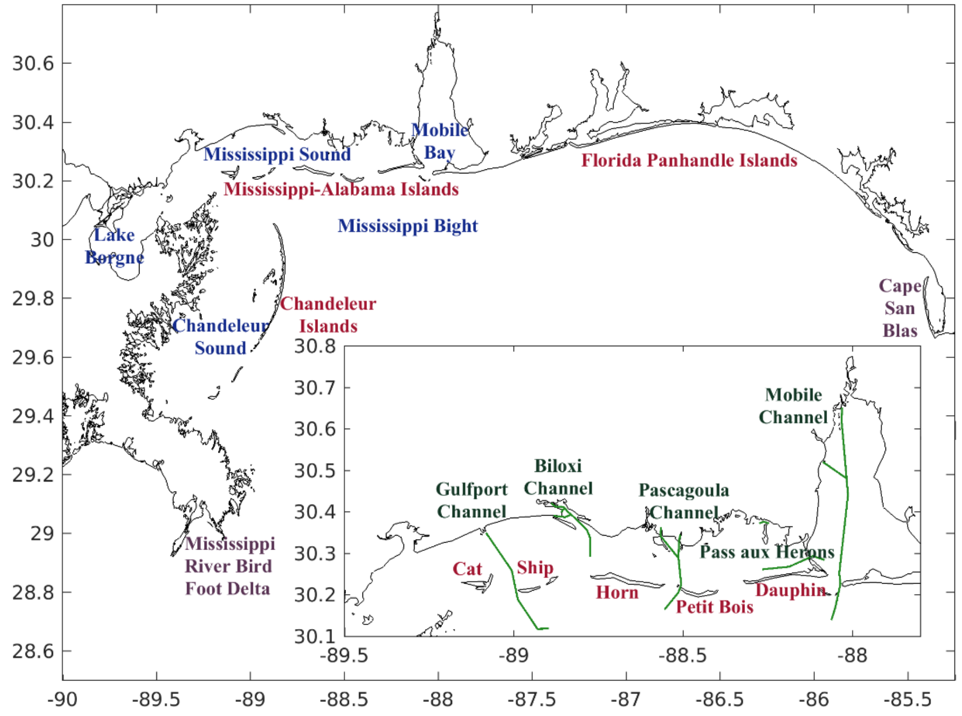

Figure 1.1 Map of the Mississippi Bight and Mississippi Sound

The Mississippi Bight extends from the Mississippi River bird foot delta, Louisiana, in the west to Cape San Blas, Florida. Waterbody names are given in blue while red text indicates islands. The insert in the lower right zooms in on the Mississippi Sound to highlight the shapes and locations of the Mississippi-Alabama barrier islands (Cat, West and East Ship, Horn, Petit Bois, and Dauphin Island). Additionally, major shipping channels are marked in green. Coordinates for the channels were taken from the National Oceanic and Atmospheric Administration's Raster Nautical Charts, available at nauticalcharts.noaa.gov.

Landward of the islands is the shallow coastal lagoon of the Mississippi Sound. Freshwater input to the Mississippi Sound comes from Lake Borgne to the northwest and Mobile Bay to the northeast as well as a collection of smaller rivers to the north. Some of the Mississippi River outflow also turns northeast and enters both the Mississippi Bight and Sound.

The Sound exchanges water with the Bight through gaps in the Mississippi-Alabama chain called passes. Several of these passes were artificially deepened to create shipping channels in the mid-nineteenth century, and regular dredging maintains depths to allow larger vessels access to the ports (Morton, 2007; Kjerfve, 1983). These channels include the Gulfport, Pascagoula, and Mobile shipping channels. Another shipping channel extends from Biloxi.

## 1.2 Barrier Island Formation and Evolution

The origin of the northern Gulf of Mexico barrier islands can be traced to the Holocene epoch around 8,000 years ago (Otvos, 1981; Gal, 2018; Hollis, 2018). Louisiana barrier islands like the Chandeleurs evolved through a progradation of a previous river lobe of the Mississippi River called the St. Bernard delta. Due to subsequent reworking, the Chandeleur chain is considered deltaic transgressive. The majority of sediment supply comes from riverine input in the form of fine-grained silt and clay (Coleman et al., 1998). Diminishing sediment supply, anthropogenic activity, and storm impacts have all contributed to island thinning and landward retreat. This study, though, is primarily concerned with the Mississippi-Alabama barrier islands. Unlike the Chandeleur chain, the Mississippi-Alabama barrier islands resulted from aggradation of material upwards from the seafloor (Otvos, 1970). Grain sizes for the chain are larger than the Chandeleur Islands, and sediment follows an east to west transport pathway. While more robust than the Chandeleur Islands, the Mississippi-Alabama barrier islands have also suffered net land loss. The islands' role in Mississippi Sound and Bight circulation should be explored since the chain is undergoing change.

Surveys and sediment cores give indications of how the islands evolved over the last several centuries and millennia, and the history of ports and maritime traffic in the area also means detailed nautical charts of various degrees of accuracy exist back to the late eighteenth century (Rosati and Stone, 2009; Otvos, 1970). The longer geologic record suggests the chain used to be more extensive. The chain as a whole ran largely uninterrupted from Mobile Bay to the St. Bernard delta (Otvos, 1981). However, net subaerial land loss and volume reduction have affected every island. Even accounting for cartographer error, subsequent nautical charts in the last two centuries show evidence of land loss (Morton, 2007).

East and West Ship Island once formed a larger single island which has seen repeated storm breaching. Likewise, Petit Bois Island made up the western extent of Dauphin Island. Like Ship Island, hurricane breaches eventually separated the island into two barrier islands. Indeed, tropical cyclone impacts in the northern Gulf of Mexico have occurred with some regularity over the last 2,500 years (Bregy et al., 2018).

Lateral migration reworks the barrier island chain (Morton, 2007; Gal, 2018; Hollis, 2018). An alongshore current moves primarily east to west in the northern Gulf of Mexico, so the Mississippi-Alabama barrier islands migrate westward with the littoral drift (Morton, 2007). Cat Island serves as an exception; the presence of the St. Bernard delta to the southwest shelters the island and restricts westward translation. Cypress stumps east of the “T” bar suggest the island extended further east previously, but the controlled tidal flow as a result of the delta has helped to rework the island into its present shape (Otvos and Carter, 2013).

Westward translation occurs in spurts with sediment eroding from the eastern tips of the islands and resettling on the western edges. Sediment also fills in the passes between the islands as areas to the west become the new passes (Morton, 2007). However, an imbalance exists in this sediment redistribution. Erosion of the eastern ends of the islands exceeds the rate of accretion on the western sides, so the islands lose area as they drift.

Morton (2007) linked some of the sediment starvation to dredging of the shipping channels. Dredging allows larger vessels to bring products to and from ports like Gulfport, Pascagoula, Biloxi, and Mobile. Deeper passes interrupt sediment transport across the gaps between the islands (Twichell et al, 2013). Dredging also removes a portion of the deposited sediment to offshore locations, so less autochthonous material is available to either be re-suspended or provide the foundation for the new western tips of the islands (Sallenger, et al., 2007; Morton, 2007). While sustainment of the shipping channels is vital to maritime commerce, the dredged channels partially starve islands to the west.

Vegetation change provides another indication the Mississippi-Alabama barriers have undergone change. Comparisons of aerial photography in conjunction with ground surveys show a reduction in woody areas on Horn Island over the past seven decades (Jeter and Carter, 2016). Petit Bois Island and East Ship Island saw a die-off of all slash pines following Hurricane Katrina in 2005 while Horn Island lost more than three-quarters of its slash pine population (Otvos and Carter, 2008). Woody habitats never represented a sizeable percentage of total vegetation on the islands; however, diminishment of their percentage of vegetated land denotes a shift in flora species dominance (Lucas and Carter, 2013). Shrubs and trees are components of a mature ecosystem, and the islands are becoming more and more marked by their lack of established vegetation. This change affects how sediment is moved, captured, and retained during daily wind and wave action as well as by punctuated events such as storms.

## 1.3 Mississippi Sound and Bight Circulation Drivers

Multiple environmental parameters drive circulation in the northern Gulf of Mexico. From a physical forcing standpoint, winds, riverine discharge, and tides modulate circulation patterns in the Mississippi Sound and Bight. However, mesoscale eddies can also impact the southern portion of the Mississippi Bight.

### 1.3.1 Tides

Tidal ranges of less than 1 m across the Mississippi Sound make the region micro-tidal, yet tides still produce a clear diurnal response (Eleuterius and Beaugez, 1979). Courtier's criterion uses four tidal harmonic constituents to determine which regions have diurnal, semi-diurnal, or mixed tides (Courtier, 1938). The criterion, known as the form number, F, is given in (Eq. 1.1).

$$F = \frac{O_1+K_1}{M_2+S_2} \qquad \text{(Eq. 1.1)}$$

The ratio of the sum of the principal lunar diurnal constituent, $O_1$, and the luni-solar diurnal constituent, $K_1$, to the sum of the principal lunar semi-diurnal constituent, $M_2$, and the principal solar semi-diurnal constituent, $S_2$, yields the form number. Values of $F \leq 0.25$ indicate semi-diurnal tides while $F \geq 3$ corresponds to diurnal tides. F values between 0.25 and 3 denote a mixture of semi-diurnal and diurnal tides. Using amplitudes of $O_1$=0.169 m, $K_1$=0.162 m, $M_2$=0.039 m, and $S_2$=0.033 m from tide gage 8744117 in Biloxi, Mississippi, the location clearly has diurnal tides with F=4.60. Diurnal tides dominate throughout the northern Gulf of Mexico.

The three primary harmonic constituents are $K_1$ with a period of 23.93 hours, $O_1$ with a period of 25.82 hours, and the principal solar diurnal constituent, $P_1$, with a period of 24.07 hours. The close timing of these main constituents makes separating the effects of tides from the effects of other phenomena with similar periods difficult.

These phenomena include inertial periods and the land-sea breeze. The Coriolis parameter, shown in (Eq. 1.2), increases with latitude, $\varphi$, towards the poles, and the inertial period for a given area is equal to $2\pi/f$. The angular velocity of the Earth, $\Omega$, can be found by dividing $2\pi$ by the length of the sidereal day. Since the Mississippi Bight and Sound extend from approximately 28.5°N to 30.5°N, inertial periods for the regions vary between 25.08 hours and 23.58 hours. Likewise, differential heating and cooling of the land and water creates a land and sea breeze dynamic that is especially prominent in warmer months. Additionally, a diurnal rotation of the winds matching the timing of the solar cycle can be observed, most notably at the beginning of spring and end of fall (Dai and Deser, 1999). These forcing cycles occur on a roughly 24-hour time scale, so the three main tidal constituents, inertial oscillations, and wind dynamics all have nearly identical periods.

$$f = 2\Omega sin\varphi \qquad \text{(Eq. 1.2)}$$

Gravitational circulation has been observed in the island passes; currents at the surface tend to flow into the Mississippi Bight while bottom currents point into the

Mississippi Sound (Kjerfve, 1983). However, shifts in transport direction at the surface and at depth through the passes also reflect diurnal forcing from tides (Kjerfve, 1983).

### 1.3.2 Rivers

The Mississippi Sound receives freshwater from Mobile Bay and a host of smaller rivers. While the majority of the Mississippi River outflow turns southwest along the Louisiana coast, part of the discharge exits east into the Mississippi Bight. Some fraction of the Mississippi River discharge enters the Mississippi Sound, but the quantity is uncertain. From the eastern side of the barrier chain, brackish water flows out from Mobile Bay and turns southwest in an alongshore current (Cipriani and Stone, 2001). Though lacking the high volume discharge of the Mississippi River and Mobile Bay, rivers such as the Pearl, Pascagoula, Jordan, and Biloxi among others contribute to the low salinity waters in the Sound.

### 1.3.3 Winds

Winds also play an important forcing role for nearshore environments. The Northeast Trade Winds act as the dominant wind source. Fall and winter see northerly and northeasterly winds while southeasterly winds characterize summer (Johnson, 2008; Chang and Oey, 2013). Easterly, southwesterly, and westerly winds also occur in parts of the northern Gulf of Mexico, and on temporal scales of days to weeks, considerable variability in wind strength and direction occurs throughout the study region.

Between October and April, roughly 20 to 30 fronts pass through the northern Gulf of Mexico; these fronts are driven by one of three atmospheric phenomena: the Gulf of Mexico cyclone, the Artic surge, or the mid-latitude cyclone (Stone et al., 2004). Frontal passage occurs on 3-to-7 day time scales (Keen, 2002; Rogers and Rohli, 1991;

Roberts et al., 1989). The fronts can move parallel or perpendicular to the northern Gulf of Mexico coast, but frontal passages at acute angles to the coast occur more often. While these brief events will be largely averaged out in findings presented in Chapter II, they contribute to month to month variability seen over the course of a year.

A land and sea breeze dynamic emerges from April to September with the cycle becoming more pronounced as the summer season progresses. Winds originate offshore during the day producing the sea breeze while weaker magnitude winds pointing offshore take over at night for the land breeze (Hill et al., 2010). Since the Louisiana and Mississippi–Alabama coasts run nearly perpendicular to one another, an offset in direction and timing of the land to sea breeze occurs throughout the study area.

### 1.4 Previous Studies

Hurricane Katrina carried sand off the Chandeleur Islands and shifted Dauphin Island northward (Sallenger, et al., 2007). Land and ship surveys by Fritz et al. (2007) established the surge height as well as the erosional extent of the islands after the storm. Figure 1.2 highlights a longer history by showing topological changes in the barrier islands from 1847 until 2006 (Morton, 2007).

Cat Island, shown in Figure 1.2a, resembles a horizontal “T”. In 1848, the crossbar had an almost equal extent to the north and south. The southern portion of the crossbar suffered ongoing erosion over subsequent decades. The entire barrier shows a consecutively smaller perimeter, and a series of inland cuts are present in the latest survey. Aerial photographs and ship surveys noted a breach in the crossbar of the “T” after Katrina (Fritz, et al., 2007).

Ship Island underwent the most extreme change; on average, the island has lost approximately half a million cubic meters of sediment per year since 2004 (Eisemann et al., 2018). Figure 1.2b shows the separation, reconnection, and re-separation of East and West Ship Islands. In the post-Katrina survey, East Ship Island was all but wiped out. While Ship Island appears as East and West Ship Islands in the default island configuration model runs in this study; the breach between the islands was closed by engineering efforts in 2019 (Perez, 2019). This study was completed in the midst of the restoration process, so the model domain does not account for bathymetric and topographic changes in the different stages of the restoration.

As for Horn Island, seen in Figure 1.2c, the eastern edge experienced ongoing erosion over the 157-year period reducing the lateral extent of the barrier. Westward migration in conjunction with antecedent geology has given the island a slight “elbow” shape (Gal, 2018).

Documents from the US Army Corps of Engineers and the United States Geological Survey (USGS) illustrate the intermittent connection between Petit Bois and Dauphin Islands. In Figure 1.2d, the 1848 record sees the islands connected while a substantial pass exists between them by 1917. Later surveys show the eastern edge of Petit Bois being cut back and curling landward. The southern coastline has also retreated landward.

Dauphin Island, Figure 1.2e, experienced thinning of its northeast corner and a shifting and intermediate connection to Pelican and Sand Islands on its southeastern side. The width of the island has also thinned considerably, and hurricane Katrina breached the center of the island. The breach coincided with a paleochannel in the subsurface (Hollis, 2018). Fritz et al. (2007) found a landward migration of the whole island during Katrina.

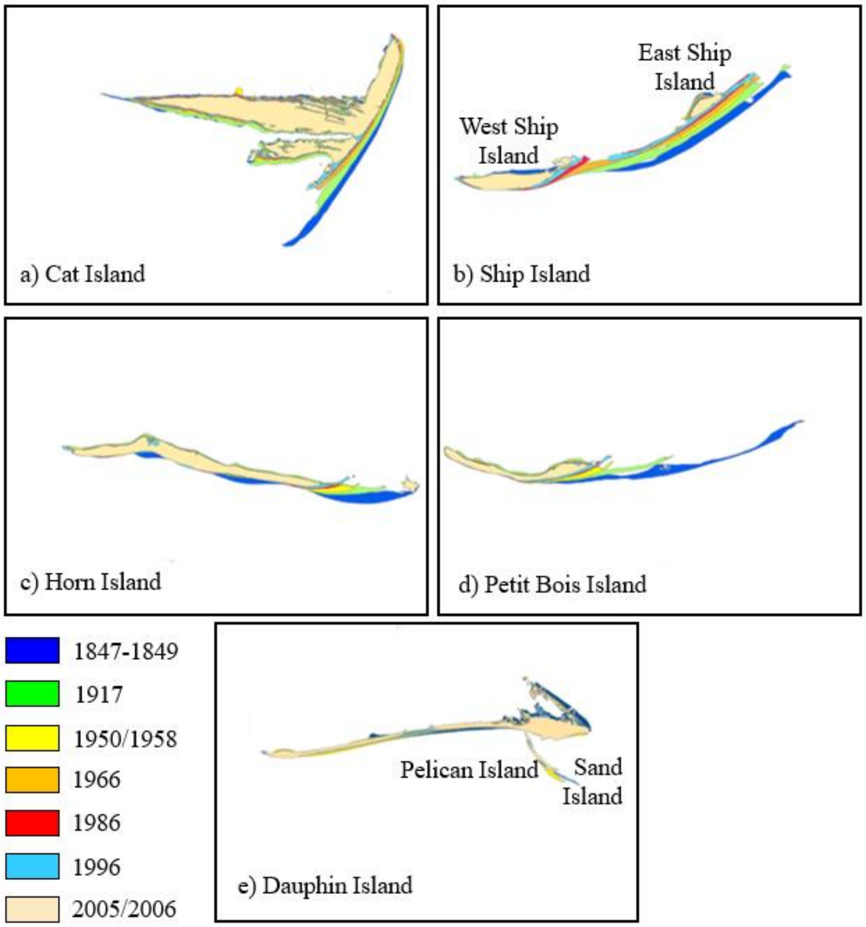

Figure 1.2 Map of the subaerial extent of the Mississippi-Alabama barrier islands from 1847 through 2006

Reproduced and consolidated from Morton (2007).

## 1.5 Barrier Island Restoration Efforts

Ongoing initiatives to bolster the Mississippi-Alabama barrier islands against future storms include the US Army Corps of Engineers-led Mississippi Coastal Improvements Program (MsCIP) restoration of Ship Island and the Round Island Marsh

Restoration project overseen jointly by the Mississippi Department of Environmental Quality and the Mississippi Department of Marine Resources (DOI&USGS, 2016; MDEQ, 2016).  As for Dauphin Island, the State of Alabama has been cooperating with the US Geological Survey and the US Army Corps of Engineers on the Alabama Barrier Island Restoration Assessment to collect data on the region south of Mobile Bay and direct any restoration efforts (Conzelmann et al., 2018).  Multiple US Geological Survey reports have indicated the vulnerability not only of the Mississippi-Alabama barrier island chain but the Mississippi and Alabama coasts as well (Pendleton et al., 2010; Twichell et al., 2013).  Incorporation of scientific data into policy decisions is crucial for successful restoration and management projects (Dolan and Wallace, 2012).  This study addresses the circulation changes brought about by island loss compared to climatological and tropical cyclone-influenced circulation.

While the disappearance of a single island in isolation is unlikely, the removal scenario requires relatively few modifications to an existing model, so observed changes can be more reliably attributed to the island's absence.  As such, results can serve as a baseline for future scenarios such as westward island chain translation, pass enlargement, or breaches to islands.  Three hypotheses played into the design of the island loss experiments.  First, larger shifts in circulation patterns were expected near the removed islands.  The two islands chosen had smaller subaerial extent and histories of erosion, so strong, study area-wide circulation changes were not anticipated.  Second, since the islands chosen for removal lie on opposite ends of the Mississippi-Alabama barrier island chain, circulation changes brought about by one island loss scenario should not resemble circulation changes caused by removal of the other island.  Third, removal of the larger island should produce higher magnitude and wider spread modifications to circulation. As Chapter IV details, island removal results only partially support these hypotheses.

# CHAPTER II – VARIABILITY OF MISSISSIPPI SOUND AND BIGHT CIRCULATION

In order to evaluate circulation changes caused by the removal of a barrier island, observed variability in circulation must first be characterized. To that end, data from a collection of observational platforms were examined to extract patterns, and their associated variances, in circulation in the Mississippi Bight and Sound on time scales ranging from days to seasons. Chapter II examines variability in patterned circulation, i.e. seasonality, while Chapter III looks at tropical storms and hurricanes to isolate changes in circulation driven by non-cyclical forcing.

## 2.1 Data

### 2.1.1 High Frequency Radar

High frequency radar (HFR) data provide near-real time surface current maps over a wide study region with only a limited number of stations. In 1955, D. D. Crombie noted patterned interference in military radar and developed a system to retrieve surface current information from high frequency radar (Paduan and Graber, 1997). In the following decades, commercially-available HFRs became regular components of observing networks. The Central Gulf of Mexico Ocean Observing System (CenGOOS) uses 5 and 25 MHz direction-finding SeaSonde HF radars produced by Coastal Ocean Dynamics Radar (CODAR) Ocean Sensors (COS) (Howden, et al., 2011). The systems pair a transmit antenna with a set of receive antennas consisting of a monopole and cross-loop dipoles. Radio waves emitted by the transmit antenna backscatter off surface gravity waves. The strongest reflected signal occurs at one-half the transmitted wavelength, known as Bragg scattering. Once retrieved, the deep-water dispersion relation is used to subtract out the phase speed leaving the Doppler-shifted radial current speed towards and away from the site. In order to generate a two-dimensional surface current map, radial currents must be combined from multiple sites.

The CenGOOS HFR network has five sites. The two 25 MHz sites are located at the Silver Slipper Casino (Waveland, Mississippi) and the Pass Christian Yacht Club (Pass Christian, Mississippi). Installation of the stations followed the January 2016 opening of the Bonnet Carré Spillway. The higher frequency enables surface current estimates closer to shore with 1 km resolution, but the HFRs have limited range. Figure 2.1 shows the locations of the 25 MHz sites and grid points to which surface currents can be mapped. The higher frequency also tends to result in coverage loss during pulses of freshwater since the SeaSonde antennas perform poorly in low salinity and calm sea state conditions. Hence, the grid shown in Figure 2.1 represents an ideal grid; data does not exist for every grid point at all times.

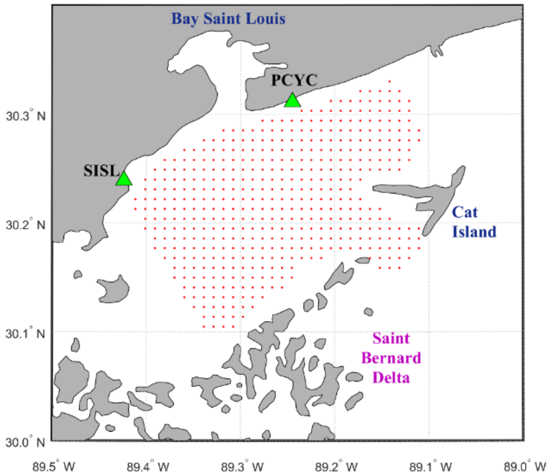

Figure 2.1 Map of 25 MHz HFR coverage domain

The locations of the Silver Slipper Casino, Mississippi, (SISL) and Pass Christian Yacht Club, Mississippi, (PCYC) sites are marked by green triangles. Grid points to which surface currents can be mapped are shown by red dots, and the locations of Cat Island, the Saint Bernard Delta, and Bay Saint Louis have been marked for reference within the study region.

The three 5 MHz sites are located on Singing River Island (Pascagoula, Mississippi), Gulf State Park (Orange Beach, Alabama), and Henderson Beach State Park (Destin, Florida). The sites were put back into operation in May 2010 after the Deepwater Horizon Oil Spill. These HF radars are long range meaning spatial resolution has a coarser 6 km grid (Figure 2.2), but the coverage region can extend several hundred kilometers offshore. Additionally, since the 5 MHz sites cover the Mississippi Bight rather than the Mississippi Sound, freshwater input causes little change in coverage though other factors do cause time-varying coverage, i.e. radar performance, ionospheric interference, etc.

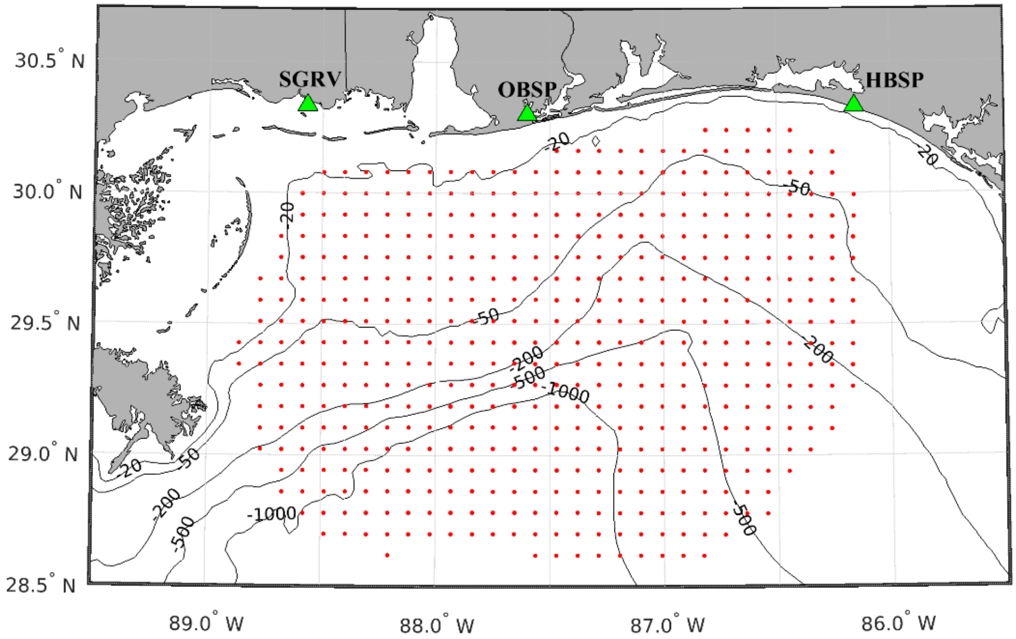

Figure 2.2 Map of 5 MHz HFR coverage domain

The locations of the Singing River Island, Mississippi, (SGRV), Gulf Shores (Orange Beach) State Park, Alabama, (OBSP), and Henderson Beach (Destin) State Park, Florida, (HBSP), sites are marked by green triangles. Grid points to which surface currents can be mapped are shown by red dots. Contours for the 20, 50, 200, 500, and 1000 m isobaths give indications on depth ranges throughout the study region.

Time-varying coverage and equipment takedown left sizeable gaps in the surface current record, so the length of record for the HFRs and the other datasets differ. Surface current data from 8 years of HFR coverage were used for the 5 MHz network. Monitoring began in May 2010, and multiple month gaps in coverage left several years patchy. Consequently, the longer record helped to provide fuller coverage for each month. In contrast, the 25 MHz sites started in February 2016, so 4 years of data were not available at the time of this study.

### 2.1.2 Buoy Measurements

Moored buoys operated by the National Data Buoy Center (NDBC) and the University of Southern Mississippi as well as a coastal station operated by the NDBC offer point source measurements for a variety of atmospheric and oceanic parameters. Atmospheric parameters include air temperature, atmospheric pressure, and wind speed and direction. Standard atmospheric data also includes wave height, average and dominant wave period, and water temperature. This study used data recorded at three locations. The first was NDBC buoy 42040 located in the southwest Mississippi Bight at 29.18°N, 88.21°W. The second was buoy 42067, operated by the University of Southern Mississippi, at 30.0423°N, 88.6473°W. Located south of Horn Island on the 20 m isobath, the buoy was recovered and not redeployed in 2017, so data availability ceased in July 2017. The third site was the NDBC Coastal-Marine Automated Network (C-MAN) station FMOA located by Fort Morgan in Alabama, at 30.228°N, 88.024°W. The pressure sensor on FMOA was not in operation for 2017. Red stars indicate the positions of the three buoys in Figure 2.3.

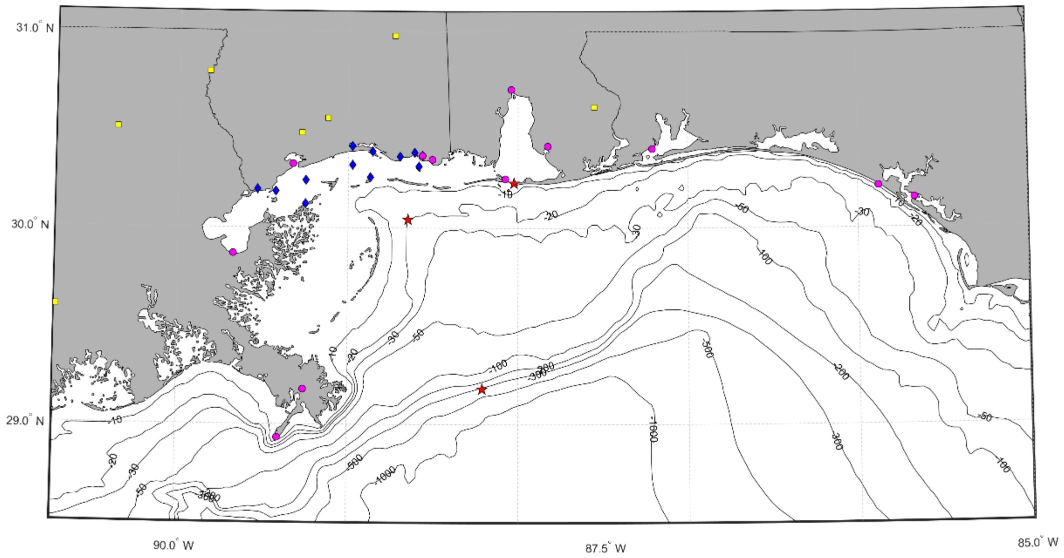

Figure 2.3 Locations of observing platforms

Red stars show the positions of buoy 42067 (top left), buoy 42040 (top right), and the FMOA C-MAN station (top right).  The twelve USGS-MDMR hydrological stations that collect bottom temperature and salinity data are depicted with blue diamonds while yellow squares mark the locations of USGS stream gages.  Magenta circles show the tide gages used in this study.

### 2.1.3 Hydrological Stations

The US Geological Survey and the Mississippi Department of Marine Resources jointly operate 14 hydrological stations in the western Mississippi Sound (MDMR, 2009). Twelve of the 14 stations record bottom water column temperature and conductivity data. Station numbers and names are given in (Table 2.1), and the location of the stations are marked by blue diamonds in Figure 2.3.  The Gibbs Seawater Toolbox was used to convert conductivity to salinity (McDougall and Barker, 2011).

Gridded temperature and salinity fields were generated for the western Sound to examine temporally varying horizontal gradients for the years 2014 to 2017, a period chosen since all 12 sites had coincident data.  Data gridding was accomplished using a cubic interpolation with Delaunay triangulation for spatial interpolation after monthly means were calculated (Watson, 1992).

Table 2.1 USGS-MDMR Hydrological Stations

| Station | Description | Latitude | Longitude |
|---|---|---|---|
| 1 | Pascagoula River | 30.3678°N | 88.5631°W |
| 2 | Round Island | 30.3136°N | 88.5833°W |
| 3 | West Pascagoula River | 30.3827°N | 88.6084°W |
| 4 | Graveline Bayou | 30.3629°N | 88.6947°W |
| 5 | Biloxi Bay at Point Cadet Harbor | 30.3883°N | 88.8572°W |
| 6 | East Ship Island | 30.2575°N | 88.8708°W |
| 7 | Central Mississippi Sound | 30.3200°N | 88.9758°W |
| 8 | Back Bay of Biloxi | 30.4156°N | 88.9758°W |
| 9 | Shell Bank Lighthouse | 30.2414°N | 89.2489°W |
| 10 | St. Joseph Lighthouse | 30.1844°N | 89.4261°W |
| 11 | East Pearl River | 30.1947°N | 89.5342°W |
| 14 | Mississippi Sound near Grand Pass | 30.1228°N | 89.2503°W |

### 2.1.4 Tide Gages

The Center for Operational Oceanographic Products and Services (CO-OPS) hosts water level predictions and observations on the National Oceanic and Atmospheric Administration’s (NOAA’s) Tides and Currents website. Tidal predictions result from the harmonic analysis of tidal constituents.

Three tide gage locations were selected for each of the four states that bound the Mississippi Bight: Louisiana, Mississippi, Alabama, and the Florida panhandle. This subset yielded water level variation across the northern Gulf coast within the study region. Station information is given in (Table 2.2), and locations of the gages are marked by magenta circles in Figure 2.3.

Table 2.2 NOAA Tide Gages

| Station | Description | Latitude | Longitude |
|---|---|---|---|
| 8729840 | Pensacola, FL | 30.4033°N | 87.2100°W |
| 8729210 | Panama City Beach, FL | 30.2133°N | 85.8783°W |
| 8729108 | Panama City, FL | 30.1517°N | 85.6667°W |
| 8732828 | Weeks Bay, AL | 30.4167°N | 87.8250°W |
| 8735180 | Dauphin Island, AL | 30.2500°N | 88.0750°W |
| 8737048 | Mobile State Docks, AL | 30.7050°N | 88.0400°W |
| 8741041 | Dock E, Port of Pascagoula, MS | 30.3483°N | 88.5050°W |
| 8741533 | Pascagoula NOAA Lab, MS | 30.3683°N | 88.5633°W |
| 8747437 | Bay Waveland Yacht Club, MS | 30.3250°N | 89.3250°W |
| 8760721 | Pilottown, LA | 29.1783°N | 89.2583°W |
| 8760922 | Pilots Station East, SW Pass, LA | 28.9317°N | 89.4067°W |
| 8761305 | Shell Beach, LA | 29.8683°N | 89.6733°W |

### 2.1.5 Stream Gages

The US Geological Survey operates stream gages across the Unites States. Station locations for this study were chosen based on major riverine input to the Mississippi Sound, the distance of a gage from the Sound, and whether the station data record reported discharge. Five USGS stations were used for stream estimates for the Pascagoula, Biloxi, Wolf, Pearl, and Alabama Rivers. Additionally, stations on the Gulf Intracoastal Waterway and Tangipahoa River were selected to represent the Mississippi River and Lake Ponchartrain respectively. Stream gage station information is provided in (Table 2.3). Yellow squares indicate the locations of the stream gages in Figure 2.3.

Table 2.3 USGS Stream Gages

| Station | Description | Latitude | Longitude |
|---|---|---|---|
| 02479000 | Pascagoula River (Merrill, MS) | 30.9781°N | 88.7269°W |
| 02481000 | Biloxi River (Wortham, MS) | 30.5586°N | 89.1219°W |
| 02481510 | Wolf River (Landon, MS) | 30.4836°N | 89.2744°W |
| 02489500 | Pearl River (Bogalusa, LA) | 30.7931°N | 89.8208°W |
| 07381331 | Gulf Intracoastal Waterway (Houma, LA) | 29.5981°N | 90.7100°W |
| 07375500 | Tangipahoa River (Robert, LA) | 30.5064°N | 90.3617°W |
| 02428400 | Alabama River (Claiborne, AL) | 30.6150°N | 87.5506°W |

## 2.2 Methods

### 2.2.1 Quality Control

Generating a resultant velocity vector field from the HF radars can be challenging, and a number of uncertainties are introduced prior to the final measurement. Radial components from multiple HFRs rarely align orthogonally. As such, several algorithms have been designed to approximate alignment based on the proximity of the measurements and the angle of alignment between the radial vectors. The CODAR software suite has one option (Lipa and Barrick, 1983). Another is an open source option from the radio operators working group (ROWG) (Kaplan, et al., 2007). Radial products are temporally and spatially averaged to improve the signal-to-noise ratio. Figure 2.4 shows the average uncertainty in cm/s for each grid cell within the 5 MHz domain. To be considered, grid points had to have data with uncertainties less than 5 cm/s at least 10% of the time. In addition to averaging, consideration of the Geometric Dilution of Precision (GDOP) enables quantification of surface current uncertainty. Figure 2.5 gives GDOP maps for the zonal (top plot) and meridional (bottom plot) components of velocity at each grid point.  Considering both components, the central Mississippi Bight has the lowest GDOP values while grid points near the outer bounds of HFR coverage have the highest.  Surface current speeds exceeding 200 cm/s were removed as part of quality control.  For annual and seasonal averages, vectors with more than 5 cm/s uncertainty were excluded, and days with fewer than 22 hours of coverage were removed.

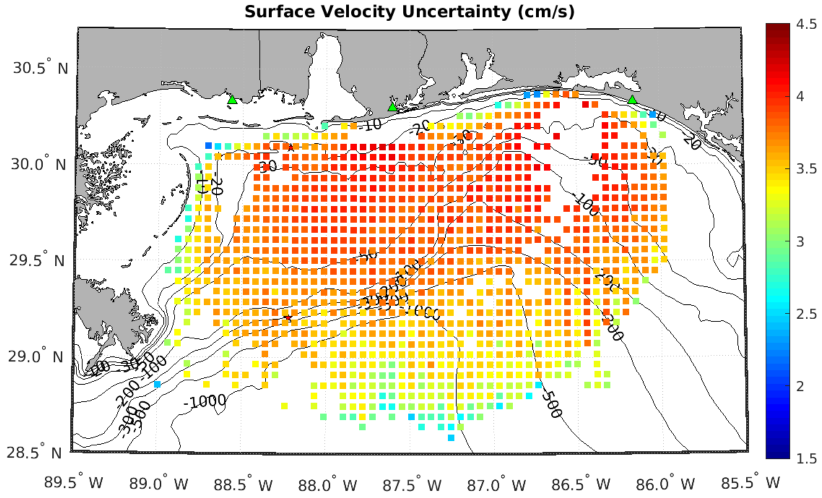

Figure 2.4 Surface current uncertainty

The colors of each square depict average uncertainty values for each 5 MHz grid cell that had coverage at least 10% of the length of the surface current time series.

Uncertainty thresholds were raised to 20 cm/s, and days with fewer than 22 hours were included for the hurricane season analysis.  Tropical cyclone periods (storm generation to dissipation) rarely exceed two weeks, so the emphasis was placed on hourly surface current changes rather than climatological averages.  Currents speeds during such storm periods sometimes exceeded seasonally-averaged currents by an order of magnitude.  Increased velocity uncertainty does not consistently accompany higher current speeds.  However, larger velocity magnitudes are more forgiving of uncertainties, and the higher uncertainty thresholds provide more data for storm period analysis.

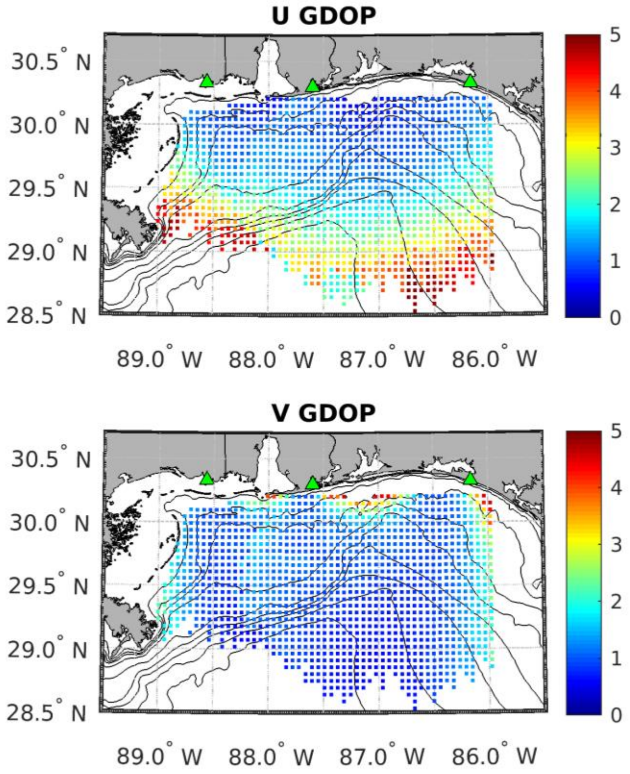

Figure 2.5 Geometric Dilution of Precision maps for 5 MHz high frequency radars

Geometric Dilution of Precision (GDOP) values between 0 and 5 are shown for each grid point to which velocities are mapped. U (zonal) GDOP values are displayed in the top plot; V (meridional) GDOP values are displayed in the bottom plot. Locations of the 3 high frequency radars are marked by green triangles.

Unreliable measurements from the other data sources had been replaced with flag values, which are preset values well above or below expected ranges in the measurements. Any values matching the flag values were replaced with NaN. The Louisiana tide gages each had notations that data for those sites were preliminary, so value ranges across the time series were checked for outliers and gaps. Several stations reported water levels more than 10 cm above predicted water levels persisting several weeks or months. The cause for this is uncertain, but given this trend, analysis of these stations will be reported but variability trends will not be based on Louisiana water levels.

### 2.2.2 Time Averaging and Covariance Calculation

For average HFR surface current vector maps, means of daily averages, for days with at least 22 hours of data, were taken at each grid point for every grid point containing at least 2 days of data. Periods under consideration ranged from one day to seasonal, but averages presented in section 2.3 concentrate on monthly means to best capture the annual signal. Covariance matrices were calculated for each grid point using zonal and meridional components of surface velocity, and eigenvalues and eigenvectors were found for each 2x2 covariance matrix. The larger eigenvalue denoted the semi-major axis, and eigenvectors were used to find the orientation of the semi-major and semi-minor axes. Covariance ellipse plots were generated from these calculations.

### 2.2.3 Power Spectra

Many of the results presented in section 2.3 refer to monthly means and standard deviations from those means, but power spectral density analysis provided insights into shorter term dominant frequencies for each dataset used in this study. Methodology for completing the fast Fourier transforms (FFTs) in MATLAB followed the process outlined by Frigo and Johnson (1998). Exclusion of NaN values from the time series preceded power spectral density analysis as did removal of the mean, to pre-whiten data. Possible linear trends were also removed before analysis. The length of the fast Fourier transform was found by raising 2 to the logarithm base 2 of the temporal length of the time series plus 1. The number of frequency bins were set to half the length of the FFT, and the frequency vector was obtained by dividing the product of the Nyquist frequency and the number of frequencies by the number of frequency bins. A discrete Fourier transform (DFT) of the pre-whitened, de-trended data transformed the data from the time domain to the frequency domain. Power spectral densities resulted from multiplying the DFT by its complex conjugate and dividing that product by the length of the FFT. Symmetric portions of the power spectral density were removed to avoid repetitive information. The process highlighted key frequencies of variability.

## 2.3 Results

### 2.3.1 Mississippi Bight Circulation

Results for Mississippi Bight circulation came primarily from HFR-derived surface currents. From 2010 to 2017, 5 MHz HFR data produced surface velocity estimates at 1,361 coordinate pairs, and 1,126 of those pairs met the criteria for averaging with 2 to 1,239 days contributing to each average. Without the 22 hours per day requirement, the number of data points available for averaging ranged from 2 to more than 3,000 depending on the grid point. Grid points falling between 29.4°N to 30.1°N and 88.5°W to 86.5°W tended to have more than 500 days of available data while grid points closer to the boundaries of HFR coverage had less than 200 days. Given the time-varying coverage, having the most consistent coverage in the central study area where overlapping radial vectors occur more frequently makes sense.

Average current speeds for every season fell short of 6 cm/s and monthly averages were less than 10 cm/s. Average speeds at individual grid points tended to be under 15 cm/s with a few exceptions along the northern and southern bounds of the HFR domain. Given the fewer days included in the averaging process for these areas, this result is not surprising.

Two sets of average currents speeds are presented in Figures 2.6: means and standard deviations from days with 22 hours or more of coverage and means and standard deviations found using all data. Mean speeds were calculated from vector-averaged velocities, and the difference in average values results from the inclusion of different data. The disagreement between the statistics of the two demonstrates how procedures can affect results. The 22 hours of coverage threshold attempts to avoid biasing by removing data for days that do not adequately cover a full tidal cycle. Monthly means using the 22 hour criteria favor winter (January and February) and fall (September, October, and November) months for higher current speeds. However, July does have the largest mean current speeds in both sets of averages. Looking at the entire dataset, the summer months (June, July, and August) have the highest current magnitudes followed by the spring months (March, April, and May). The two averages agree on July having the highest current speeds. Monthly averages disagree beyond that, but the differences are not statistically significant given the magnitudes of the standard deviations.

The means taken using the 22 hours per day criterion will be used as representatives of monthly patterns since they include data from all portions of the tidal cycle. It would, however, be remiss not to note that the lower spring and summer current speeds may result from inconsistent coverage during those months. More years of data may present different statistics.

Changes in flow direction indicate a shift in flow regimes throughout the calendar year. Long-range HFR coverage begins south of the Mississippi-Alabama barrier islands, so surface current data is often sparse in that region. From the coverage that does exist, a westward longshore current is present during the winter and early spring months, but the current reverses direction and points east during summer months before transitioning back to westward in the fall. Consistent outflow can be seen from Mobile Bay as well as bays in Florida between the OBSP and HBSP sites. Finally, though a dominant flow direction is sometimes present in the monthly climatologies, mean surface current direction and speed vary throughout the Mississippi Bight.

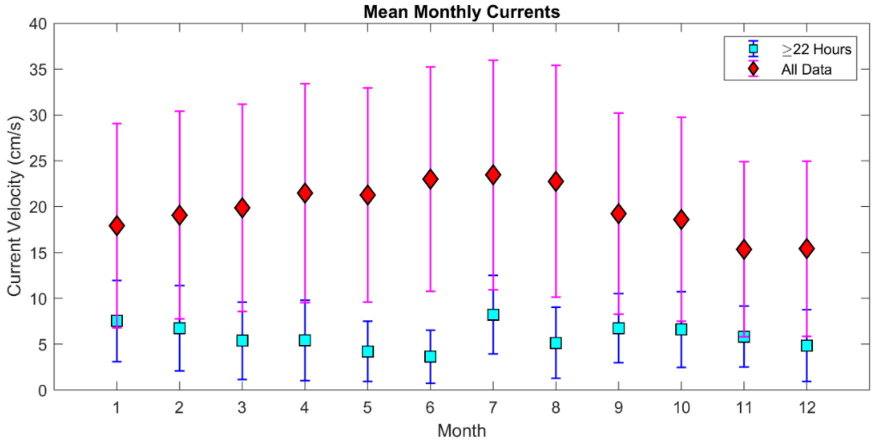

Figure 2.6 Mean monthly surface current speeds

Cyan squares give the average monthly surface current magnitude across the Mississippi Bight with standard deviations given by blue lines. Data used in these averages came from days with at least 22 hours of coverage. Red diamonds give the average monthly current speed using all available data, and magenta lines show standard deviations from those means.

Surface current monthly climatologies sometimes seem to contain eddies. The climatologies only include 8 years of data, so monthly averages can show an eddy that was present in the region during one year but not during the others. Likewise, flow in the same month from one year to the next can be quite different. Averaging the different flow patterns can produce patches of randomly oriented surface currents in a climatological current field. To give a few examples, an apparent cyclonic eddy appears in the northeast corner of the domain during February and March. Likewise, an anticyclonic feature can be seen in the northwest domain in May. Surface currents point in seemingly random directions in the easternmost portion of the HFR domain in the same month. Finally, a cyclonic feature appears in October in the south-central Mississippi Bight. Mesoscale eddies do enter the Mississippi Bight on occasion. Eddies would alter circulation in the Mississippi Bight, but a longer climatology would average out their effects. The monthly climatologies give a reasonable picture of how circulation evolves throughout a year, but unusual features, like eddies, will not be discussed as they may not be present year to year.

Mean January surface currents mostly stay under 15 cm/s. In Figure 2.7, a channel of southwest flow can be seen south of the OBSP site; the flow moves south then turns eastward further south in the Bight. Covariance ellipses shown in Figure 2.8 have a median semi-major axis of 110 cm/s and a median semi-minor axis of 39 cm/s. Though some ellipses at the edge of HFR coverage have semi-major axes larger than 800 cm/s, the majority stay under 200 cm/s. The ellipses become more circular in the central Bight.

Mean current speeds in February stay largely below 10 cm/s. Southward flow extends south of the OBSP site. In Figure 2.9, regions of southeastward currents can be seen south of Dauphin Island as well as in the southeastern Mississippi Bight. Figure 2.10 depicts covariance ellipses for February. Semi-major axes orient along bathymetric contours to about 30 m depths. The median semi-major axis is 150 cm/s while the median semi-minor axis is 45 cm/s. Ellipses are more rounded than in January.

As in February, mean March surface currents stay under 10 cm/s across most of the domain, but westward flow occurs throughout the Mississippi Bight. Figure 2.11 shows currents point westward in the northern Bight, southwestward in the western Bight, and northwestward in the eastern Bight. In Figure 2.12, the median semi-major axis length is 124 cm/s, and the semi-minor axis length is 50 cm/s. Covariance ellipses were more circular than the previous two months, especially in the western Bight.

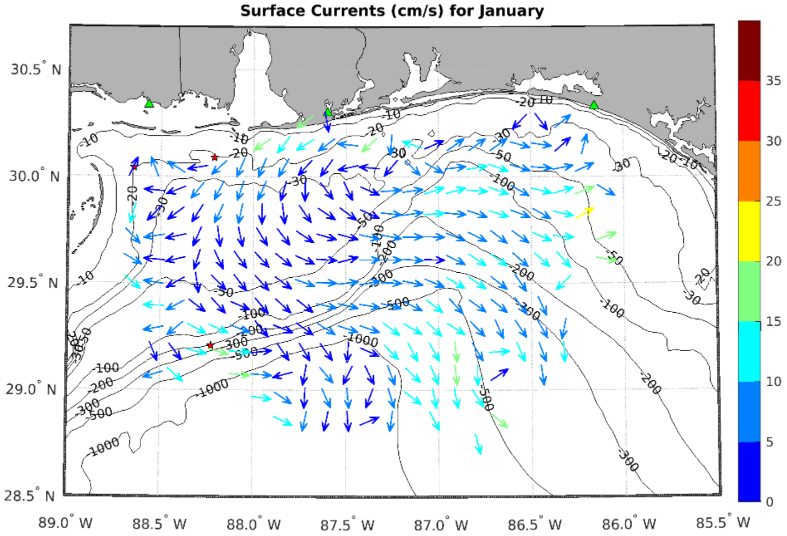

Figure 2.7 Mean surface currents for January

Arrow direction indicates the direction of flow while arrow color indexes velocity magnitude in cm/s. HF radar locations are marked in green. Only one-quarter of the HFR grid points are plotted for visual clarity.

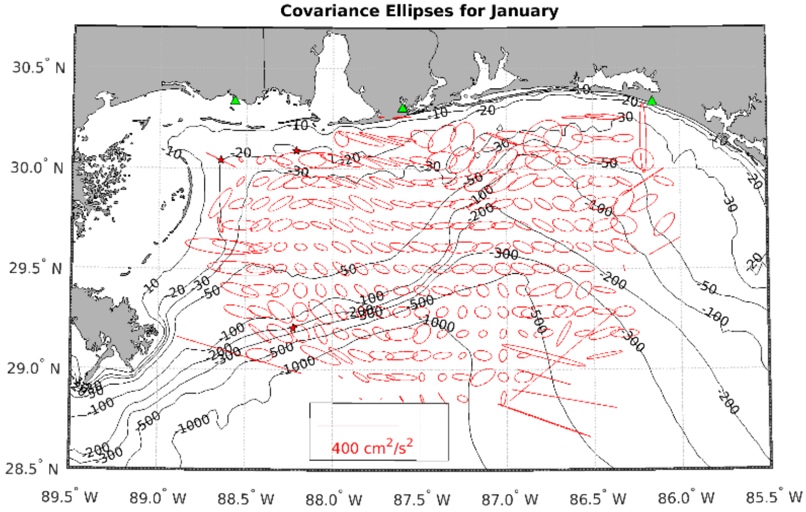

Figure 2.8 Covariance ellipses for mean January currents

Ellipses were calculated based on the covariance matrices for each grid point. Units on the reference bar are $cm^2/s^2$ for area, but the semi-major and semi-minor axes have units of cm/s. Angle depicts tilt direction of the semi-major axis while eccentricity of ellipse shows the ratio of the semi-major axis to the semi-minor axis. As with Figure 2.7, covariance ellipses are only shown for one-quarter of the grid.

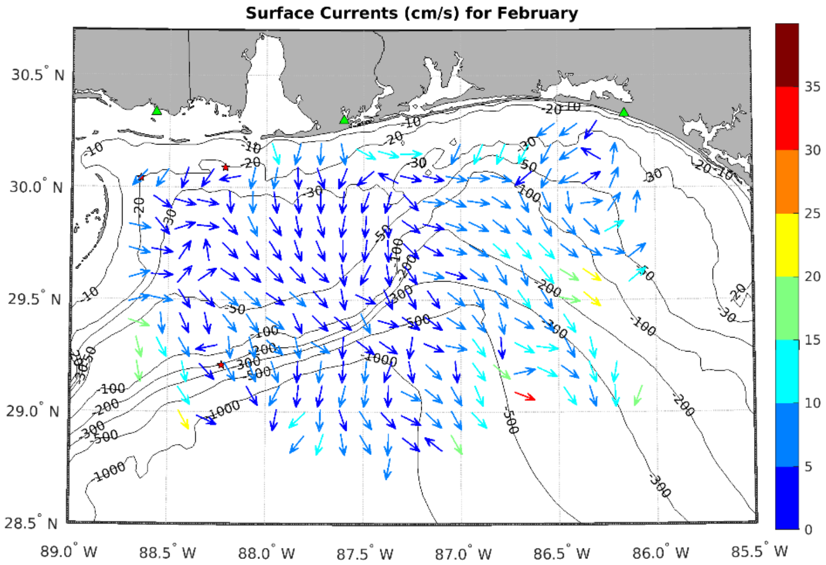

Figure 2.9 Mean surface currents for February

Same as Figure 2.7 but for February.

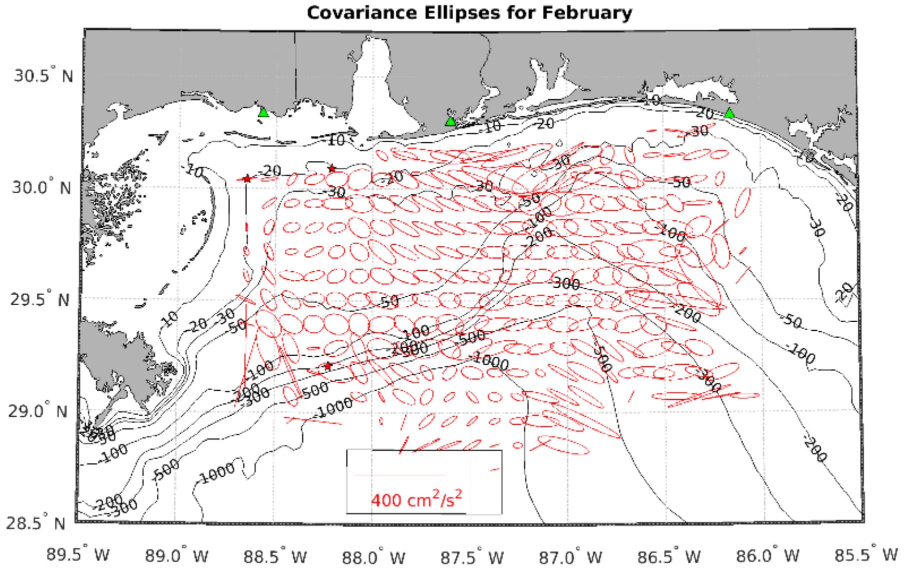

Figure 2.10 Covariance ellipses for mean February currents

Same setup as Figure 2.8.

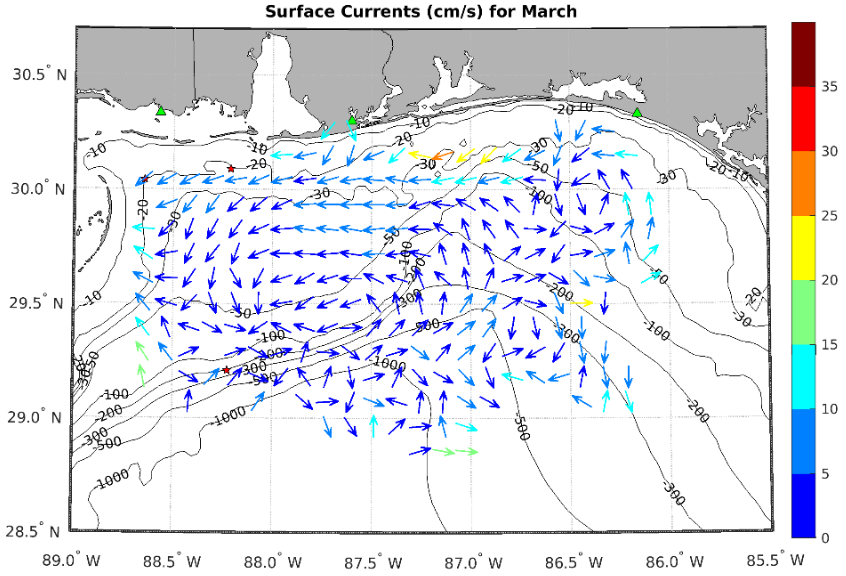

Figure 2.11 Mean surface currents for March

Same as Figure 2.7 but for March

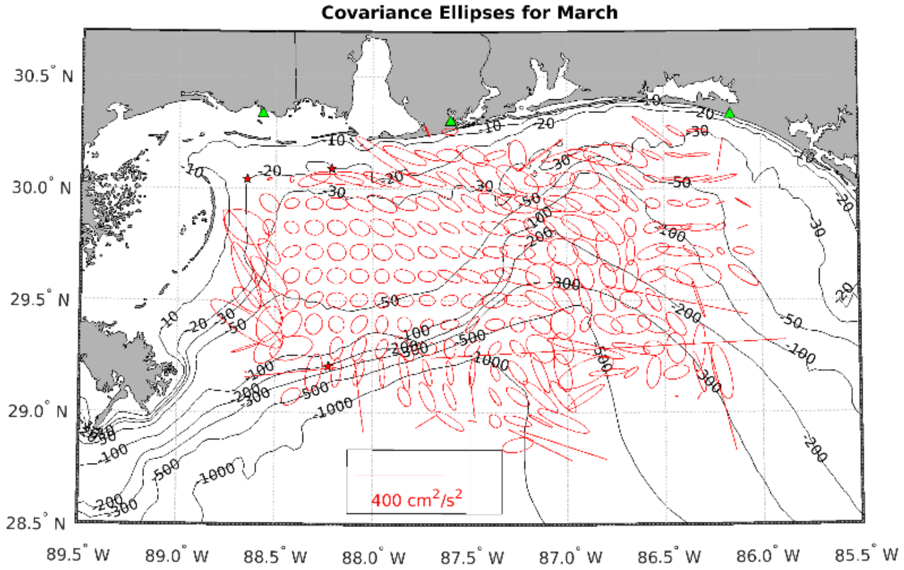

Figure 2.12 Covariance ellipses for mean March currents

Same as Figure 2.8 but for March.

Surface currents in April stayed under 5 cm/s except along the northern and southern boundaries of the HFR coverage.  A channel of westward flow can be seen south of the Mississippi-Alabama barrier islands in Figure 2.13.  Currents point south from the OBSP site, and flow moves southwest over the De Soto Canyon.  The southeastern Bight is characterized by eastward and southward surface currents while the southwestern and south-central Bight see westward currents.  In Figure 2.14, covariance ellipse size and eccentricity resemble January covariance ellipses, but semi-major axes align with isobaths shallower than about 40 m.  Median lengths for the semi-major and semi-minor axes are 107 cm/s and 42 cm/s respectively.

Mean current speeds in May ranged between 0 and 10 cm/s except for isolated grid points near the edge of HFR coverage.  Surface currents flow south from the entrance to Mobile Bay and west in the north-central and northeastern Bight in Figure 2.15.  The southwest flow across De Soto Canyon that was present in April continues in May, but the southeastern Bight sees eastward currents.  In Figure 2.16, ellipse sizes decreased from April to May; the median semi-major and semi-minor axes fall to 96 cm/s and 41 cm/s respectively.  Some isobaths alignment can be seen near the coast, and covariance ellipses have high eccentricity there.

Mean June currents depicted in Figure 2.17 stay under 10 cm/s.  Current directions range from southeastward to southward south of the Mississippi-Alabama barrier islands, northward in the southwestern Bight, and eastward in the eastern Bight. Semi-major axes on the covariance ellipses shown in Figure 2.18 run east-west, northwest-southeast, and north-south.  Median semi-major and semi-minor axes lengths decrease; they are 95 cm/s and 38 cm/s in June.

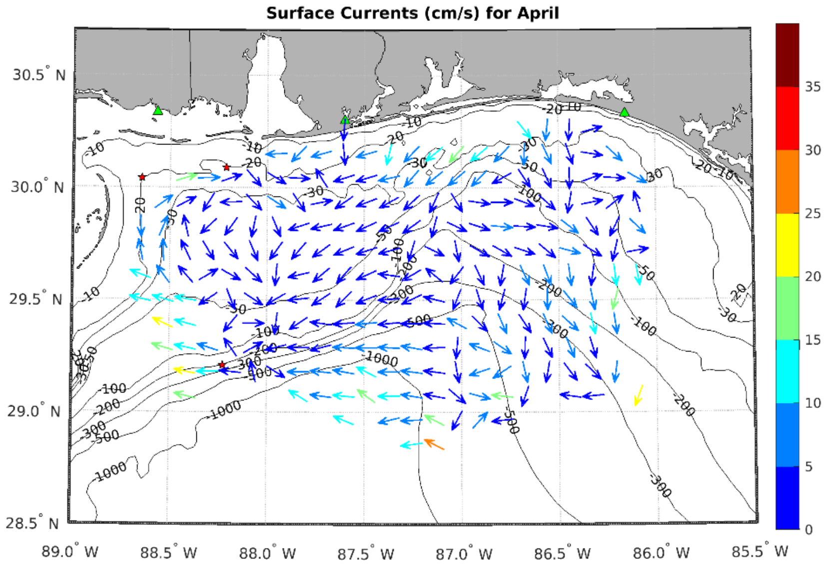

Figure 2.13 Mean surface currents for April

Same as Figure 2.7 but for April.

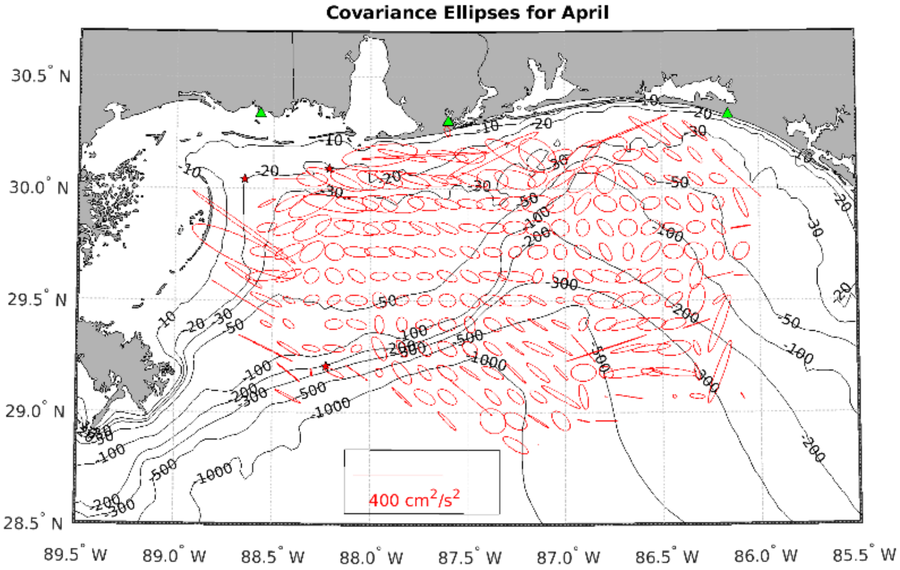

Figure 2.14 Covariance ellipses for mean April currents

Same as Figure 2.8 but for April.

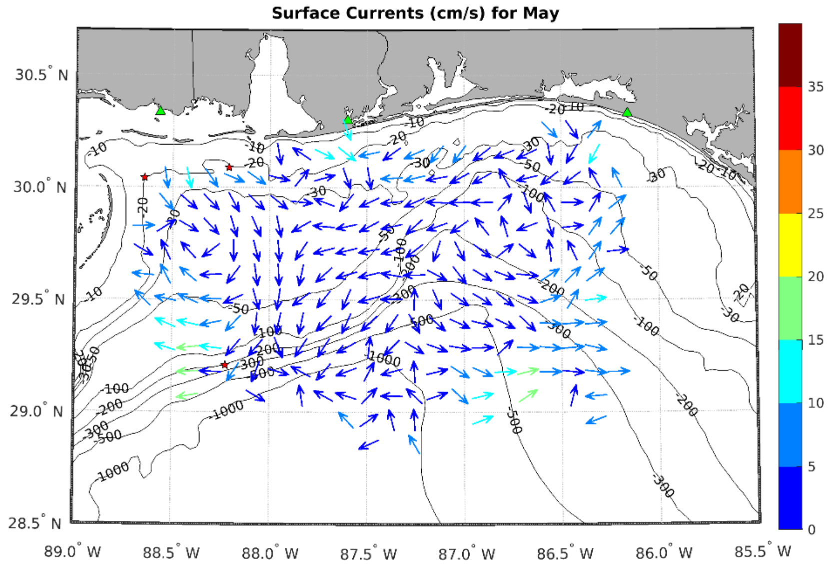

Figure 2.15 Mean surface currents for May

Same as Figure 2.7 but for May.

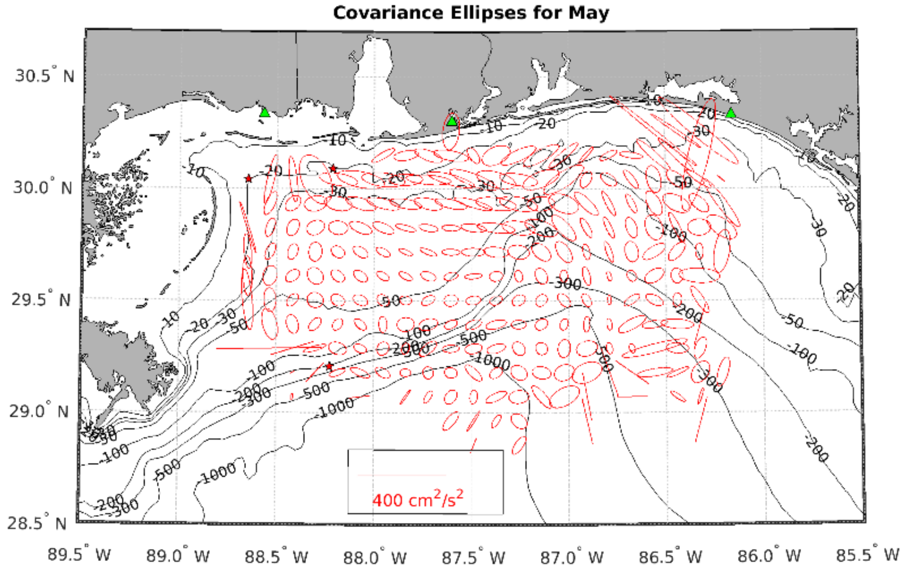

Figure 2.16 Covariance ellipses for mean May currents

Same as Figure 2.8 but for May.

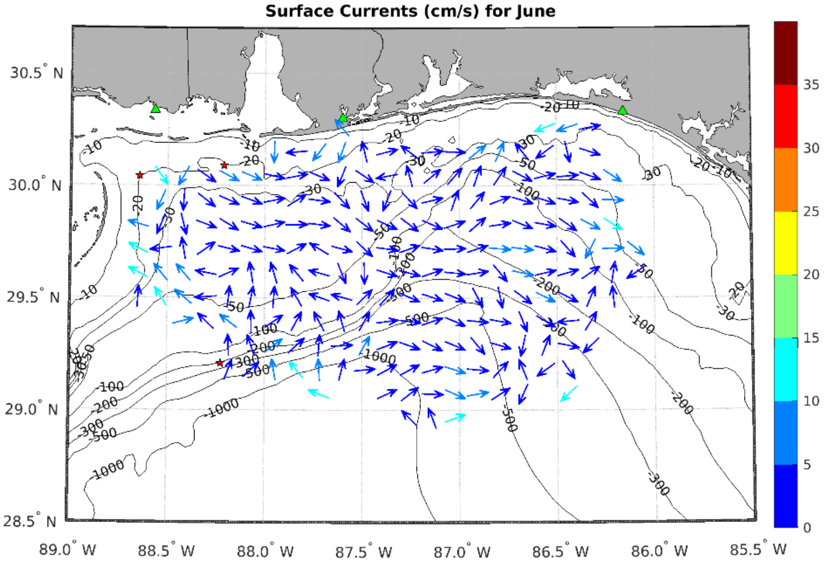

Figure 2.17 Mean surface currents for June

Same as Figure 2.7 but for June

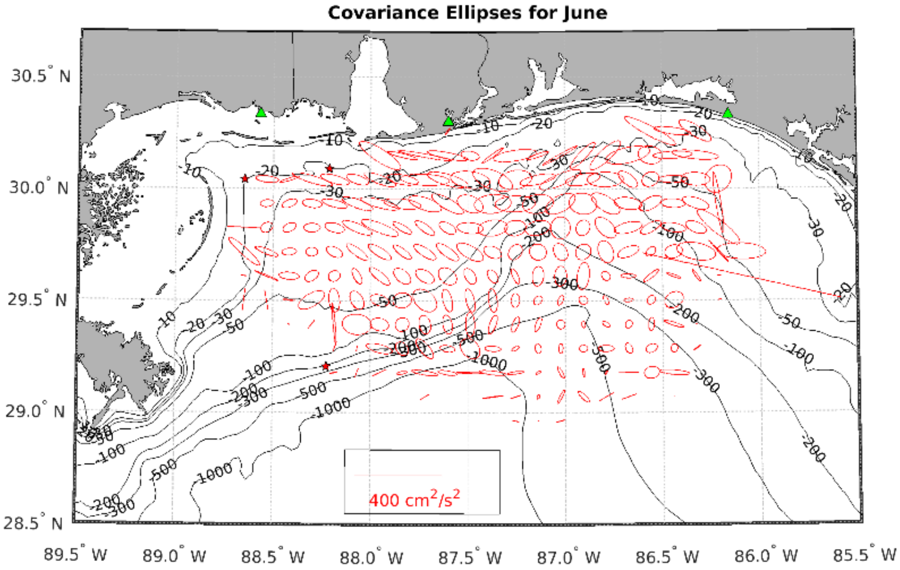

Figure 2.18 Covariance ellipses for mean June currents

Same as Figure 2.8 but for June.

Mean current speed increases in July with the majority of the domain falling between 0 and 15 cm/s, but isolated areas have speeds between 15 and 25 cm/s. Figure 2.19 shows a southeastward flow from the Mississippi-Alabama barrier islands, an eastward flow in the eastern Bight as well as in the southwestern Bight. The median semi-major axis length increased to 113 cm/s from the June median value while the median semi-minor axis length decreased slightly to 36 cm/s. Figure 2.20 shows covariance ellipses for July which oriented predominantly east-west and northwest-southeast.

August mean current speeds stay under 15 cm/s for most of the domain. The southeastward surface flow south of the Mississippi-Alabama barrier islands that was present in both June and July remains during August (Figure 2.21). Similar to July, currents in the southeast and southwest Mississippi Bight point eastward, but flow also moves to the east in the northeast Bight. A channel of southward flow can be seen south of the OBSP site. As in previous months, August covariance ellipse semi-major axes follow bathymetry contours in shallow water, but ellipses shown in Figure 2.22 align with some of the <100 m isobaths off the northern Florida shelf. Median lengths for the semi-major and semi-minor axes are 102 cm/s and 32 cm/s. Ellipse size increases dramatically in the south-central and southeastern Mississippi Bight.

September mean surface current speeds stay mostly under 15 cm/s, and the majority of the HFR coverage area had westward currents in contrast to the eastward currents present during the summer months. Figure 2.23 shows westward currents in the northwest Bight turning southward. Semi-major axes of covariance ellipses in Figure 2.24 orient east-west except for grid points over the Florida shelf where ellipses align northwest-southeast and north-south. Median semi-major and semi-minor axes are 121 cm/s and 32 cm/s respectively.

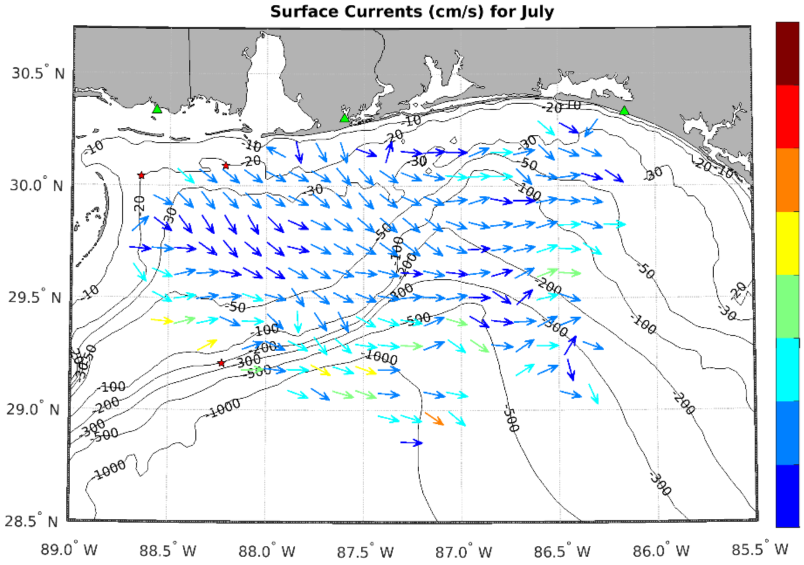

Figure 2.19 Mean surface currents for July

Same as Figure 2.7 but for July.

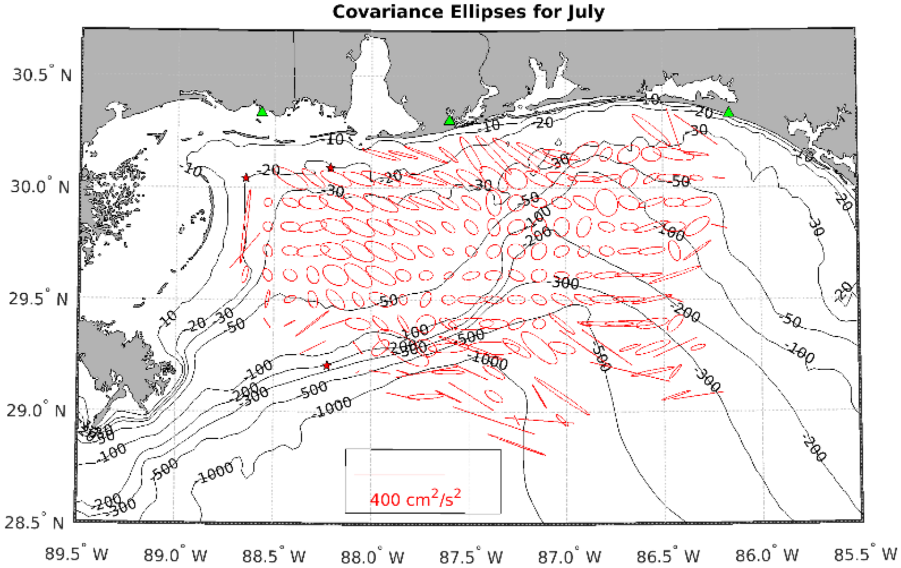

Figure 2.20 Covariance ellipses for mean July currents

Same as Figure 2.8 but for July.

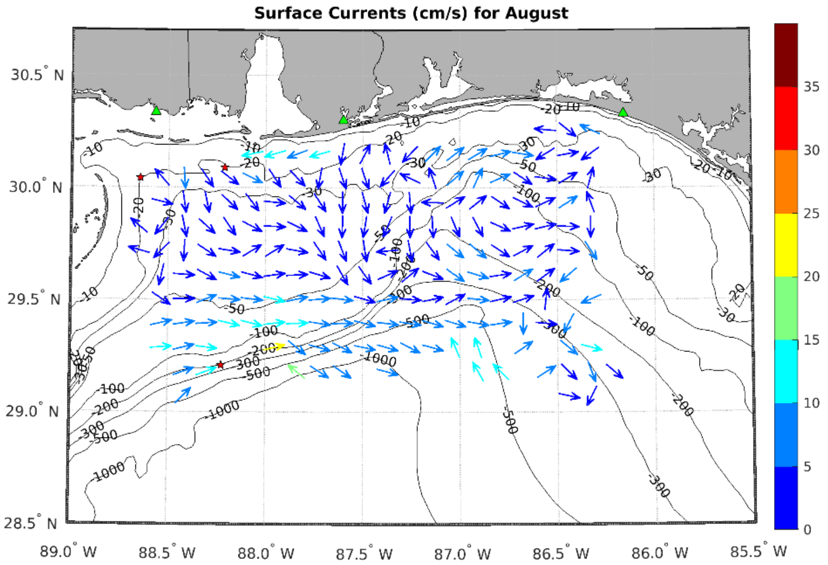

Figure 2.21 Mean surface currents for August

Same as Figure 2.7 but for August.

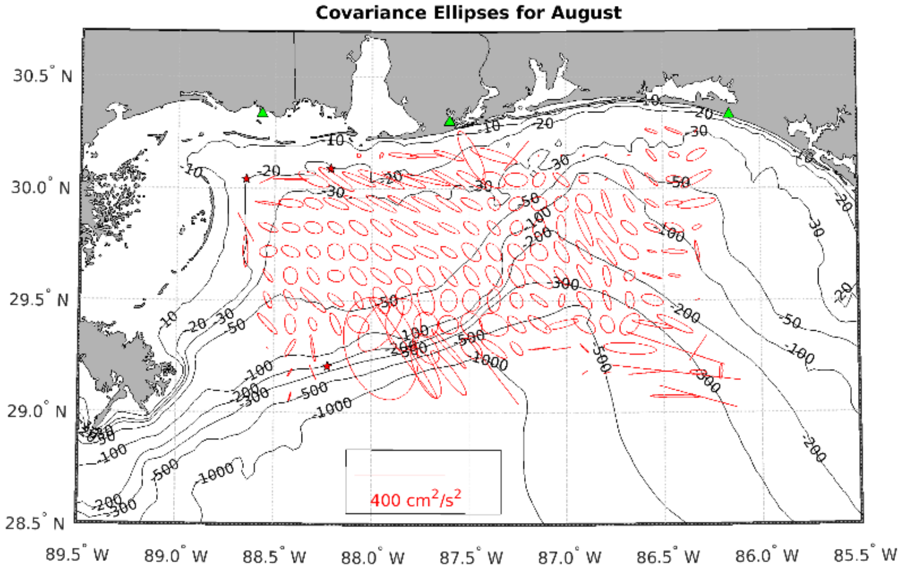

Figure 2.22 Covariance ellipses for mean August currents

Same as Figure 2.8 but for August.

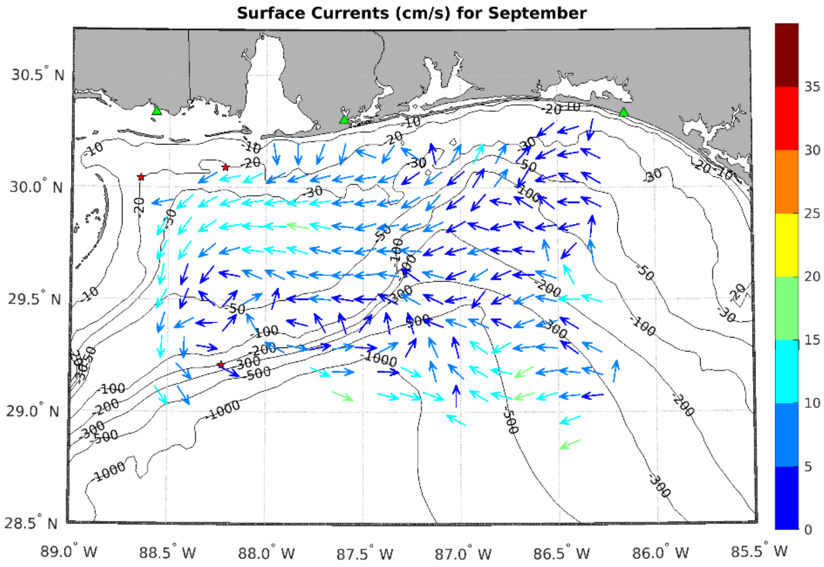

Figure 2.23 Mean surface currents for September

Same as Figure 2.7 but for September.

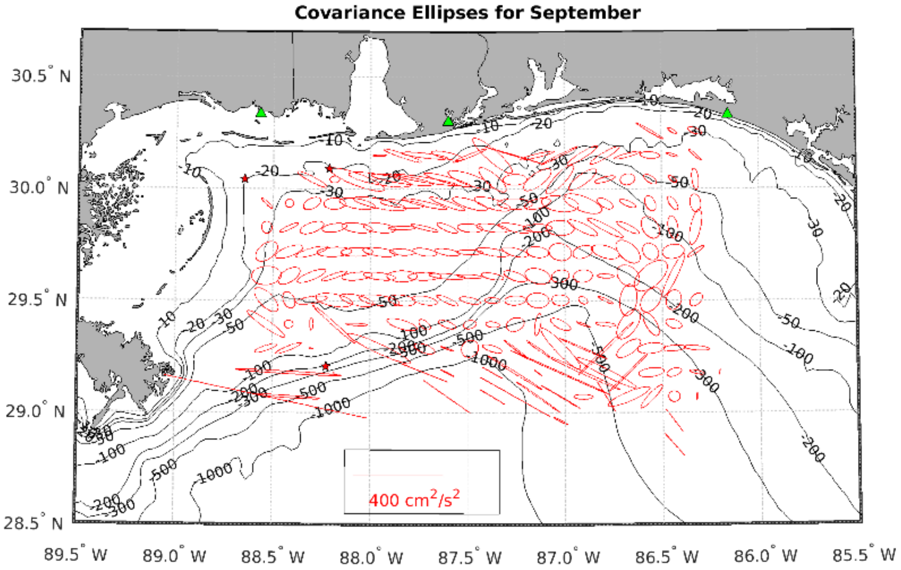

Figure 2.24 Covariance ellipses for mean September currents

Same as Figure 2.8 but for September.

General westward flow occurs in October as well, and mean current speed range from 0 to 5 cm/s. A channel of southwest flow appears in Figure 2.25 south of the OBSP site. Flow moves west in the northern Bight and northwest in the eastern Bight. Median semi-major and semi-minor axes for October are 161 cm/s and 36 cm/s, so October has the largest ellipses. The ellipses also have high eccentricity. Figure 2.26 shows the covariance ellipses which orient east-west across the study area.

As in previous months, mean November surface current speeds stay under 15 cm/s, and directionality largely points to the west. Figure 2.27 shows southwest flow from Mobile Bay and south of the OBSP site. Westward currents mark the central and southeastern Mississippi Bight, but southeastern currents appear in the western Bight. Flow moves south from bays in the Florida panhandle southwest of the HBSP site. November covariance ellipses mostly align west-east in Figure 2.28 with median semi-major and semi-minor axis lengths of 118 cm/s and 26 cm/s.

December mean surface current speeds fall between 0 and 15 cm/s, and a larger variety of current directions appears. Figure 2.29 shows southward flowing currents from the OBSP site, eastward currents in the eastern Bight, westward currents in the northwest Bight, and southward currents from the Florida panhandle southwest of the HBSP site. Covariance ellipses in Figure 2.30 align east-west and have median semi-major and semi-minor axes of length 116 cm/s and 33 cm/s respectively. Power spectra for different regions within the study domain all point to a 1 cycle per day (cpd) frequency for both zonal and meridional components of velocity; however, the power spectra are noisy. Small peaks at 2 cpd appear for the northwestern Bight, but the magnitudes of the peaks are an order of magnitude less than the 1 cpd peaks. These results agree with the time series analysis of surface current directions.  Velocity vectors rotate 360° over an approximately 24 hour period.

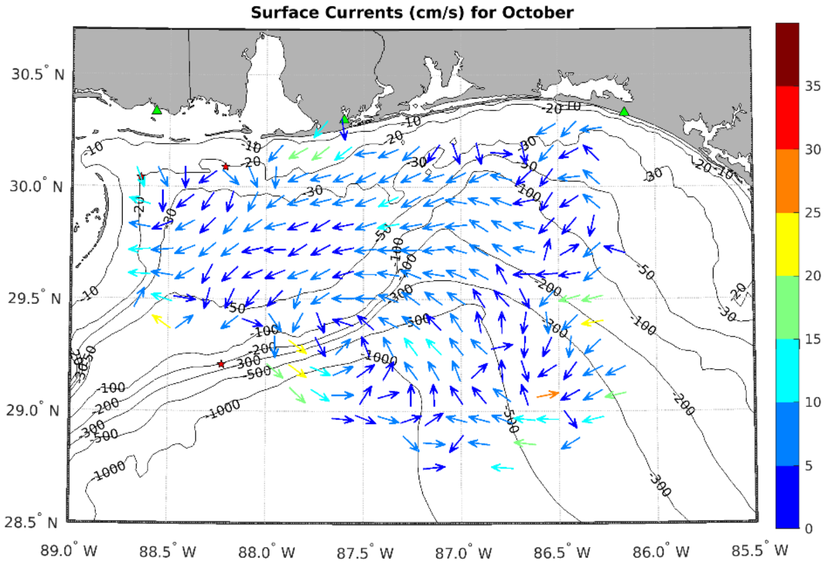
Surface Currents (cm/s) for October

Figure 2.25 Mean surface currents for October

Same as Figure 2.7 but for October.

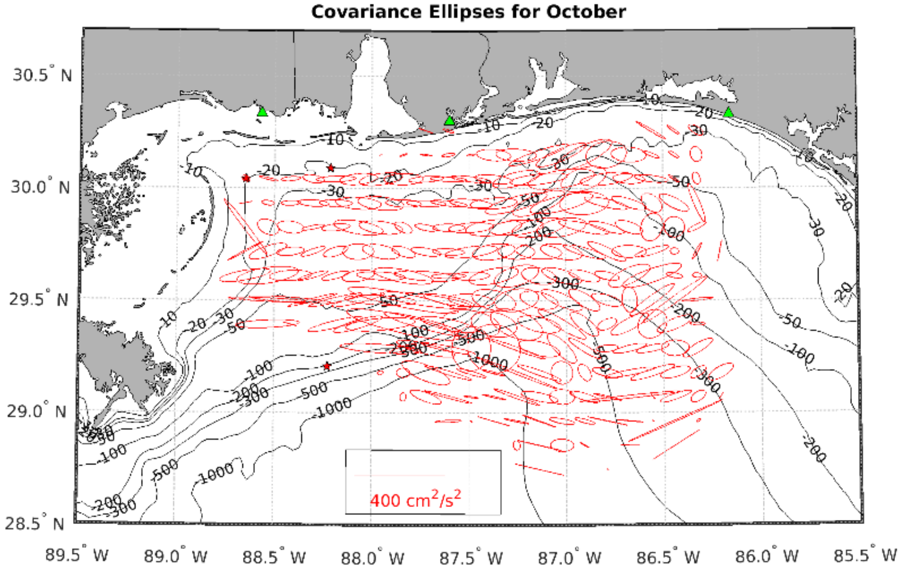
Covariance Ellipses for October

Figure 2.26 Covariance ellipses for mean October currents

Same as Figure 2.8 but for October.

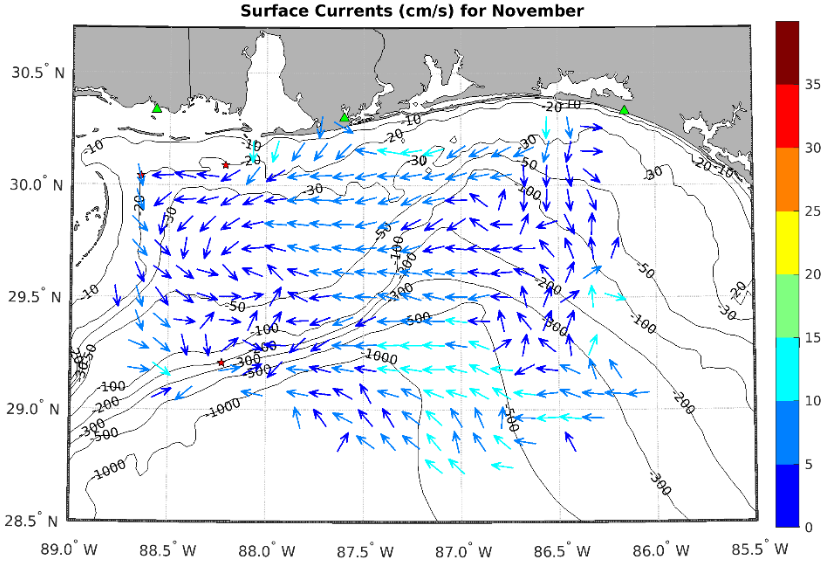

Figure 2.27 Mean surface currents for November

Same as Figure 2.7 but for November.

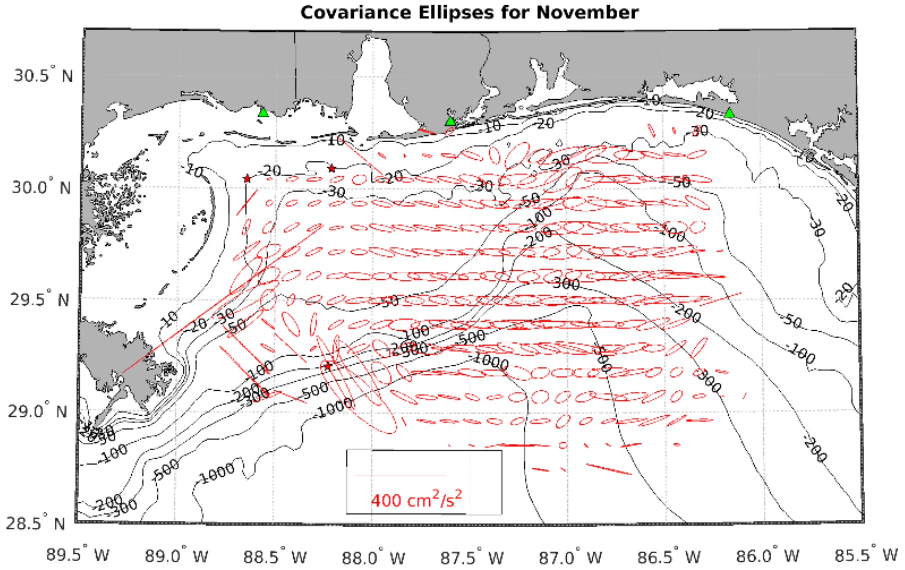

Figure 2.28 Covariance ellipses for mean November currents

Same as Figure 2.8 but for November.

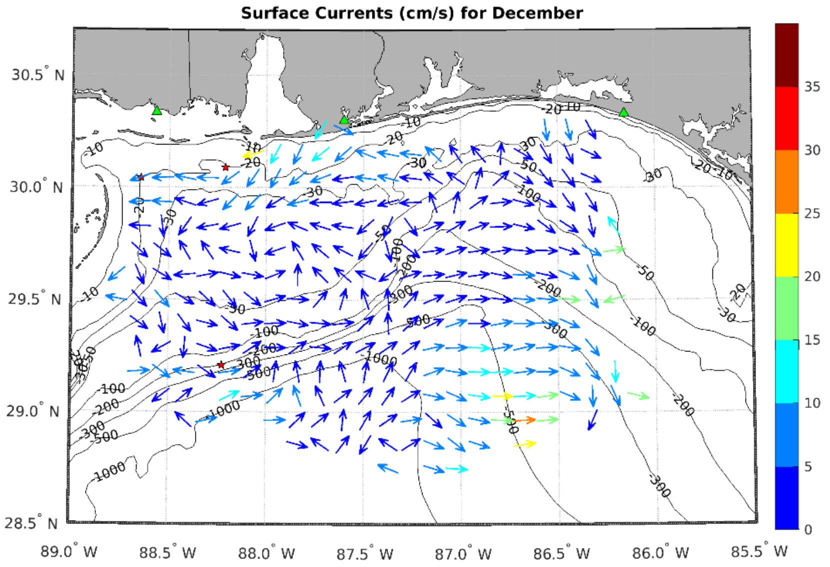

## Figure 2.29 Mean surface currents for December

Same as Figure 2.7 but for December.

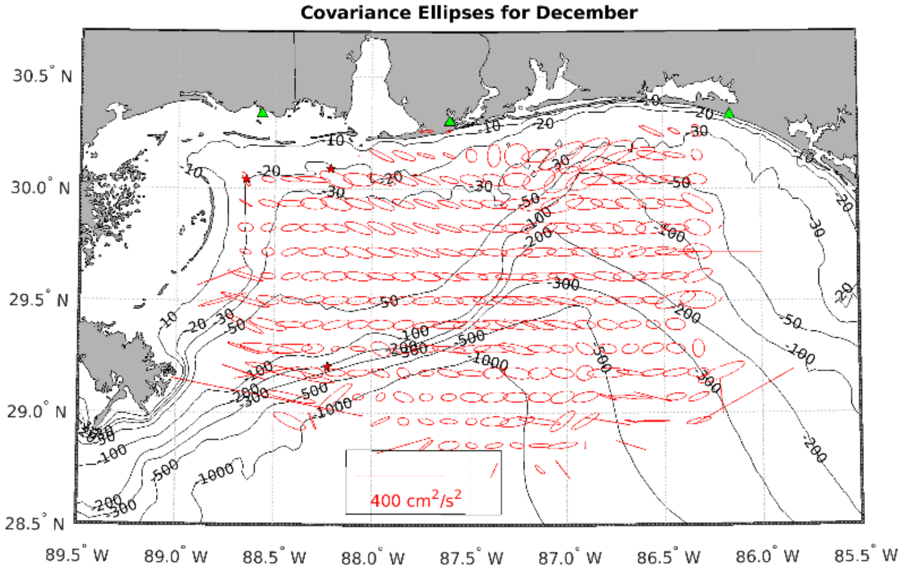

## Figure 2.30 Covariance ellipses for mean December currents

Same as Figure 2.8 but for December.

Monthly mean values from the two buoys and the C-MAN station give insights into the near surface atmospheric conditions as well as more details for the surface ocean in the Mississippi Bight. Results for monthly climatological averages are shown in Figures 2.31 through 2.42. Wind direction frequency is presented in histogram form since monthly averages misrepresent dominant wind directions. Shown in Figures 2.31, 2.32, and 2.33, wind speeds peak October to February. Higher magnitudes occur with tropical cyclones, but these events last less than 2 weeks. Consequently, the average wind speeds from June to September fall below those seen in winter months.

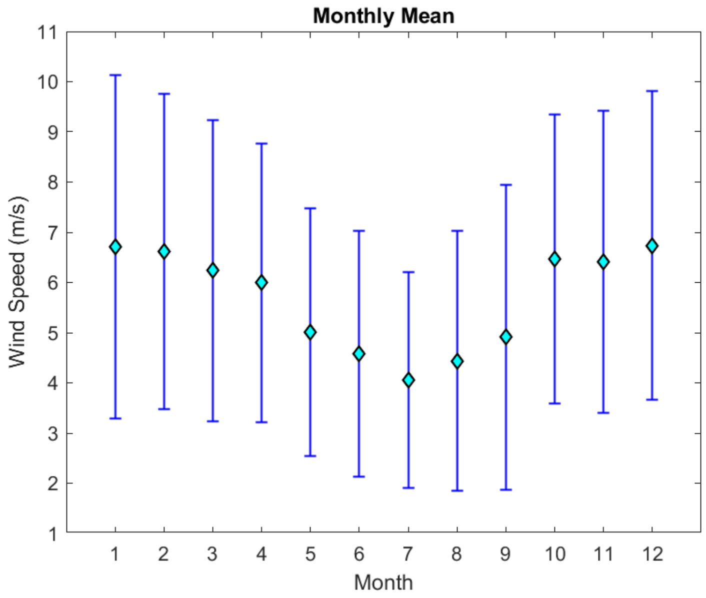

Figure 2.31 Mean monthly wind speeds at NDBC buoy 42040

Monthly climatologies, shown with cyan diamonds, were calculated using 2014 through 2017 data; the blue lines show standard deviations from the means.

Gulf-wide wind patterns see a shift from northeasterly and northerly in fall and winter to southeasterly in spring and summer (Chang and Oey, 2013; Johnson, 2008). The patterns at the three sites in the Mississippi Bight differ somewhat from these results. Distributions shown in Figures 2.34, 2.35, and 2.36 reveal northeasterly winds for

September through January. The USM buoy, Figure 2.36, has a secondary peak in January for northerly winds while a smaller easterly peak occurs in the November distribution for buoy 42040, Figure 2.34. Smaller southeasterly peaks also are present in the December and January histograms for buoy 42040 and the December data for the USM buoy. Southeasterly winds dominate at all three sites March through May, and southwesterly winds take over in July and August. Dominant wind directions do not agree between the sites in February and June. In February, buoy 42040 shows southeasterly winds. FMOA has northeasterly and southerly wind peaks, and the USM buoy shows a preference for southerly and southwesterly winds. As for June, buoy 42040 and FMOA see increased occurrences of southeasterly to southerly to southwesterly winds, but southerly and southwesterly winds only occur with higher frequency at the USM buoy.

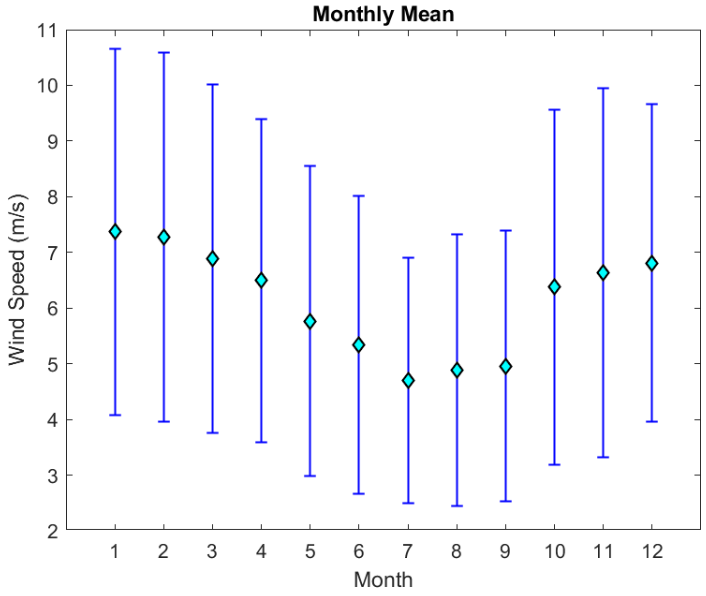

Figure 2.32 Mean monthly wind speeds at C-MAN station FMOA

Monthly climatologies, shown with cyan diamonds, were calculated using 2014 through 2017 data; the blue lines show standard deviations from the means.

In Figures 2.37, 2.38, and 2.39, January had the lowest monthly temperatures at all three sites while July and August saw the highest temperatures at roughly 28°C. The January minimum varied between 12°C and 16°C; as the shallowest station, FMOA had the lowest temperature while the most seaward location, buoy 42040, had the highest. Monthly average surface water temperatures at the USM buoy shown in Figure 2.40 followed the temperature range and pattern of buoy 42040's monthly air temperatures. Overall, measurements at the three locations aligned closely with one another.

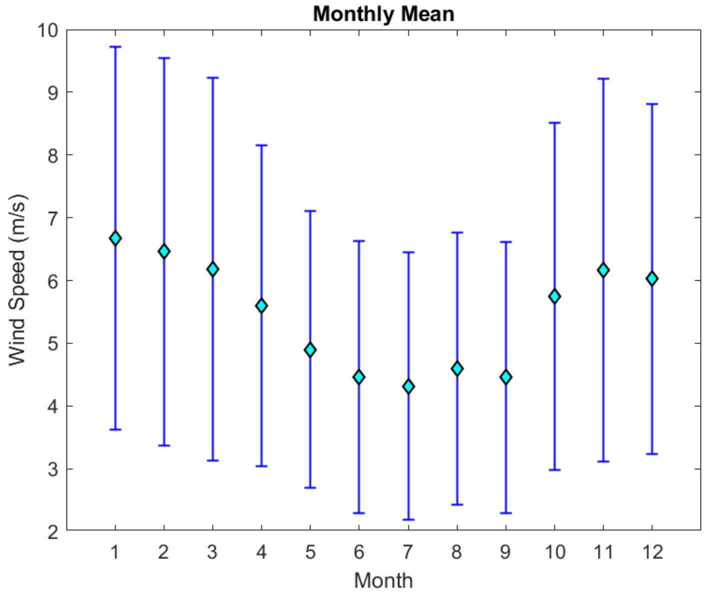

Figure 2.33 Mean monthly wind speeds at USM buoy

Monthly climatologies, shown with cyan diamonds, were calculated using 2014 through 2017 data; the blue lines show standard deviations from the means.

Some parameters were only measured at one of the three locations; these include wave heights and sea surface salinity. Buoy 42040 measures wave height; Figure 2.41 presents monthly averaged wave heights. Much like wind speed, wave heights peak October through March. Wave heights are lowest in July, but June and August also exhibit lower magnitudes. Sea surface salinity at the USM buoy, Figure 2.42, reached a minimum in June and May, and November, October, and September saw the highest salinities.

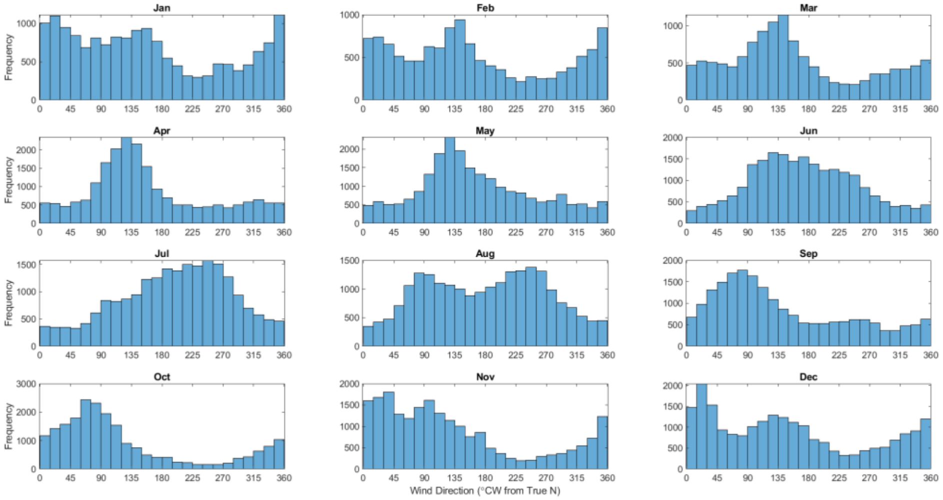

Figure 2.34 Monthly wind direction histograms at NDBC buoy 42040

Frequencies represent 15° bins.

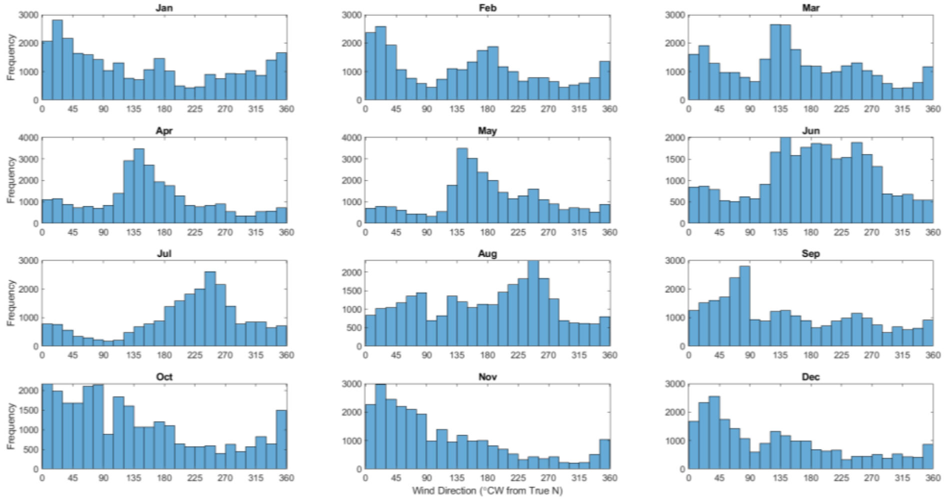

Figure 2.35 Monthly wind direction histograms at C-MAN station FMOA

Frequencies represent 15° bins.

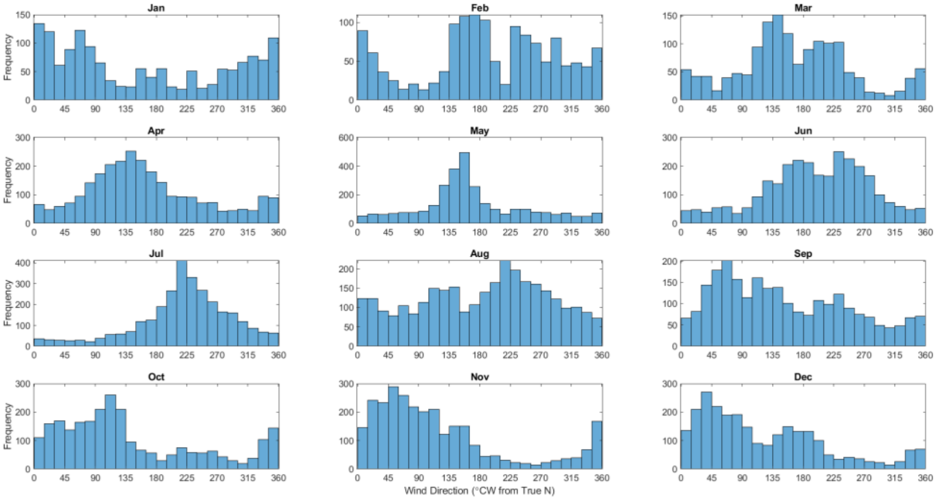

Figure 2.36 Monthly wind direction histograms at USM buoy

Frequencies represent 15° bins.

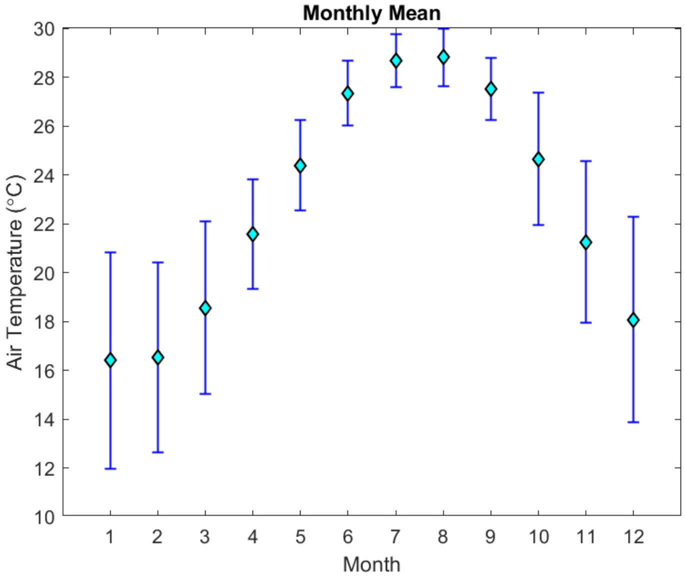

Figure 2.37 Mean monthly air temperatures at NDBC buoy 42040

Monthly climatologies, shown with cyan diamonds, were calculated using 2014 through 2017 data; the blue lines show standard deviations from the means.

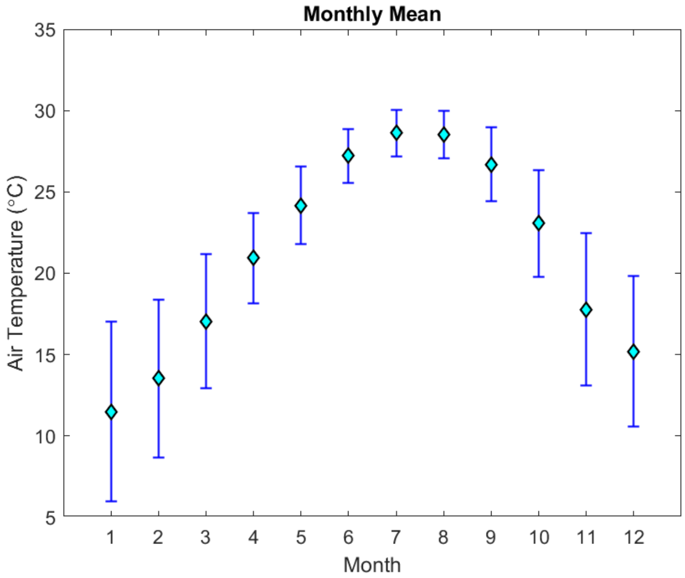

Figure 2.38 Mean monthly air temperatures at C-MAN station FMOA

Monthly climatologies, shown with cyan diamonds, were calculated using 2014 through 2017 data; the blue lines show standard deviations from the means.

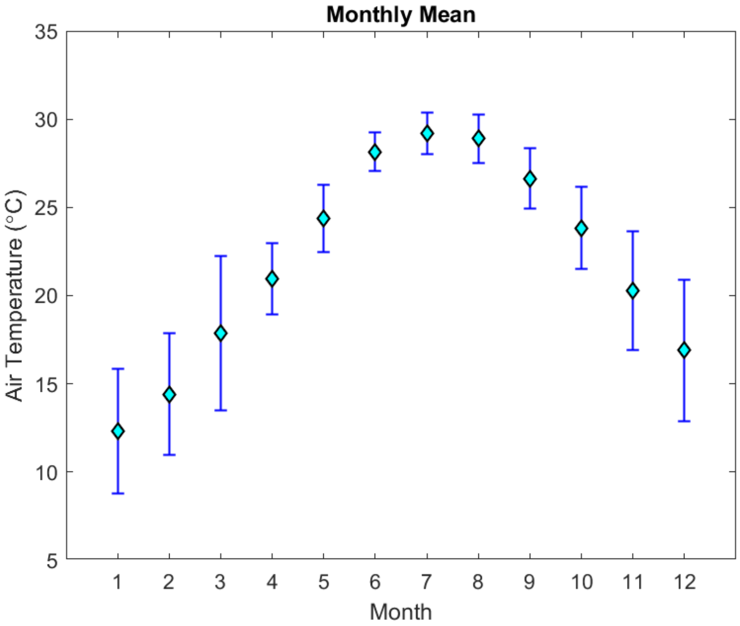

Figure 2.39 Mean monthly air temperatures at USM buoy

Monthly climatologies, shown with cyan diamonds, were calculated using 2014 through 2017 data; the blue lines show standard deviations from the means.

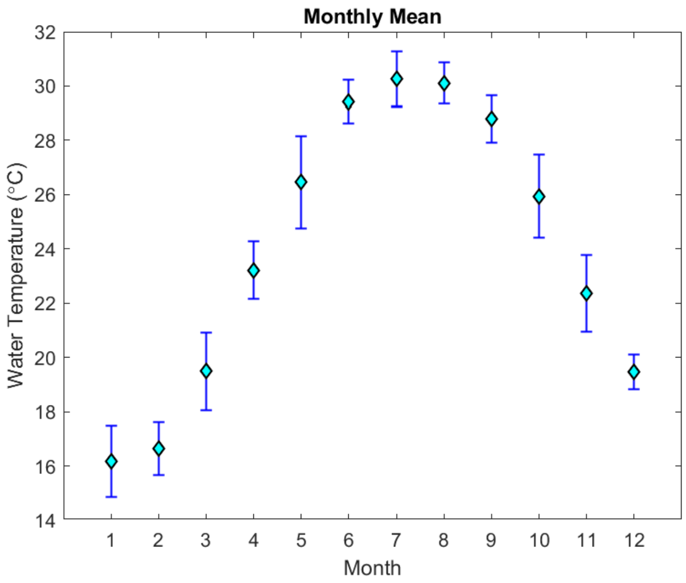

Figure 2.40 Mean monthly surface water temperatures at USM buoy

Monthly climatologies, shown with cyan diamonds, were calculated using 2014 through 2017 data; the blue lines show standard deviations from the means.

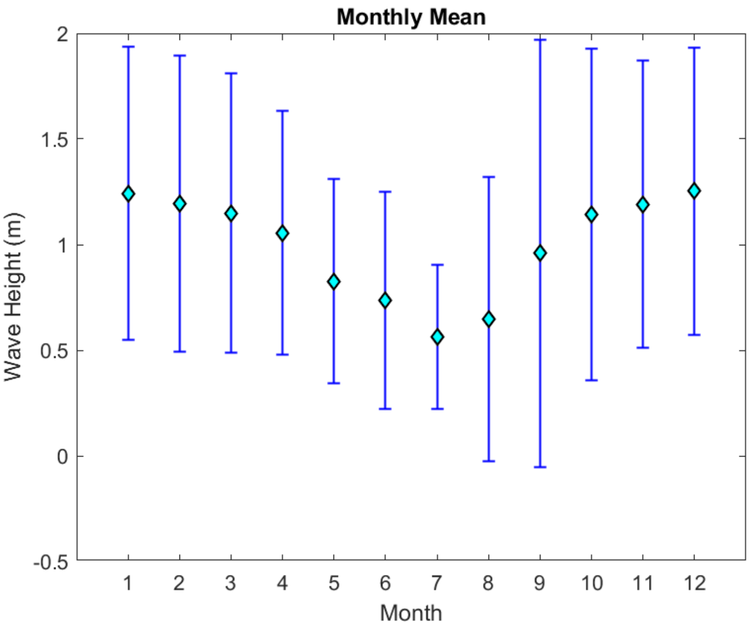

Figure 2.41 Mean monthly wave heights at NDBC buoy 42040

Monthly climatologies, shown with cyan diamonds, were calculated using 2014 through 2017 data; the blue lines show standard deviations from the means.

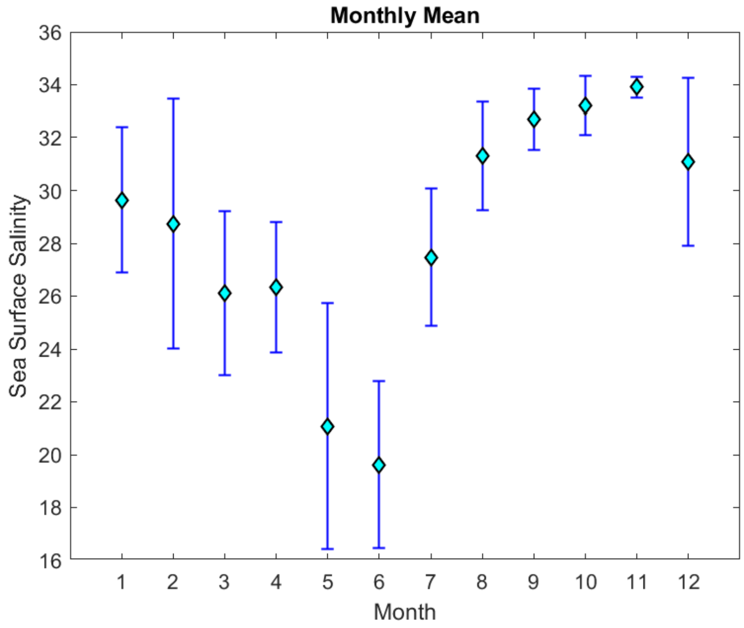

Figure 2.42 Mean monthly sea surface salinity at USM buoy

Monthly climatologies, shown with cyan diamonds, were calculated using 2014 through 2017 data; the blue lines show standard deviations from the means.

### 2.3.2 Mississippi Sound Circulation

Observational coverage of the Mississippi Sound is confined largely to the western Sound where the twelve hydrological stations and two 25 MHz HF radars are positioned. Salinity increases with distance from the shore. This horizontal gradient persists throughout the calendar year though the salinity differences vary month to month. Temperature across the entire Sound follows a distinct annual trend with minimal horizontal variation across the western Mississippi Sound.

During the month of January, shown in Figure 2.43, water temperatures everywhere in the Sound stay below14°C. Stations nearshore are approximately 1°C cooler than stations near the barrier islands, but visually the temperature field looks homogenous.  Salinity increases with distance offshore, and a channel of higher salinity water can be seen through Ship Island pass though this may be an artifact of the interpolation scheme.  Average surface currents, shown in Figure 2.44a, exhibit a southward flow from the PCYC HF radar and a southeastward flow south of the Bay of Saint Louis.  Looking southwest of the bay, flow is directed to the southwest.  Little covariance occurs closer to the shore, but the semi-major axes in Figure 2.44b increased by more than 50% in the southern extent of the HFR coverage range.  The ratio of the semi-major axes to the semi-minor axes also increased.

Salinity distributions in February retain the trends seen in the January averages, but the temperature range increases to 13-15°C.  No consistent temperature patterns emerge during February as seen in Figure 2.45.  In Figure 2.46, a southeastern channel of flow extends from the SISL HFR that turns eastward south of the Bay of Saint Louis. Flow moves southward and southwestward from the PCYC HFR.  A channel of northeastern flow extends from the Saint Bernard Delta towards Cat Island.  The island seems to act as a diversion point with currents turning north northeastward north of the island and southwestward southwest of Cat Island.  Speeds tend to stay below 10 cm/s, but the size of the covariance ellipses are larger relative to January.  However, the increase in covariance ellipse size increases with distance from the HF radars.

Temperatures increase to 17-20°C in March.  A cooler patch of water can be seen south of the Bay of Saint Louis in Figure 2.47 while temperatures are 1-2°C warmer closer to shore with the warmest temperatures occurring north of Horn Island.  The salinity range decreased from February to March.  The southern Sound freshened, and the channel of higher salinity water became harder to differentiate from the surrounding waters. In Figure 2.48a, average surface currents demonstrate a southeastern flow emanating outward from the SISL HFR that turned eastward south of the PCYC HFR. As in February, flow diverts at Cat Island. Currents point northeast north of the island and southwest south of the island. At the southern extent of the coverage area, a few vectors point northward. Semi-major axes range from 50 to 100 cm/s in Figure 2.48b, and the ellipses orient southwest-northeast.

By April, water temperatures warm to 21-24°C with most of the western Sound falling right at 22°C as seen in Figure 2.49. The area south of Back Bay Biloxi exhibited the warmest temperatures while the region south of the Bay of Saint Louis had the coolest. The horizontal salinity gradient decreased from March to April. Stations further from the coast maintained higher salinities, but the overall range in salinity dropped. In Figure 2.50, surface currents pointed southeast from both the SISL and PCYC sites, but flow turned southwest to the southwest of SISL and east to the southeast of the Bay of Saint Louis. A distinct channel of east northeast surface currents dominated the month of April to the west of Cat Island. Covariance ellipses were larger compared to the previous month, but the pattern of increasing semi-major axis length with distance from the HFRs remained. The increasing semi-major axis lengths likely result from small sample size as grid points further from the HFRs have less temporal coverage than grid points closer to the HFRs. Uncertainty and GDOP values are also higher at the edge of the HFR domain.

Average water temperatures in May stayed around 25°C with the stations at Round Island and Graveline Bayou seeing slightly warmer measurements at 26°C and 27°C respectively (Figure 2.51). The channel of higher salinity water entering the Sound through Ship Island Pass disappeared; salinity increased from north to south rather than aligning on and offshore.  May presents the most uniform surface current pattern with velocity vectors pointed northeast across the majority of the western Mississippi Sound in Figure 2.52a.  Small regions of east southeastward flow can be observed near the two HFRs, but the northeastern flow dominates everywhere else.

As for June, average monthly temperatures range 28-30°C with temperatures increasing west to east as shown in Figure 2.53.  Similar to May, the salinity range in the western Sound is lower compared to late winter and early spring.  In terms of surface velocity, HFR coverage of the Sound was highly variable resulting in few vectors being available for the monthly average.  Where coverage exists in Figure 2.54a, flow to the northeast echoes the May climatology.  In Figure 2.54b, the semi-major axes align southwest to northeast in the southern portions of the HFR grid, and the covariance ellipses close to the HFRs appear nearly circular with semi-major axes less than 50 cm/s.

July temperatures range from 29°C to 31°C with the nearshore hydrological stations being warmer than those further into the Sound.  In Figure 2.55, increased salinity with distance from the coast reemerged, but the channel of higher salinity through Ship Island Pass was not present.  From January to June, the eastern portion of the western Sound was 7-9 fresher than the western edge.  During July though, the difference decreases to 5-6.  Patchy HFR coverage makes surface current analysis difficult.  In Figure 2.56a, a small region in the eastern half the Western Sound showed east to northeast flow, but what vectors exist elsewhere contradict one another.  Covariance ellipses align southwest to northeast, and the semi-major axis lengths exceed those of the semi-minor axes (Figure 2.56b).

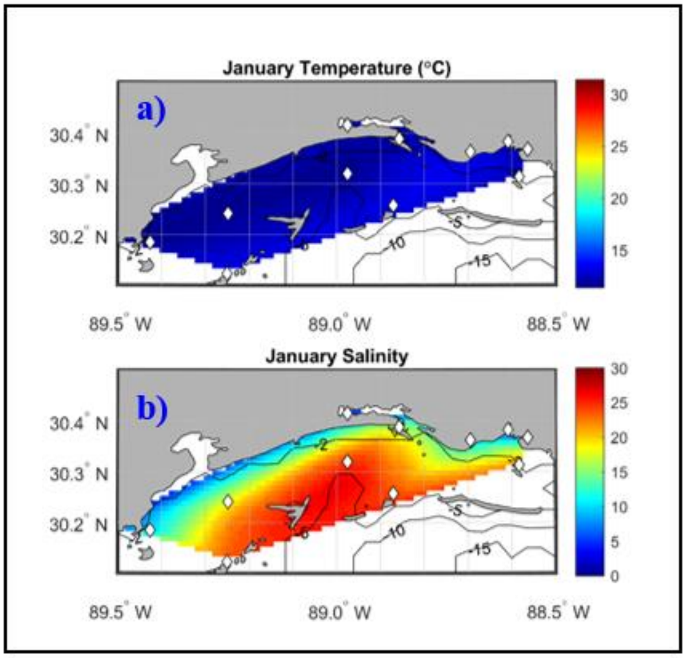

Figure 2.43 January distributions of temperature and salinity

January monthly mean a) bottom temperature and b) bottom salinity fields for the western Mississippi Sound. Locations of the hydrological stations are given by white diamonds, and interpolation between those points was accomplished using a cubic interpolation with Delaunay triangulation (Watson, 1992).

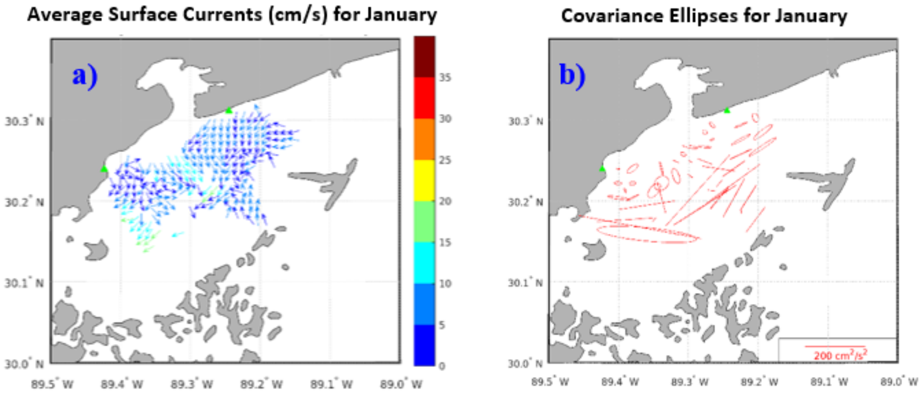

Figure 2.44 January mean surface currents and covariance ellipses

a) Average surface currents, in cm/s, for the month of January as measured by 25 MHz HF radars. Velocity magnitudes are indicated by the color bar on the right. b) Covariance ellipses based on the semi-major and semi-minor axes of covariance. Reference bar has units of $cm^2/s^2$ for area, but semi-major and semi-minor axes have length cm/s. The HFR grid has been subsampled to every other grid point to provide better visual acuity. Green triangles give the locations of the HF radars at SISL (western site) and PCYC (eastern site).

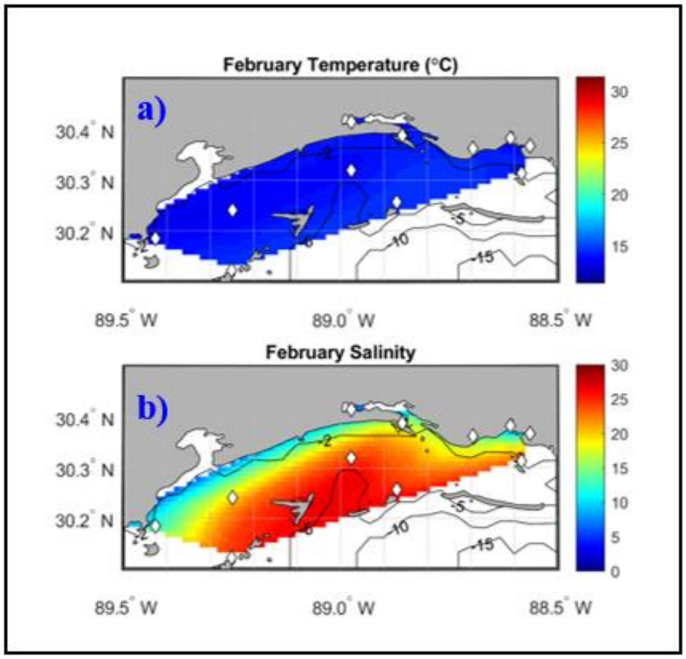

## Figure 2.45 February distributions of temperature and salinity

February monthly mean a) bottom temperature and b) bottom salinity fields for the western Mississippi Sound. Locations of the hydrological stations are given by white diamonds, and interpolation between those points was accomplished using a cubic interpolation with Delaunay triangulation (Watson, 1992).

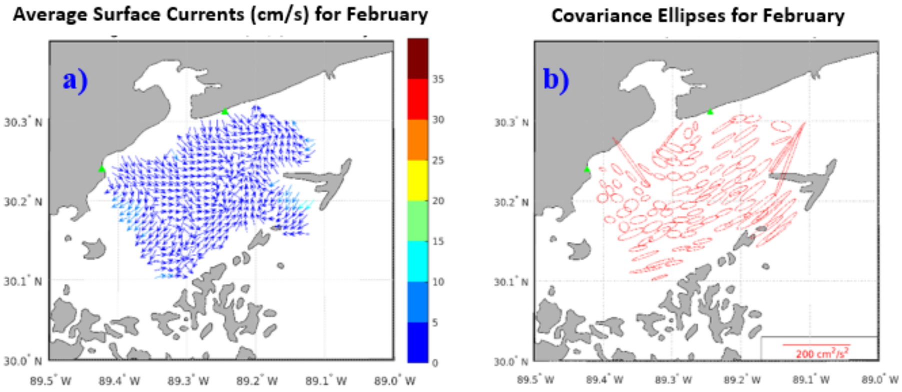

## Figure 2.46 February mean surface currents and covariance ellipses

a) Average surface currents, in cm/s, for the month of February as measured by 25 MHz HF radars. Velocity magnitudes are indicated by the color bar on the right. b) Covariance ellipses based on the semi-major and semi-minor axes of covariance. Reference bar has units of $cm^2/s^2$ for area, but semi-major and semi-minor axes have length cm/s. The HFR grid has been subsampled to every other grid point to provide better visual acuity. Green triangles give the locations of the HF radars at SISL (western site) and PCYC (eastern site).

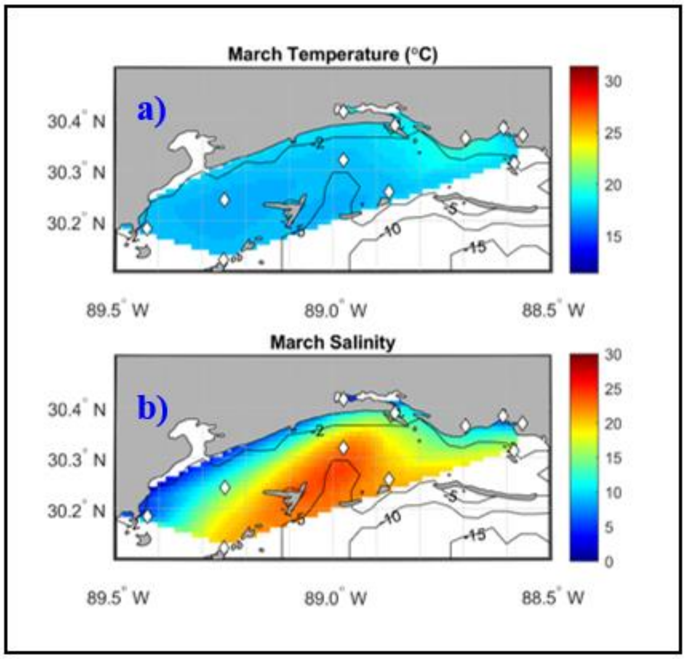

## Figure 2.47 March distributions of temperature and salinity

March monthly mean a) bottom temperature and b) bottom salinity fields for the western Mississippi Sound. Locations of the hydrological stations are given by white diamonds, and interpolation between those points was accomplished using a cubic interpolation with Delaunay triangulation (Watson, 1992).

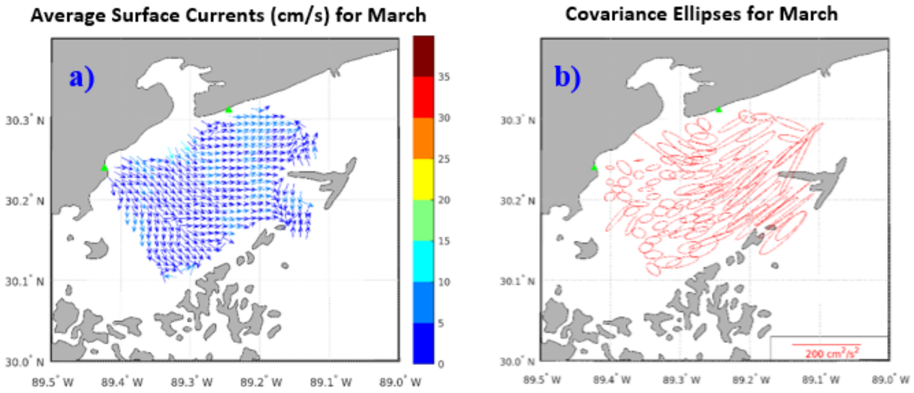

## Figure 2.48 March mean surface currents and covariance ellipses

a) Average surface currents, in cm/s, for the month of March as measured by 25 MHz HF radars. Velocity magnitudes are indicated by the color bar on the right. b) Covariance ellipses based on the semi-major and semi-minor axes of covariance. Reference bar has units of cm2/s2 for area, but semi-major and semi-minor axes have length cm/s. The HFR grid has been subsampled to every other grid point to provide better visual acuity. Green triangles give the locations of the HF radars at SISL (western site) and PCYC (eastern site).

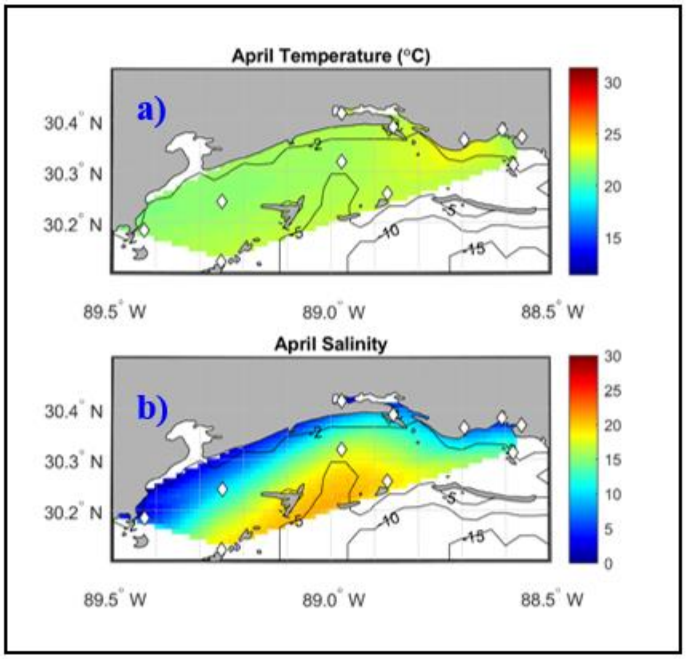

Figure 2.49 April distributions of temperature and salinity

April monthly mean a) bottom temperature and b) bottom salinity fields for the western Mississippi Sound. Locations of the hydrological stations are given by white diamonds, and interpolation between those points was accomplished using a cubic interpolation with Delaunay triangulation (Watson, 1992).

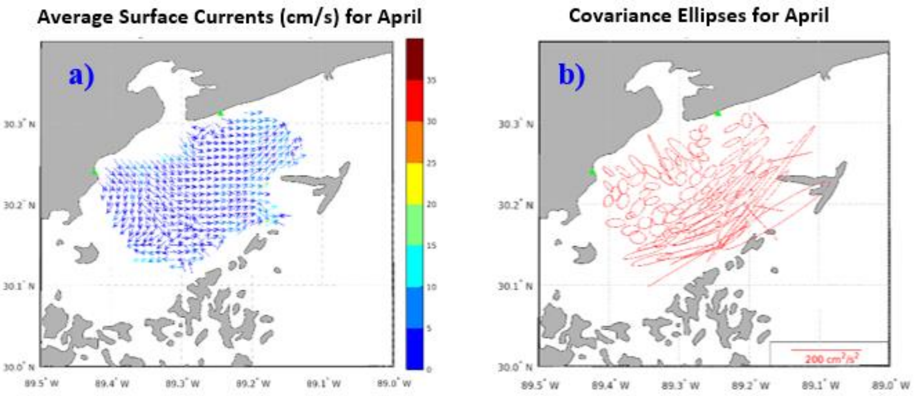

Figure 2.50 April mean surface currents and covariance ellipses

a) Average surface currents, in cm/s, for the month of April as measured by 25 MHz HF radars. Velocity magnitudes are indicated by the color bar on the right. b) Covariance ellipses based on the semi-major and semi-minor axes of covariance. Reference bar has units of $cm^2/s^2$ for area, but semi-major and semi-minor axes have length cm/s. The HFR grid has been subsampled to every other grid point to provide better visual acuity. Green triangles give the locations of the HF radars at SISL (western site) and PCYC (eastern site).

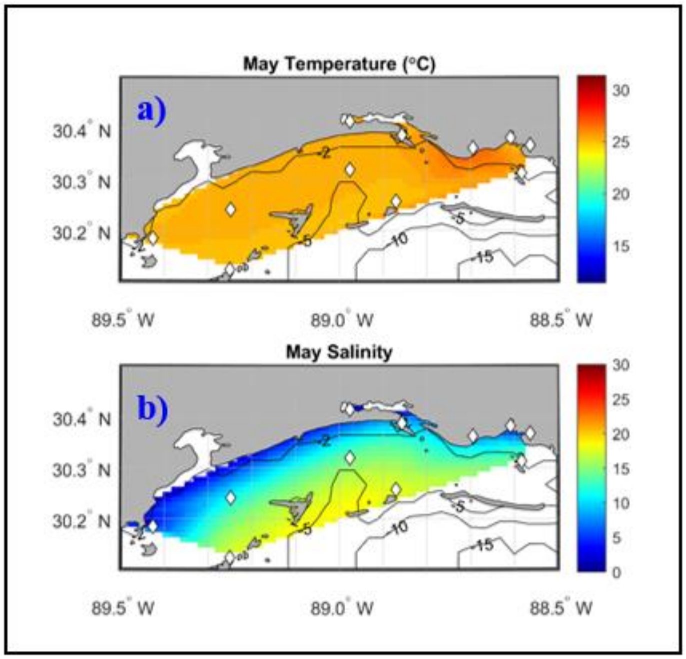

Figure 2.51 May distributions of temperature and salinity

May monthly mean a) bottom temperature and b) bottom salinity fields for the western Mississippi Sound. Locations of the hydrological stations are given by white diamonds, and interpolation between those points was accomplished using a cubic interpolation with Delaunay triangulation (Watson, 1992).

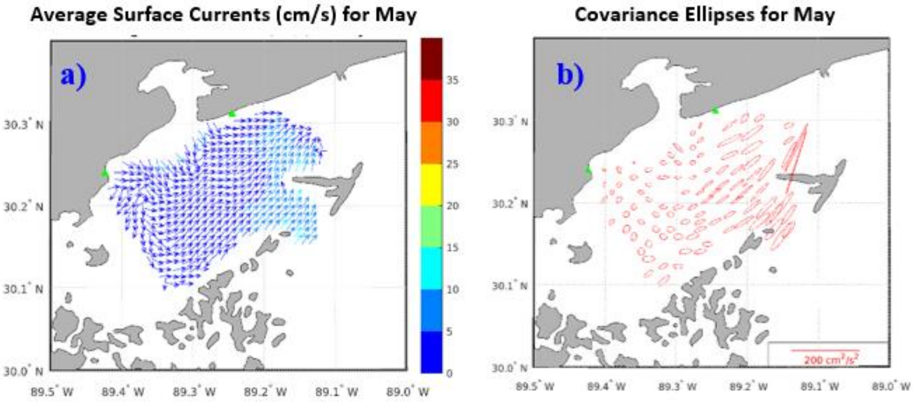

Figure 2.52 May mean surface currents and covariance ellipses

a) Average surface currents, in cm/s, for the month of May as measured by 25 MHz HF radars. Velocity magnitudes are indicated by the color bar on the right. b) Covariance ellipses based on the semi-major and semi-minor axes of covariance. Reference bar has units of cm$^2$/s$^2$ for area, but semi-major and semi-minor axes have length cm/s. The HFR grid has been subsampled to every other grid point to provide better visual acuity. Green triangles give the locations of the HF radars at SISL (western site) and PCYC (eastern site).

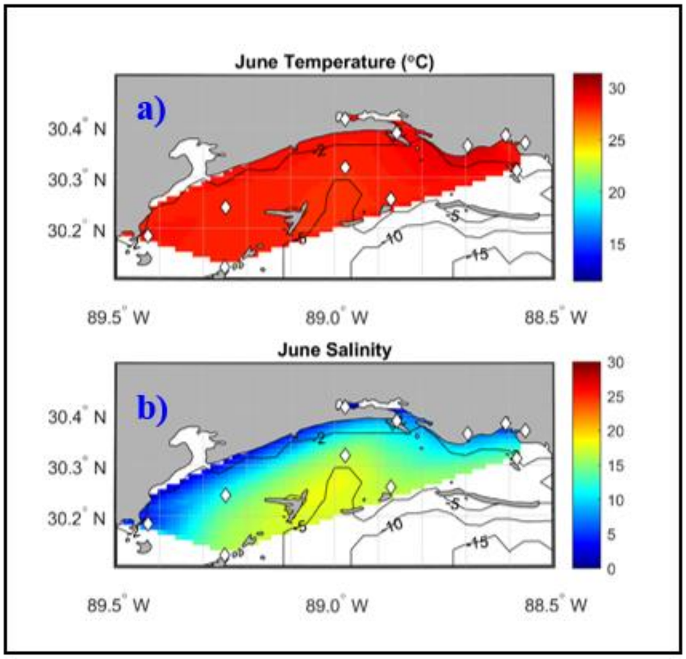

Figure 2.53 June distributions of temperature and salinity

June monthly mean a) bottom temperature and b) bottom salinity fields for the western Mississippi Sound. Locations of the hydrological stations are given by white diamonds, and interpolation between those points was accomplished using a cubic interpolation with Delaunay triangulation (Watson, 1992).

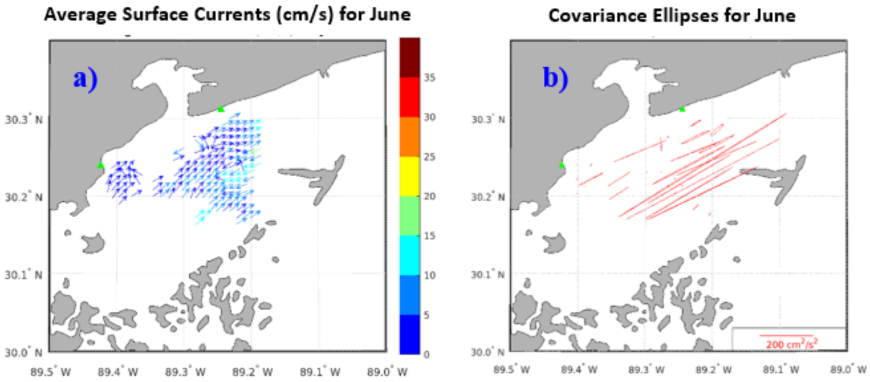

Figure 2.54 June mean surface currents and covariance ellipses

a) Average surface currents, in cm/s, for the month of June as measured by 25 MHz HF radars. Velocity magnitudes are indicated by the color bar on the right. b) Covariance ellipses based on the semi-major and semi-minor axes of covariance. Reference bar has units of $cm^2/s^2$ for area, but semi-major and semi-minor axes have length cm/s. The HFR grid has been subsampled to every other grid point to provide better visual acuity. Green triangles give the locations of the HF radars at SISL (western site) and PCYC (eastern site).

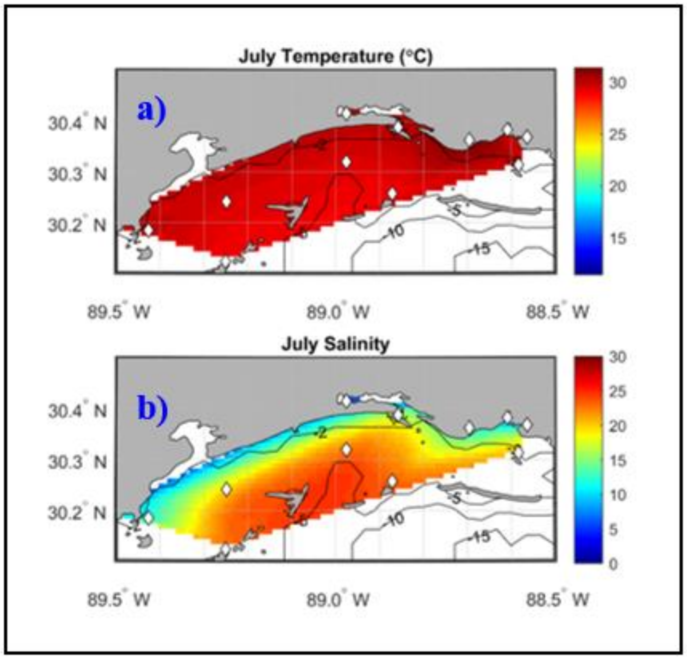

Figure 2.55 July distributions of temperature and salinity

July monthly mean a) bottom temperature and b) bottom salinity fields for the western Mississippi Sound. Locations of the hydrological stations are given by white diamonds, and interpolation between those points was accomplished using a cubic interpolation with Delaunay triangulation (Watson, 1992).

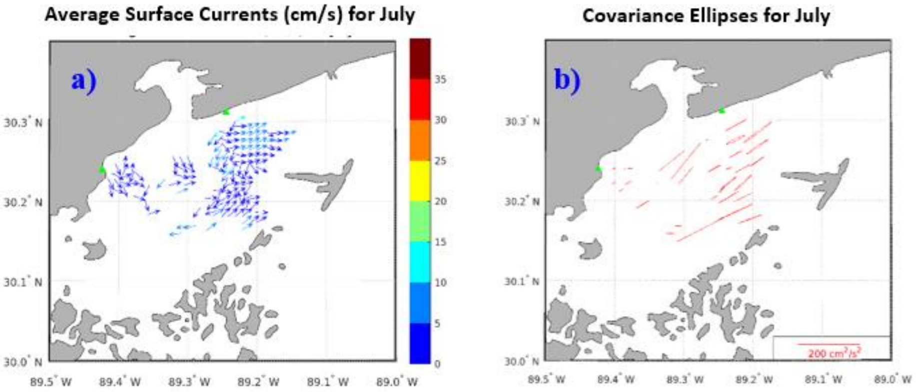

Figure 2.56 July mean surface currents and covariance ellipses

a) Average surface currents, in cm/s, for the month of July as measured by 25 MHz HF radars. Velocity magnitudes are indicated by the color bar on the right. b) Covariance ellipses based on the semi-major and semi-minor axes of covariance. Reference bar has units of $cm^2/s^2$ for area, but semi-major and semi-minor axes have length cm/s. The HFR grid has been subsampled to every other grid point to provide better visual acuity. Green triangles give the locations of the HF radars at SISL (western site) and PCYC (eastern site).

Average August temperatures make it the warmest month in the year with the whole study region falling between 30°C and 31°C.  Increased salinity also occurred at each hydrological station, and half of the western Mississippi Sound saw average salinity values above 20 (Figure 2.57).  The northeastward flow observed in the previous months gave way to southwest surface currents in August with a small patch of westward flow close to the SISL HFR.  South of the PCYC HFR in Figure 2.58a, currents point southward then turn eastward.  The covariance ellipses shown in Figure 2.58b continued to be large with high semi-major axes compared to the semi-minor axes.

While temperatures peak during July and August, salinities peak during the fall months with different stations in the Sound exhibiting maximum salinity between September and December.  Figure 2.59 shows temperatures in September drop to 28-29°C with the western stations staying 1°C cooler than the central and eastern stations throughout the month.  By contrast, salinity dropped at the western stations compared to August while the central and eastern stations saw increased salinity.  The southwestward currents of August shifted southward in September.  A small area south of PCYC saw currents turning eastward (Figure 2.60a).  As with the summer months, covariance ellipses in Figure 2.60b aligned southwest to northeast.

October saw a further decrease in water temperatures to 24-25°C.  The hydrological stations further offshore were a little warmer, but the difference was less than 1°C.  In Figure 2.61, salinity values increased across the western Mississippi Sound, and the East Ship Island station, as well as the East Pearl River station,  experienced the highest salinity during October.  High variability in HFR coverage left few days available for monthly averages, but what velocity vectors do exist suggest a dominant southward flow similar to September though isolated vectors also point westward in the western extent of the HFR grid (Figure 2.62a). Figure 2.62b shows covariance ellipses followed the patterns described in September.

As with October, the hydrological stations in the southern Sound had slightly warmer temperatures in November than the stations in marsh and back bay environments, but the difference was <1°C (Figure 2.63). Temperatures fell to 18-19°C in November, but five of the twelve stations had the highest salinity of the year. Five additional stations had monthly means comparable to September averages. The western half of the western Mississippi Sound had flow pointing west to southeast while flow in the eastern half had a more cohesive southwestward direction (Figure 2.64a). In a departure from earlier months, covariance ellipses in the western half of the region oriented north to south while covariance ellipses in the eastern half followed bathymetry contours (Figure 2.64b).

Water temperatures cooled down further in December to 15-16°C with no visual horizontal gradient present across the western Mississippi Sound in Figure 2.65. High salinity values also continued into December with the stations in the center Sound and at Saint Joseph Island experiencing the highest salinities during the year. Current patterns shown in Figure 2.66a in November carry into December though current speeds increase overall by 1-2 cm/s. Covariance ellipse patterns and semi-major axis sizes also show little change (2.66b).

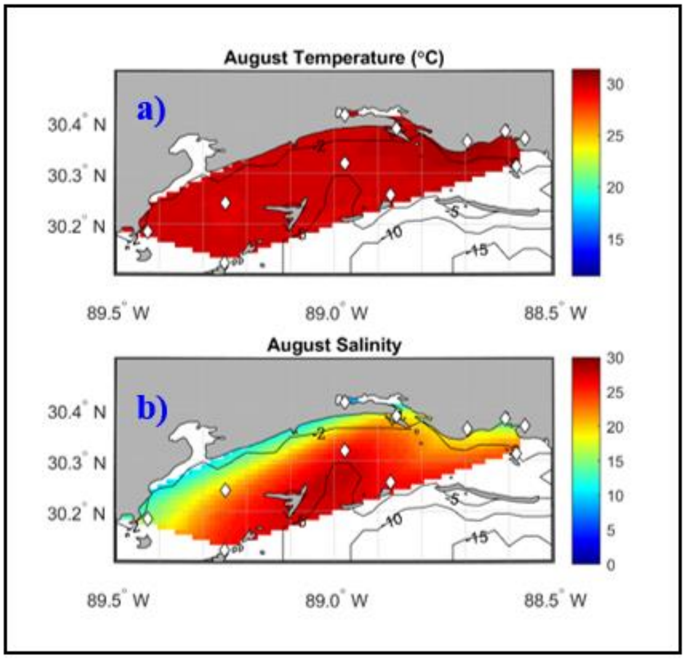

Figure 2.57 August distributions of temperature and salinity

August monthly mean a) bottom temperature and b) bottom salinity fields for the western Mississippi Sound. Locations of the hydrological stations are given by white diamonds, and interpolation between those points was accomplished using a cubic interpolation with Delaunay triangulation (Watson, 1992).

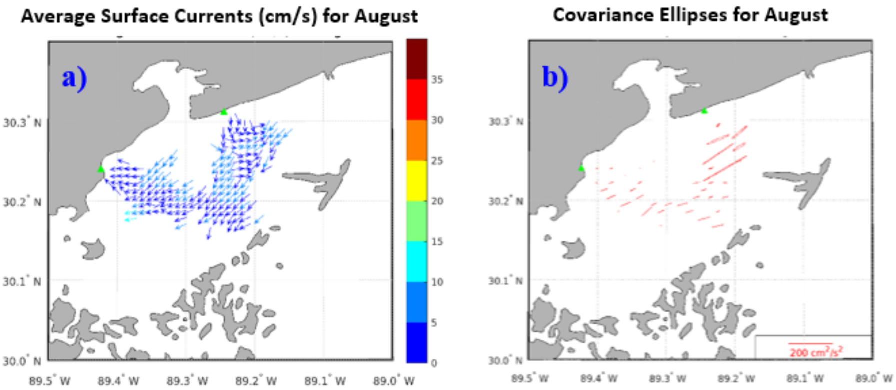

Figure 2.58 August mean surface currents and covariance ellipses

a) Average surface currents, in cm/s, for the month of August as measured by 25 MHz HF radars. Velocity magnitudes are indicated by the color bar on the right. b) Covariance ellipses based on the semi-major and semi-minor axes of covariance. Reference bar has units of $cm^2/s^2$ for area, but semi-major and semi-minor axes have length cm/s. The HFR grid has been subsampled to every other grid point to provide better visual acuity. Green triangles give the locations of the HF radars at SISL (western site) and PCYC (eastern site).

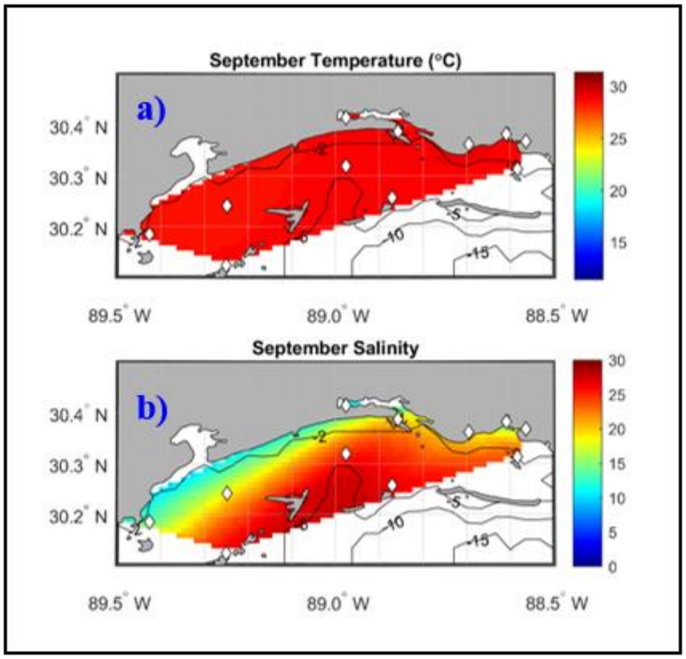

Figure 2.59 September distributions of temperature and salinity

September monthly mean a) bottom temperature and b) bottom salinity fields for the western Mississippi Sound. Locations of the hydrological stations are given by white diamonds, and interpolation between those points was accomplished using a cubic interpolation with Delaunay triangulation (Watson, 1992).

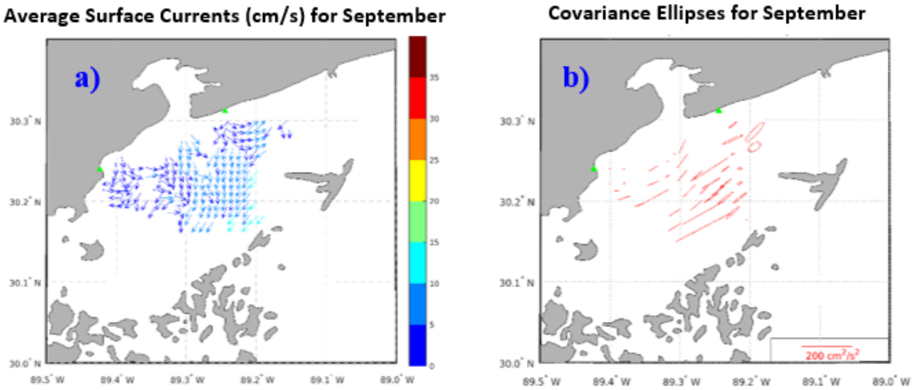

Figure 2.60 September mean surface currents and covariance ellipses

a) Average surface currents, in cm/s, for the month of September as measured by 25 MHz HF radars. Velocity magnitudes are indicated by the color bar on the right. b) Covariance ellipses based on the semi-major and semi-minor axes of covariance. Reference bar has units of $cm^2/s^2$ for area, but semi-major and semi-minor axes have length cm/s. The HFR grid has been subsampled to every other grid point to provide better visual acuity. Green triangles give the locations of the HF radars at SISL (western site) and PCYC (eastern site).

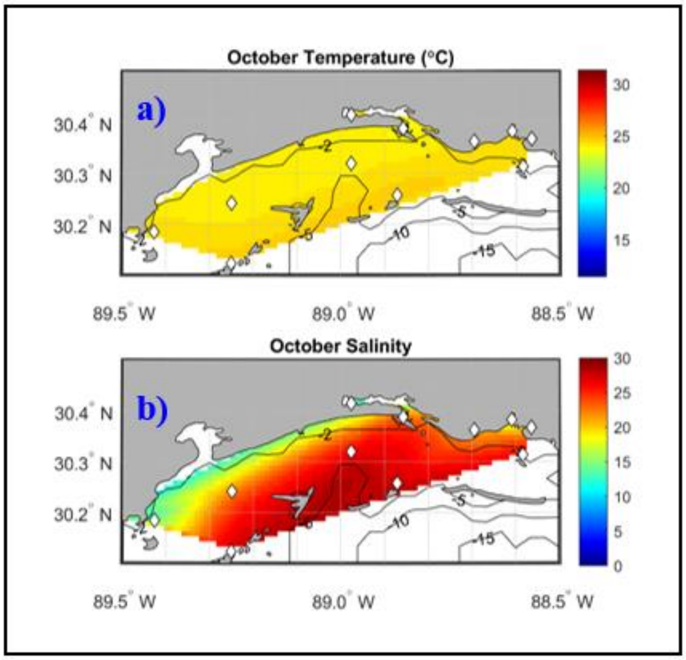

Figure 2.61 October distributions of temperature and salinity

October monthly mean a) bottom temperature and b) bottom salinity fields for the western Mississippi Sound. Locations of the hydrological stations are given by white diamonds, and interpolation between those points was accomplished using a cubic interpolation with Delaunay triangulation (Watson, 1992).

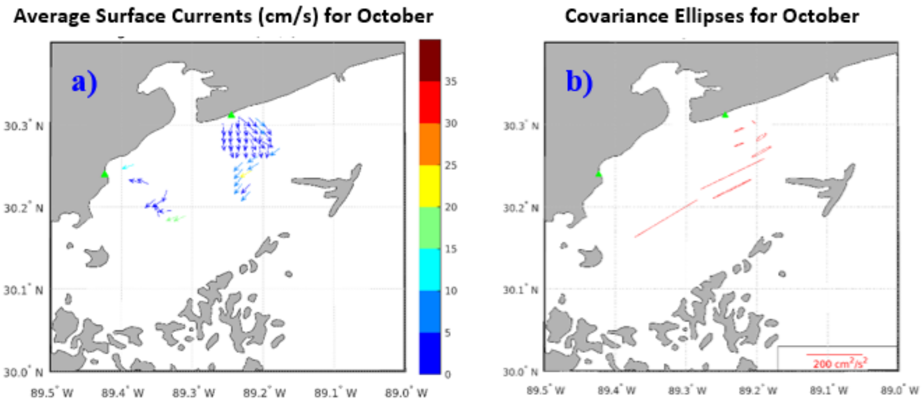

Figure 2.62 October mean surface currents and covariance ellipses

a) Average surface currents, in cm/s, for the month of October as measured by 25 MHz HF radars. Velocity magnitudes are indicated by the color bar on the right. b) Covariance ellipses based on the semi-major and semi-minor axes of covariance. Reference bar has units of $cm^2/s^2$ for area, but semi-major and semi-minor axes have length cm/s. The HFR grid has been subsampled to every other grid point to provide better visual acuity. Green triangles give the locations of the HF radars at SISL (western site) and PCYC (eastern site).

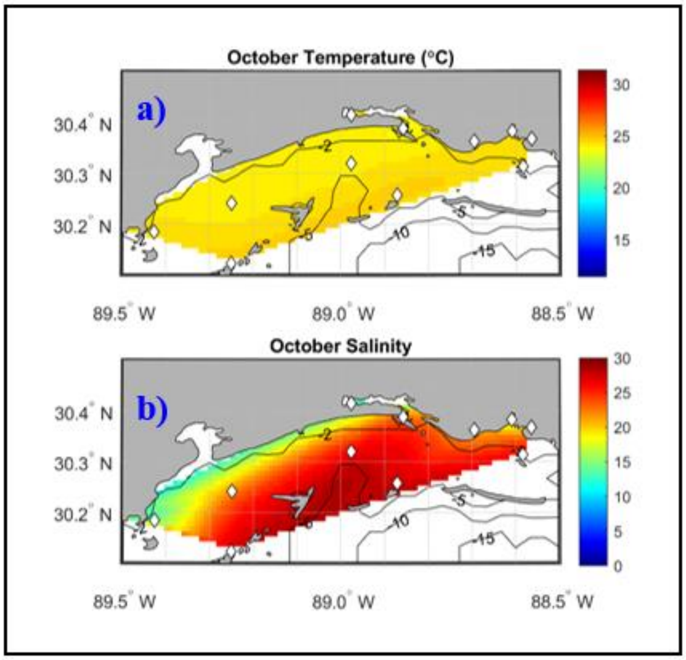

Figure 2.63 November distributions of temperature and salinity

November monthly mean a) bottom temperature and b) bottom salinity fields for the western Mississippi Sound. Locations of the hydrological stations are given by white diamonds, and interpolation between those points was accomplished using a cubic interpolation with Delaunay triangulation (Watson, 1992).

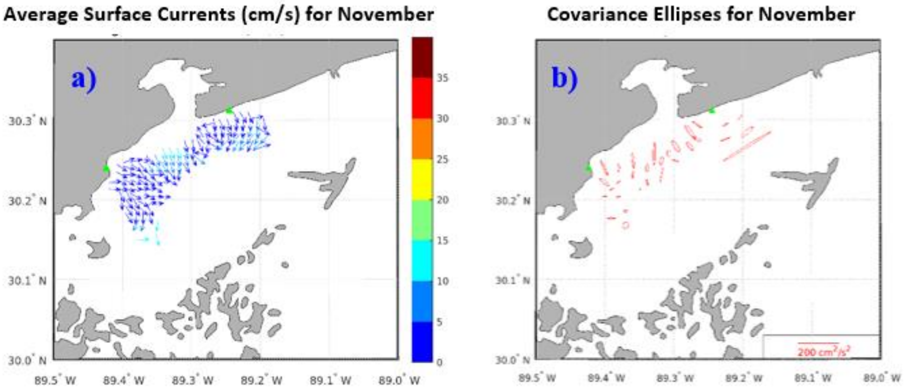

Figure 2.64 November mean surface currents and covariance ellipses

a) Average surface currents, in cm/s, for the month of November as measured by 25 MHz HF radars. Velocity magnitudes are indicated by the color bar on the right. b) Covariance ellipses based on the semi-major and semi-minor axes of covariance. Reference bar has units of cm$^2$/s$^2$ for area, but semi-major and semi-minor axes have length cm/s. The HFR grid has been subsampled to every other grid point to provide better visual acuity. Green triangles give the locations of the HF radars at SISL (western site) and PCYC (eastern site).

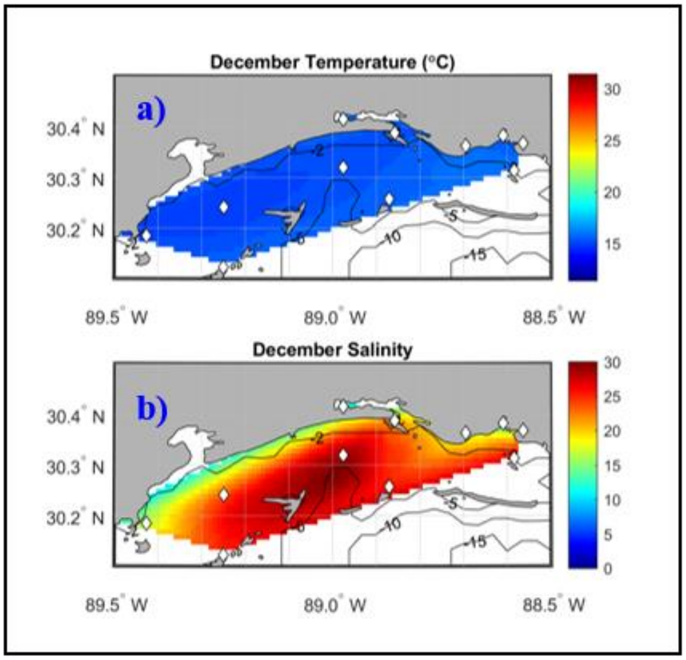

Figure 2.65 December distributions of temperature and salinity

December monthly mean a) bottom temperature and b) bottom salinity fields for the western Mississippi Sound. Locations of the hydrological stations are given by white diamonds, and interpolation between those points was accomplished using a cubic interpolation with Delaunay triangulation (Watson, 1992).

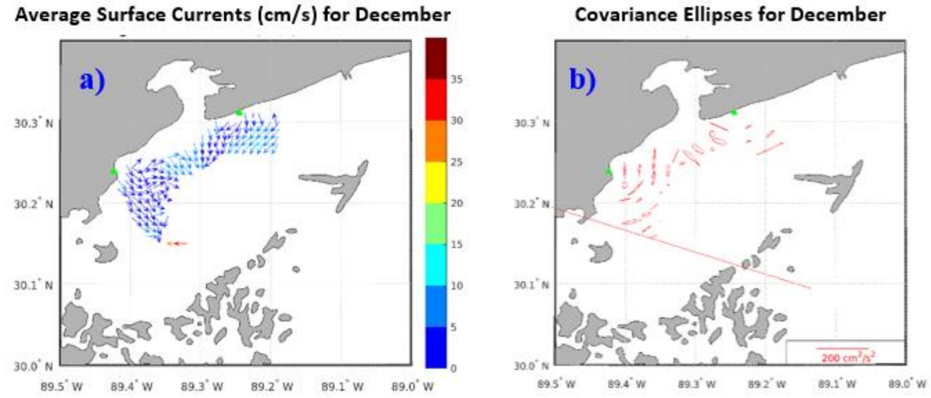

Figure 2.66 December mean surface currents and covariance ellipses

a) Average surface currents, in cm/s, for the month of December as measured by 25 MHz HF radars. Velocity magnitudes are indicated by the color bar on the right. b) Covariance ellipses based on the semi-major and semi-minor axes of covariance. Reference bar has units of $cm^2/s^2$ for area, but semi-major and semi-minor axes have length cm/s. The HFR grid has been subsampled to every other grid point to provide better visual acuity. Green triangles give the locations of the HF radars at SISL (western site) and PCYC (eastern site).

Results from the time series of the USGS-MDMR hydrological stations indicate diurnal signals, and to a smaller extent semi-diurnal signals, comprise the majority of short term variability (less than 1 week) in the western Mississippi Sound. Standard deviation values and examination of time series point to significant salinity changes in a 24 hour period which is consistent with changes in surface current directions in the western Sound. Temperature fluctuations are much smaller. Figures 2.67 and 2.68 give the salinity and temperature power spectra for station 11, located at the Pearl River near the state line between Mississippi and Alabama. This station exhibits the 1 cpd peak for both salinity and temperature, so it is being used as a representative station for the western Mississippi Sound. Salinity and temperature variability in the western Mississippi Sound lean towards time scales at or less than 1 day. Peaks appear at 1cpd for all the stations. Station 4, in Graveline Bayou, Mississippi, also shows a 2 cpd peak in salinity while station 2, near Round Island, has a small 0.2 cpd peak. As for temperature, station 4 has peaks at 2 cpd and 3 cpd too. However, the commonality among the stations is the diurnal fluctuations.

Chapter I noted that multiple diurnal tidal constituents occur near the 24 hour period as does the land-sea breeze cycle and inertial period for the study region. Tides most likely dominant the observed diurnal variability. Given the shallow depths of the Sound, sustained stratification is unlikely, so inertial oscillations would play an insignificant role. Likewise, differential heating is more pronounced during warmer summer months, so fluctuations due to the land-sea breeze cycle would only play a controlling role for part of the year.

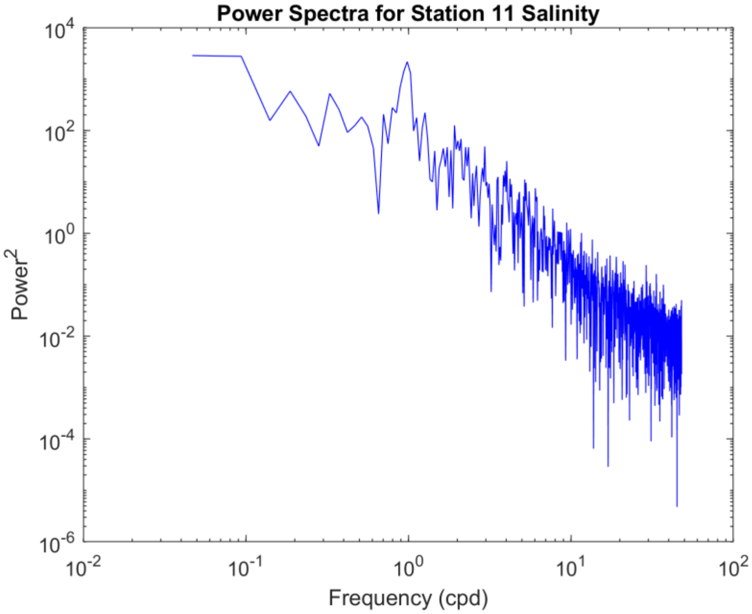

Figure 2.67 Salinity power spectra for the East Pearl River hydrological station

Power spectral density for bottom salinity measured at USGS-MDMR station 11 (East Pear River at the CSX Railroad Crossing). Frequencies are given in cycles per day (cpd); salinity is a ratio without units.

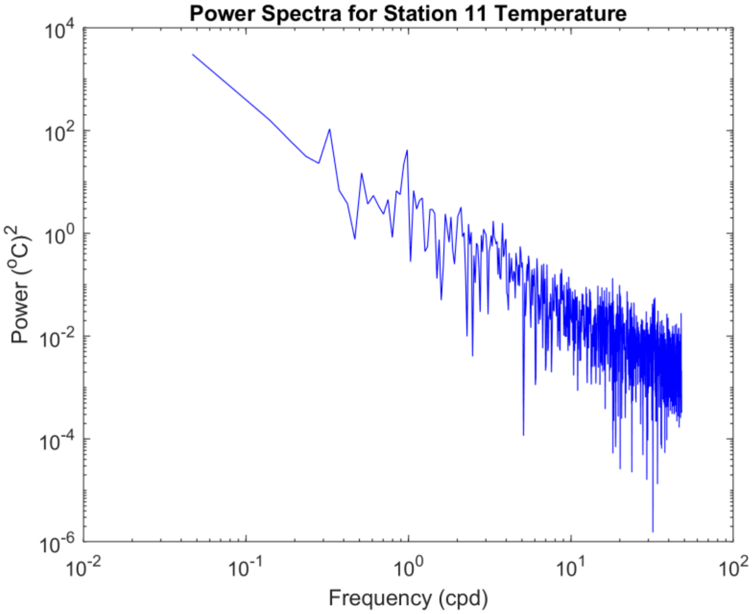

Figure 2.68 Temperature power spectra for the East Pearl River hydrological station

Power spectral density for bottom temperature measured at USGS-MDMR station 11 (East Pear River at the CSX Railroad Crossing). Frequencies are given in cycles per day (cpd); temperature peaks have units (°C)$^2$.

The Mississippi Sound is a river-dominated lagoon, so discussion of circulation should include analysis of riverine influence.  Riverine discharge falls into a unique category since some of the rivers in the region flow into the Mississippi Sound, others flow into the Sound but have mouths near island passes that allow water exchange between the Mississippi Sound and Bight, and the Mississippi River and Mobile Bay empty partially into the Sound and partially into the Bight.  However, since discharge occurs along the coast, riverine analysis has been included with Mississippi Sound circulation.

Monthly discharge averages showed differing results for the different rivers. Monthly mean discharge estimates with associated standard deviations can be seen for each of the 7 stream gages in Figure 2.69 through Figure 2.70.  Some standard deviation ranges are actually lower since the lower bound suggests discharge can be negative; this is not true for any gage.  Discharge tends to peak in spring and reach its minimum in fall.

Gage 02428400 (Alabama River) exhibits the highest discharge in January and April and lowest July through October.  Standard deviation values increase with increasing monthly mean.  Discharge for gage 02479000 (Pascagoula River) reached a maximum in March and April and a minimum in September and October.  As with gage 02428400, standard deviation values were larger for months with higher discharge.  June provided an exception to this trend; while discharge was higher, the standard deviation discharge values for June was the largest of the year.  Standard deviation values for gages 02481000, 0281510, and 02489500 increased and decreased in conjunction with monthly mean values.  May and June had the highest monthly mean discharge for gage 02481000 (Biloxi River); September through November saw the lowest monthly mean discharge.

Discharge peaked March through June at gage 02481510 (Wolf River), and monthly discharge reached its lowest in September and October. Gage 02489500 (Pearl River) recorded the lowest discharge in September and October and highest discharge in March and April. April had the highest monthly mean; March saw the largest standard deviation. Standard deviations remained low for most of the year at gage 07375500 (Tangipahoa River); nearly identical monthly mean values accompanied these low standard deviation values. Exceptions to the trend include March and August which had significantly higher mean discharges and standard deviations. Standard deviations for gage 07381331 (the Gulf Intracoastal Waterway) were nearly equal for every month. This is unsurprising since the water levels at the gage are tidally affected (Louisiana Water Data Support Team, 2019). January, February, and July had the highest mean discharges; September and October had the lowest. The more consistent monthly mean discharge values are not unexpected at gages 07375500 and 07381331. The first connects to Lake Ponchartrain; the second is a Mississippi River tributary. Flow in both locations would be heavily influenced by engineering projects designed to keep the lake and the river from overflowing.

Power spectra for the stream gages show a weak discharge peak at 1 cpd. Some of the gages have smaller peaks at 2 cpd or less than 1 cpd, but the power spectra are noisy. In looking at time series for the gages, diurnal variability is present, but the magnitude of fluctuation is not equal month to month. Gage height and discharge can vary significantly within a 24 hour period. In river locations where ocean tides do not play a role, these changes are due to evapotranspiration and snowmelt (Wicht, 1941; Reigner, 1996). Rates of evaporation throughout the solar cycle cause water level changes; transpiration by plants along the river banks add to this effect. Additionally, as temperatures and radiative fluxes change throughout the day, snowmelt rates change (Lundquist and Cayan, 2002). The distance of the stream gages used in this study from headwaters would suggest snowmelt rates have little bearing on daily discharge fluctuations. Consequently, short term variability can be attributed to evapotranspiration.

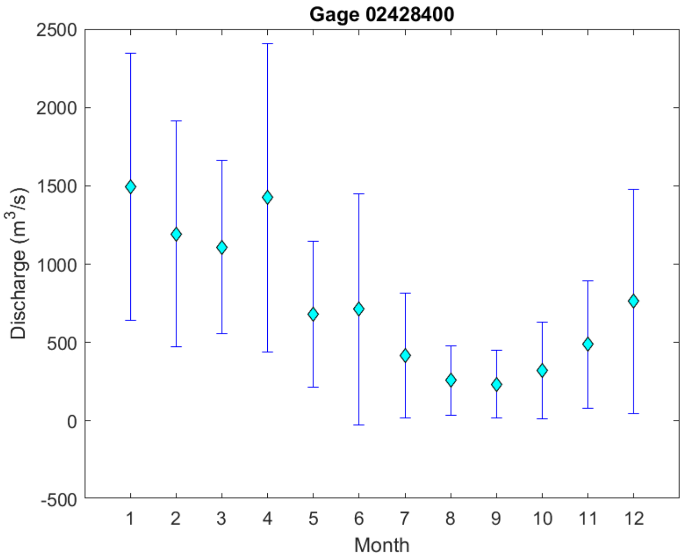

Figure 2.69 Monthly mean discharge for the Alabama River

Cyan diamonds mark average monthly discharge ($m^3/s$), and blue lines indicate standard deviations from the means.

Unlike the other gages, tidal influence is present at a stream gage on the Gulf Intracoastal Waterway (07381331). Figure 2.76 gives the power spectra for gage 07381331. This location was selected because it does not echo patterns seen at the other gages. The power spectra are noisy, but the highest peak appears at 1 cpd. Smaller peaks can be seen at 0.1 cpd, 0.2 cpd, and 0.6 cpd. Different tidal constituents can partially explain these peaks as can evapotranspiration. While other high frequency changes in discharge can be seen, the 24 hour period is the dominant short term signal in discharge.

Month to month variations in discharge are also present at gage 07381331 though the high standard deviation values make these differences insignificant.

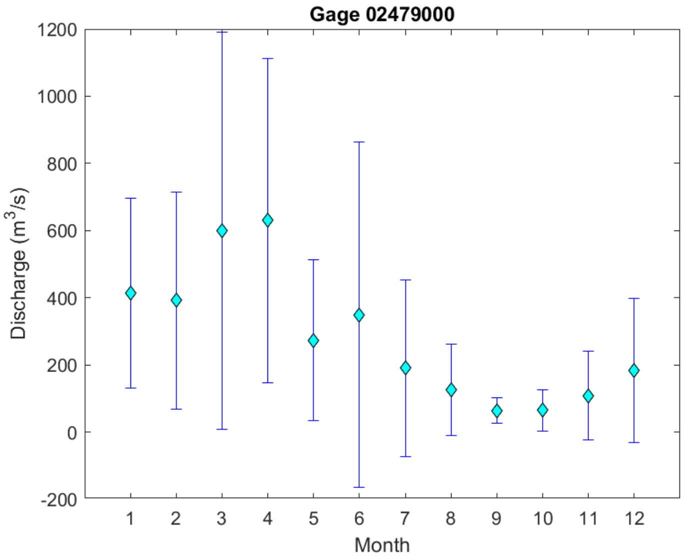

Figure 2.70 Monthly mean discharge for the Pascagoula River

Same setup as Figure 2.69.

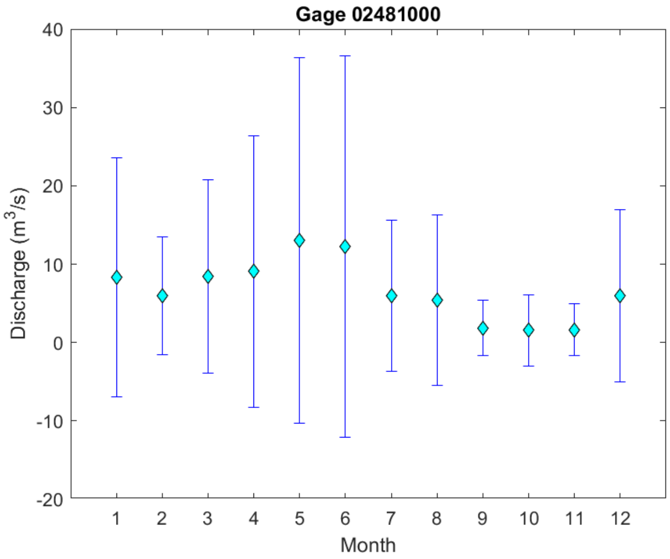

Figure 2.71 Monthly mean discharge for the Biloxi River

Same setup as Figure 2.69.

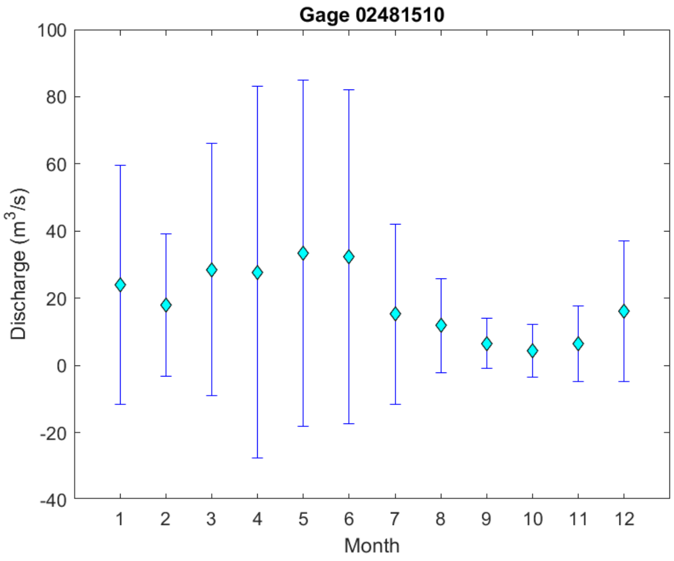

Figure 2.72 Monthly mean discharge for the Wolf River

Same setup as Figure 2.69.

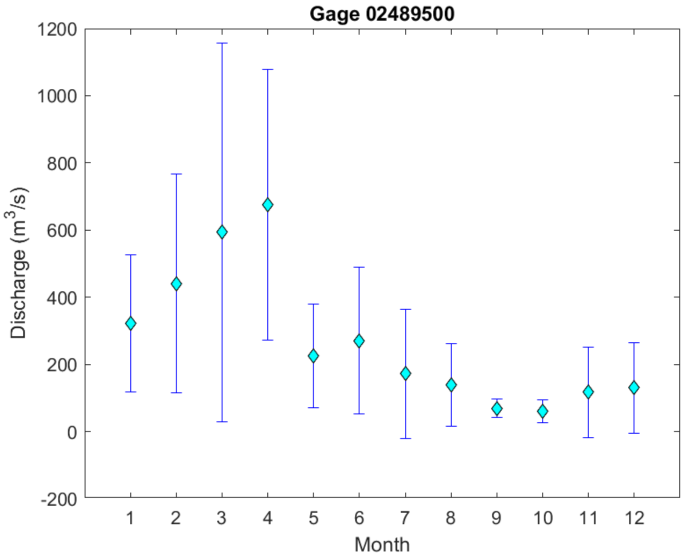

Figure 2.73 Monthly mean discharge for the Pearl River

Same setup as Figure 2.69.

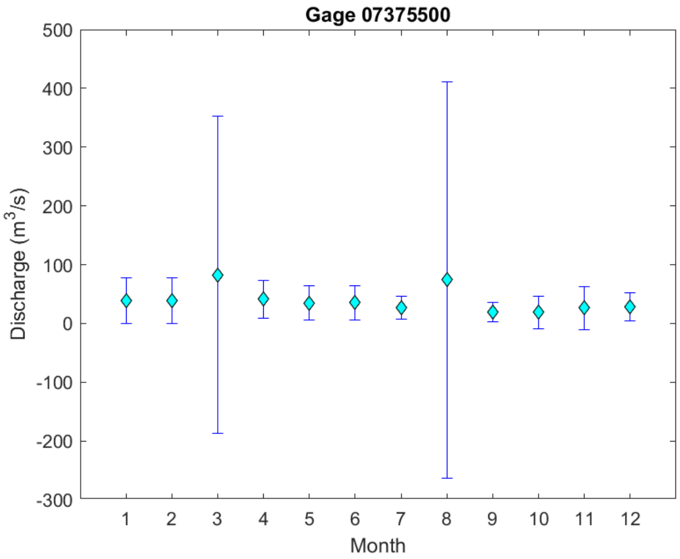

Figure 2.74 Monthly mean discharge for the Tangipahoa River

Same setup as Figure 2.69.

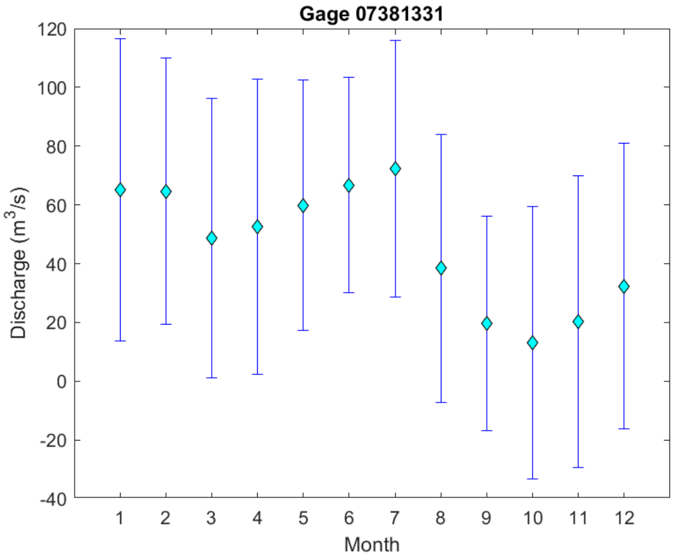

Figure 2.75 Monthly mean discharge for the Gulf Intracoastal Waterway

Same setup as Figure 2.69. The USGS notes this location is tidally-influenced.

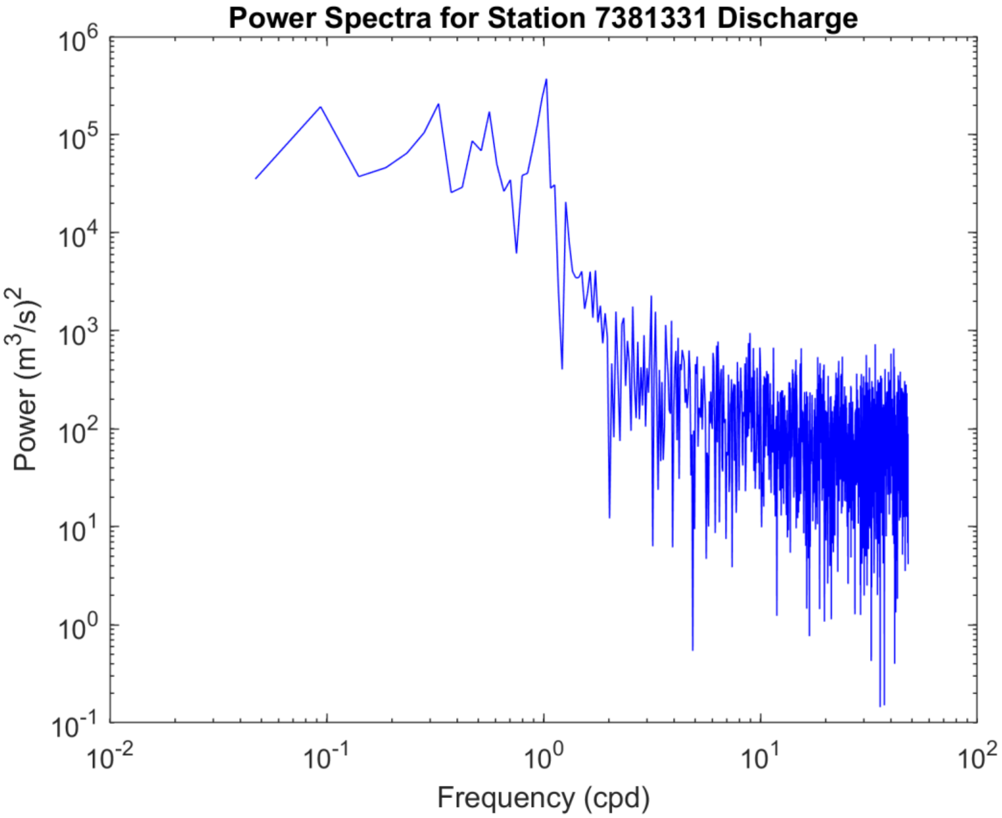

Figure 2.76 Discharge power spectra for the stream gage on the Gulf Intracoastal Waterway

Power spectra for discharge have power in units (m$^3$/s)$^2$ and frequencies in cycles per day (cpd). Unlike the other stream gages, this station has known tidal influence.

Coastal water level measurements also grant insights into circulation. The locations of the tide gages in Louisiana and all of the Florida tide gages place them outside the boundaries for the Mississippi Sound, but the coastal measurements make this dataset akin to the stream gages. Water levels are given with respect to mean sea level. Water level analysis for the tide gage measurements are included with the Mississippi Sound circulation.

Average water levels for the gages remain elevated compared to the mean sea level for most of the year. Figure 2.77 gives mean water levels for the twelve gages examined in this study. The Florida means are given by blue circles, the Alabama means by green diamonds, the Mississippi by red squares, and the Louisiana means by orange triangles. While the values, in general, stay above zero, the highest mean was <0.3 m at gage 8761305. The lowest was just under -0.15 m at gage 8760721 (Pilottown), but the gage deviates from the monthly pattern seen for the rest of the gages. Analysis of the 0860721 gage time series shows increased disagreement between the predicted and observed water levels in the second half of the year. As mentioned before, Louisiana water level data is preliminary. Looking at all 12 stations, standard deviations value are almost as high as the mean water level values.

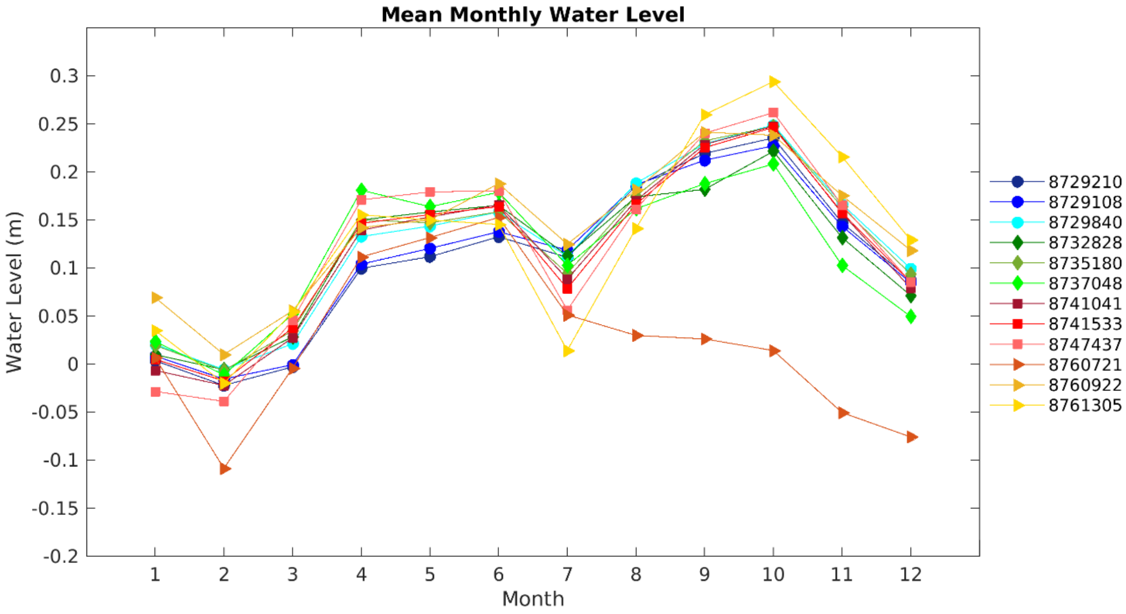

Figure 2.77 Monthly mean water levels

Average water level for three Florida (circles), three Alabama (diamonds), three Mississippi (squares), and three Louisiana (triangles) tide gages. Gage numbers use the NOAA National Ocean Service numbering.

Time series analysis of the tide gages confirm a microtidal range, and the power spectra indicate diurnal frequencies are principal frequencies for the region. Figures 2.78

and 2.79 show the power spectra for harmonically predicted water levels and observed water levels for gage 8741533 (NOAA Pascagoula Laboratory). Many of the other gages exhibit similar peaks, so this station was chosen for its central placement within the study area and for its representativeness of the other gages. Predicted water levels have peaks at 1 cpd, 2 cpd, and 4 cpd. A smaller 3 cpd peak is also present. Since the predicted water levels come from tidal harmonics, all four peaks are expected. The 1 cpd diurnal peak is the largest. The observed power spectra are significantly noisier. A 1 cpd peak is present, and smaller peaks, such as the 2 cpd semi-diurnal peak, can also be seen. However, fluctuations in water level on time scales less than 1 month tend to happen on a 24 hour period. The daily oscillations are common to all 12 gages.

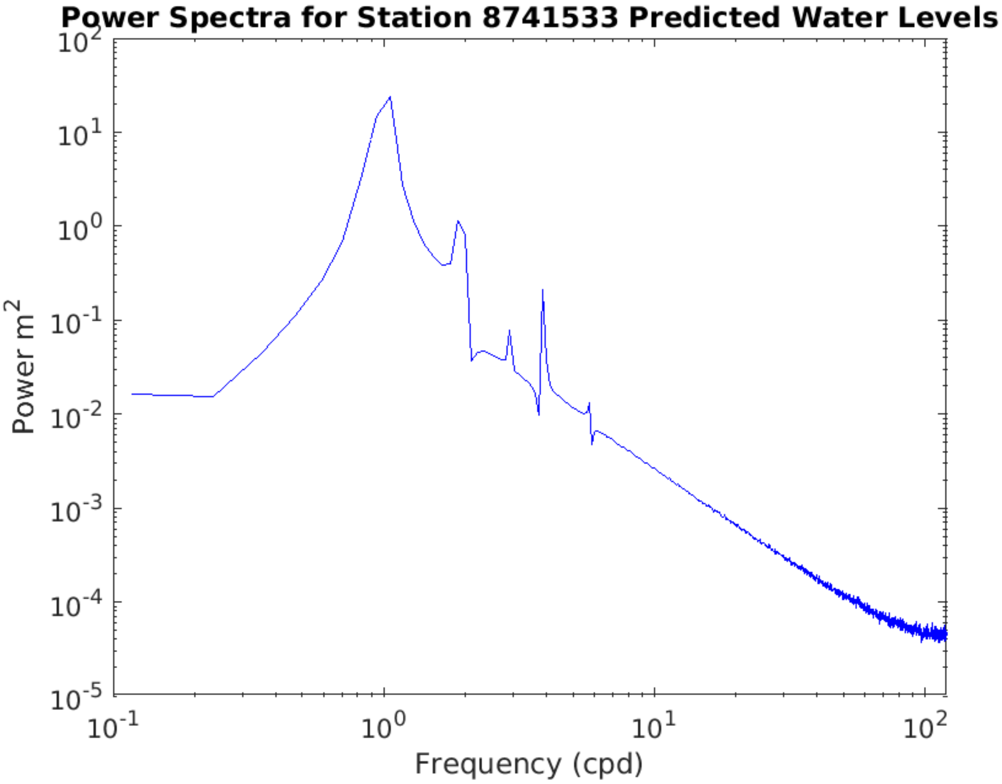

Figure 2.78 Power spectra for predicted water levels at the Pascagoula NOAA Laboratory

Power spectra for water levels have power in units $(m)^2$ and frequencies in cycles per day (cpd).

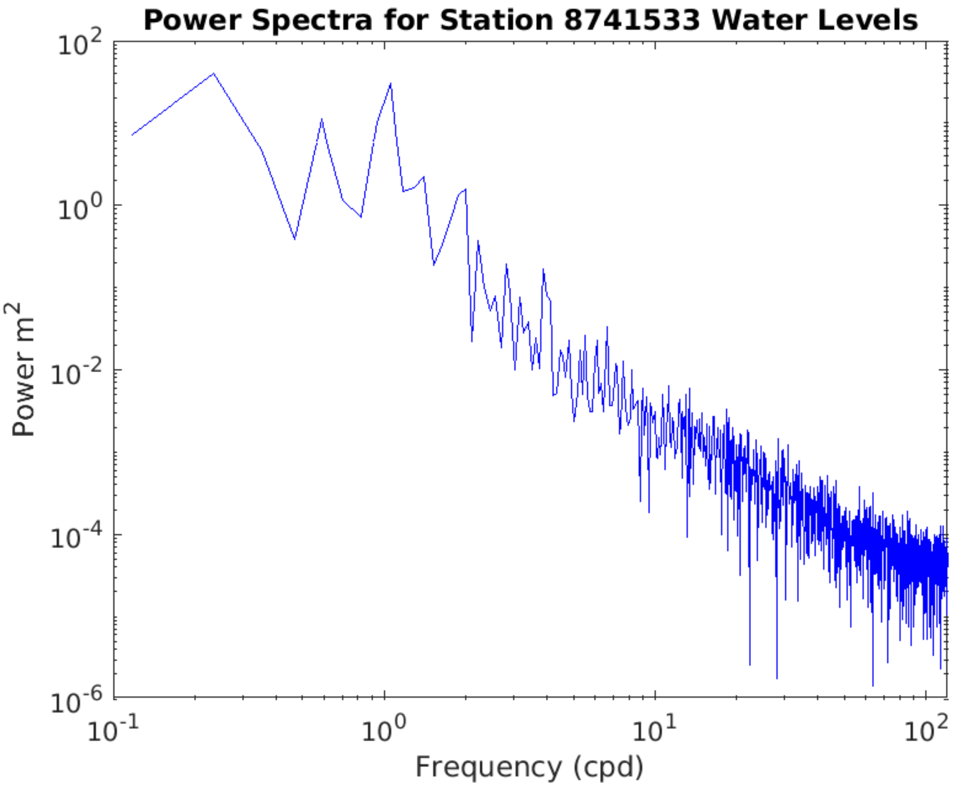

Figure 2.79 Power spectra for measured water levels at the Pascagoula NOAA Laboratory

Power spectra for water levels have power in units (m)$^2$ and frequencies in cycles per day (cpd).

### 2.3.3 Exchange Between the Mississippi Sound and Bight

Direct measurements inside the passes between the barrier islands are rare. One of the USGS-MDMR hydrological stations captures bottom salinity and temperature by East Ship Island, and the 25 MHz HFRs have intermittent coverage of Ship Island Pass. The other passes lack coverage. As such, observations are not readily available, and previous studies tend to be confined to one or two seasons of a single year. To that end, predictions from the Northeast Gulf of Mexico Operational Forecast System (NEGOFS) provided qualitative information on water exchange between the Mississippi Sound and Bight. Results from NEGOFS were compared to a 1980 observational study done by the

US Army Corps of Engineers, and where available, observations from the datasets described previously in this chapter were used to ground truth the NEGOFS results (Kjerfve, 1983).

NOAA's National Ocean Service (NOS) produces current, temperature, and salinity estimates using a nested three-dimensional finite volume community ocean model (FVCOM) that uses wind fields generated from National Weather Service Doppler sites (Wei et al, 2014). The 3-hour product gives parameter estimates at 51 locations throughout the Mississippi Sound, but this study is concerned with 6 locations: Ship Island Pass, Dog Keys Pass, Horn Island Pass, Petit Bois Pass, and 2 sites in Main Pass. Mean surface and bottom currents are presented graphically in Figures 2.80 through 2.91. Arrows for currents have been enlarged for visibility; all locations are in-water locations. Mean monthly surface and bottom temperatures and salinities are given in Figures 2.92 and 2.93 respectively.

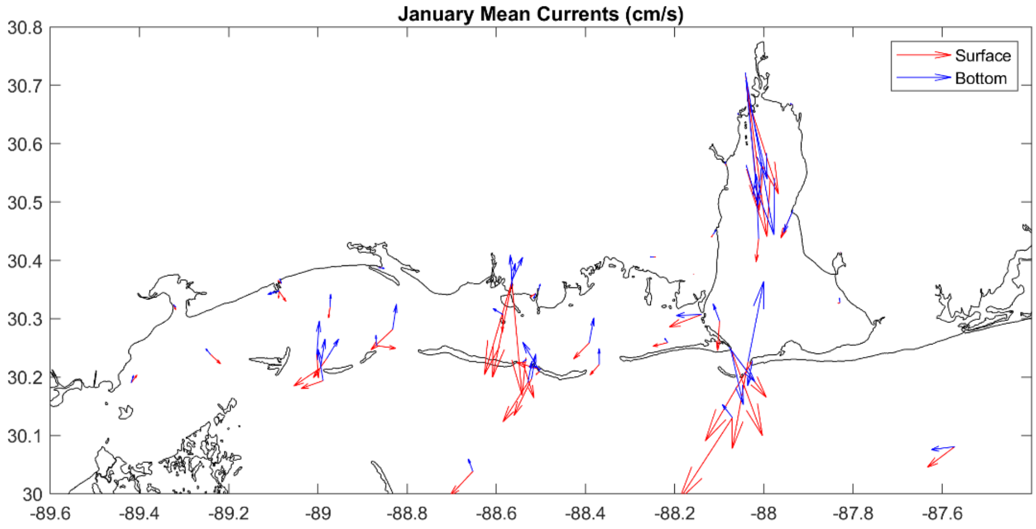

Figure 2.80 January mean surface and bottom currents for NEGOFS

Mean monthly velocity vectors for the surface and bottom of the 51 NEGOFS stations.

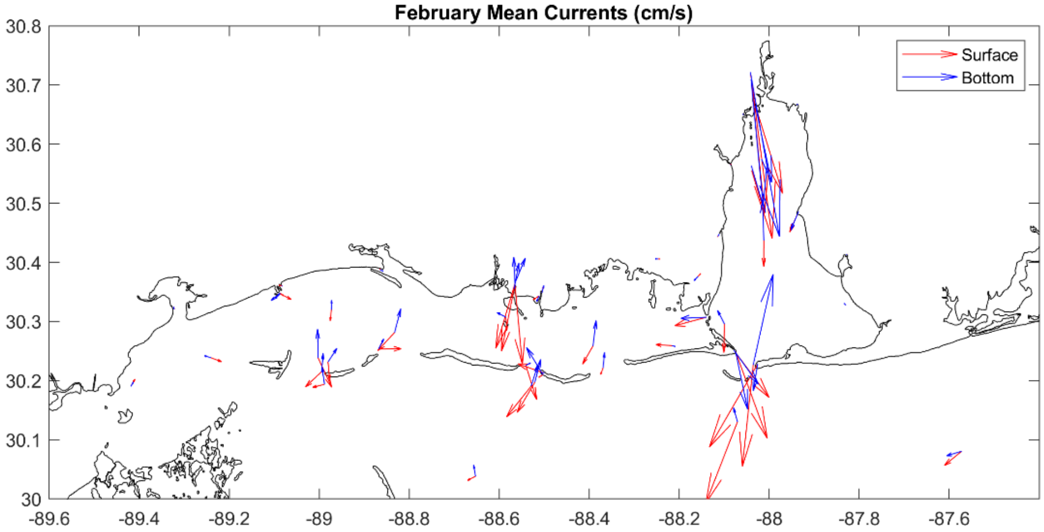

Figure 2.81 February mean surface and bottom currents for NEGOFS

Mean monthly velocity vectors for the surface and bottom of the 51 NEGOFS stations.

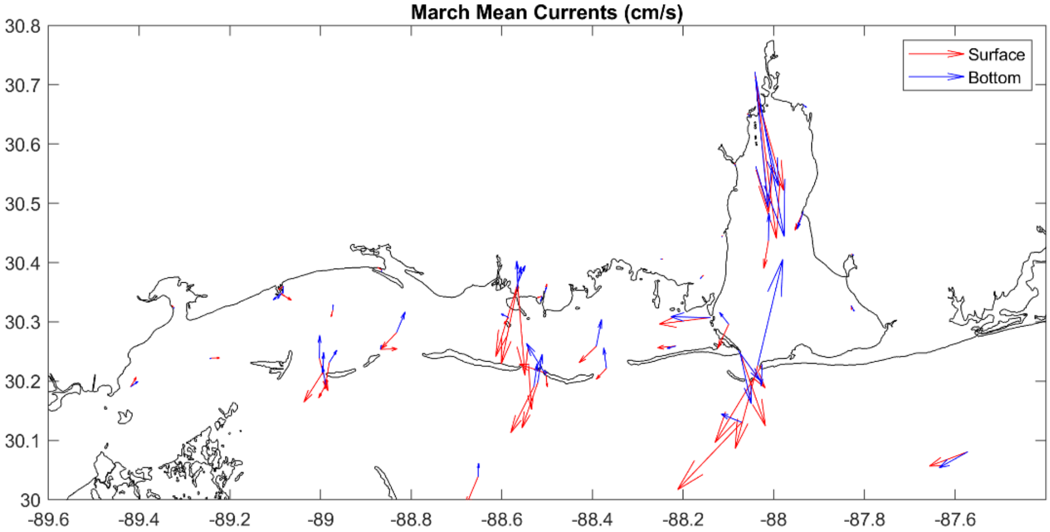

Figure 2.82 March mean surface and bottom currents for NEGOFS

Mean monthly velocity vectors for the surface and bottom of the 51 NEGOFS stations.

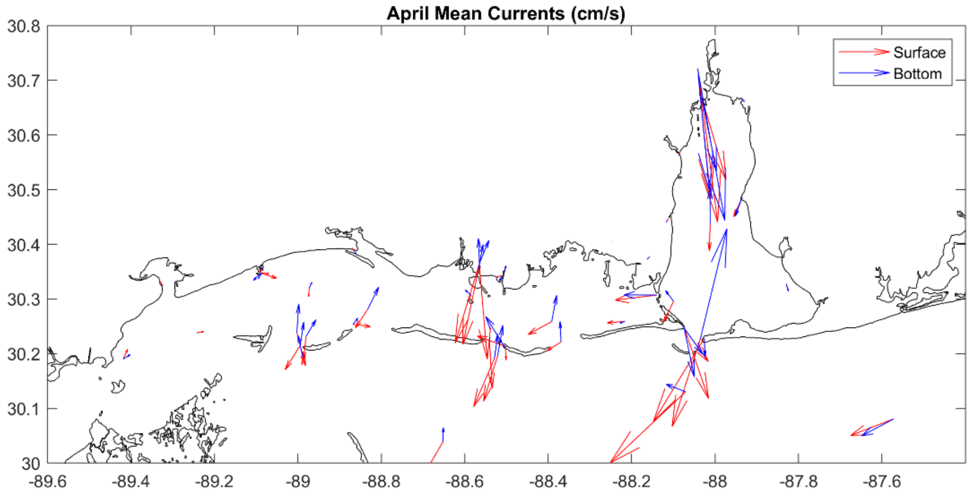

Figure 2.83 April mean surface and bottom currents for NEGOFS

Mean monthly velocity vectors for the surface and bottom of the 51 NEGOFS stations.

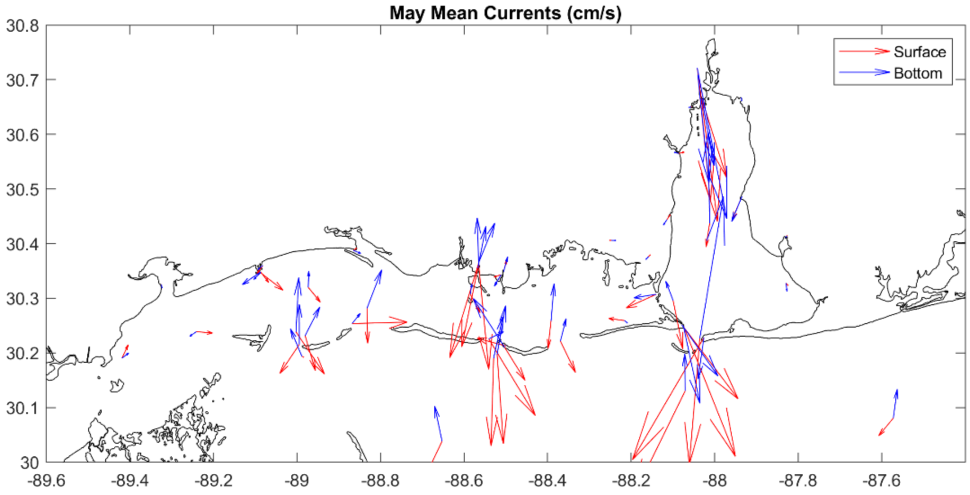

Figure 2.84 May mean surface and bottom currents for NEGOFS

Mean monthly velocity vectors for the surface and bottom of the 51 NEGOFS stations.

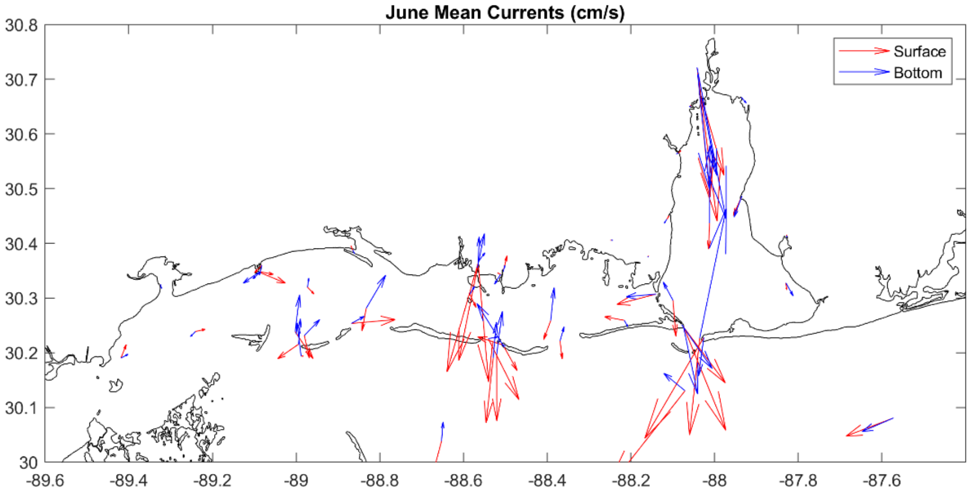

Figure 2.85 June mean surface and bottom currents for NEGOFS

Mean monthly velocity vectors for the surface and bottom of the 51 NEGOFS stations.

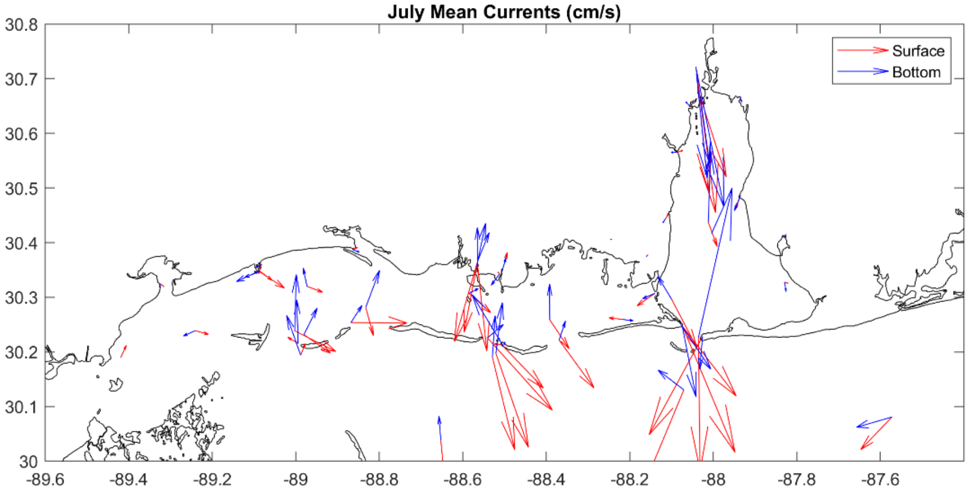

Figure 2.86 July mean surface and bottom currents for NEGOFS

Mean monthly velocity vectors for the surface and bottom of the 51 NEGOFS stations.

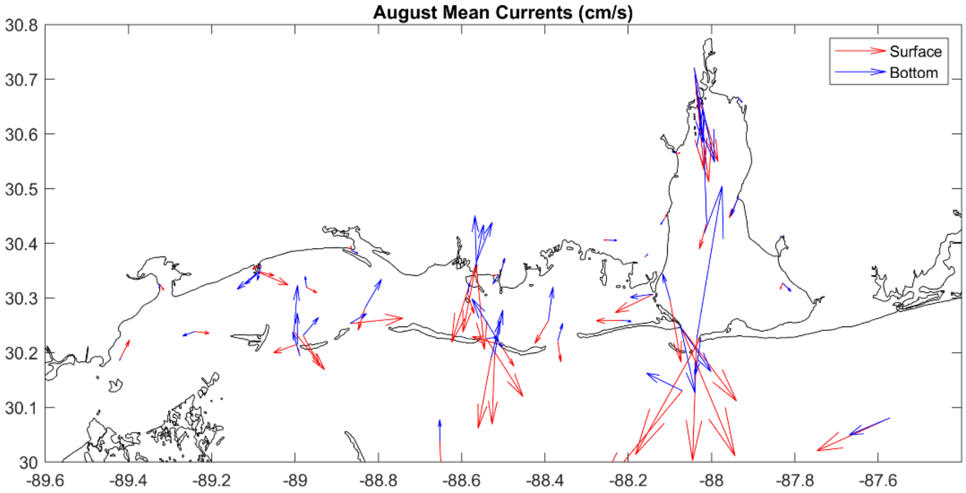

## Figure 2.87 August mean surface and bottom currents for NEGOFS

Mean monthly velocity vectors for the surface and bottom of the 51 NEGOFS stations.

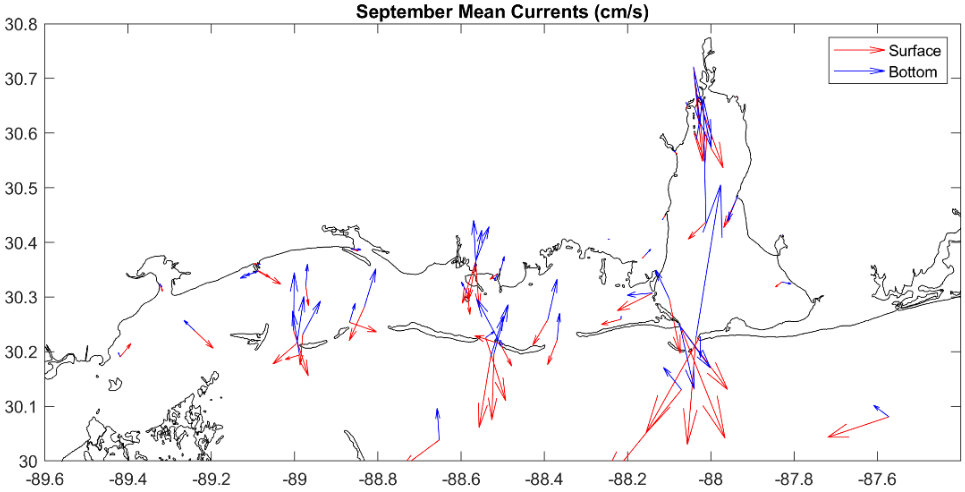

## Figure 2.88 September mean surface and bottom currents for NEGOFS

Mean monthly velocity vectors for the surface and bottom of the 51 NEGOFS stations.

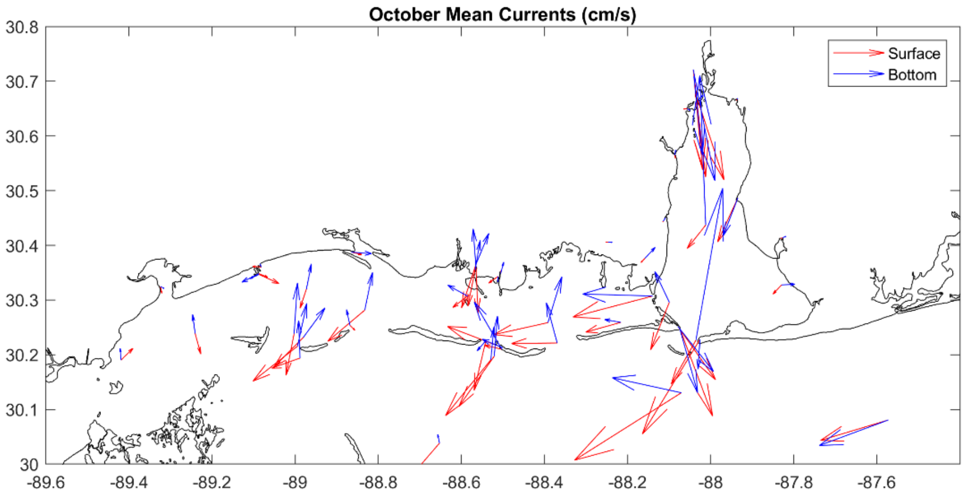

Figure 2.89 October mean surface and bottom currents for NEGOFS

Mean monthly velocity vectors for the surface and bottom of the 51 NEGOFS stations.

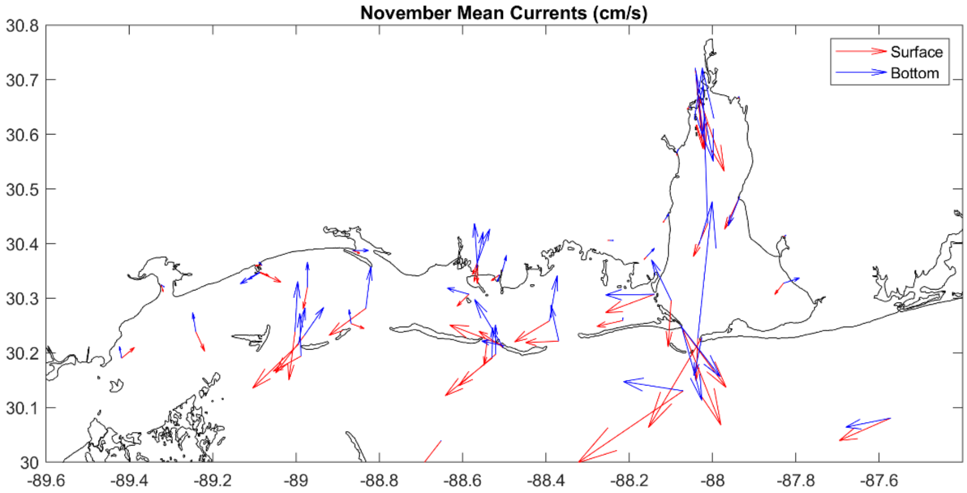

Figure 2.90 November mean surface and bottom currents for NEGOFS

Mean monthly velocity vectors for the surface and bottom of the 51 NEGOFS stations.

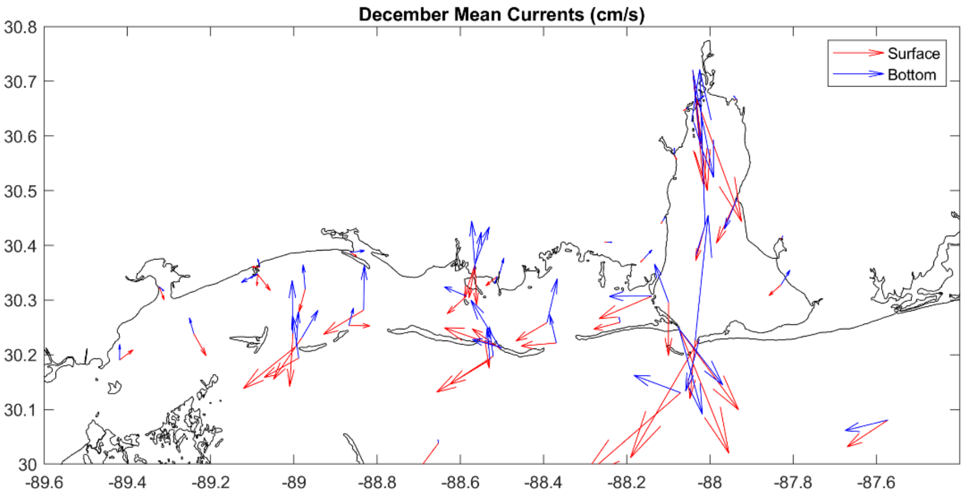

Figure 2.91 December mean surface and bottom currents for NEGOFS

Mean monthly velocity vectors for the surface and bottom of the 51 NEGOFS stations.

Unlike currents observed in the northwest Mississippi Sound and most of the Mississippi Bight, monthly surface and bottom currents show relatively little variation month to month. Mean current speeds and their associated standard deviations vary by less than 3 cm/s for Ship Island Pass, Dog Keys Pass, and Petit Bois Pass. Mean values do fluctuate for Horn Island Pass and Main Pass, but accompanying changes in standard deviations make these differences insignificant. Where multiple NEGOFS grid points exist in and near the passes, a 90°-180° spread in current direction persists through the year at the surface and at the bottom. Surface current directions consistently point into the Mississippi Bight ranging southwest to southeast while bottom current directions point into the Mississippi Sound. The only exception to this pattern is the west side of Main Pass where surface and bottom currents both flow to the southeast just east of Dauphin Island. By contrast, the surface currents in the eastern side of Main Pass flow southwest while bottom currents flow north northeast. Surface and bottom currents in Main Pass have the highest mean speeds throughout the year but also exhibit the largest variability. Dog Keys Pass has the lowest current magnitudes. Petit Bois Pass has the second lowest speeds at the bottom while Ship Island Pass has the second lowest at the surface. High direction and magnitude variability and similar mean currents from one month to the next suggest seasonality plays a minor role in water exchange between the Mississippi Sound and Bight in terms of NEGOFS output.

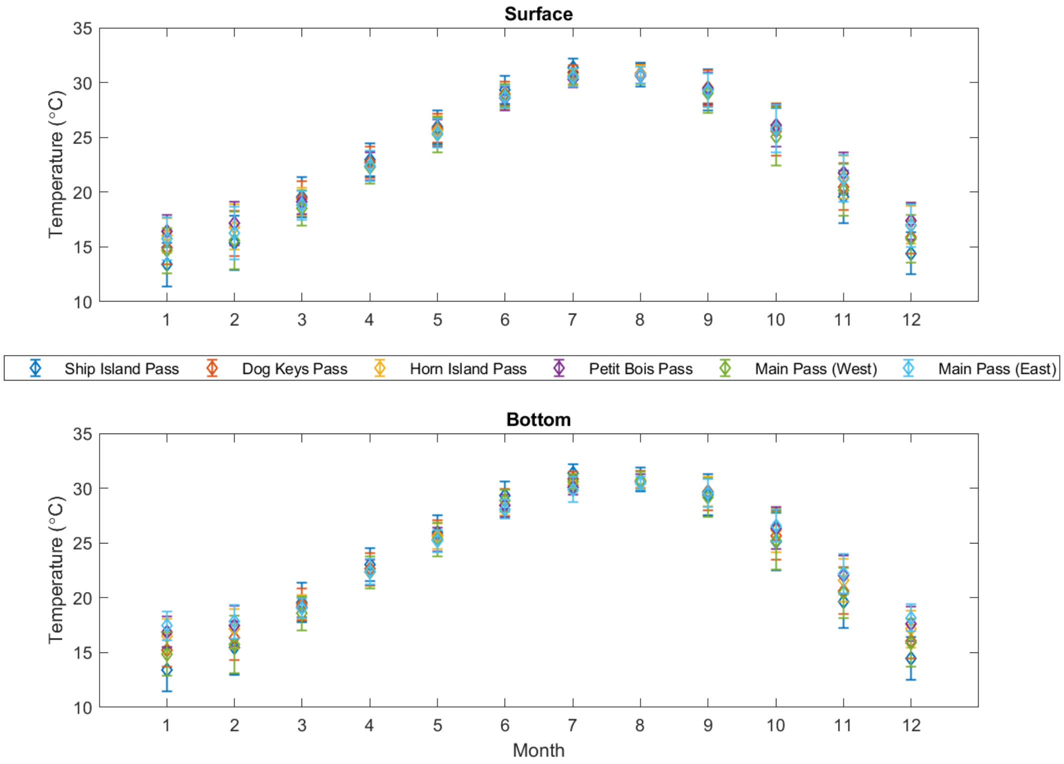

Figure 2.92 Monthly mean NEGOFS temperatures in the barrier island passes

Mean monthly temperatures and standard deviations for the surface (top) and bottom (bottom) of 6 stations located in the passes between barrier islands.

In terms of estimated temperature and salinity in the passes, seasonality can be seen clearly in temperature and to a smaller degree in salinity. When considering standard deviations, no discernible difference exists between surface and bottom temperature. Temperatures in every pass reach their lowest in December and January and their highest in July and August, so these patterns agree with the observations of the hydrological stations in the Mississippi Bight. Horizontal temperature ranges in the Mississippi Sound vary by less than 1°C from one pass to another for most of the year, but temperatures November through February differ by 2-3°C. Surface and bottom salinities do not align closely from pass to pass. Ship Island Pass and the western side of Main Pass had the lowest salinities throughout the year. Salinity values in the eastern half of Main Pass were lower and had higher standard deviations than bottom salinity means and standard deviations. Across all passes though, February through April saw fresher waters while October through December had the highest salinity in every pass.

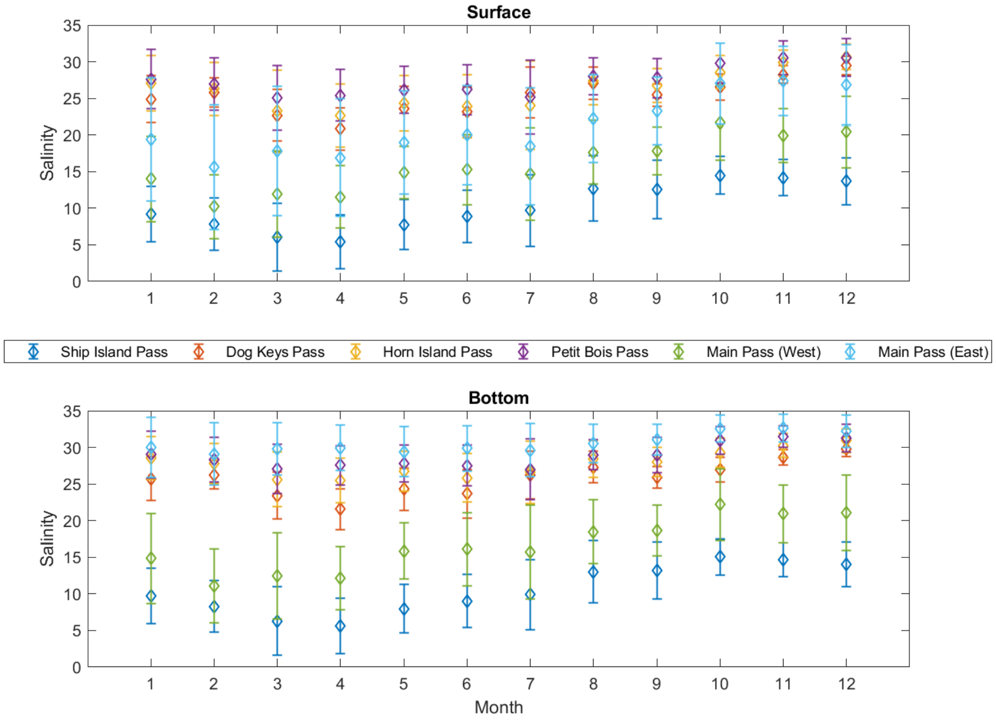

Figure 2.93 Monthly mean NEGOFS salinities in the barrier island passes

Mean monthly salinities and standard deviations for the surface (top) and bottom (bottom) of 6 stations located in the passes between barrier islands.

The 182-day average surface and bottom currents presented in Kjerfve (1983) reflect a net surface outflow of water from the Mississippi Sound into the Mississippi

Bight, mostly to the southwest. Surface current velocities are depicted by red arrows in Figure 2.94 while bottom velocities have blue arrows. Two current meters were deployed in Dog Keys Pass. The western site shows southeast flow into the Bight while the eastern site shows southwest flow into the Bight. Directional shifts across the widths of passes can be seen in the NEGOFS monthly averages as well. However, the surface northwest oriented velocities pointing into the Mississippi Sound in Ship Island Pass and the northeast velocities west of Cat Island disagree with the NEGOFS and 25 MHz HFR surface velocities. While this may be the result of a 7-month average compared to the 1-month averages for the 2014-2017 data, surface outflow is present at these locations from April through October. Subaerial land loss and island migration could explain directional disagreement between the two time periods.

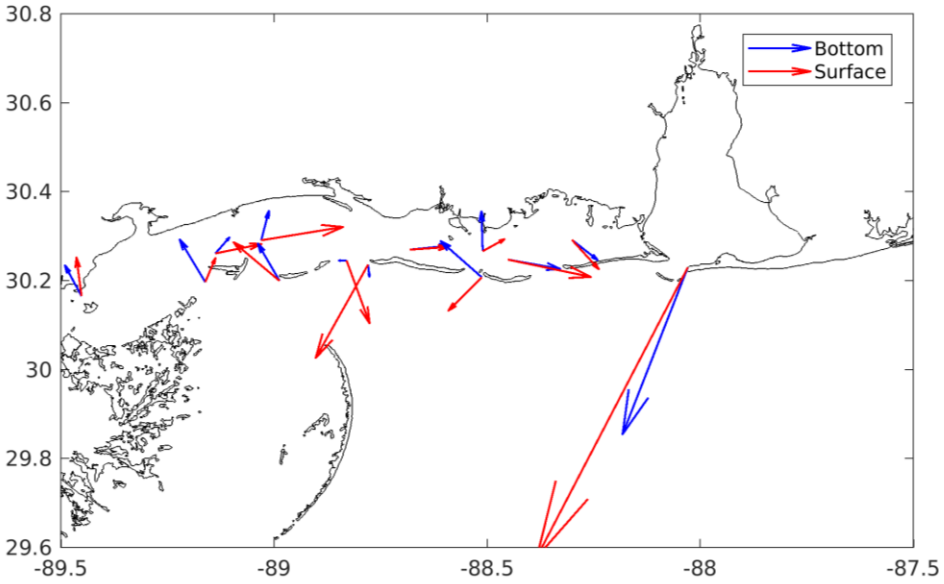

Figure 2.94 Mean surface and bottom currents from the Kjerfve 1983 study

Measurements represent a 182 average from April 1980 through October 1980; values retrieved from Kjerfve (1980).

In terms of bottom salinity and temperature, USGS-MDMR hydrological stations 2, 5, 9, and 10 had NEGOFS positions nearby, so these sites provided points of comparison. The locations of these sites are shown graphically in Figure 2.95, and (Table 2.4) and (Table 2.5) give the monthly root-mean-square errors (RMSEs) in bottom salinity and temperature between the two. The magnitude of change increased east to west. Salinity RMSE exceeded 8 in winter and summer for stations 9 and 10. Temperature differences never exceeded 2.5°C.

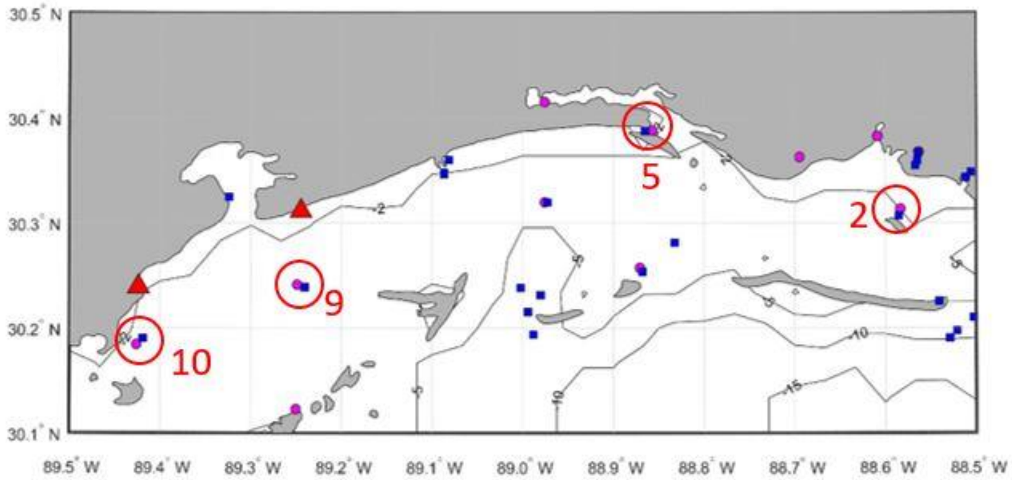

Figure 2.95 Comparison locations between USGS-MDMR observations and NEGOFS

For reference, the positions of the two 25 MHz HFRs are given by red triangles. Magenta circles denote hydrological station positions while blue squares show NEGOFS locations. Red circles mark the four comparison locations: station 2, station 5, station 9, and station 10 from the USGS-MDMR stations.

Table 2.4 Root-Mean-Square Error between Observed and Predicted Bottom Salinity

| Month | Station 2 | Station 5 | Station 9 | Station 10 |
|---|---|---|---|---|
| January | 3.0 | 1.2 | 7.9 | 9.2 |
| February | 5.9 | 0.2 | 10.8 | 11.7 |
| March | 3.3 | 0.4 | 7.4 | 6.2 |
| April | 0.9 | 0.1 | 4.2 | 3.6 |
| May | 1.5 | 3.1 | 2.9 | 4.5 |

Table 2.4 (continued)

| | | | | |
|---|---|---|---|---|
| June | 0.8 | 4.8 | 2.7 | 4.6 |
| July | 4.9 | 0.1 | 9.4 | 11.0 |
| August | 3.9 | 0.8 | 7.2 | 12.8 |
| September | 3.1 | 1.1 | 5.0 | 11.7 |
| October | 2.8 | 3.4 | 6.6 | 10.6 |
| November | 2.0 | 2.2 | 8.5 | 10.9 |
| December | 0.1 | 1.4 | 9.3 | 12.5 |

Table 2.5 Root-Mean-Square Error between Observed and Predicted Bottom Temperature

| Month | Station 2 | Station 5 | Station 9 | Station 10 |
|---|---|---|---|---|
| January | 2.2°C | 0.4°C | 1.8°C | 1.7°C |
| February | 1.7°C | 0.3°C | 1.8°C | 1.7°C |
| March | 0.8°C | 0.3°C | 2.4°C | 1.8°C |
| April | 0.2°C | 0.2°C | 1.5°C | 1.2°C |
| May | 0.2°C | 0.1°C | 0.6°C | 0.6°C |
| June | 0.2°C | 0.0°C | 1.2°C | 0.8°C |
| July | 0.7°C | 0.3°C | 1.9°C | 1.2°C |
| August | 0.7°C | 0.2°C | 1.3°C | 0.9°C |
| September | 0.7°C | 0.3°C | 1.0°C | 0.9°C |
| October | 1.0°C | 0.0°C | 1.1°C | 0.7°C |

Table 2.5 (continued)

| | | | | |
|---|---|---|---|---|
| November | 1.4°C | 0.1°C | 1.3°C | 0.8°C |
| December | 0.4°C | 2.1°C | 0.4°C | 0.9°C |

## 2.4 Discussion

The circulation variability found in this study agrees broadly with results presented in previous literature. Hourly surface current speeds in the Mississippi Bight rarely exceed 1 m/s, and magnitudes usually stay below 0.5 m/s. Current directions have high temporal and spatial variability. Surface current directions in the Mississippi Sound and Bight show 360° rotation on diurnal timescales, and coastal water levels fluctuate primarily with the tides. Several geographical features setup cohesive channels of flow. Riverine outflow points like the Mississippi River, Mobile Bay, Pensacola Bay west of the Destin HFR site, and Choctawhatchee Bay nearest the Destin site are among these coastal features. Dominant outflow directions rotate about 45° throughout the year whereas velocities above the De Soto Canyon shift northeast to southwest. Wind (origin) directions exhibit more directional variability in the Mississippi Bight than Gulf-wide studies; southwesterly winds peak in July and August in the Mississippi Bight.

Where model output or observations exist, surface and bottom current directions change west to east across island passes, and the islands themselves appear to disorganize and split current patterns. Most of the passes have surface and bottom currents separated by at least 90° with surface currents pointing into the Bight, and bottom currents directing water into the Sound. Temperature distributions show horizontal homogeneity, so salinity works as a much better indicator of sustained horizontal gradients. This study highlights region-specific circulation, but the overall circulation patterns agree with annual patterns and dominant frequencies of variability observed by Ohlman and Niiler (2005), Johnson (2008), and Howden and Kern (2013).

The uniqueness of the study area lies in coastline orientation and the resiliency of the barrier islands. The Louisiana coast and Mississippi-Alabama-Florida panhandle coasts run nearly perpendicular to one another. This orthogonal alignment of a mostly east-west coast and mostly north-south coast could partially explain differences in wind directions between this study and other literature that examines a much larger domain. As mentioned previously, the Mississippi-Alabama barriers have undergone multiple rounds of segmentation and westward translation. Consequently, larger passes allow more water exchange between the Mississippi Sound and Mississippi Bight. Overall bottom salinity in the Mississippi Sound has increased since the 1980 study (Kjerfve, 1983). The different observational platforms reveal patterns in circulation are location-specific suggesting bathymetry and subaerial land play controlling roles in influencing circulation along with winds and tides.

# CHAPTER III – PERTURBATION OF THE MISSISSIPPI SOUND AND BIGHT BY TROPICAL CYCLONES

As punctuated events, tropical storms and hurricanes fall into a unique category. Most occur within the designated hurricane season, June 1 through November 30, but storms have developed well before and after these dates. Several generalizations have been attached to tropical cyclones, but exceptions exist. Sea surface temperatures above 26.5°C tend to sustain and strengthen tropical cyclones, and strong vertical wind shear usually works to weaken the storms (Palmen, 1948). Many Atlantic basin storms can be traced back to tropical waves coming off the western African coast, and atmospheric ridges (highs) and troughs (lows) serve to steer tropical cyclones. Additionally, more intense storms tend to have smaller radii of tropical storm force winds since the center of rotation becomes better defined. However, no two storms are identical, and the storms do not conform to seasonal patterns or have repeated, systematic behavior. Each tropical cyclone claims a unique genesis, path, wind field, and neighboring atmospheric conditions. Consequently, impacts on circulation in the Mississippi Sound and Mississippi Bight by tropical storms and hurricanes deserve a separate analysis.

## 3.1 Atlantic Hurricane Record

Storm data used in this analysis came from the Atlantic Hurricane Database. The database synthesizes available records for all recorded Atlantic basin storms from 1851 onwards into a best estimate re-analysis product (Landsea et al., 2004). Storm data from the Northeast and North Central Pacific Hurricane Record were also retrieved since Pacific basin storms occasionally transit across Mexico into the Gulf of Mexico. Four such storms have come within 10° of the Mississippi Bight, as bounded by 28.5°N, 30.5°N, 86°W, and 89°W, since the start of the Pacific record in 1949, but none of those storms came into the Gulf of Mexico as tropical storms or hurricanes. The only storms to approach or enter the Mississippi Bight did so as remnants, so while this analysis included the Pacific record, no storms fit the criteria detailed below for Gulf of Mexico tropical cyclones.

Storm eye coordinates for individual storms provided storm locations throughout each storm's duration, and maximum sustained wind speed, converted from knots to m/s, at the eyewall were used as the metric for storm intensity. Wind radial extent estimates for 34, 50, and 64 knot winds are available starting with the 2004 hurricane season, and these extents provided the cone of influence (radius of tropical storm force winds) related to each storm. Unfortunately, the hurricane database does not track positions of nearby atmospheric troughs or ridges. Trough and ridge information is detailed in individual storm reports, but only data pertaining directly to the storms were available in the hurricane database.

The hurricane database gives 6 hour time steps between measurements. As overlapping data records exist for high frequency radar, tide and stream gages, buoys, and hydrological stations from 2014 until 2017, those four years were considered for this analysis. However, the preliminary analysis included storms from previous years to set a baseline against which to gage oceanic response to each storm.

This study cannot provide statistics on the Mississippi Bight and Sound's responses to tropical cyclones for three reasons. First, a four year period does not provide a long enough time series to capture the variability in tropical cyclones which impact the northern Gulf Coast. Second, data availability varies from one storm to the next, so even if multiple storms have similar tracks and intensities, a one-to-one quantitative comparison is rarely possible. Third, only one storm passed through the study domain during the four year period, so the study period lacks data for multiple direct strike storms. This study can, however, supply qualitative analysis of individual storms and examine whether any general conclusions can be formed for hurricane seasons within the time frame considered. Results will inevitably change if a longer temporal period is considered.

In considering the 2004-2017 seasons for preliminary wind field analysis, nautical mile distance for the radial extents of storm winds had to be converted into geographic coordinates to determine which storms' cones of influence impinged on the northern Gulf of Mexico. First, radial distances were converted from nautical miles to kilometers. Assuming the earth to be an oblate spheroid, the World Geodetic System of 1984 datum was employed to convert kilometer distance into distance along parallels and meridians in order to find the latitudes and longitudes corresponding to wind radial extents at each time moment for each quadrant of a storm. Storm eye coordinates served as the reference coordinates for the calculations. Plots were then generated showing cones of influence.

### 3.2 Isolating Gulf of Mexico Storms

Establishing a threshold for storms which directly impacted the study area proved challenging as most data sets used in this project only overlapped with 5-20 storms, and each storm had a unique path, lifetime, intensity, and formation time within the calendar year. The Gulf of Mexico is a semi-enclosed sea. Tropical cyclones outside the Gulf are unlikely to cause direct or indirect changes to circulation in the Mississippi Sound and Bight. Consequently, only storms that entered or formed within the Gulf of Mexico or storms that had wind fields that entered the Gulf of Mexico were considered for this study. Data from NDBC buoy 42040 were used to examine atmospheric conditions at buoy when tropical cyclones were in the Gulf of Mexico. Measurements date back to 1995, so data exist for more than 20 hurricane seasons.

Unfiltered buoy wind speed and buoy wave height data were compared to tracks and times of Atlantic basin storms to see which storms coincided with peaks in the wind and wave time series. Time series for wind speed and wave height at buoy 42040 are given in Figures 3.1 and 3.2 with the arithmetic means denoted by green and orange lines respectively, and blue and red vertical bars highlight each hurricane season. Data peaks refer to values 1, 2, and 3 standard deviations above the mean. Red lines show the 1st, 2nd, and 3rd standard deviations above the mean in Figure 3.1 while yellow lines give these values in Figure 3.2. While wind speed and wave height data do not have normal distributions, deviations about the mean provided a first pass isolation of wind events.

The time series analysis gave cursory confirmation that several dozen Gulf storms occurred in tandem with anomalous measurements at the buoy. As an example, the strongest peaks occurred during hurricanes Georges (1998), Ivan (2004), and Katrina (2005). In terms of wind speed, higher magnitudes occurred during certain hurricane seasons, but higher wind speeds also happened annually during the October to April period when winter cold front passages occur (Roberts et al., 1989). Extreme wave heights (>5 m), though, occurred almost exclusively during hurricane season months.

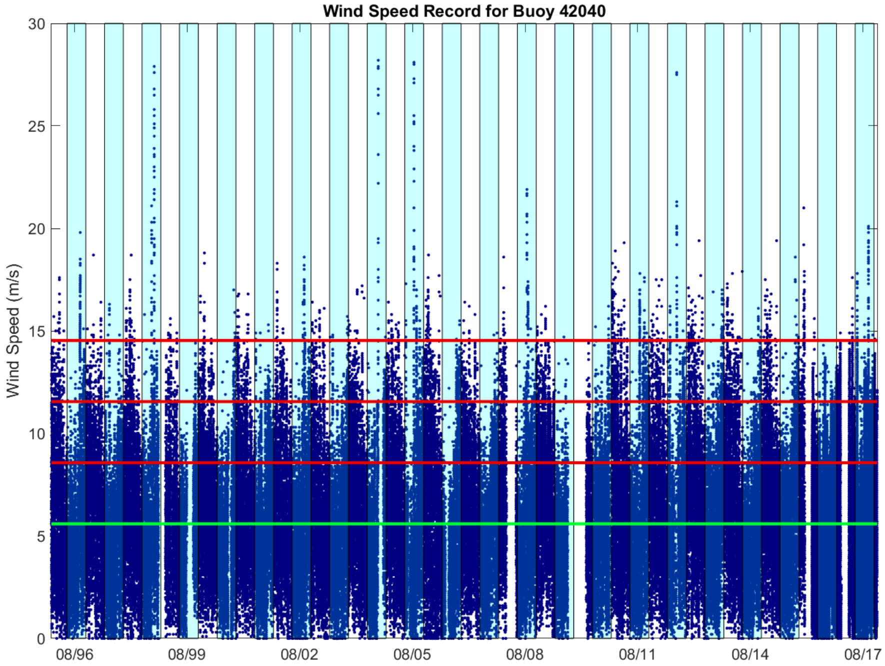

Figure 3.1 Time series of buoy 42040 wind speeds

Blue circles show 10 m wind speeds recorded at the buoy from January 1996 through December 2017. The light blue bars denote the hurricane season interval for each calendar year. The green line gives the mean wind speed for the whole time series with the 1st, 2nd, and 3rd standard deviations above the mean marked by red lines.

Since peaks occurred in both the wind and wave height records during hurricane seasons, wind speeds were plotted against wave heights to establish whether a correlation existed between the two datasets when tropical cyclones were in the Gulf. Easterly alongshore winds can elevate water levels through a geostrophic response; however, water levels were not measured at the buoy. Increased wave height should also accompany increased wind speed, and buoy 42040 measures wave height. Wind speed measurements were restricted to winds coming from the east northeast to east southeast during times when one or more tropical cyclones were in the Gulf of Mexico. A quadratic fit best represents the relationship between wind speed and wave height for all wind speeds. However, for easterly winds above 25 knots (12.86 m/s), linear regression fit best describes the relationship between wind speed and wave height during storm periods. The plot and regression line are displayed in Figure 3.3.

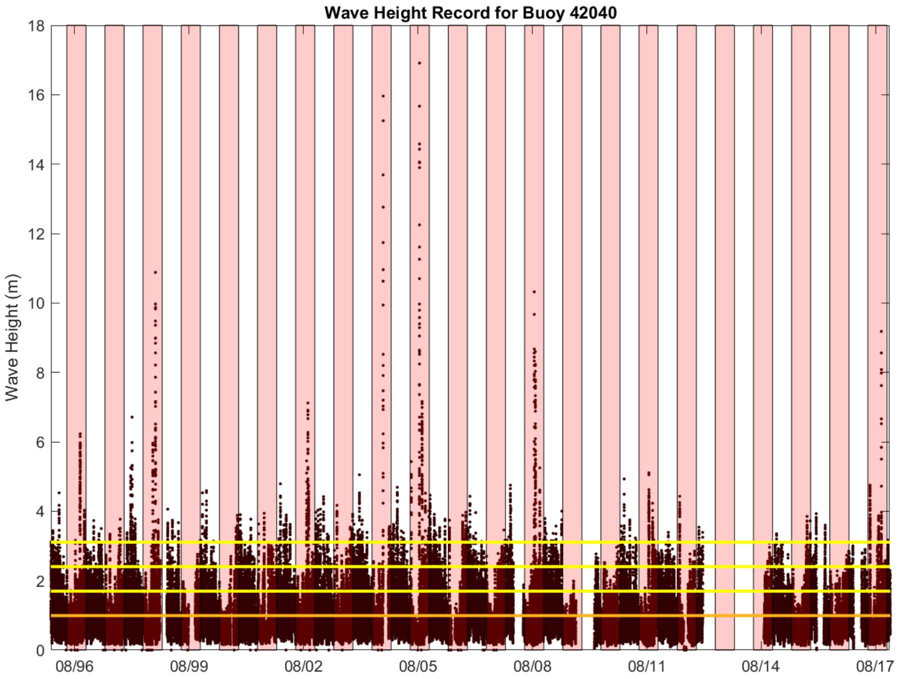

Figure 3.2 Time series of buoy 42040 wave heights

Dark red circles show wave heights recorded at the buoy from January 1996 through December 2017. The pale red bars denote the hurricane season interval for each calendar year. The orange line gives the mean wave height for the whole time series with the 1st, 2nd, and 3rd standard deviations above that mean marked by yellow lines.

Following confirmation that buoy measurements could show storm-induced winds and waves, three-variable scatter plots were generated using a combination of hurricane database and buoy measurements. From the database, maximum sustained wind speed at the storm's eyewall, the distance of the storm's eye from the buoy, and minimum pressure in the eye were considered. Additionally, wind radial extents for the four quadrants of the storm, forward direction speed of the storms, and changes in storm intensity were also calculated. Wave height, wind speed, wind direction, air temperature, and atmospheric pressure were utilized from the available buoy measurements. Distance from the storm's eye to the buoy was used consistently as the x-axis variable, but the variables along the y and z (color) axes changed. The Bay of Campeche is the furthest location within the Gulf of Mexico from buoy 42040 at approximately 12°, so 12° was set as the maximum distance. This allowed the inclusion of all Gulf storms even though more distance storms are less likely to cause changes to Mississippi Bight circulation. Logical indexing was used to retrieve only those storms that entered the Gulf of Mexico. Substantial scatter marked every plot regardless of variable choice.

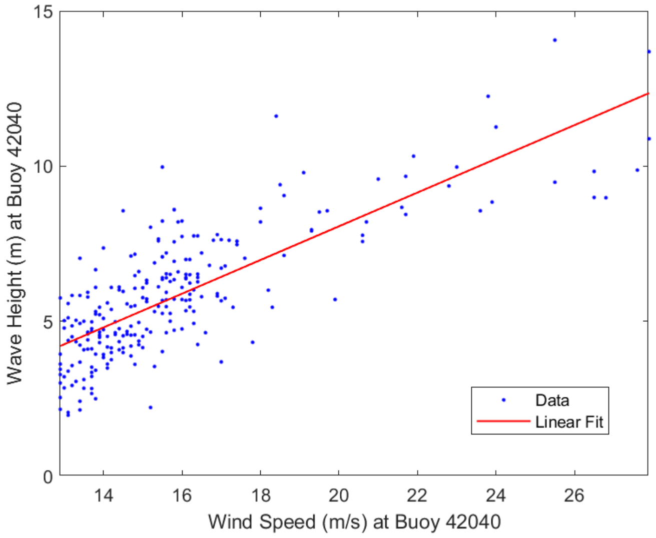

Figure 3.3 Comparison of easterly wind speeds to wave heights

Blue circles display wind speed comparisons to wave heights, both measured at NDBC buoy 42040 while the red line shows a linear regression. Data have been limited to winds coming from the east northeast (56.25° clockwise from north) to east southeast (123.75° clockwise from north) that have speeds above 25 knots (12.86 m/s) during Gulf storm periods.

Gulf of Mexico storms had a highly variable relationship with measurements taken at the buoy. Plots demonstrate a linear decay trend for wind speeds at the buoy compared to buoy-to-storm distance with $R^2$ values below 0.3. $R^2$ values near 1 do not automatically prove a correlation between variables; residuals should also be considered. Figure 3.4b gives the residuals plot for Figure 3.4a. Patterns in residuals, i.e. linear, sinusoidal, high or low bias, call linear regression results into question. Residuals should have randomized distribution. This occurs in Figure 3.4b. Given the small sample size, the low $R^2$ value is to be expected. At best, meteorological and hydrographic parameters at the buoy have only a weak correlation to Gulf storms. Future studies that include a collection of direct strike and further afield Gulf storms spanning multiple decades may yield different results, but the varied characteristics of individual tropical cyclones will likely frustrate any study.

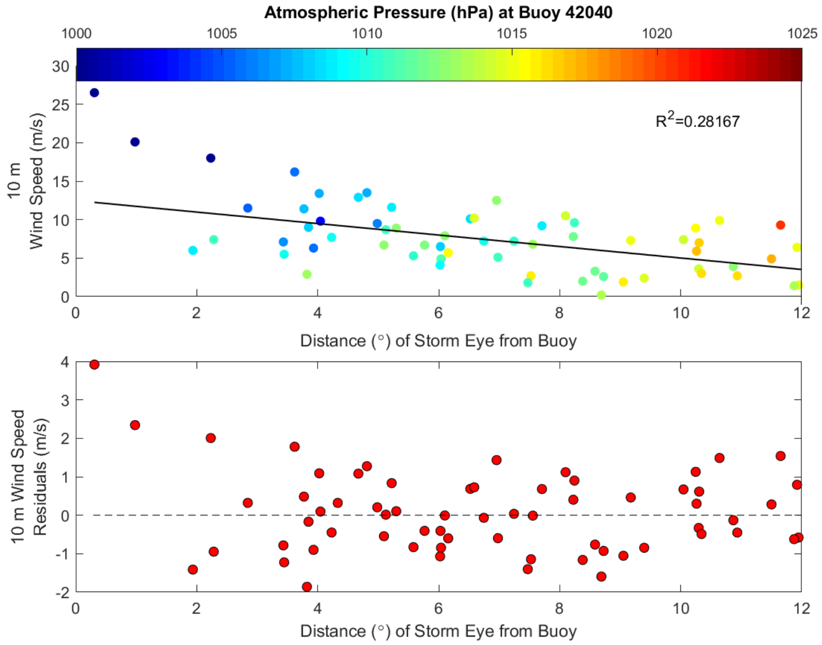

Figure 3.4 Scatter plot on buoy 42040 measurements for Gulf of Mexico storms

(Top) Scatter plot with distance from the buoy to the storm eye on the x-axis, 10 m wind speed at the buoy measured on the y-axis, and atmospheric pressure at the buoy on the color axis. The black line shows the linear regression fit to the data. (Bottom) Residuals from the regression line for 10 m wind speeds.

Ho et al. (1987) constructed a hurricane climatology based on tropical cyclone parameters for storms in the Gulf of Mexico and in the Atlantic; as with this study, the climatology found no concrete correlation between parameters due to small sample size. The climatology subdivided the U.S. Gulf and east coasts into sections where tropical cyclones had made landfall. The study considered storm central pressure, radius of maximum winds, storm forward speed, direction of the tropical cyclones, coastal sections, and storm locations. Using non-parametric tests, no similarities were found for storms in the northern Gulf of Mexico east of Texas (Ho et al., 1987). The authors suggested the irregularity of the Louisiana-Mississippi-Alabama coastlines could be a contributing factor to the variable response of the coast to tropical cyclones, and storm distance was the only parameter corresponding to damage. In that vein, the present study also shows a weak relationship between storm distance and changes in the hydrographic parameters of the Mississippi Sound and Bight.

The 3-variable plot process was repeated for the northwest, northeast, southeast, and southwest 34 knot wind radii. Historically, most storms that approach the Mississippi Bight enter the Gulf of Mexico from the southeast (i.e. through the Yucatan Channel, across Cuba, the Straits of Florida, and the Florida peninsula), so winds northeast and northwest of the storm eye will influence the study region first. Therefore, 3-variable scatter plots with regression fits for the northeast and northwest quadrants are presented in Figures 3.5 and 3.6. While still low, the $R^2$ value for Figure 3.6 exceeds the value in Figure 3.4, and the residuals for both plots have a random distribution.

Beyond tracking variable changes at buoy 42040 against Gulf storms, storm orientation with respect to the Mississippi Bight was divided into four categories: southeast, southwest, northeast, and northwest storms. Rotation speed combined with the forward speed of storms generates higher winds to the right of the propagation direction of a tropical cyclone. This effect creates an imbalance in the distribution of winds around the eyewall. Consequently, the storm’s location relative to the Mississippi Bight can control the magnitude of response the area feels.  Storms can have complex paths though, so any given storm might shift its position relative to the region.  As such, the initial position of a storm's eye relative to the center of the Mississippi Bight when it first entered the Gulf of Mexico or its generation location within the Gulf was used as the approach direction.

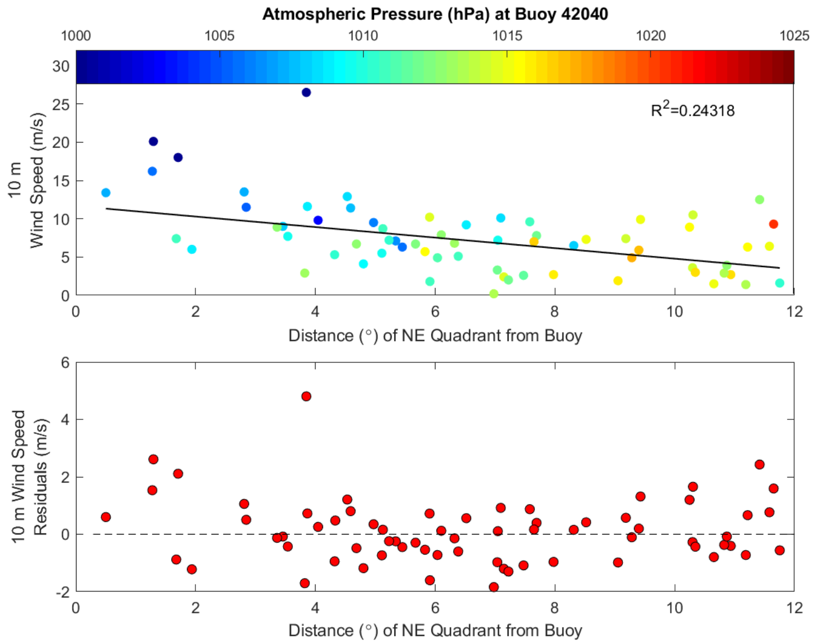

Figure 3.5 Scatter plot on buoy 42040 measurements for the northeast quadrant of Gulf of Mexico storms

(Top) Scatter plot with distance from the buoy to a storm's 34 knot northeast quadrant wind radius on the x-axis, 10 m wind speed at the buoy measured on the y-axis, and atmospheric pressure at the buoy on the color axis.  The black line shows the linear regression fit to the data.  (Bottom) Residuals from the regression line for 10 m wind speeds.

According to tracks from the Atlantic and Pacific Hurricane Databases, 631 named storms formed or entered the Gulf of Mexico from 1851 through 2017; of those storms, 125 passed through some portion of the Mississippi Bight.  Year by year Gulf of Mexico storm results are given in Figure 3.7.  Storms approaching the study area from the southeast made up 51% of Gulf storms while storms coming from the southwest accounted for 47%. Storms approaching or forming to the northeast and northwest of the Mississippi Bight represent less than 1% of the total.

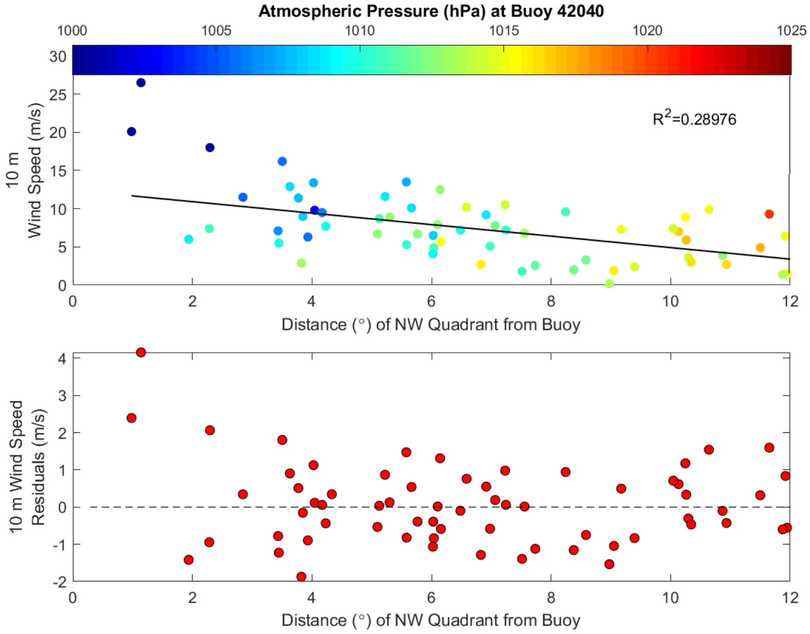

Figure 3.6 Scatter plot of buoy 42040 measurements for the northwest quadrant of Gulf of Mexico storms

Same as Figure 3.4 but for the northwest quadrants of storms.

As the rest of Chapter III will demonstrate, Gulf storms do not consistently produce anomalous results in the coastal ocean of the northern Gulf of Mexico. Some storms further away match up to increased current speeds or wave heights while closer storms occur in tandem with calm sea state conditions. Irregularity in the Mississippi Sound and Bight's response coincides with the nature of tropical cyclones. Factors ranging from wind radii to locations of nearby fronts to propagation speed all convolute categorization of storms. Future storm data should be utilized to see if a more concrete pattern develops over time.

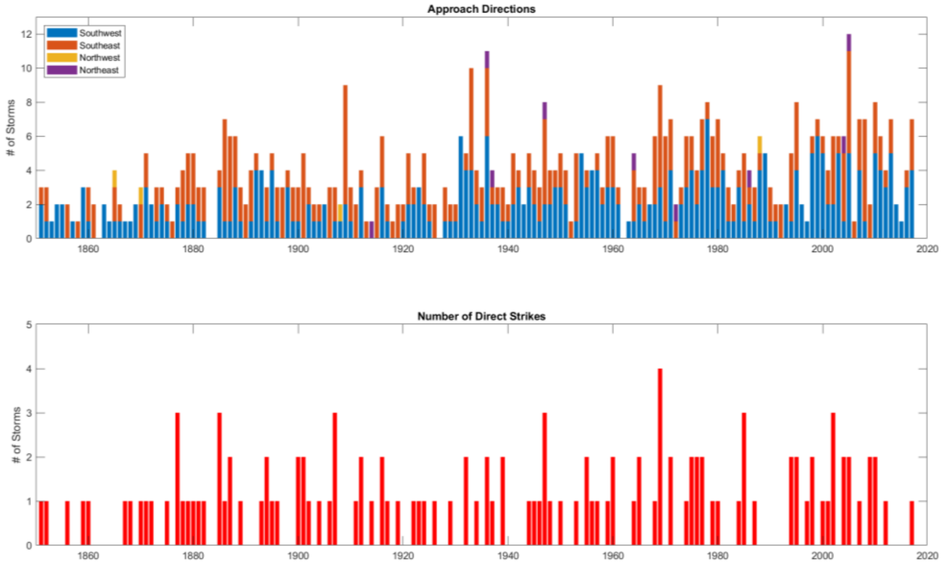

Figure 3.7 Statistics for Gulf of Mexico and direct strike tropical cyclones

(Top) Year to year totals of tropical storms and hurricanes that entered or formed in the Gulf of Mexico. Storms are split into initial approach direction to the center of the Bight. (Bottom) The number of tropical storms and hurricanes to pass through the Mississippi Bight each year.

## 3.3 Coincident Observations During Hurricane Seasons and Storm Periods

Since buoy data indicated tropical cyclones inside the Gulf of Mexico can impact wind speeds and wave heights in the study area, observations from the other datasets were used to examine hurricane seasons in their entirety while also considering storm periods of Gulf tropical cyclones.

Only 14 named storms entered the Gulf of Mexico from 2014 through 2017. Figure 3.8 shows the tracks of the storms relative to the Bight, outlined in red. Using estimates from the Atlantic Hurricane Database, the sizes of the blue circles indicate the maximum radius from the storm's eye where 34 knot winds were sustained. However, the shape of the wind field is somewhat misleading. The database gives wind radii for the northeast, northwest, southwest, and southeast quadrants. The 34 knot wind radius of the northeast quadrant usually extends further than the other quadrants, and the eastern half the storm almost always has higher wind speeds than the western half. Consequently, the shaded regions represent the maximum area of possible direct forcing by each storm; in actuality, the wind fields have more lobate distributions.

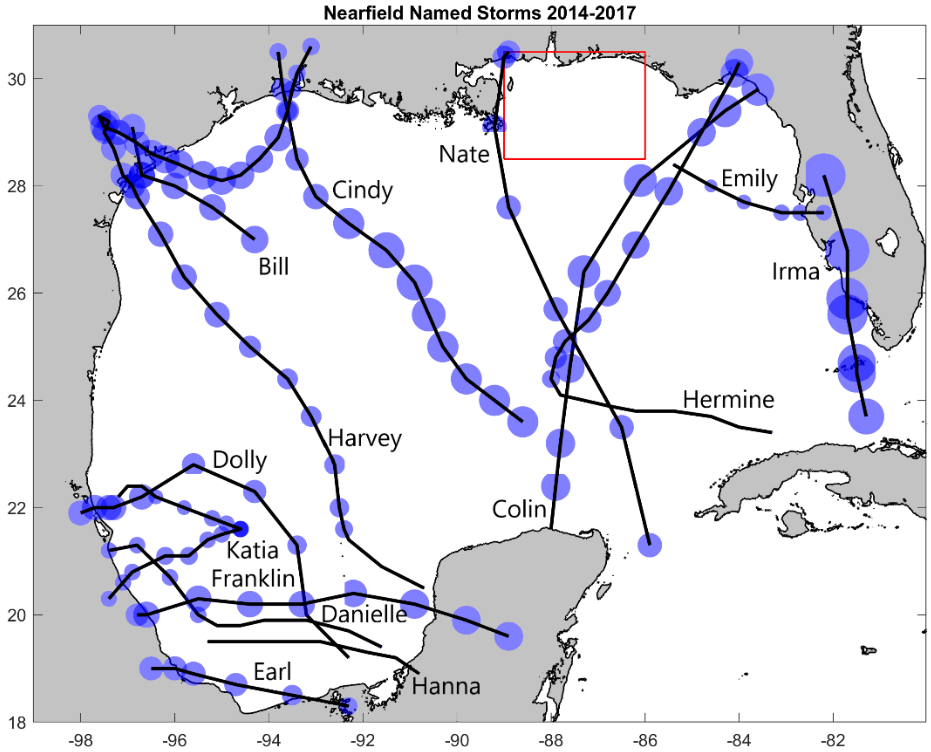

Figure 3.8 Gulf of Mexico storms during 2014-2017 hurricane seasons

The bolded black lines denote eye positions for each named storm for the duration it remained within the Gulf of Mexico. The Mississippi Bight is outlined by the red rectangle. The coastline of the Gulf of Mexico is given by the thin black line. The sizes of the circles show the maximum radius of sustained 34 knots for each storm at each 6-hour track position. Most storms have unequal wind extent, so the radius often reflects a northeastern lobe of higher magnitude wind. As such, the circles show the maximum possible areas of direct influence by the storms.

As a caveat on the results presented in this chapter, storms statistics and analysis reflect the period of study and data availability. While the 2017 hurricane season fell in the 90th percentile of active hurricane seasons for the Gulf of Mexico, the other three years experienced relatively low cyclonic activity. By contrast, the 2005 hurricane season had the most number of named storms in the hurricane record, and 12 storms entered the Gulf of Mexico, shown in Figure 3.9, compared to the 14 for the four year period of this study.

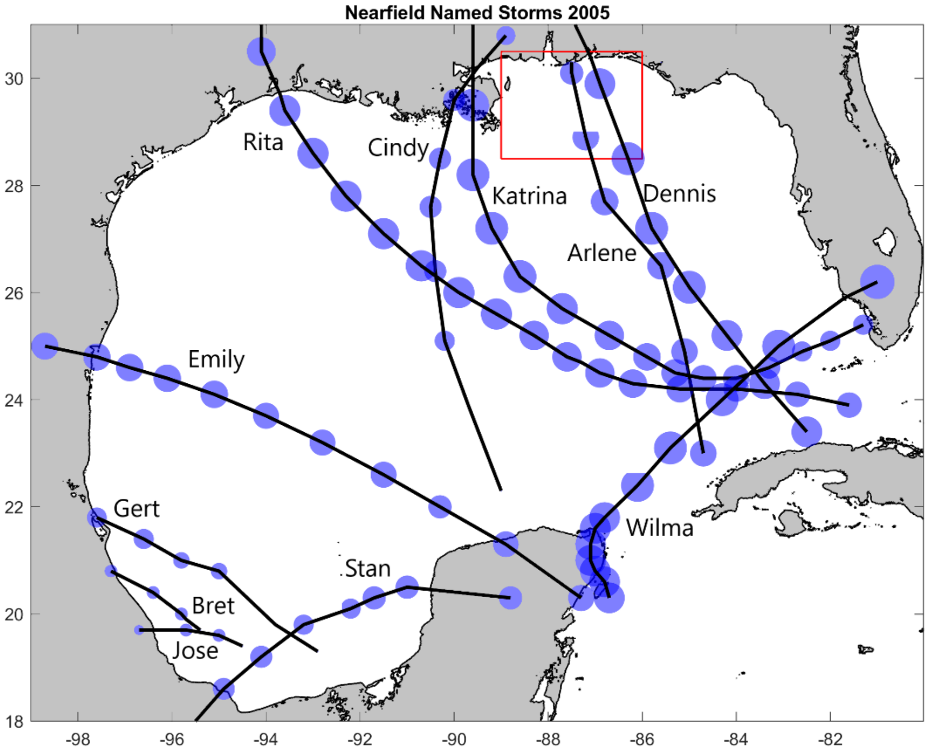

Figure 3.9 Gulf of Mexico named storms during 2005 hurricane season

As with Figure 3.7, tracks are given by bolded black lines, and the extent of >34 knot wind fields at each recorded eye location are shown with blue circles. Tropical storm Tammy is not included as it had been downgraded to a tropical depression prior to entry into the Gulf of Mexico, so the track is only a single point.

Eddy kinetic energy (EKE) provides a scalar indicator of the energy of currents. The HF radar coverage area spans bathymetric depths ranging from 20 m to more than 1,000 m. Within the coverage area, coastal regions have variable continental shelf width and different coastline orientations, so surface current speeds and directionality vary widely throughout the study area. Figure 3.10 shows the division of the coverage area into 9 sections with each section being outlined in red, and cyan stars mark the center of each section. Calculations of the spatially-averaged EKE per unit mass for each section at each time moment used (Eq. 3.1). The sum of squared zonal and meridional components of velocity, $u_i$ and $v_i$, for each grid point minus the monthly averages of each section, $u_{ave}$ and $v_{ave}$, divided by twice the number of velocity vectors, N, used in each calculation yielded the time-varying EKE for each section. Since chapter II focused primarily on monthly means to describe surface circulation changes throughout the year, monthly u and v averages were retained as a reference by which to gauge EKE anomalies. Hourly EKE estimates with fewer than 20 vectors were discarded as sample sizes below 20 misrepresented the EKE across the section.

$$EKE = \frac{1}{2N}\sum_{i=1}^{N}(u_i - u_{ave})^2 + (v_i - v_{ave})^2 \qquad \text{(Eq. 3.1)}$$

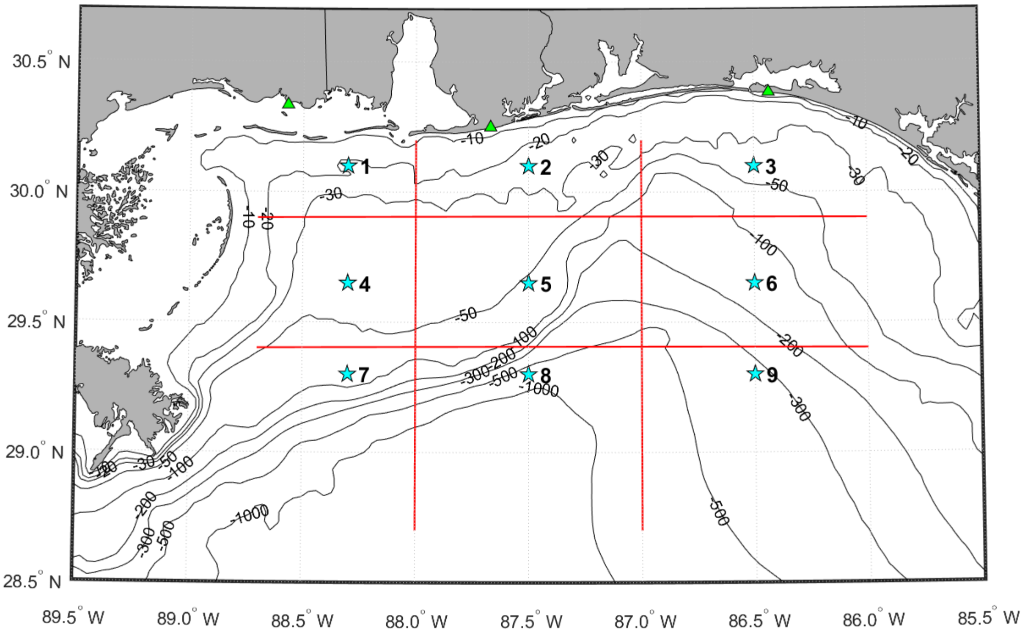

Figure 3.10 Subsections of 5 MHz HFR coverage

Data were divided into 9 subsections as denoted by the red lines; cyan stars show the center of each section. The 5 MHz HF radar sites are marked by green triangles.

Uncertainty values for surface current magnitudes and directions were consistently higher in sections 7 and 9, and roughly half the hurricane season lacked sufficient coverage in those sections. By contrast, section 4, 5, and 6 had the most consistent coverage, so the EKE plots in Figures 3.11 through 3.14 show results for sections 4-6.

### 3.4 Results

The first two hurricane seasons of this study witnessed less intense and fewer tropical cyclones while the second two years saw a larger number of storms and overall more intense tropical cyclones. From the hurricane database, the number of days where at least one tropical cyclone was extant in either the Pacific or Atlantic, in the Atlantic basin, and in the Gulf of Mexico were calculated. The results are given in (Table 3.1) to give a relative measure of cyclonic activity per year. Global refers to both Atlantic and Pacific Basin storm days. The 2014 and 2015 hurricane seasons had less than 80 Atlantic basin hurricane days, and only 8% and 3% of those days saw tropical cyclones in the Gulf. By contrast, 2016 and 2017 had more than 100 Atlantic hurricane days with Gulf of Mexico storms accounting for 12% and 25% of those days respectively. Likewise, in terms of global storms days, Atlantic storms were present for a larger percentage of the hurricane seasons in 2016 and 2017 than in 2014 and 2015.

Table 3.1 Tropical Cyclone Days During Study Period

| Year | Global | Atlantic | Gulf of Mexico |
|---|---|---|---|
| 2014 | 147 | 75 | 6 |
| 2015 | 169 | 79 | 2 |

Table 3.1 (continued)

|  |  |  |  |
|---|---|---|---|
| 2016 | 161 | 105 | 13 |
| 2017 | 146 | 104 | 26 |

Out of 8 named storms, 2 entered the Gulf of Mexico in 2014. Tropical storm Dolly (AL052014, 09/01/2014-09/03/2014) remained in the southwestern Gulf (Beven, 2015). Tropical storm Hanna (AL092014, 10/22/2014-10/28/2014) formed from the remnants of the Eastern Pacific tropical storm Trudy; it achieved tropical depression status in the Bay of Campeche but did not intensify into a tropical storm until it exited the Gulf of Mexico (Cangialosi, 2014).

In 2015, 1 of the 11 Atlantic basin storms entered the Gulf of Mexico. Tropical storm Bill (AL022015, 06/16/2015-06/18/2015) formed in the northwestern Gulf and dissipated hours after making landfall by Matagorda Island on the Texas coast on June 16, 2015 (Berg, 2015).

The number of Gulf tropical cyclones quadrupled in 2016. As a whole, the season saw 15 named storms: 9 stayed in the Atlantic, 4 entered the Gulf, and 2 passed through the Caribbean. Tropical storm Colin (AL032016, 06/05/2016-06/07/2016) made landfall near Big Bend, Florida, so it was the first 2016 Gulf storm (Pasch and Penny, 2017). Tropical storm Danielle (AL042016, 06/09/2016-06/21/2016) formed and stayed in the southwestern Gulf (Beven, 2016). Hurricane Earl (AL052016, 08/02/2016-08/06/2016) intensified from a tropical storm to a category 1 hurricane in the Caribbean Sea; the hurricane made two landfalls in Belize, weakened to a tropical storm while crossing Guatemala, and passed briefly through the southwest Gulf of Mexico before making a final landfall near Veracruz, Mexico (Stewart, 2017). Like Colin, hurricane Hermine (AL092016, 08/28/2016-09/03/2016) also made landfall near Big Bend, Florida as a category 1 hurricane (Berg, 2017).

The 2017 hurricane season saw 17 named storms with 7 entering the Gulf. Tropical storm Cindy (AL032017, 06/20/2017) evolved into a widespread, disorganized storm from an equally widespread low pressure area in the southern Gulf. The storm moved northward and made landfall by Cameron, Louisiana (Berg, 2018). Tropical storm Emily (AL062017, 07/30/2017-08/01/2017) formed in the northeastern Gulf and exited the Gulf across the Florida peninsula (Pasch et al., 2018). Hurricane Franklin (AL072017, 08/07/2017-08/10/2017) became a tropical storm near Nicaragua and Honduras but did not intensify into a category 1 hurricane until it entered the southern Gulf of Mexico; the storm dissipated within a day of making landfall close to Vega de Alatorre, Mexico (Beven, 2018). Hurricane Harvey (AL092017, 08/17/2017-09/01/2017) had devolved to remnants but strengthened again in the Bay of Campeche before ultimately becoming a category 4 hurricane (Blake and Zelinsky, 2018). The storm made two landfalls along Texas, churned offshore of the Texas coast for nearly a week, and made a third landfall by Cameron, Louisiana. As Harvey started to dissipate, hurricane Irma (AL112017, 08/30/2017-09/12/2017) spun up from a tropical depression to a major hurricane in less than two days (Cangialosi et al., 2018). The category 5 hurricane made 7 landfalls and eventually weakened as it slid northward along the Florida peninsula expanding horizontally as it weakened. Hurricane Katia (AL132017, 09/05/2017-09/09/2017) remained in the southwestern Gulf; the category 2 hurricane de-intensified to a category 1 before landfall by Tecolutla, Mexico (Avila, 2017). Hurricane Nate

(AL162017, 10/04/2017-10/08/2017) started out as a rain-intensive tropical storm near Nicaragua, but the tropical cyclone strengthened and became more concentrated upon entry to the southern Gulf of Mexico (Beven and Berg, 2018). The first U.S. landfall clipped the mouth of the Mississippi River, and the second occurred near Biloxi, Mississippi. This made Nate the only direct strike storm of the four year study period.

High frequency radar coverage for the 2014 hurricane season was patchy; section 5 had the most consistent coverage. The largest EKE peak in Figure 3.11, about 1600 $cm^2/s^2$, occurred in mid-May, and the second half of June saw a 1400 $cm^2/s^2$ peak. No HFR coverage exists for Dolly, and only a 400 $cm^2/s^2$ peak could be seen when Hanna was in the Gulf of Mexico. Florida and Alabama water levels in Figures 3.15a and 3.16a stayed under 1 m amplitude with the highest water levels predating Hanna by 1 week. Water level variations increased in both states during the month of November, but water levels during and after both tropical cyclones did not show magnitude changes larger than 0.5 m. In Figure 3.17a, water levels did not exceed 1 m above or 1 m below mean sea level, and water levels during both storm periods did not depart from patterns observed in the rest of the hurricane season. The Louisiana water levels in Figure 3.18a actually saw reduced ranges in water level variation during the storm periods than the weeks preceding and following Dolly's and Hanna's time in the Gulf. Temperature at the East Ship Island hydrological station varied daily and seasonally throughout the hurricane season, Figure 3.19a. Salinity at the station increased before each storm entered the Gulf and decreased during the storm periods, but 1-2 day salinity variations during the remaining the hurricane season had larger magnitudes. The highest salinities were observed from July through October. In Figure 3.20a, daily and seasonal temperature changes at the Back

Bay Biloxi station echoed trends seen at the East Ship Island station. As at the East Ship Island station, salinities reached a maximum July through October. No high magnitude or prolonged salinity changes occurred during either storm period. The East Pearl River station displayed similarities to the other two stations. Small 1-3 increases in salinity happened in tandem with the two tropical cyclones in Figure 3.21a, but as with the other stations, variations did not change noticeably in terms of magnitude or direction from the rest of the hurricane season.

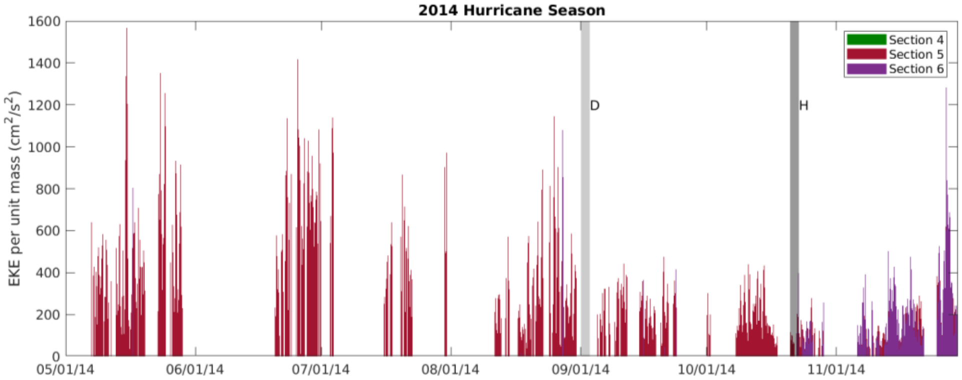

Figure 3.11 Eddy kinetic energy during the 2014 hurricane season

Eddy kinetic energy per unit mass for subsections 4-6 of the 5 MHz high frequency radar coverage region. Gray bars indicate storm periods for tropical cyclones that came into the Gulf of Mexico.

As with 2014, HFR coverage for the 2015 hurricane season had several gaps, so most of the EKE record comes from surface current measurements in sections 5 and 6. The HFRs were down during tropical storm Bill. EKE, shown in Figure 3.12, peaked around 1200 $cm^2/s^2$ in the latter half of October, but smaller >1000 $cm^2/s^2$ peaks occurred in the second week of May, the last week in June, and the first week in July. In Figure 3.15b, a 1 m peak in water level happened at the Florida tide gages at the same time as the highest EKE peak. Variations in water level increased during the month of November. No deviations from daily and longer term variability were observed while

Bill was in the Gulf of Mexico. The Alabama, Mississippi, and Louisiana tide gages in Figures 3.16b, 3.17b, and 3.18b show no indication of storm events during the 2015 hurricane season. The tide gages show the same increased water level in late October as the Florida tide gages. Temperature measurements were not available for the majority of the 2015 hurricane season. A decrease in salinity of almost 10 followed Bill’s time in the Gulf of Mexico at the East Ship Island station; this salinity change was the largest of the hurricane season, Figure 3.19b. Temperatures at the Back Bay Biloxi station varied daily and seasonally with no abrupt increases or decreases. Salinity at the station, shown in Figure 3.20b, stayed near 0 during Bill’s time in the Gulf, but the low salinity started in mid-May and continued through the beginning of July. Salinity increased from May to November with a short 1-2 drop in mid-September. In Figure 3.21b, temperatures at the East Pearl River station fluctuated daily and seasonally, but no high magnitude changes happened during Bill. Salinity stayed near 0 for May and June except for a brief increase while Bill was in the Gulf, but the magnitude of change was not the largest of the hurricane season. Larger variations and higher salinities occurred July through October.

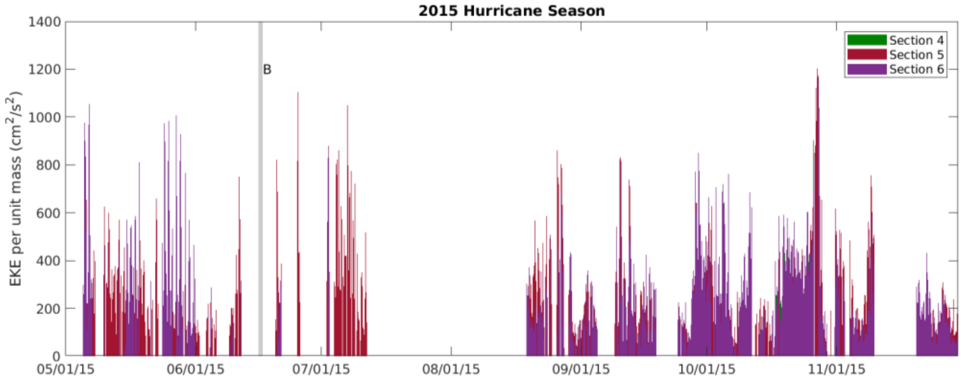

Figure 3.12 Eddy kinetic energy during the 2015 hurricane season

Same design as Figure 3.11.

EKE coverage in sections 4-6 for the 2016 hurricane season improved drastically from the previous 2 years; the only gaps in coverage occurred in the last week of May and the first week of June.  EKE in Figure 3.13 peaked in mid-August 2016 at >1,400 $cm^2/s^2$, but ~1,200 $cm^2/s^2$ peaks coincided with the storm periods for tropical storms Colin and Danielle.  A similar 1,200 $cm^2/s^2$ peak happened in the first half of July.  No EKE peak coincided with Earl, and Hermine aligned with a smaller 1,000 $cm^2/s^2$ peak. EKE values frequently exceeded 800 $cm^2/s^2$ from May until September then decreased for the remainder of the hurricane season.  At the Florida tide gages in Figure 3.15c, 1 m water levels above mean sea level accompanied Colin and Hermine, but no appreciable peaks happened during Danielle and Earl.  Water levels at the Alabama tide gages in Figure 3.16c mimicked the Florida water levels.  Mississippi water levels in Figure 3.17c also displayed similar behavior, but a <1 m dip in water level occurred when Danielle was in the Gulf.  No abrupt or prolonged changes in water level could be seen at the Louisiana tide gages in Figure 3.18c.  Gaps in the salinity time series for the East Ship Island station happened in May and parts of October and November.  No salinity data exist for Colin, but a 5 increase accompanied Danielle.  Salinity did not change during Earl or Hermine, but a >10 decrease could be seen in late August between the 2 storms. The temperature record in Figure 3.19c showed daily and seasonal variations but no clear indication of storm impacts.  In keeping with other years, temperatures at the Back Bay Biloxi station varied daily and seasonally; the only irregularity was a 5°C drop the week after Earl in the first half of August.  In figure 3.20c, salinity measured at the station dropped to nearly 0 at the same time as the temperature decrease.  Salinity increased around mid-September and remained elevated for the rest of the hurricane season.

Salinity started near 0 at the beginning of May, rose to approximately 15 before dropping back to 0 in mid-May. A second salinity increase to about 15 preceded Colin's time in the Gulf before decreasing again to near 0 after the storm. No distinct temperature or salinity changes happened during Danielle, Earl, or Hermine, but temperature and salinity decreased dramatically in August between Earl and Hermine. This drop could be seen at the East Ship Island station as well. The East Pearl River station in Figure 3.21c evidenced daily and seasonal fluctuations and the same 1-2 decrease in temperature in August recorded at the other 2 stations. Salinity was highest in July as wells as October through November, and 10-15 increases in salinity occurred while Colin, Danielle, and Hermine were in the Gulf of Mexico. Danielle occurred at the beginning of the increased salinity in late June that continued until the second week of August. Earl's time in the Gulf happened partway through the elevated salinity period.

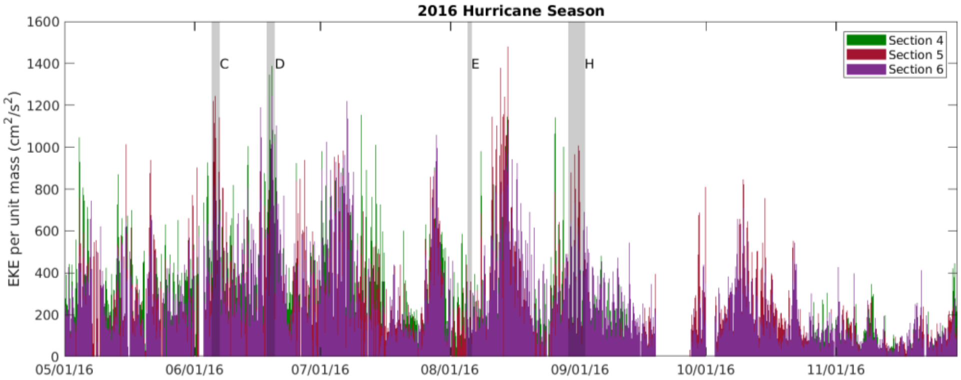

Figure 3.13 Eddy kinetic energy during the 2016 hurricane season

Same design as Figure 3.11.

The 2017 hurricane season exhibited the highest overall EKE and the most complete surface current coverage of the four year period. Two of the three 5 MHz HFRs were taken down before hurricane Nate, so no EKE estimates are available for that storm period. In Figure 3.14, a 3,500 $cm^2/s^2$ peak occurred during tropical storm Cindy, and the period after Hurricane Harvey made landfall along central Texas had EKE values above 2,500 $cm^2/s^2$. Likewise, the end of hurricane Irma's duration in the Gulf as it slid up the Florida peninsula registered >3,000 $cm^2/s^2$. Hurricane Katia was also present in the southwestern Gulf of Mexico during this time, so the effects from one storm cannot be separated from the other. Another 3,000 $cm^2/s^2$ peak can be seen in the last week of May, and EKE values topped 1,000 $cm^2/s^2$ throughout May and July. EKE values stayed under 500 $cm^2/s^2$ during hurricane Franklin's time in the Gulf of Mexico. Water levels exceeded 1 m during Cindy and Nate, and water levels fell to near -1 m during Irma at the Florida tide gages shown in Figure 3.15d. Higher magnitude water level changes did not accompany the other storms. In Figure 3.16d, Alabama water levels rose above 1 m above mean sea level for Cindy, neared 1 m for Harvey, and nearly reached 2 m during Nate. As with the Florida tide gages, water levels in Alabama fell to almost -1 m after Irma's time in the Gulf. The other storms period showed little change compared to the days before and after the storms. Water levels in Mississippi as seen in Figure 3.17d echoed the patterns from the Alabama gages. Louisiana water levels had similar responses to Cindy, Harvey, and Nate; however, the decrease in water level during Irma was not present, Figure 3.18d. Unlike the other states, a >1 m increase in water level preceded Nate's landfalls by almost a week. Gages in all four states measured a 0.5-1 m increase in water level during the first week of May that did not correspond to any Gulf storm. In Figure 3.19d, salinity measurements at the East Ship Island station were not available in June, the first half of July, and the second week of November. Likewise, temperature data were missing for the last 3 weeks of November. Data for the rest of the season showed daily and seasonally-varying temperature, but temperatures dropped by 1-

3 °C during Cindy, Emily, Harvey, and after Irma.  Salinity increased during Emily and to a lesser extent during Franklin.  A multi-week increase in salinity encompassed the time Harvey was in the Gulf; likewise, salinity increased in the weeks leading up to Nate's entrance into the Gulf but fell after the storm dissipated.  Figure 3.20d shows bottom temperature and salinity for the Back Bay Biloxi station.  Temperature decreased during Cindy while salinity dropped nearly to 0.  Emily formed in the Gulf as salinity rose, but salinity fell as the storm exited the Gulf.  Salinity stayed near 0 during Franklin but rose as Harvey transited north through the Gulf.  No salinity data were present for Irma or Katia, but temperature decreased after Harvey and Irma.  Nate's time in the Gulf occurred in tandem with a 2 week period of cooler temperatures and increased salinity.  Salinity dropped after Nate made landfall but rose again in November.  Temperature decreased by 2-4 °C for Cindy, Harvey, and Irma at the East Pearl River station, Figure 3.21d.  Salinity stayed near 0 in May, Jun, and the first half of July, but large increases in salinity occurred in the first week of May, mid-May, and during Cindy.  Salinity peaks also happened at the same time Emily, Franklin, and Harvey were in the Gulf, and salinity decreases followed Franklin, Harvey, and Irma.  The weeks leading up to Nate's formation and the period where the storm was in the Gulf had the highest salinity of the hurricane season.  Variations in salinity increased in October and November.

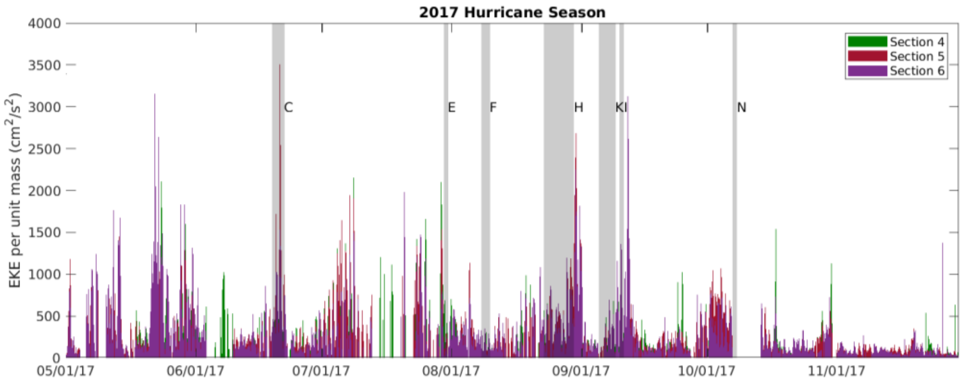

Figure 3.14 Eddy kinetic energy during the 2017 hurricane season

Same design as Figure 3.11.

The 2016 and 2017 hurricane seasons offered better years for tropical cyclone study even though 2/3 of the 5 MHz sites were taken down in advance of Nate. No surface current data exists for the one direct strike storm of the 4 year period, but data does exist, not only for the storm periods of 10 tropical cyclones but also for the two weeks leading up to and following the storms' time in the Gulf of Mexico. Figures 3.22 to 3.31 give surface current feather plots for vector-averaged velocities for 1 of the 9 HFR subsections. A commonality between the plots is a switch between northward flowing currents to southward flowing currents on a roughly 24-hour timescale. Vertical red lines in each of the plots indicate the dates during which storms stayed within the Gulf of Mexico. Each time series was examined for surface current magnitude increases or directional shifts during the storm periods compared to the two weeks before and after the storm period.

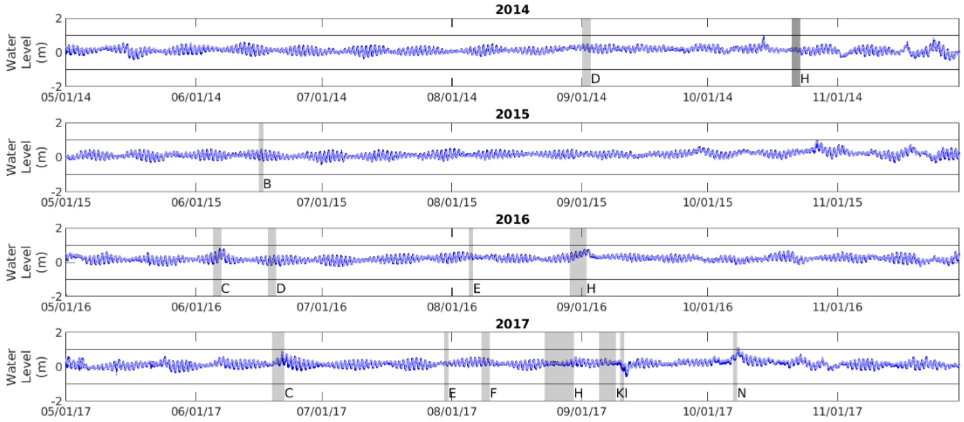

Figure 3.15 Florida water levels during the 2014-2017 hurricane seasons

Water level time series, referenced to mean sea level, for the 2014-2017 hurricane seasons; gray bars denote storm periods of Gulf of Mexico tropical cyclones.

In 2016, currents during the 4 Gulf storms exhibited some increase or directional shift, but changes to current speed and magnitude were not extreme compared to daily variations outside the storm periods. In Figure 3.22, current speeds ranged from 30 cm/s to 50 cm/s during non-storm days. During Colin’s time in the Gulf, current speeds peaked near 80 cm/s; however, the 24-hour alternation in current direction did not change. A similar pattern emerged for Danielle in Figure 3.23; current speeds during the storm period went from 60 cm/s to 80 cm/s compared to the 30 cm/s to 60 cm/s before and after the storm. Current speeds in Figure 3.24 range from 10 to 70 cm/s, but speeds during Earl stay below 40 cm/s. The one peculiarity comes in that currents remain southward flowing during the storm and for several days after. This period marks a multiday departure from the 24-hour rotation in current direction. Finally, southward currents during Hermine’s time in the Gulf stayed under 30 cm/s, but when the switch to northward flow occurred, speeds increased to almost 80 cm/s. This differed from currents outside the storm period in Figure 3.25. Speeds varied between 20 and 100 cm/s, but northward and southward currents had equivalent magnitudes.  Currents during storm periods do not stand out visually from the surrounding weeks, but some fluctuation in speed or direction can be seen with each storm.

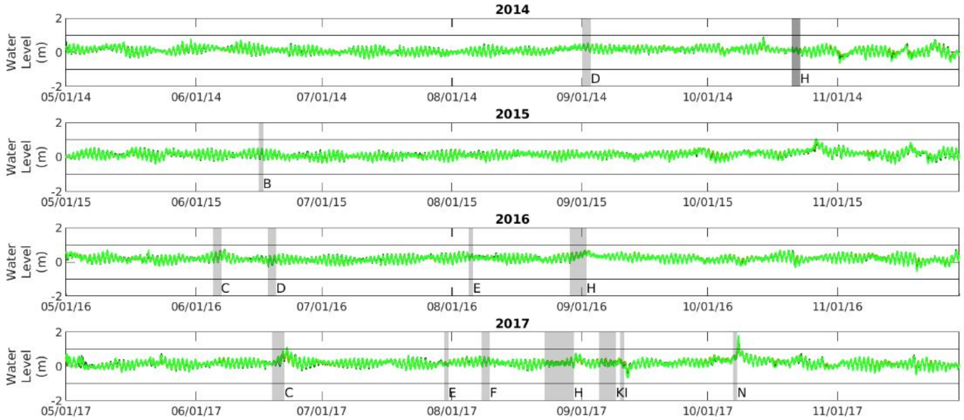

Figure 3.16 Alabama water levels during the 2014-2017 hurricane seasons

Same setup as Figure 3.15.

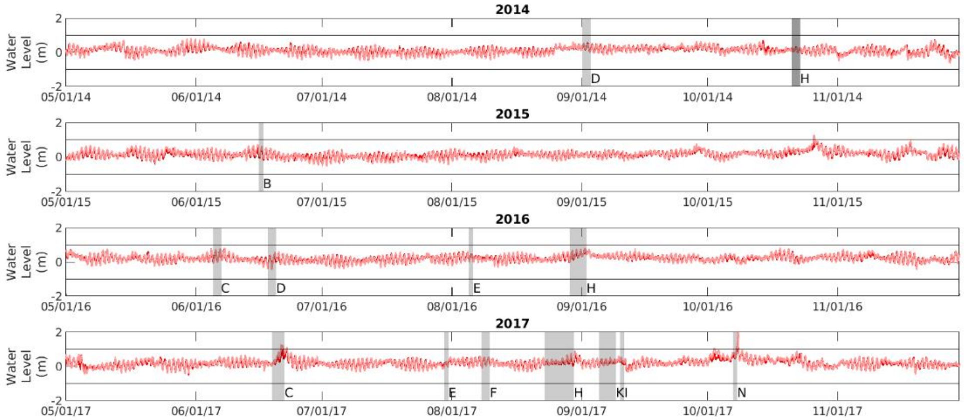

Figure 3.17 Mississippi water levels during the 2014-2017 hurricane seasons

Same setup as Figure 3.15.

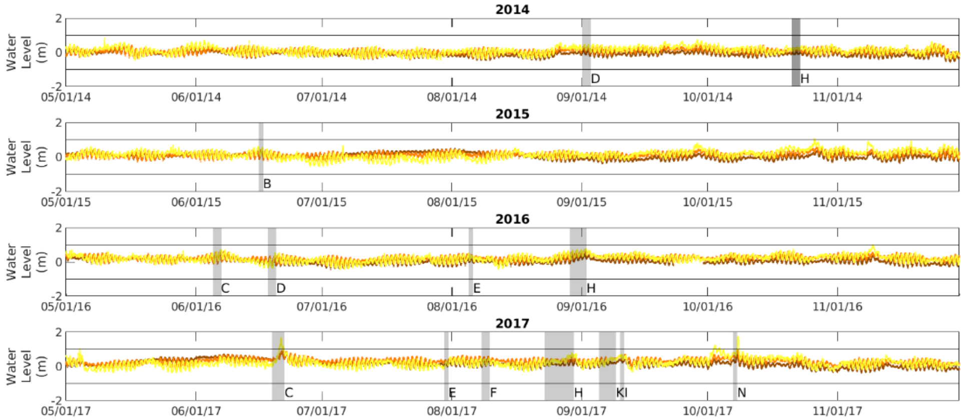

Figure 3.18 Louisiana water levels during the 2014-2017 hurricane seasons

Same setup as Figure 3.15.

Feather plots for the 2017 Gulf tropical cyclones also contain changes to current speed and direction for storm versus non-storm periods. Surface current data are not available for hurricane Nate since the HFRs were taken down prior to the storm's closest approach, so the plots only show currents affected by storms further away. In Figure 3.26, current speeds range from 20 cm/s to 40 cm/s. Speeds increase to over 80 cm/s during Cindy's time in the Gulf, and the north to south rotation gives way to strictly northward flowing currents. During Emily's stay in the Gulf, current speeds stay on the low end of the 10 cm/s to 70 cm/s range seen in the feather plot, and no apparent interruption occurs to the cycling between northward and southward flow, Figure 3.27. In Figure 3.28, Franklin's storm period also lacks any change to current speed and direction. Hurricane's Harvey and Irma happened in quick succession, and Katia was in the southwestern Gulf while Irma came through the Caribbean Sea and slid up the Florida peninsula. Given the timing of these storms, impacts to currents from one storm can be seen in the feather plot of another, and as mentioned earlier, Katia's influence on

Mississippi Bight currents cannot be differentiated from Irma's. Figures 3.29, 3.30, and 3.31 show surface currents for the weeks before, during, and after Harvey's, Irma's, and Katia's time in the Gulf. Speeds ranged from 20 cm/s to 60 cm/s, and the north to south reversal in direction marked most of the time series. The daily directional shift did not cease during Harvey, but as the storm approached Louisiana, northward currents reached nearly 100 cm/s. Katia's time in the Gulf happened during a multiday period of northward facing currents with magnitudes less than 40 cm/s that gave way to southward currents up to 80 cm/s during Irma. As with 2016, none of the storm periods produced extreme current speed (more than 150 cm/s), but several of the 2017 tropical cyclone periods occurred in tandem with elevated current speeds and a preferential current direct either to the north or south.

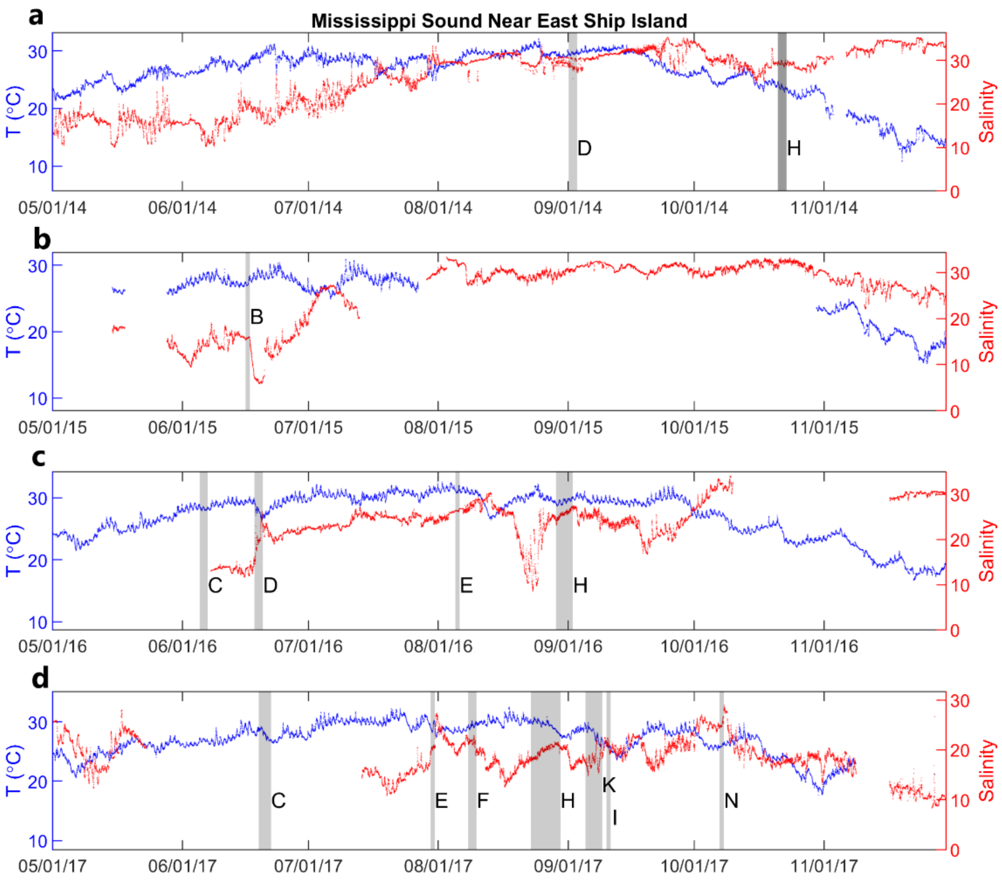

Figure 3.19 Hurricane season bottom temperature and salinity near East Ship Island

Bottom temperature (blue) and salinity (red) measured at USGS-MDMR station 6 (Mississippi Sound near East Ship Island) for the hurricane seasons in a) 2014, b) 2015, c) 2016, d) 2017. Gray bars denote storm periods of tropical cyclones while in the Gulf of Mexico, and the letters are the first letter of the cyclone's name.

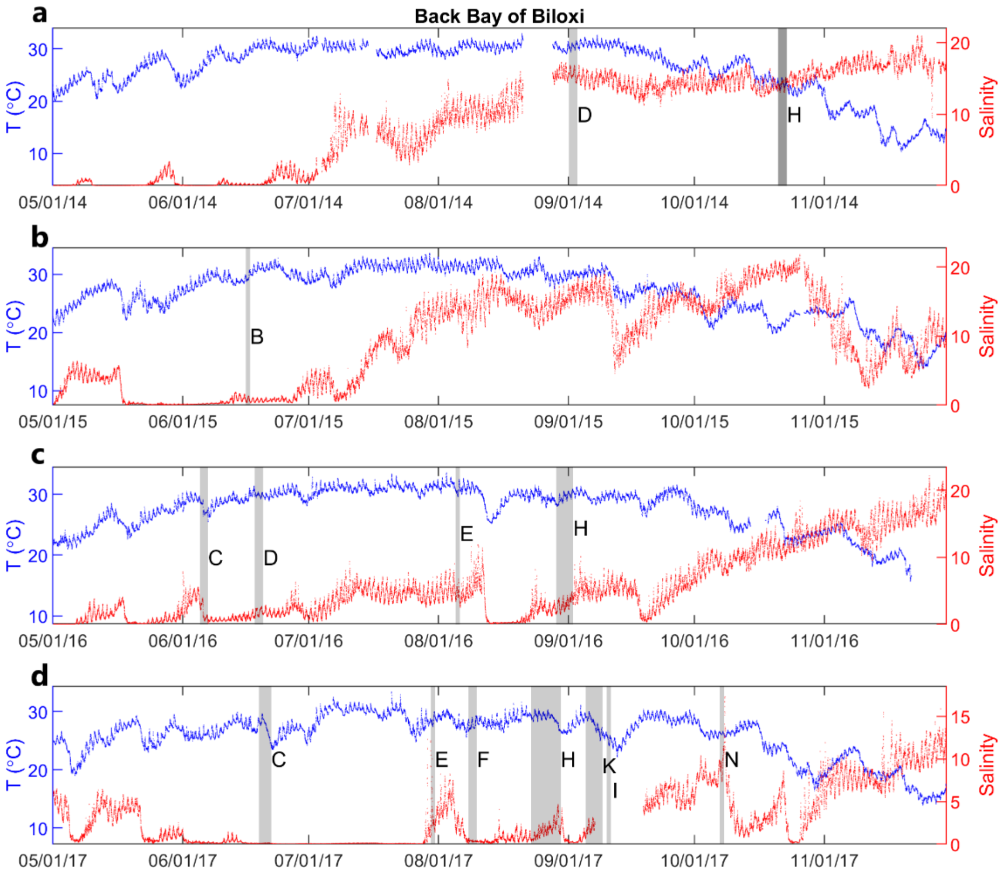

Figure 3.20 Hurricane season bottom temperature and salinity at Back Bay of Biloxi

Bottom temperature (blue) and salinity (red) measured at USGS-MDMR station 8 (Back Bay of Biloxi) for the hurricane seasons in a) 2014, b) 2015, c) 2016, d) 2017. Gray bars denote storm periods of tropical cyclones while in the Gulf of Mexico, and the letters are the first letter of the cyclone's name.

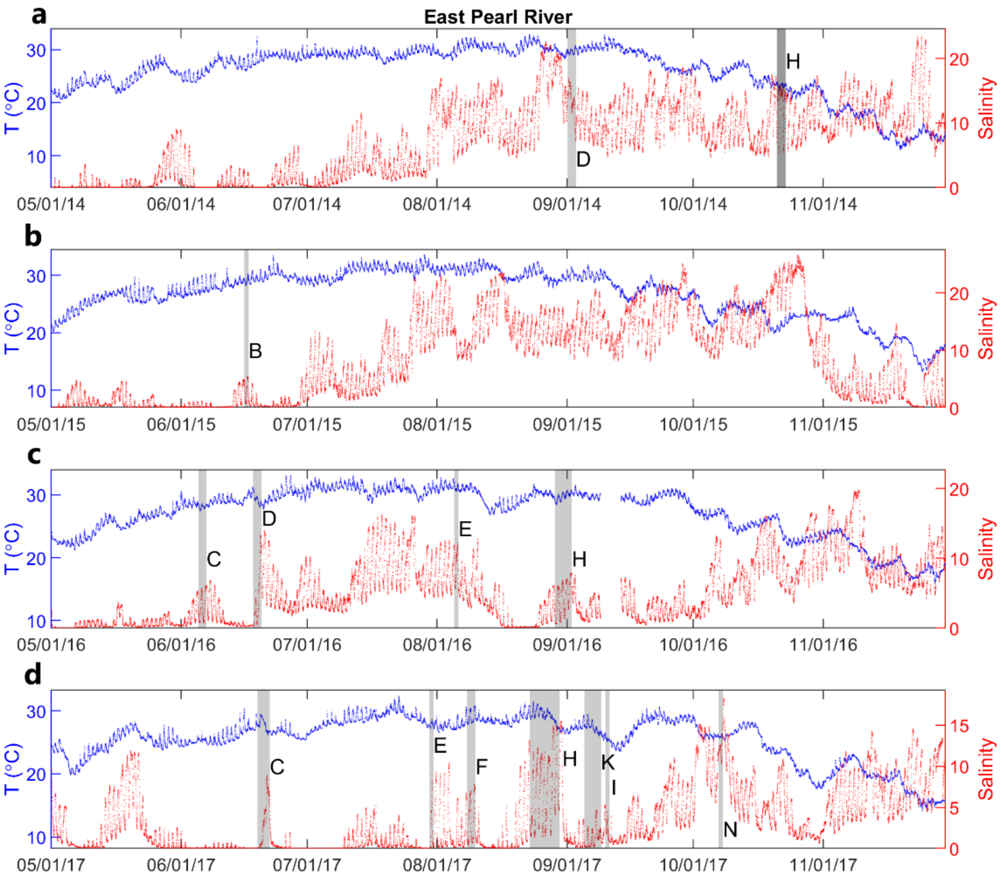

Figure 3.21 Hurricane season bottom temperature and salinity at East Pearl River

Bottom temperature (blue) and salinity (red) measured at USGS-MDMR station 11 (East Pearl River at the CSX Railroad Crossing) for the hurricane seasons in a) 2014, b) 2015, c) 2016, d) 2017. Gray bars denote storm periods of tropical cyclones while in the Gulf of Mexico, and the letters are the first letter of the cyclone’s name.

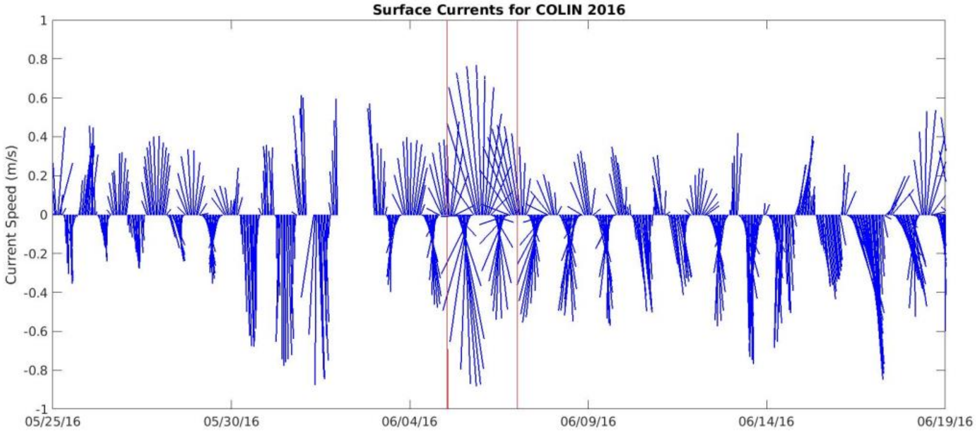

# Figure 3.22 Surface currents for tropical storm Colin in HFR section 5

Vector-averaged currents for the 2 weeks leading up to Colin’s entrance into the Gulf of Mexico, the period the storm stayed in the Gulf as denoted by red lines, and the 2 weeks following the period the storm was in the Gulf.

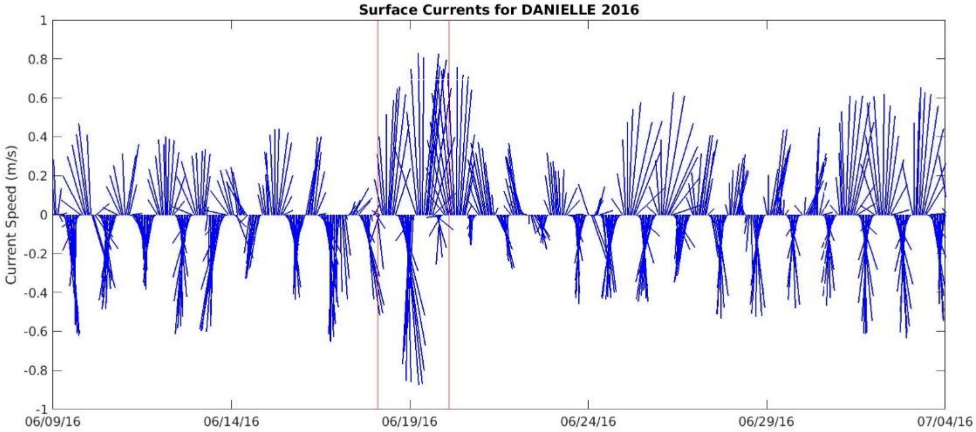

# Figure 3.23 Surface currents for tropical storm Danielle in HFR section 4

Same design as Figure 3.22.

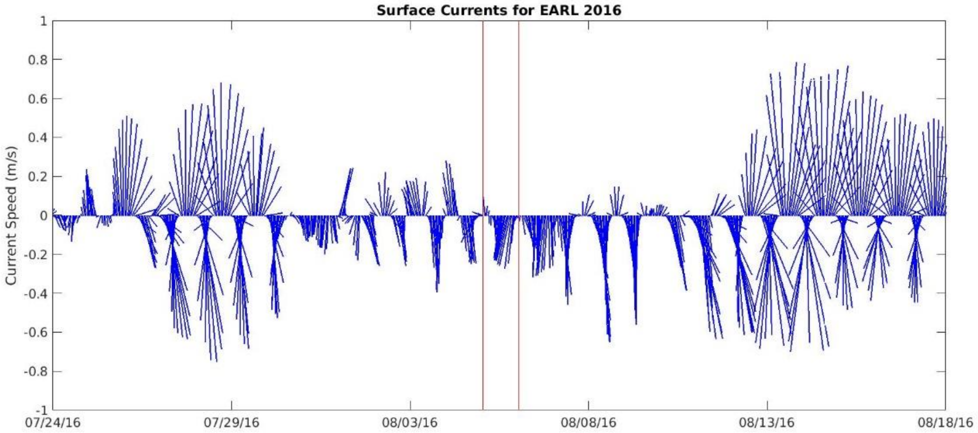

Figure 3.24 Surface currents for hurricane Earl in HFR section 5

Same design as Figure 3.22.

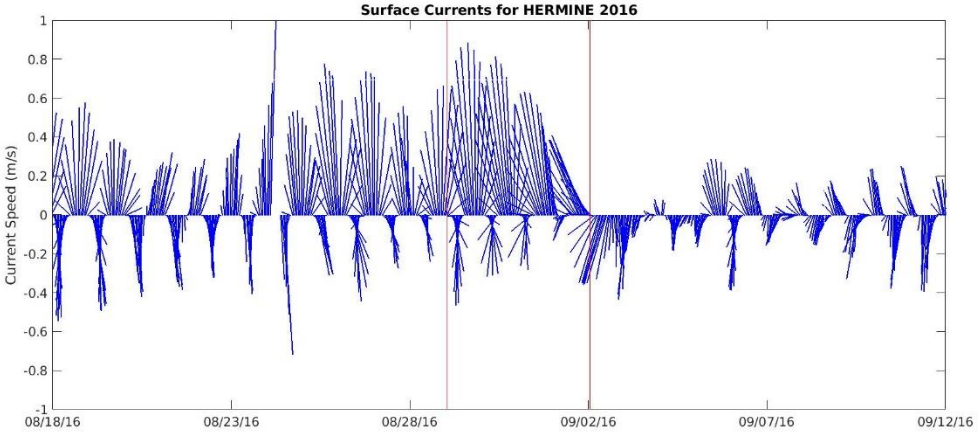

Figure 3.25 Surface currents for hurricane Hermine in HFR section 5

Same design as Figure 3.22.

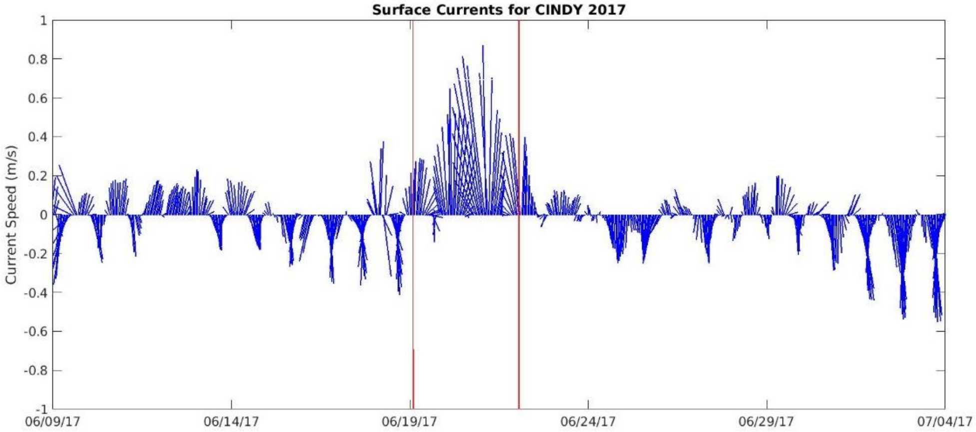

Figure 3.26 Surface currents for tropical storm Cindy in HFR section 5

Same design as Figure 3.22.

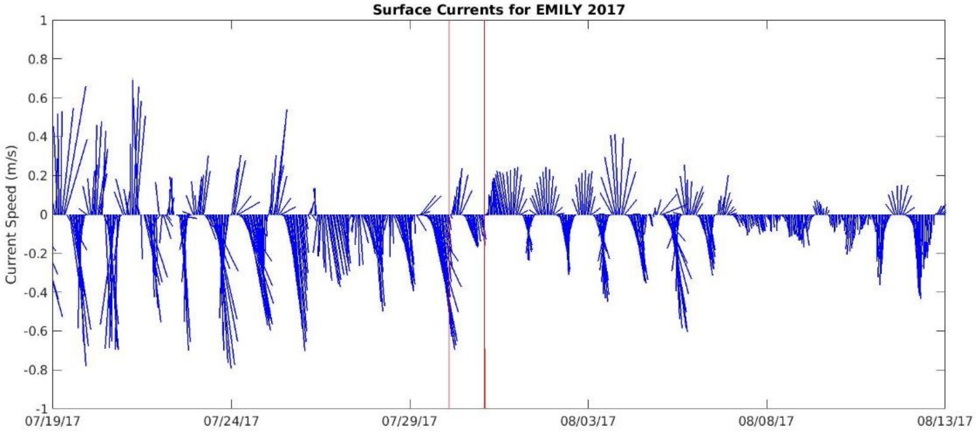

Figure 3.27 Surface currents for tropical storm Emily in HFR section 2

Same design as Figure 3.22.

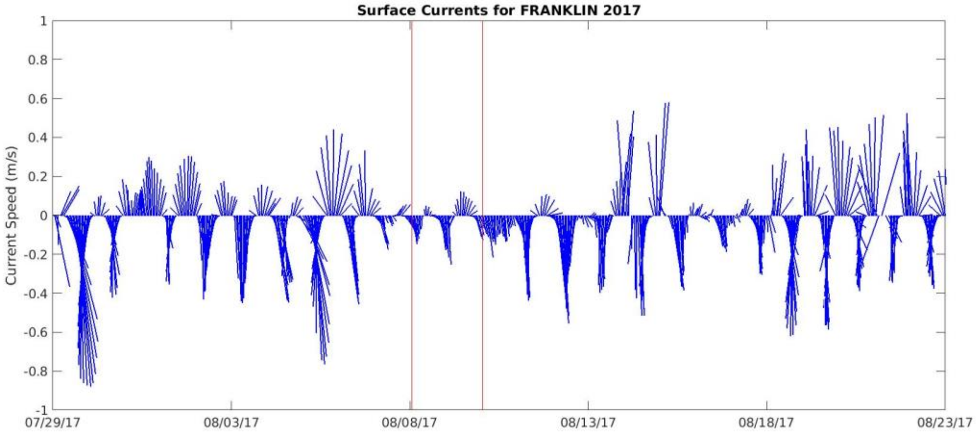

Figure 3.28 Surface currents for hurricane Franklin in HFR section 5

Same design as Figure 3.22.

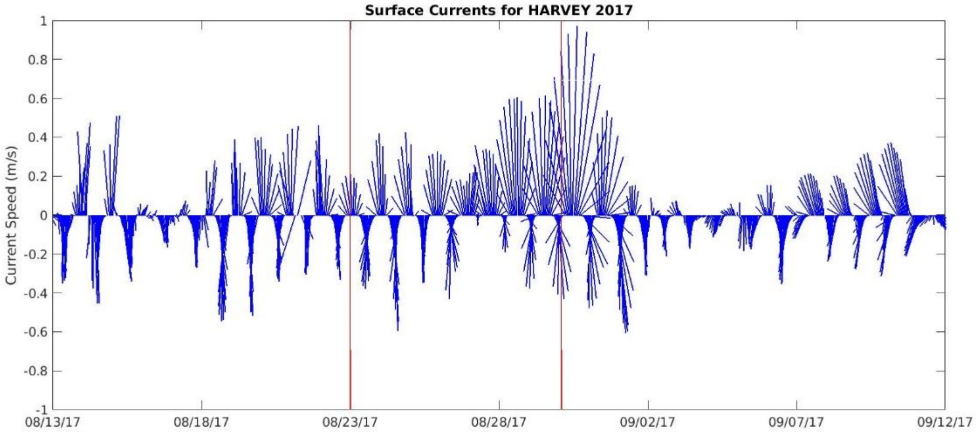

Figure 3.29 Surface currents for hurricane Harvey in HFR section 5

Same design as Figure 3.22.

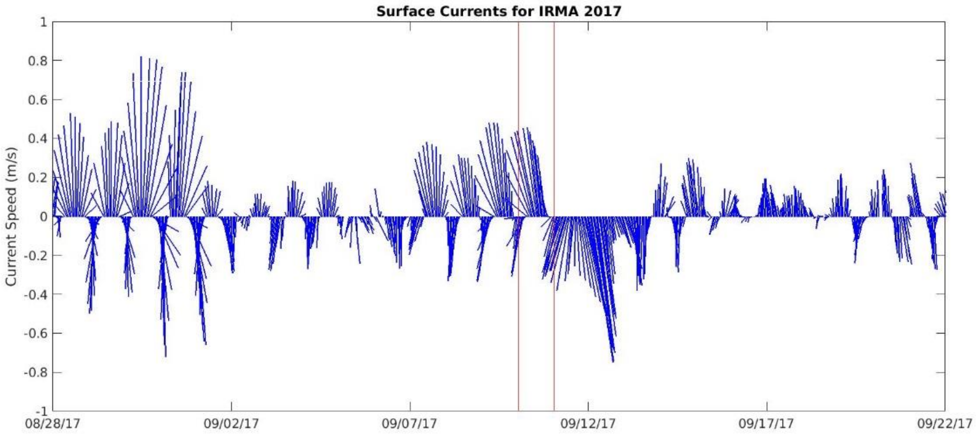

Figure 3.30 Surface currents for hurricane Irma in HFR section 6

Same design as Figure 3.22.

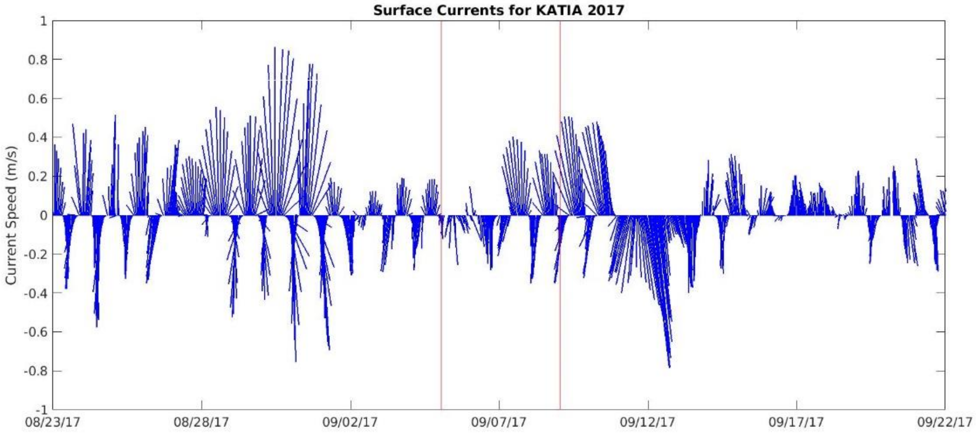

Figure 3.31 Surface currents for hurricane Katia in HFR section 6

Same design as Figure 3.22.

## 3.5 Discussion

Of the 1,848 Atlantic basin storms, 631 (34%) came into or formed in the Gulf of Mexico, and 125 tropical cyclones (7%) passed through the Mississippi Bight. This study covers only 14 of the 631 Gulf of Mexico storms and 1 of the 125 direct strike storms. While statistics cannot be generated from this small sample size, an examination of these storms within the context of their hurricane seasons grants insight into the degree to which storms can perturb the Mississippi Bight and the temporal scales on which those perturbations happen. Three of the four hurricane seasons showed the conflicting and minimal response of circulation within the Mississippi Sound and Bight to Gulf of Mexico storms. The 2017 hurricane season offered more storms for study and included the only storm to transit through the study area. Data suggest Gulf storms raise water levels along the coasts for a few hours to a few days. Salinity increases as a storm approaches from the south and decreases after the storm either dissipates or exits the Gulf, and EKE sharply increases if a storm moves close enough to the study area. However, many of these results rely on data from 2017 only, so additional years are needed for a more complete study.

In general, eddy kinetic energy (EKE) per unit area peaked either in the days leading up to a cyclone’s approach or at the time of closest approach. There were, however, EKE peaks in each year unassociated with nearfield storm periods. This speaks to the importance of studying the whole hurricane season. Tropical cyclones do not form in isolation of other atmospheric phenomena, and while storm periods may produce anomalous responses in the Mississippi Sound and Bight, the magnitude of the response can pale in relation to non-storm periods.

While each storm had a unique evolution, qualitative comparisons can be made. Bottom temperatures sometimes dropped during a storm’s closest approach. Salinity dropped after a storm dissipated or left the Gulf, and water levels across the northern Gulf coast rose following the storm passage through the Gulf. Hurricane Irma offered a notable exception to this behavior since water levels dropped as Irma got closer to the

Mississippi Sound and Bight. Finally, changes in hydrographic properties associated with tropical cyclone approach tended to last less than 1 week after the storm’s approach. However, these results were not equally true for all Gulf storms, and the study lacked HFR data for the one direct strike storm. The four year period of this study suggests storms cause relatively minor impacts to circulation, but a different study focusing on multiple direct strike tropical cyclones would likely produce different results.

# CHAPTER IV – BARRIER ISLAND REMOVAL SCENARIOS

## 4.1 CONCORDE Synthesis Model Development

### 4.1.1 COAWST Model Basis

The Coupled Ocean-Atmosphere-Wave-Sediment Transport (COAWST) model was designed to provide a high resolution estimation of coastal marine environments, and the Regional Ocean Modeling System (ROMS)-based COAWST model for the Mississippi Sound and Bight (ROMSmsb) utilizes the COAWST framework for a 400-m horizontal resolution coastal ocean model for the northern Gulf of Mexico (Warner, et al., 2008; Warner, et al., 2010; Pan, et al., 2017). The ROMSmsb effort began as the COnsortium for oil exposure pathways in COastal River-Dominated Ecosystems (CONCORDE) Synthesis Model (Greer et al., 2018).

The primitive equations of motion drive ROMS which employs terrain-following vertical coordinates and orthogonal curvilinear horizontal coordinates. ROMSmsb retains ROMS as the oceanic component with 24 $\sigma$ vertical levels. The default atmospheric forcing for COAWST comes from the 3-hour temporal resolution North American Regional Reanalysis (NARR) (Mesinger et al., 2006). ROMSmsb can utilize NARR, but the 1-hour temporal resolution CONCORDE Meteorological Analysis (CMA) was designed for use in the model domain, so runs evaluated in this study used CMA forcing or CMA-derived forcing (Fitzpatrick and Lau, 2018). ROMSmsb is not a two-way coupled model; CMA supplies atmospheric forcing to ROMSmsb.

Also included in COAWST are the Simulating Waves Nearshore (SWAN) model for waves and the Community Sediment Transport Model System (CSTMS) for sediment dynamics; while both are undergoing development for ROMSmsb, this study was concerned with the atmospheric and oceanic portions of the model.

### 4.1.2 Regional Ocean Modeling System

The Regional Ocean Modeling System (ROMS) utilizes the primitive equations under Boussinesq and hydrostatic approximations to model physical oceanographic conditions. This means calculation of seven state variables using seven equations: three momentum balance equations, advection-diffusion equations for salinity and temperature derived from the conservation equations for mass of salt and heat, the nonlinear equation of seawater state, and the continuity equation. The state variables include the three components of velocity (u, v, and w), potential temperature (T), salinity (S), pressure (P), and density ($\rho$).

While these equations make up the primitive equations, handling of the turbulent flux terms in the equations introduces additional unknowns which require some turbulent closure scheme. Typically, this is accomplished with a two-equation turbulent model (Warner et al., 2005). The Mellor-Yamada and Mellor-Yamada 2.5 schemes have been used in other ocean circulation models as well as in ROMS. However, as the original COAWST model couples a sediment transport model with ROMS, ROMSmsb utilizes the generic length scale methodology from COAWST detailed by Umlauf and Burchard (2003) and implemented by Warner et al. (2005) into ROMS since Mellor-Yamada 2.5 results in poor sediment transport simulations.

The formulation of the primitive equations and their use in numerical modeling of geophysical fluids, specifically the atmosphere, is often credited to Lewis Richardson and Vilhelm Bjerknes (Richardson, 1922; Bjerknes, 1914). However, the derivation of the equations followed from centuries of work. Charney et al. (1950) heralded in weather forecasts by computerized, numerically-integrated barotropic models, but the inclusion of the primitive equations did not follow until the latter half of the twentieth century when computing power improved. Bryan and Cox (1967) developed the first circulation model for the ocean during the 1960s. Use of the primitive equations has since become the norm in hydrodynamic models.

The version of ROMS employed in this study resulted from iterative development; details can be found in a number of publications. Shchepetkin and McWilliams (2003; 2005) describe the handling of the horizontal component of the pressure gradient in terrain-following models and the numerical methods used in ROMS. Marchesiello et al. (2001) discussed options and difficulties in using open boundary conditions. Moore et al. (2004) enumerated on the creation of the tangent linear and adjoint modules of ROMS while Moore et al. (2011) detailed procedures for data assimilation into ROMS. Warner et al. (2005) evaluated the formulation of multiple two equation turbulent closure schemes via generic length scale equations for use in ROMS. Finally, the development of COAWST is detailed in Warner et al. (2005) and Warner et al. (2010). ROMSmsb was adapted from the COAWST model.

### 4.1.3 CONCORDE Meteorological Analysis

The CONCORDE Meteorological Analysis (CMA) provides atmospheric forcing for ROMSmsb at 0.01° spatial grid spacing and hourly temporal intervals. CMA combines variable fields from the Real-Time Mesoscale Analysis (RTMA), the North American Mesoscale (NAM) Forecast System, the Next Generation Weather Radar (NEXRAD) Level-III, and the Advanced Very High Resolution Radiometer (AVHRR)

(Fitzpatrick and Lau, 2018). The CMA product was developed for the CONCORDE project. However, the scripts and retrieval procedures have been made publicly available, so new CMA files can be generated beyond the duration of the CONCORDE project.

Fitpatrick and Lau (2018) detail the procedures to retrieve and calculate fields for CMA and outline creation of daily atmospheric forcing files. The 10-m meridional and zonal wind components, sea level pressure, and 2-m air temperature from RTMA are mapped to the CMA horizontal grid using bilinear interpolation, and RTMA air temperature, sea level pressure, and dew point enabled calculation of relative humidity. The NAM Forecast System analysis and short-term forecast fields of long-wave radiation, short-wave radiation, and cloud cover percentage are likewise bilinearly interpolated to the CMA grid. Of the National Doppler Radar Sites included in NEXRAD Level-III, the KMOB (Mobile, Alabama) and KLIX (New Orleans, Louisiana) fall closest to the CMA grid, so nearest neighbor interpolation-mapped precipitation rates to the horizontal model grid are performed from the closest radar site. Ten-day averaged sea surface temperatures (SSTs) centered on day 6 were calculated from daily AVHRR SST output and then interpolated to the CMA grid using a distance weighting algorithm. Daily SST values were repeated for each hour of the day. Finally, sensible heat flux and surface momentum stresses are computed from the Coupled Ocean-Atmosphere Response Experiment (COARE) algorithm using the interpolated fields from RTMA, NAM Forecast System, and AVHRR. CMA files were generated daily, but the collection of CMA files were mapped to the ROMSmsb horizontal grid using bicubic interpolation to yield a single CMA file for use in ROMSmsb runs.

### 4.1.4 Gridding and Bathymetry

The land mask and bathymetry of ROMSmsb were developed for the CONCORDE project. Bathymetry generation involved the synthesis of output from a digital elevation model and field surveys. Bathymetric depths, dated 2001, taken from the National Centers for Environmental Information (NCEI) 3 arc-second coastal relief model provided initial input for the Bathymetric Dynamic Digital Elevation Model (BDDEM); depths were updated year by year with National Ocean Service hydrographic surveys performed in the region from 2001 through 2011 and interpolated to a 90-m resolution grid (NOAA, 2001; O'Brien et al., 2014). The 400-m raw and smoothed model bathymetry grids were created from the BDDEM output grid using a Fortran-based software called gridpak developed by Wilkin and Hedström (1998). Two algorithms smoothed the bathymetry 6 times using a modified Shapiro filter. The gridpak software also generated an initial land mask, and the mask was then edited in post-processing using a MATLAB script called editmask developed by Shcherbina (2014).

### 4.1.5 Nesting and Forcing Files

Three forcing files are fed to the ROMSmsb input file: atmospheric, boundary, and riverine input. The atmospheric model is described above while boundary and riverine input are discussed below.

ROMSmsb uses one-way nesting; forcing along lateral boundaries is taken from the Navy Coastal Ocean Model (NCOM). Output from the 3 hourly 1-km horizontal resolution Gulf of Mexico regional application of NCOM was sub-gridded through linear interpolation to match the spatial resolution of ROMSmsb, so results supplied values along the ROMSmsb boundaries. The Coupled Ocean Atmosphere Mesoscale Prediction

System (COAMPS) provided atmospheric inputs for NCOM while the regional model, in turn, took its boundary inputs from the global Hybrid Coordinate Ocean Model (HYCOM) (Kara et al., 2006; Martin et al., 2008; Martin et al., 2009). Like ROMSmsb, NCOM uses curvilinear horizontal coordinates, σ vertical levels, and the primitive equations with Boussinesq and hydrostatic approximations.

The riverine input file contains input for 17 rivers, but outflow for the larger rivers was split into multiple mouth locations, each with their own coordinates and time-varying flow. Salinity was set to zero for each river, and discharge estimates came from US Geological Survey daily discharge time series available from https://waterdata.usgs.gov/nwis/dv/. The model does not account for all riverine sources; as an example, no freshwater discharge comes from Lake Ponchartrain. Figure 4.1 shows the locations of each riverine source within the model domain.

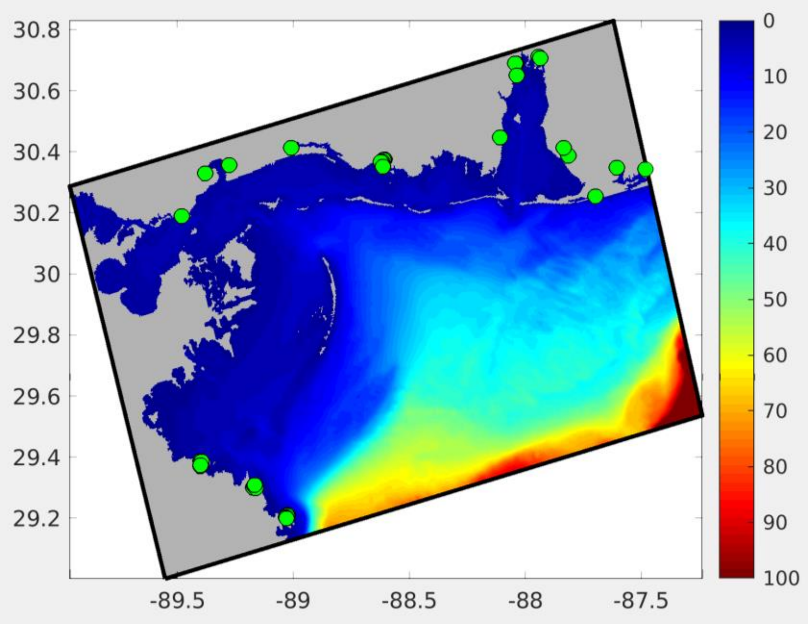

Figure 4.1 Riverine input locations in the ROMSmsb domain

Green circles give the locations of 17 rivers included in the ROMSmsb input files. The model domain is outlined in black with land areas colored gray. Bathymetry is colored according to depth in meters.

## 4.2 Data-Model Agreement

### 4.2.1 CMA Validation

Multiple rounds of CONCORDE Meteorological Analysis (CMA) validation have been completed by Fitzpatrick and Lau (2018) as well as by members of the CONCORDE modeling group. Consequently, the validation covered here investigates CMA's ability to capture repeated events, specifically the land-sea breeze cycle. As discussed in Chapter I, the land-sea breeze dynamic becomes dominant from June through August. This atmospheric phenomenon plays a key role in summer atmospheric forcing, so the atmospheric model should be able to represent the cycle.

Winter front identification through temperature gradient, sea level pressure, and relative humidity was also investigated, but no comparative observational results existed for the model domain. As such, confirmation of successful winter front identification would be subjective at best. The CMA domain is limited to the northern Gulf of Mexico which has been a historically more difficult area in which to automate front detection. Front identification typically uses two or more parameters to classify fronts; these can include temperature gradients, pressure isobars, etc. (Cox, 1916). Fronts travel southeast across the continental United States, and from the perspective of the study area, winter fronts can approach from the northwest, the west, or the southwest (Rogers and Rohli, 1991; Roberts et al., 1989). Atmospheric conditions preceding frontal passage include falling pressure, warmer temperature, and higher humidity; by contrast, post-front passage sees higher pressure, cooler temperatures, and lower relative humidity (Cox, 1916). Shifts in wind direction can also indicate frontal passage, but as Chapter II noted, the shape of the coastline complicates studies based on wind direction.

Local maxima in sea level pressure were correlated to local minima in air temperature. Calculation of temperature gradients across the CMA domain whenever 1025 hPa occurred between October and April was used to assess potential front positions, and when available, decreases in relative humidity were also monitored. However, the analysis only identified 12-16 fronts in the 2015-2017 CMA period. Results are not presented here; instead, CMA validation focused on the sea breeze cycle and land breeze cycle.

Isolation of the land-sea breeze dynamic follows the methodology outlined in Hill et al. (2010). CMA output was limited to June, July, and August. Hill et al. (2010) focused on buoys 42040 and 42007 as wells as the NOAA stations KGPT (Gulfport Airport, Mississippi) and KBVE (Boothville, Louisiana). Consequently, the indices of the nearest model grid points to those locations were identified. Hill et al. (2010) used radar data to remove days with precipitation events as these days would be uncharacteristic of land-sea breeze days (Hill et al., 2010). In CMA, hours exceeding a rainfall rate of $5x10^{-5}$ $kg/m^2s$ (4 mm/day) were excluded to accomplish a similar goal. Likewise, hours with wind speeds exceeding 14.4 m/s were removed since the Beaufort wind scale qualifies speeds from 0 to 14.4 m/s as light, gentle, moderate, fresh, and strong breezes. Hourly averaging of the remaining data generated typical June, July, and August sea breeze cycle days over a 24 hour period. Conversion of the dataset to Central Daylight Time then allowed comparison to Figure 3 in Hill et al. (2010).

In Figure 4.2, wind speed magnitudes at the Gulfport Airport location have nearly identical magnitudes to those given in Figure 3 of Hill et al. (2010). However, peak magnitudes start around local noon in CMA whereas Hill et al found magnitudes peaking around 8:00 CDT. Also, CMA has lower wind speeds from 0:00 CDT to 10:00 CDT and from 20:00 CDT to 23:00 PM CDT. Overall though, wind directions agreed for all three months. CMA exhibited larger wind speed ranges at both buoy locations while Hill et al. (2010) found magnitudes only varying between 2 m/s and 4 m/s. Directionality in June did not agree well, but July and August directionality mimicked the Hill et al. (2010) study. As for buoy 42040, CMA wind directions agreed in August, but magnitudes did not. July wind directions did not match, and the minimum in July happened at 14:00 CDT rather than at 18:00 CDT as given in Hill et al. (2010). CMA performed well in that rotation of the wind velocities occurred with the same timing exhibited in Hill et al. (2010).

Hill et al. (2010) additionally analyzed the time-evolving temperature gradient between KGPT (Gulfport Airport) and buoy 42007 which lie 47 km apart. The distance between the stations matches in the CMA grid. Results in Figure 4.3 for CMA and Figure 8 in Hill et al. give the temperature gradient in K/km. In this instance, the gradient is equal to the air temperature at KGPT minus the air temperature at buoy 42007 divided by the diagonal distance between the two. Hill et al. (2010) split the 24 hours of each month into two regimes: negative (warmer ocean) and positive (warmer land). The negative temperature gradient occurs from 0:00 CDT to 9:00 CDT and from 19:00 CDT to 23:00 CDT, and the positive gradient remains from 9:00 CDT to 19:00. The CMA results not only preserve this trend but more clearly demonstrate it. The Gulfport land site is warmer than the sea site during the majority of daylight hours, but the sea site becomes warmer at night. Hill et al. (2010) found a -3.5 K to 3.0 K range in temperature differences between the two sites; CMA displayed a -4.8 K to 2.4 K range in temperature differences.

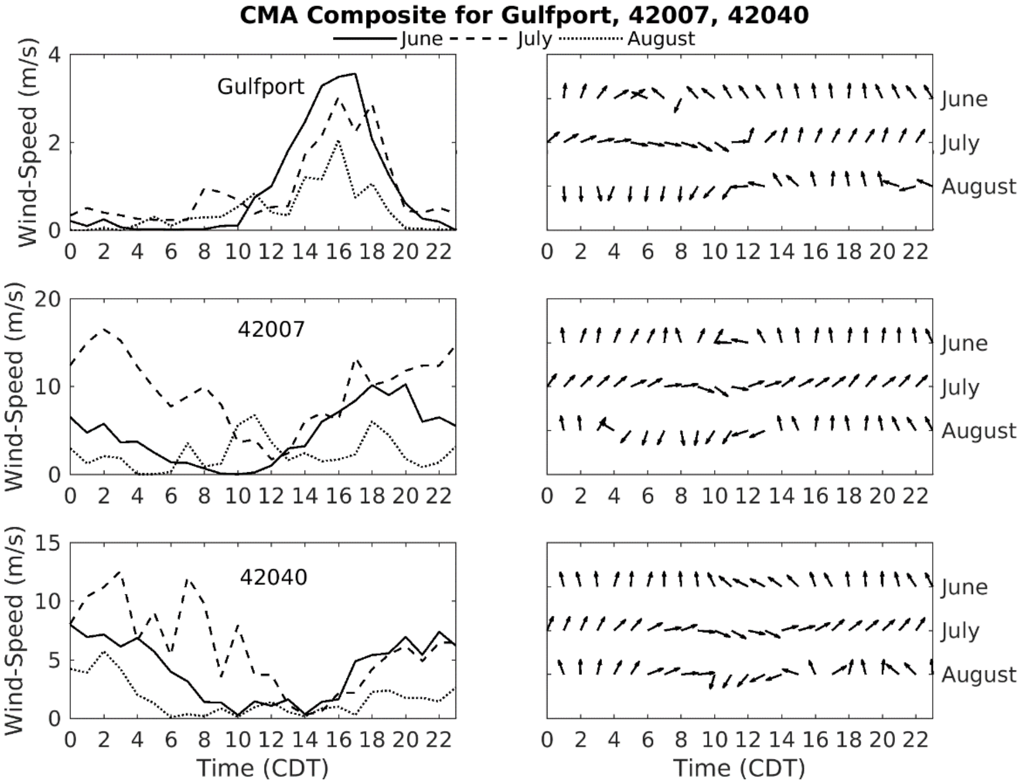

Figure 4.2 Composite CMA sea breeze wind fields for June, July, and August

Magnitudes of average wind velocities for KGPT (top left), buoy 42007 (middle left), and buoy 42040 (bottom left) and their associated directions (right panel) for the months June, July, and August. Directions are north (up), east (left), south (down), and west (right).

Though the CMA results did not perfectly replicate trends in the Hill et al. (2010) study, CMA did exhibit the correct pattern in temperature gradient anomaly. Wind speed changes and directional shifts also loosely followed results from Hill et al. (2010). Given the difference in study years and products used, the CONCORDE Meteorological Analysis does represent the land breeze and sea breeze cycles satisfactorily in terms of temperature gradients and wind speed and direction evolution during a 24-hour period.

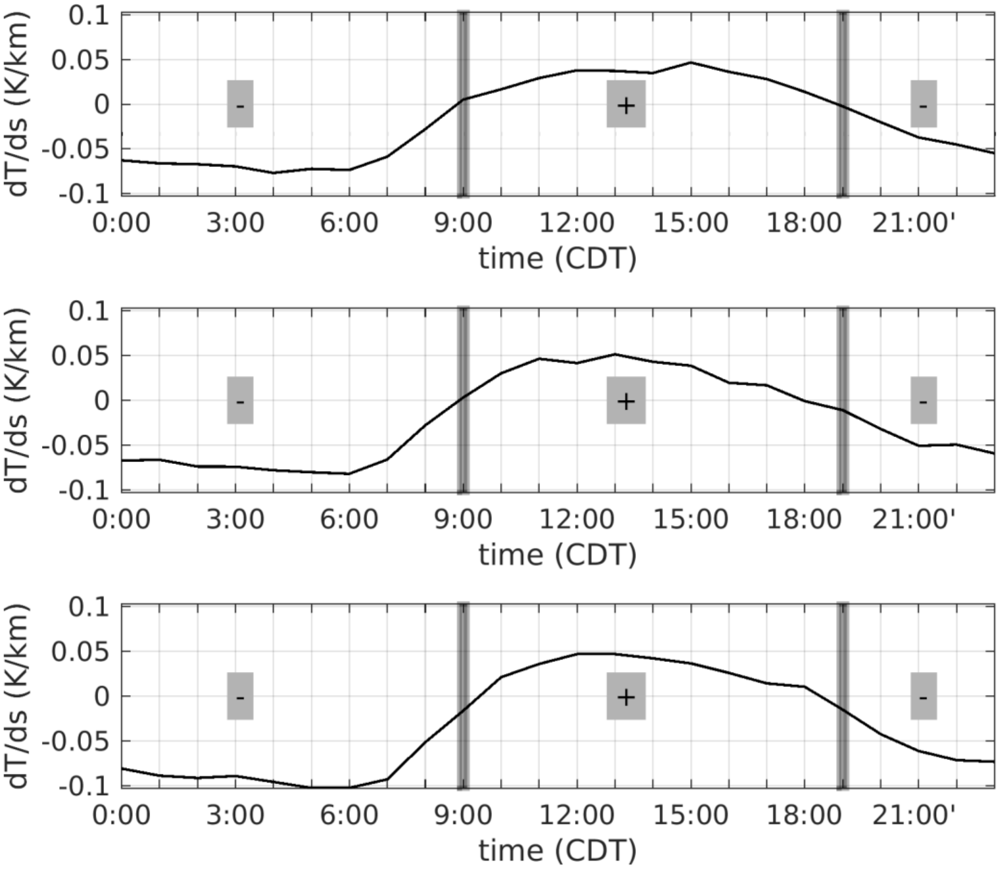

Figure 4.3 Temperate gradient for June, July, and August between Gulfport and buoy 42007

Temperature differences across the 47 km separation distance of the Gulfport Airport station minus the buoy 42007 station for June (top), July (middle), and August (bottom).

### 4.2.2 ROMSmsb Validation

Since CMA forcing was not available until 04/15/2015, a 14 month ROMSmsb run was executed from 01/01/2014 using North American Regional Reanalysis for atmospheric forcing. Subsequent runs used in this study used output from the NARR-forced run as initial conditions for hot start runs. Atmospheric forcing for the output detailed in this chapter utilized CMA forcing. The first month of output after April 2015 was excluded to avoid any contamination related to the change in atmospheric forcing.

ROMSmsb validation focused on two datasets: 5MHz HF radar-derived surface currents and near-bottom temperature and salinity measured by the 12 USGS-MDMR hydrological stations in the western Mississippi Sound. Earlier model validation efforts compared model output against data collected during the field campaigns of CONCORDE.

In keeping with previous validation efforts, some results are presented in Taylor diagram form. Taylor diagrams provide a way to evaluate model-data agreement based on three criteria within a single plot (Taylor, 2001). On a polar coordinate system, the magnitudes of the data and model standard deviations function as radii. The data standard deviation is at 0° while the model standard deviation is at 90°. The correlation coefficient given by (Eq. 4.1) runs the curved axis from 0 at 90° clockwise to 1 at 0°. In (Eq. 4.1), D represents observational data, M represents model output, overbars denote means, σ gives standard deviations, and N is the number of discrete points used for comparison; (Eq. 4.1) and (Eq. 4.2) follow from equations (1) and (2) in Taylor (2001). Within the Taylor plot, a series of concentric circles centered on the data standard deviation display the centered root mean square errors. (Eq. 4.2) gives the formula for calculating centered root mean square errors. Given this setup, model-data agreement occurs as the model standard deviation draws equal to the data standard deviation, the centered root-mean-square error goes to zero, and the correlation coefficient goes to one.

More simply put, the data standard deviation acts as the reference point, and model results should fall close to that point.

$$R = \frac{\frac{1}{N}\sum_{i=1}^{N}(D_i-\bar{D})(M_i-\bar{M})}{\sigma_D\sigma_M} \qquad \text{(Eq. 4.1)}$$

$$RMSE = \sqrt{\frac{1}{N}\sum_{i=1}^{N}[(D_i-\bar{D})-(M_i-\bar{M})]^2} \qquad \text{(Eq. 4.2)}$$

A technique was developed to compare HFR velocities against model velocities. CenGOOS HF radar surface velocities represent hourly products averaged over 6x6 km$^2$ regions for the 5 MHz sites and 1x1 km$^2$ regions for the 25 MHz sites. By contrast, ROMSmsb has 400x400 m$^2$ resolution and a user-defined file generation of 12 hours. The northwest HFR domain overlaps the southeast ROMSmsb domain, but the discrepancy in resolution requires some averaging to enable comparison of data and model results over the effective depth of the HFR-derived surface currents.

Consequently, logical indexing found model grid points that fell within a bounding box 3 kilometers north, south, east, and west of an HFR velocity grid point. The procedure for converting the 3 km distance into longitude and latitude bounds is detailed in section 3.1. Velocities of the model grid points falling within the HFR grid cell went into the spatial average.

Since ROMSmsb utilizes σ layers for its vertical grid, model velocities had to be averaged over the effective depth range of the HFRs. Wavelengths, λ, of the transmitted HFR radio signals can be found by dividing the speed of light, c=3x10$^8$ m/s, by the center frequency, f, of the HFR in Hz (1/s), seen in (Eq. 4.3). Wavelengths of surface gravity waves that Bragg scatter the signal have one-half the wavelength of the transmitted signal, and the depth of influence of those surface gravity waves determines effective depths of radial currents measured by the direction-finding Seasonde HF radars. Stewart and Joy (1974) found the commonly accepted equation that estimates effective depth, d, by comparison of HFR-derived currents to in situ measurements. (Eq. 4.4) depends on the assumption that current speeds decrease linearly with depth.

$$\lambda_{HFR} = \frac{c}{f} \qquad \text{(Eq. 4.3)}$$

$$d = \frac{\lambda_{HFR}}{8\pi} \qquad \text{(Eq. 4.4)}$$

The 5 MHz sites center frequencies range from 4.54 MHz to 4.75 MHz meaning effective depth ranges from 2.63 m to 2.51 m, so an average value of 2.57 m was used for effective depth. The 25 MHz sites operate at 25.4 MHz and 25.6 MHz center frequencies meaning effective depth is approximately 0.47 m. However, insufficient 25 MHz velocity measurements existed for the duration of the model runs to provide adequate points for comparison since the HFRs were installed in February 2016.

ROMSmsb σ layers at each grid point for each time step were transformed to depth estimates using σ transform and stretching functions in conjunction with the free surface and critical depth variables outputted by the model (Shchepetkin and McWilliams, 2005; Song and Haidvogel, 1994). Horizontal velocities were retrieved for all layers falling within the HFR effective depths. Depth-averaged velocities were then taken at each time step for each grid point prior to the averaging of model velocities for grid points occurring within each HFR spatial cell. The depth-range-averaged and spatially-averaged model velocities, converted to cm/s, were then compared to 12-hour-averaged HFR-derived surface velocities.

Looking over the shared domain and throughout the year long model run, mean velocities and standard deviations are close for HFR and ROMSmsb velocities. The mean zonal velocity was -2 cm/s with a standard deviation of 9 cm/s, and the meridional component mean was -1 cm/s with a standard deviation of 10 cm/s. The observational means were 1 cm/s and -3 cm/s with standard deviations of 13 cm/s and 9 cm/s respectively. However, agreement varied widely across the shared domain. Figures 4.4 and 4.5 split the model-observations pairs up by location. In order to keep all the results on one plot, model and observational standard deviations were divided by the observational standard deviation for each grid cell. This means all observational points were set equal to 1 and marked by “Ref”, and the normalized model standard deviation at 1 shows the line of best agreement. The highest correlation coefficient for zonal velocities reached 0.8, but certain locations had negative correlations as low as -0.5. Over the entire shared domain, zonal velocities had higher correlation coefficients and lower centered root mean square errors (RMSE) than meridional velocities.

Model meridional velocities tended to either have much higher or much lower standard deviations than observations. The worst negative correlation coefficient equaled -0.7 while the best equaled 0.9. However, the meridional velocities for HFR coordinates south of Mobile Bay had correlations coefficients larger than 0.6 and root mean square errors near zero, so that region had the best agreement in terms of north-south currents. Points of the Taylor diagrams are displayed in the model domain across the HFR 6x6 km$^2$ grid cells; values are broken up between correlation coefficients in Figures 4.6 and 4.9, centered RMSE in Figures 4.7 and 4.10, and normalized model standard deviations in Figures 4.8 and 4.11.

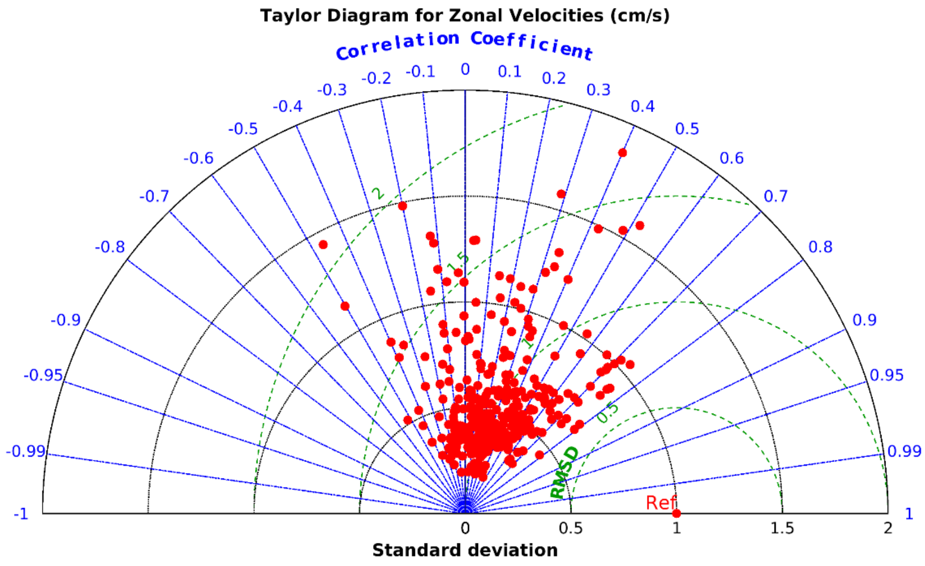

Figure 4.4 Taylor diagram for observation to model zonal velocities

Relationship of ROMSmsb zonal (U) velocities to HFR observational zonal velocities (Ref) with respect to standard deviation (dotted black lines), center root mean square error (dashed green lines), and correlation coefficient (dot-dashed blue lines). To collocate comparison pairs, observational and model standard deviations have been normalized using the observational standard deviations.

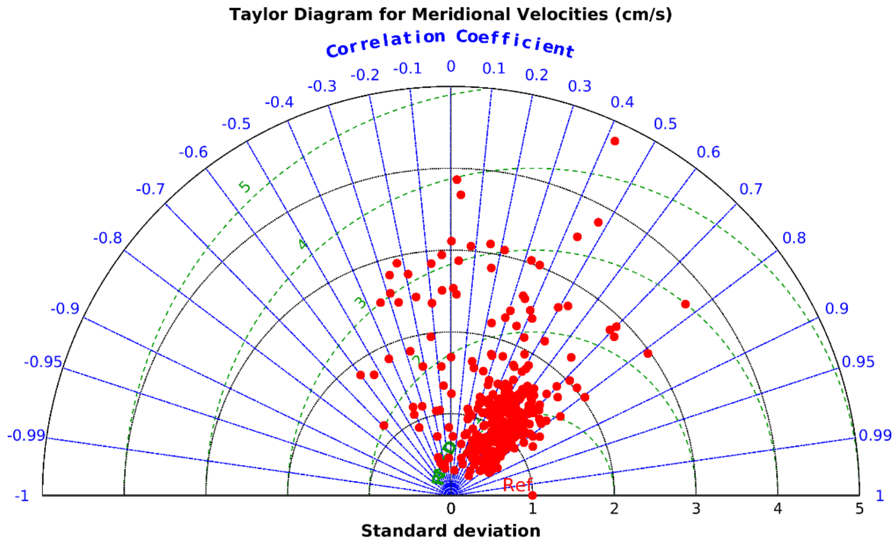

Figure 4.5 Taylor diagram for observation to model meridional velocities

Relationship of ROMSmsb meridional (V) velocities to HFR observational meridional velocities (Ref) with respect to standard deviation (dotted black lines), center root mean square error (dashed green lines), and correlation coefficient (dot-dashed blue lines). To collocate comparison pairs, observational and model standard deviations have been normalized using the observational standard deviations.

Model standard deviations for zonal velocities have much smaller values for most of the shared domain than HFR standard deviations. However, correlation coefficients nearing 1 occur near the eastern model boundary and south of Petit Bois Island. Low root mean square errors lie along a diagonal extending southwest from the Fort Morgan peninsula to the southern model boundary south of Dauphin Island. Across the three parameters, good agreement occurs south of Petit Bois Island east to the Fort Morgan peninsula. This means correlation coefficients exceed 0.6, and the same area has root mean square errors near 0. Some of the 6x6 km$^2$ cells also have a model to observation standard deviation ratio ranging from 0.8 to 1.2. However, the worst agreement happens at the western edge of the HFR coverage near the Chandeleur Islands, along the southern model boundary, and in the southeast corner of the model domain. Correlation becomes negative, and model standard deviations are more than twice the magnitude of the observational standard deviation. The area of poor agreement occurs where HFR velocities have the highest uncertainty and highest GDOP. Overall, HFR and ROMSmsb velocities match most closely in the eastern part of the shared domain but disagree near the edges of HFR coverage and the model's open boundaries.

As for temperature and salinity validation in the western Mississippi Sound, different considerations made observation to model comparisons difficult. Communications with the Mississippi Department of Marine Resources and the US Geological Survey specified the hydrological stations were mounted as close to the seafloor as possible, but technical difficulties and environmental interference required some degree of shoaling. As such, the stations are only specified as bottom stations in reports, and email correspondence with the Hydrologic Data Section of the US

Geological Survey revealed station depths were recorded in depths below sea surface that varied about 1 m depending on water levels. Given the depth range, uncertainty in depths at those locations, and possible inaccuracies in model depths, depth-averaged bottom temperatures and salinities were found over the deepest 1.5 m with the same technique described above for depth-averaged surface currents.

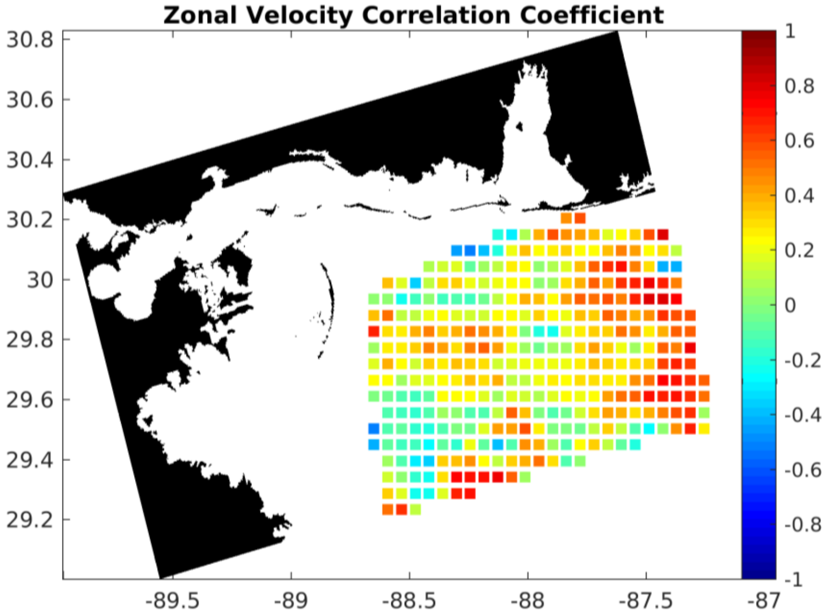

Figure 4.6 Zonal correlation coefficients for 5 MHz HFR velocity grid

ROMSmsb domain overlaid with HFR velocity grid where colors indicate correlation coefficient between observational and model surface velocities for each grid cell.

Unlike HFR surface currents, the hydrological stations yield point source measurements, so temperature and salinity for multiple model grid points were used for comparisons. The closest 10 grid points outlined a region around the location of each hydrological station. Taylor diagrams in Figures 4.12 and 4.13 show the spread of results across those points for the stations collectively as the distance and orientation of the model grid points had little influence on the model-data agreement within that radius set by the 10 nearest neighbor points.

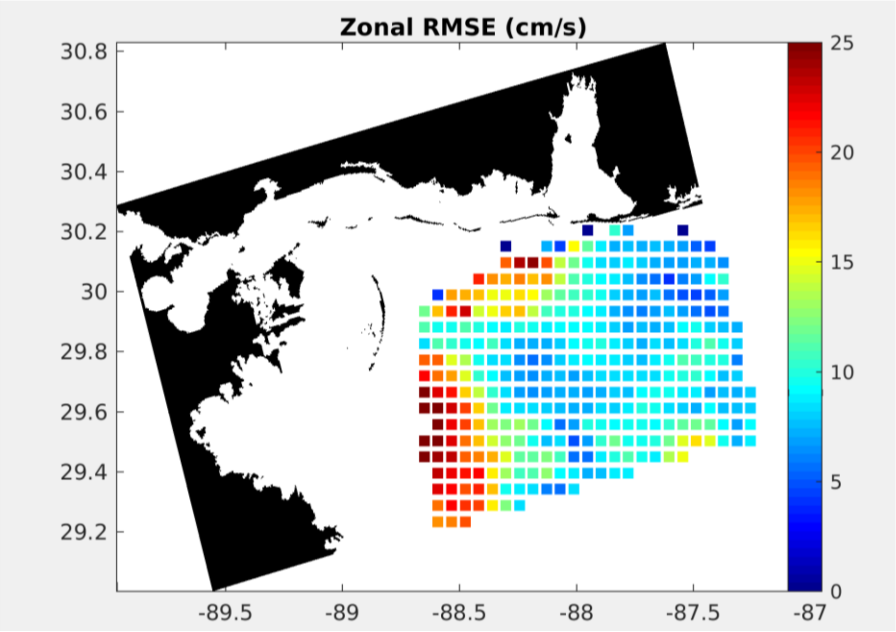

Figure 4.7 Zonal centered root mean square errors for 5 MHz HFR velocity grid

ROMSmsb domain overlaid with HFR velocity grid where colors indicate root mean square error between observational and model surface velocities for each grid cell.

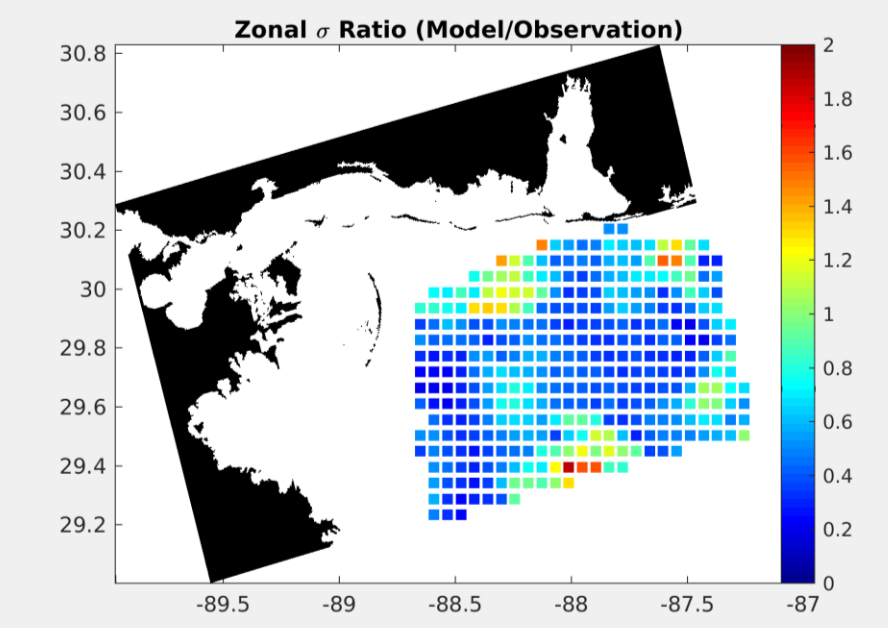

Figure 4.8 Zonal σ ratio for 5 MHz HFR velocity grid

ROMSmsb domain overlaid with HFR velocity grid where colors show the model standard deviation divided by the observational standard deviation for each grid cell.

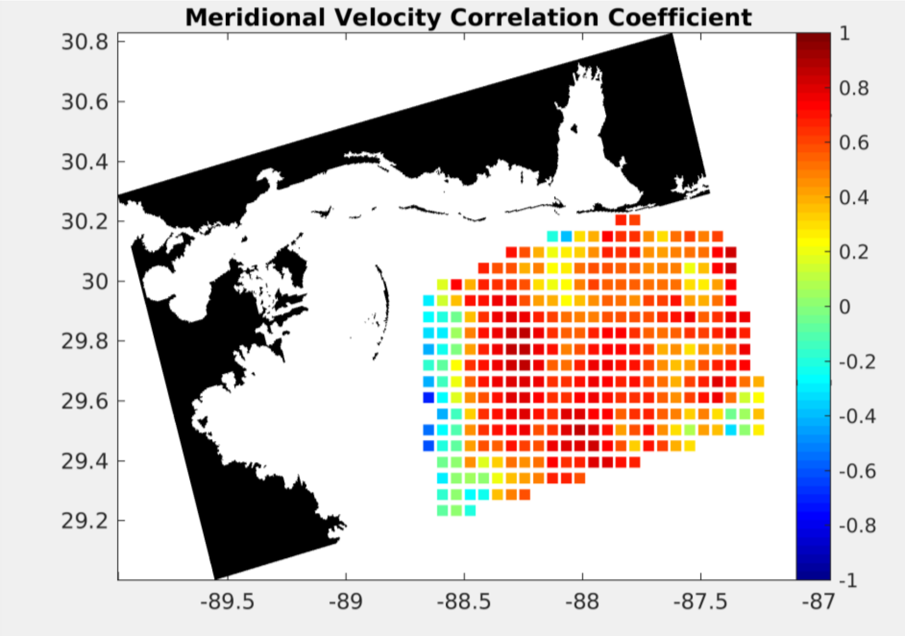

Figure 4.9 Meridional correlation coefficients for 5 MHz HFR velocity grid

ROMSmsb domain overlaid with HFR velocity grid where colors indicate correlation coefficient between observational and model surface velocities for each grid cell.

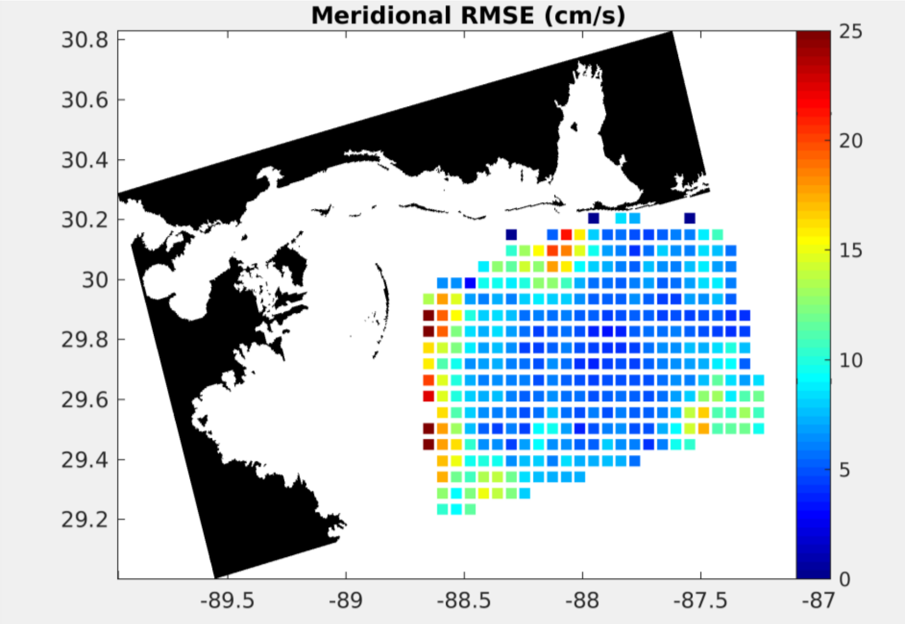

Figure 4.10 Meridional centered root mean square errors for 5 MHz HFR velocity grid

ROMSmsb domain overlaid with HFR velocity grid where colors indicate root mean square error between observational and model surface velocities for each grid cell.

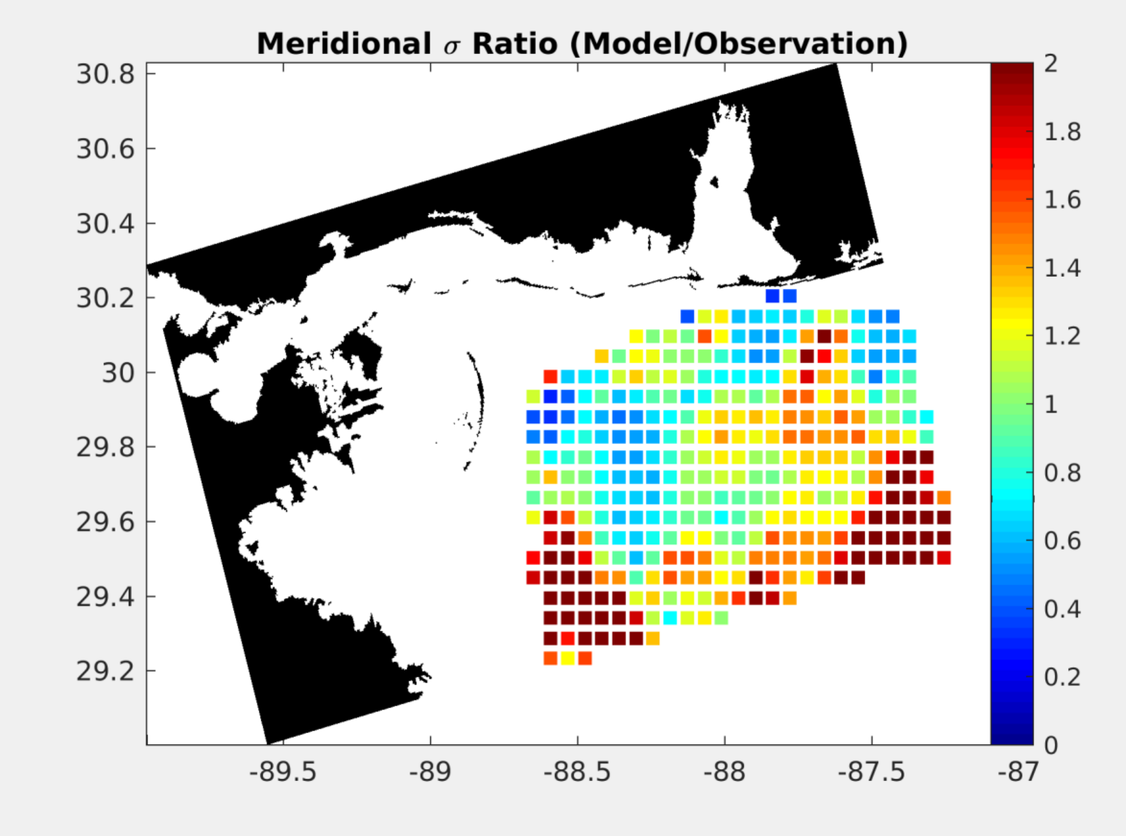

Figure 4.11 Meridional σ ratio for 5 MHz HFR velocity grid

ROMSmsb domain overlaid with HFR velocity grid where colors show the model standard deviation divided by the observational standard deviation for each grid cell.

Bottom temperatures had much better agreement than bottom salinities. Correlation coefficients in Figure 4.12 range from 0.4 to 0.7. Centered RMSE ranged from 4.5ºC to 6.5ºC. Model temperatures varied more than observational temperatures, but depth disagreement between the model and observations might be responsible for the difference. Correlation coefficients for bottom salinities ranged from <0.3 to >0.5 in Figure 4.13. Unlike with temperature, model salinities varied less than observational salinities. The mean observational bottom temperature was 24°C±6°C for the western Mississippi Sound while model bottom temperatures hovered around 25°C±6°C. While means for individual stations varied, the standard deviations remained fairly consistent station to station and for each of the 10 nearest neighbors to each location. The model was slightly warmer than observations. Mean observational salinity was 16±9 while model salinities ranged 20±5 to 24±7; the model frequency overestimated salinity.

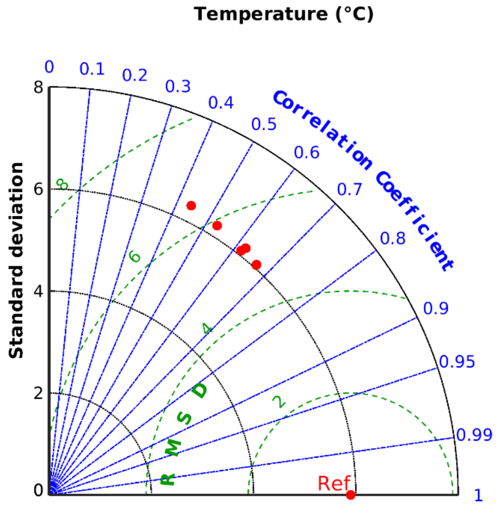

Figure 4.12 Taylor diagram for observation to model bottom temperatures

Relationship of ROMSmsb bottom temperatures to USGS-MDMR observational bottom temperatures (Ref) with respect to standard deviation (dotted black lines), center root mean square error (dashed green lines), and correlation coefficient (dot-dashed blue lines). In order to collocate comparison pairs, observational and model standard deviations have been normalized using the observational standard deviations.

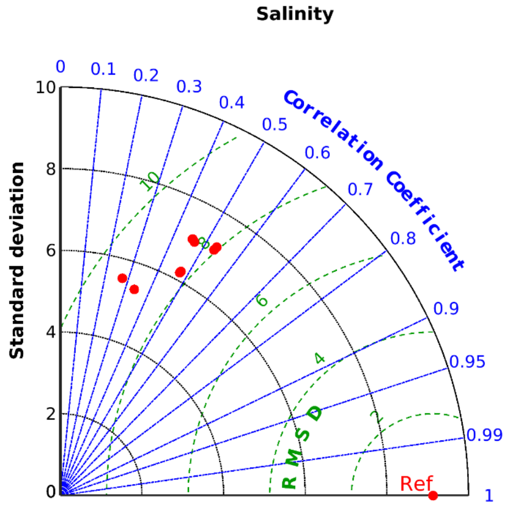

Figure 4.13 Taylor diagram for observation to model bottom salinities

Same design as Figure 4.12.

Model-data agreement analysis was completed for a 1 year period for surface currents, bottom temperature, and bottom salinity. Correlation coefficients neared 0.9 for portions of the shared HFR-ROMSmsb domain with lower RMSE values corresponding to the same points. Given the length of record used for comparison, the agreement was fairly good, especially since model grid points had to be spatially averaged, both horizontally and vertically, prior to comparisons being made. Surface current data are not without error. Section 2.2.1 discusses uncertainty in high frequency radar-derived surface currents as well as the geometric dilution of precision (GDOP). Additionally, (Eq. 4.4) makes assumptions about velocity decreasing linearly with depth. The 2-dimensional HFR currents are in many ways a dissimilar product to the 3-dimensional currents calculated by the model, but the best agreement between ROMSmsb and the observed surface currents occurs in the center and eastern portion of the shared domain where the HFR currents have the lowest uncertainties and GDOP values. Likewise, depth ranges had to be estimated for the hydrological stations since deployment depths could not be absolutely established. As detailed above, the overestimation in salinity was anticipated since freshwater outflow by Lake Ponchartrain is not properly accounted for in NCOM. Temperature comparisons have high correlation coefficients, low RMSE, and comparable standard deviations. Gaps in data coverage are numerous in the Mississippi Sound and Bight, so a true calibration of the ROMSmsb model cannot be done at this time. However, results of the ROMSmsb validation suggest the model captures circulation dynamics reasonably well over the course of a full year.

## 4.3 Island Removal

### 4.3.1 Selecting Islands for Removal

Model-simulated topographic and bathymetric change scenarios identify how extreme geologic shifts impact circulation in the Mississippi Sound and Bight. As such, a number of simulations became candidates during the initial planning of this project. The Mississippi Coastal Improvement Plan recently finished a half decade project to infill the hurricane breach between East and West Ship Island, so modeling the restored barrier island could be an option (DOI, 2016). Likewise, westward migration and segmentation have marked the island chain's history. Another modeling option could be a future island chain configuration based on linear regression of past shorelines. Simulated subaerial land changes and island breaches could also be modeled. Ultimately though, island removal was selected as the focus of this study.

The simplicity of the model runs drove this choice. Ocean models in general and coastal models, in particular, require tuning for the region and timescales of interest. Regional models require boundary forcing from global or larger regional ocean models, and finer grids for variables such as bathymetry and hydrographic properties can better resolve mesoscale processes in a region than a coarser grid used for global circulation. As section 4.5.2 details, wind speeds and directions in CMA change in the vicinity of the islands, so any land mask change in ROMSmsb requires a localized modification of the CMA forcing file at each time step. In terms of island chain segmentation and westward movement, this would involve substantial changes to the CMA file, and each additional change could lengthen model run time, cause model blow up and drive up model error with the inclusion of new equations and parameters. Additionally, any model simulation that represented a possible future island chain configuration would likewise require coastline modification for Louisiana, Mississippi, and Alabama to mimic sea level rise and salt marsh loss. Louisiana barrier island loss and/or reduction would also have to be simulated. Consequently, while the simulation has value, a simpler change scenario would better serve initial modeling efforts.

In a similar vein, the MsCIP restoration of Ship Island involves a multi-stage process. Evolving sediment dynamics rather than circulation changes would be the focus of such a model run, and to best serve the project, ROMSmsb should model predictive scenarios for each stage of the restoration.

Finally, storm-induced changes to the barriers would be an uncertain undertaking. As Chapter III detailed, storm paths and impacts do not follow concrete patterns, and atmospheric models, including CMA, do not incorporate reconnaissance data collected during storms. Substantial data assimilation and modification to CMA would be necessary for storm-impact simulations. Ultimately, island removal became the preferred option since it required one set of localized modifications to the bathymetry, land mask, and atmospheric parameters, and observed circulation changes could be more reliably ascribed to island loss as opposed to model artifacts.

Numerous surveys throughout the previous decades indicate net land loss across the barrier island chain. However, islands within the chain have not eroded equally. Eastern Dauphin Island has a Pleistocene core and a sandy shoal offshore that keeps the island stable in terms of sediment retention (Otvos and Carter, 2013). In a similar vein, woodland areas on Horn Island and the island’s sheer size mean it has weathered the past two centuries with a smaller percentage of subaerial land loss than either of its neighbors

(Jeter and Carter, 2016). The St. Bernard delta restricts Cat Island's westward migration and has a controlling influence on wind and tidally-driven currents. By comparison, Ship Island and Petit Bois Island have exhibited less resiliency.

Since Ship Island has been repeatedly breached by tropical cyclones in the last century and since East Ship suffered the most extreme land loss following Hurricane Katrina in 2005, the two components of Ship Island were removed for one set of experimental runs. Removing Ship Island offers an interesting choice since MsCIP just finished filling the breach between the two island halves (Perez, 2019). Subaerial land removal can provide support for the project by illustrating the island's role in circulation.

By contrast, anthropogenic modification trends largely drove the choice to remove Petit Bois Island in the second island loss scenario. Shipping channels enable large vessel access to ports along the northern Gulf coast. These channels are dredged on an as needed basis, and the deepening from the dredging interrupts sediment supply (Morton, 2007). The shipping channel through Horn Island Pass between Horn Island and Petit Bois lies next to the western tip of Petit Bois Island. Accretion on the island's western end is largely halted by the maintenance of the channel. Given the eastern erosion and stunted westward accretion, Petit Bois was removed in the second set of experimental runs.

Dauphin Island's western extent used to connect to Petit Bois, and cartographic records show the intermittent reconnection and separation of the islands over the past two centuries. Consequently, the western portion of Dauphin Island was included in the Petit Bois Island removal runs. Present imagery shows Dauphin Island's width narrows to 80 m near 88.2°W, and this section also matches the location of the Hurricane Katrina breach, so removal of Dauphin Island started west of the breach point. Sand Island (West Petit Bois Island), west of Petit Bois, does not belong to Petit Bois and lies on the western side of the Pascagoula shipping channel. Sand Island was therefore not included in the Petit Bois removal runs.

### 4.3.2 Bathymetry and Land Mask Changes

The removal of the islands in preparation for the model runs included three steps. First, the bathymetry variable was read into MATLAB from the netCDF grid file containing input data to ROMSmsb. Coastal land adjacent to wet grid cells has a depth value of 1 m in the model. The seafloor and barrier islands have non-integer values greater than 1 m with the subaqueous land of the islands ranging in depth from 2 to 4 m.

A MATLAB switch case script was written to generate a graphical user interface (GUI) containing a bathymetric map of the model domain with a specified color map corresponding to 0 to 20 m depths. Lines delineating the present location of the barrier islands overlaid the map as a reference. Two toggle buttons enabled shallowing and deepening of bathymetric depths via changes to the color map. Once toggling was activated, depths were changed by mouse click. Saved changes to the color corresponded to alterations to depth in the bathymetry variable. Bathymetry to the north of the island towards the mainland was shoaled by 1 m to represent landward retreat of the removed subaerial sediment.

Second, coordinates set to 0, for land, in the land mask were converted to 1, for water, for the coordinates of the removed islands. The GUI code written for bathymetric change was based on the land mask script, developed by Shcherbina (2014). Since the ROMS component of ROMSmsb employs a staggered Arakawa-C grid, the grid file contains four land masks: density, stream function, and the two components of velocity. The script functioned to match changes in the other land masks with changes made to the density land mask.

Third, once the bathymetry variable underwent change, the variable was smoothed using a linear programming smoothing algorithm coded by Sikirić et al (2009). Smoothing prevents model blowup since sharp depth changes in wet grid cells result in unrealistically large pressure gradients calculated by the model. Bathymetry had already been smoothed for previous model runs by the CONCORDE modeling group, so only 8 and 16 grid points required smoothing in the Ship Island and Petit Bois Island removal scenarios respectively. However, the introduction of additional water grid points from land removal did necessitate smoothing.

Five smoothing algorithms were compared before selection of the linear programming algorithm. Input for the algorithms included the bathymetry variable, density land mask variable, and a roughness factor that describes depth changes between adjacent cells. The roughness factor, $r_{x0}$, is given in (Eq. 4.5) where h(e) and h(e') are the bathymetric depths on the horizontal grid linear indices e and e' (Sikirić et al., 2009). In the equation, e' pertains to the indices adjacent to e. The maximum permissible roughness factor was set to 0.2, and the equation for roughness was taken from Beckman and Haidvogel (1993) and scripted by Sikirić et al. (2009). Bathymetry values in adjacent grid cells were deepened or shoaled iteratively until the $r_{x0}$ criteria was met across the model domain. The linear programming option was chosen as it modified the fewest grid points to achieve a roughness factor less than 0.2, and run time for the algorithm was <1 s. Additionally, as section 4.1.4 detailed, the domain had already been smoothed six times at generation, so the linear programming algorithm was intended to smooth any abrupt bathymetry changes in the wet cells created during island removal.

$$rx_0(h,e,e') = \left|\frac{h(e)-h(e')}{h(e)+h(e')}\right| \qquad \text{(Eq. 4.5)}$$

## 4.4 Forcing File Generation

### 4.4.1 Steady State Forcing

In the context of this study, steady state forcing refers to constant forcing where input variables remain unchanged at each boundary grid cell within the model for the length of a model run. Input files generated with constant values included the boundary forcing file, the atmospheric forcing file, and riverine input. The ocean is not in steady state, so time-invariant forcing does not present a realistic scenario. Also, this forcing, especially given the use of open boundary conditions does not offer a well-posed problem as steady state within the model domain may not be fully achieved. However, given the complexity of the model and the variability from each forcing file, a run using the simplest possible forcing helps to establish which changes can be attributed to island loss.

Qualitatively, the steady state runs were compared to time-varying forcing runs. Therefore, six steady state scenarios were run. For the control runs, the first two simulations used the existing model bathymetry and land mask. One had mean January forcing; the other utilized mean July forcing. Two runs removed West and East Ship Island under mean January and mean July forcing respectively. The final two runs removed Petit Bois Island and the western half of Dauphin Island under the two steady state scenarios.

Values from the CMA forcing file were used to calculate mean January and July conditions. Likewise, values from the interpolated NCOM file and riverine input file provided the data to generate average conditions.  The time variable within these files counts in days from a reference start date, January 1, 2014.  Consequently, the serial date equivalent of the reference date was added to each value, and the variable was converted to a date vector.  Logical indexing retained only January values by choosing 1 as the desired month respectively; averaging of values for each grid cell produced mean January conditions.  These values were duplicated along the time axis to produce variables with the same dimensions as the existing forcing files.  The time-invariant variables were written to new NetCDF files.  The same methodology was employed to produce a mean July file.  January and July were selected as the steady state conditions in order to have mid-winter and mid-summer represented.  The NCOM boundary and riverine input files underwent the same procedure.

### 4.4.2 Forcing Files for Island Removal Scenarios

Examination of the CONCORDE Meteorological Analysis (CMA) time series revealed meteorological conditions differed for over-island grid points compared to over-water grid points.  This effect was indistinguishable during wind events or times of heavy precipitation, but the fields displayed significant change during quiescent periods.  The magnitude of wind stress change was on the order of $10^{-4}$ $Nm^{-2}$.  As such, polygons were drawn around the removed island sections to capture the indices of island and near island grid cells that needed modification in conjunction with island removal (Figure 4.14).  Values within these polygons were mapped to the CMA grid and changed to NaN.  Linear interpolation of non-NaN grid points outside the polygons to grid points inside the polygons allowed estimation of CMA variables within the polygon for each time step.  Linear interpolation was chosen empirically since other interpolation schemes left some grid points with NaN values. The interpolation simulated over-water atmospheric conditions. Modified variable fields were then written to new CMA forcing files for the Ship Island and Petit Bois Island removal runs.

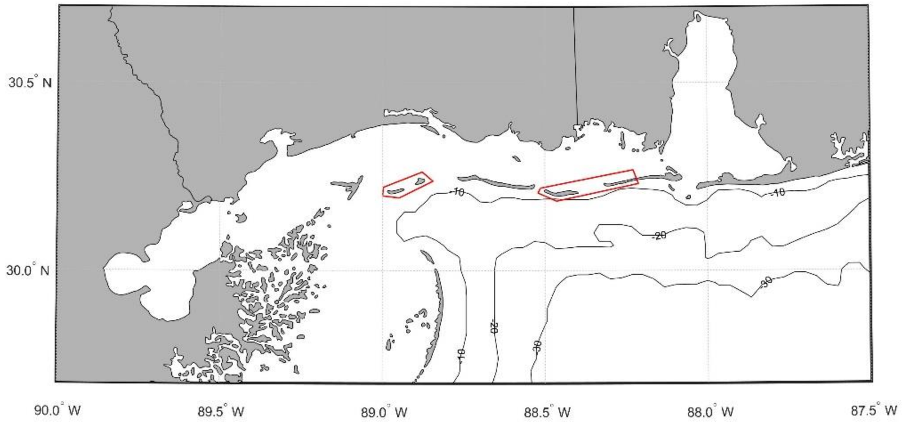

Figure 4.14 Regions modified for island removal scenarios

The red polygons indicate the regions of the ROMSmsb file modified for the Ship Island removal (left polygon) and the Petit Bois-western Dauphin Island removal. Modifications include land mask changes, bathymetric changes and smoothing, and atmospheric forcing file adjustments.

### 4.5 Output Analysis

One year model runs with time-invariant and time-variant forcing were completed for each island loss scenario to match the time length of the unmodified control files of the time varying and steady state runs. Output exists for the full year, but results presented in this chapter highlight January and July averages for time-variant and steady state forcing conditions. This choice helps highlight differences between mid-winter and mid-summer and also allows comparisons between the steady state and time varying runs.

Differences in the free surface, ζ, full water column volume transport, and vertically-integrated, depth-averaged momentum are used to showcase the response of the model domain to abrupt changes in the Mississippi-Alabama barrier island chain as well as to indicate differences between the two island removal scenarios. The terms free surface and sea surface height are used interchangeably in section 4.6. Free surface, ζ, refers specifically to time varying elevation above the geopotential surface.

After specifying the indices of the model grid corresponding to each pass in the Mississippi-Alabama barrier island chain, velocities at those indices were vertically and then spatially integrated to obtain volume transports. Average values for the u and v directions were calculated for January and July in the time varying runs. Cross sections for each island pass were also indexed, and Hovmöller plots were generated using a longitudinal transect across each existing island pass as well as a longitudinal transect over the removed islands in conjunction with the passes to the west and east of the removed islands. The cross sections served to elucidate shifts in flow throughout the water column as well as vertical salinity profile changes. Numerical integration was accomplished using the trapezoidal rule, and the stretching and transform functions described in section 4.2 were employed to retrieve depth changes between σ layers at each time step.

Flushing times for the Mississippi Sound were also calculated for each model run. A polygon-based index retrieved wet cell locations within the Mississippi Sound across all σ layers. The σ layers were then stretched and transformed to find depth intervals, and calculation of the Mississippi Sound volume was obtained for the control, Ship Island removal, and Petit Bois Island removal runs. Flushing time can be computed as a basin’s volume divided by its transports. For this study, the sum of the time-averaged transport at the 17 riverine locations that flowed into the Sound and the time-averaged transport through the 6 passes connecting the Sound to the Mississippi Bight provided the total transport.

(Eq. 4.6) and (Eq. 4.7) give the x and y components of the momentum balance equations under the Boussinesq approximation. Since steady state results and monthly averages are presented, the first term on the left hand side goes to zero. Section 4.7 examines changes in momentum as a balance to changes in the horizontal pressure gradient, so the relative importance of the advective momentum terms, the middle three terms on the left hand side, will be evaluated against the Coriolis term, final term on left hand side. Comparisons of the control and removal runs confirmed the remaining terms changes very little when islands are removed; differences are 1-3 orders of magnitude smaller than momentum changes.

$$\frac{\partial u}{\partial t} + u\frac{\partial u}{\partial x} + v\frac{\partial u}{\partial y} + w\frac{\partial u}{\partial z} - fv = -\frac{1}{\rho_*}\frac{\partial P'}{\partial x} + A_l \Delta_h u + A_v \frac{\partial^2 u}{\partial z^2} \qquad \text{(Eq. 4.6)}$$

$$\frac{\partial v}{\partial t} + u\frac{\partial v}{\partial x} + v\frac{\partial v}{\partial y} + w\frac{\partial v}{\partial z} + fu = -\frac{1}{\rho_*}\frac{\partial P'}{\partial y} + A_l \Delta_h v + A_v \frac{\partial^2 v}{\partial z^2} \qquad \text{(Eq. 4.7)}$$

## 4.6 Results

Before considering the results of the nine model runs, the three hypotheses that drove this study should be reviewed. First, magnitude changes to circulation were expected to be the largest in the vicinity of the removed islands. Second, observed changes were anticipated to be scenario specific. In other words, removing Petit Bois Island and western Dauphin Island should alter circulation differently than removing West and East Ship Island. Third, the Petit Bois Island removal was expected to produce larger magnitude and wider spread circulation changes than the removal of Ship Island. The three hypotheses resulted from intuitive reasoning. Petit Bois Island and Ship Island lie on opposite ends of the Mississippi Sound. As such, depths around the islands as well as current speeds and directions near the islands differ. Petit Bois Island has more subaerial land and sits close to Mobile Bay, which supplies a significant volume of freshwater to both the Mississippi Sound and Mississippi Bight. Ship Island is closer to Lake Borgne and the Saint Bernard Delta; the island exists in a shallower and lower energy environment. Given all these considerations, the two removal scenarios should produce distinctly different modifications to circulation in the Mississippi Sound and Bight.

Additionally, since the removal scenarios simulated island loss, the overall salinity of the Mississippi Sound was expected to increase. The barrier islands restrict exchange between the Mississippi Sound and Mississippi Bight. Island loss would open up 10-30 km of water exchange pathways. Freshwater could exit the Sound where the islands once were, and higher salinity water could likewise enter the Sound. Increased exchange would likely lead to increased salinity within the Mississippi Sound.

Initial conditions for the removal runs were set so island loss occurred on the first time step. From a visualization standpoint, the islands transformed instantly from subaerial land to subaqueous shoals, something that could eventually occur in other locations in the Gulf of Mexico in the future (Odezulu et al., 2018). This provided an abrupt geologic change to the model domain. Looking at momentum and transport time series, the Mississippi Sound and Bight took about one month to reach a new equilibrium. Any abrupt changes to the model require a period of adjustment. For the steady state runs, this meant at least part of the model domain reached steady state across all σ layers within 1-2 weeks. For the time varying runs, momentum and transport time series started exhibiting quasiperiodic behavior within a month of initialization. During the early time steps, time series mimicked a damped oscillation with amplitude decreasing with each period. Nevertheless, output from the first two months was not used in the analysis to avoid contaminating results with the model's early adjustments to island loss.

Two- and three-dimensional momentum, free surface, temperature, and salinity use a combination of clamped, closed, Chapman, and Flather boundary conditions (Flather, 1976; Chapman, 1985). To minimize modifications to ROMSmsb, the island removal runs used the same boundary conditions as the control runs. Velocity and free surface changes discussed later in this chapter reveal areas of unusually high magnitude changes in the southeast corner of the model, the southwest corner of the model, the eastern boundary, and near riverine source locations. While it is possible that island loss produces isolated changes to circulation in areas distant from the removed islands, the results are questionable. Chapman (1985) found clamped and closed conditions can result in free surface and momentum oddities near boundaries. The exact cause of the circulation changes near the boundaries is not known, but the copied boundary conditions from the control runs maybe a contributing factor.

(Table 4.1) and (Table 4.2) respectively give vertically-integrated transport differences of the removal runs minus the control runs. In the tables, transport is split between zonal, $T_u$, and meridional, $T_v$, components, and each set of values has a designator. SSPBIR indicates steady state Petit Bois Island removal differences; SSSIR denotes steady state Ship Island removal differences. TVPBIR and TVSIR represent the time varying differences for Petit Bois Island and Ship Island removals. (Table 4.1) gives January differences while (Table 4.2) gives July differences.

Results from the time-invariant and time-variant removal scenarios only partially confirmed the three hypotheses. Changes to current speed and direction, temperature, salinity, and transport did occur near the removed islands. However, removing Petit Bois Island and Ship Island yielded some qualitatively similar circulation changes. Also, circulation in portions of the Mississippi Bight responded more strongly to island loss than expected, and seasonality appeared to play a critical role in how circulation evolved with island loss. Specifically, well-stratified versus well-mixed waters made a difference as did the direction of the longshore current. Details are given in sections 4.6.1 and 4.6.2.

Table 4.1 January Transport Removal Minus Control Differences through Island Passes

| | Main | Petit Bois Island | Horn Island | Dog Keys | Ship Island | Cat Island |
|---|---|---|---|---|---|---|
| $T_u$ (SSPBIR) | 14 $m^3/s$ | -472 $m^3/s$ | -80 $m^3/s$ | -5 $m^3/s$ | -72 $m^3/s$ | 12 $m^3/s$ |
| $T_v$ (SSPBIR) | 25 $m^3/s$ | 248 $m^3/s$ | -162 $m^3/s$ | 9 $m^3/s$ | -5 $m^3/s$ | 2 $m^3/s$ |
| $T_u$ (SSSIR) | 0 $m^3/s$ | 8 $m^3/s$ | -1 $m^3/s$ | -73 $m^3/s$ | 206 $m^3/s$ | -1 $m^3/s$ |
| $T_v$ (SSSIR) | 0 $m^3/s$ | -5 $m^3/s$ | 4 $m^3/s$ | -42 $m^3/s$ | -89 $m^3/s$ | 4 $m^3/s$ |
| $T_u$ (TVPBIR) | -38 $m^3/s$ | -145 $m^3/s$ | 105 $m^3/s$ | 43 $m^3/s$ | 56 $m^3/s$ | 7 $m^3/s$ |
| $T_v$ (TVPBIR) | 41 $m^3/s$ | 345 $m^3/s$ | -148 $m^3/s$ | 14 $m^3/s$ | 27 $m^3/s$ | -5 $m^3/s$ |

Table 4.1 (continued)

| | | | | | | |
|---|---|---|---|---|---|---|
| $T_u$ (TVSIR) | 0 $m^3/s$ | -8 $m^3/s$ | -1 $m^3/s$ | -279 $m^3/s$ | 570 $m^3/s$ | -3 $m^3/s$ |
| $T_v$ (TVSIR) | -1 $m^3/s$ | 10 $m^3/s$ | 10 $m^3/s$ | 64 $m^3/s$ | 237 $m^3/s$ | -11 $m^3/s$ |

Table 4.2 July Transport Removal Minus Control Differences through Island Passes

| | Main | Petit Bois Island | Horn Island | Dog Keys | Ship Island | Cat Island |
|---|---|---|---|---|---|---|
| Tu (SSPBIR) | 28 $m^3/s$ | -142 $m^3/s$ | -1 $m^3/s$ | 23 $m^3/s$ | 16 $m^3/s$ | -2 $m^3/s$ |
| Tv (SSPBIR) | 57 $m^3/s$ | 701 $m^3/s$ | -60 $m^3/s$ | 16 $m^3/s$ | 20 $m^3/s$ | 4 $m^3/s$ |
| Tu (SSSIR) | 0 $m^3/s$ | -14 $m^3/s$ | 2 $m^3/s$ | 480 $m^3/s$ | 33 $m^3/s$ | 45 $m^3/s$ |
| Tv (SSSIR) | 1 $m^3/s$ | 16 $m^3/s$ | -27 $m^3/s$ | -173 $m^3/s$ | -441 $m^3/s$ | -20 $m^3/s$ |
| Tu (TVPBIR) | -12 $m^3/s$ | -98 $m^3/s$ | 118 $m^3/s$ | 61 $m^3/s$ | 31 $m^3/s$ | -2 $m^3/s$ |
| Tv (TVPBIR) | 113 $m^3/s$ | 796 $m^3/s$ | 136 $m^3/s$ | 53 $m^3/s$ | 22 $m^3/s$ | 2 $m^3/s$ |
| Tu (TVSIR) | -2 $m^3/s$ | 7 $m^3/s$ | 7 $m^3/s$ | 53 $m^3/s$ | 491 $m^3/s$ | 46 $m^3/s$ |
| Tv (TVSIR) | 4 $m^3/s$ | 12 $m^3/s$ | 10 $m^3/s$ | -104 $m^3/s$ | -154 $m^3/s$ | -24 $m^3/s$ |

### 4.6.1 January Run Results

Changes in circulation can best be measured with velocity and salinity. In terms of velocity, this includes surface and bottom monthly root-mean-square differences over the effective depths described in section 4.2.2. Changes in current fields give a direct look into how island loss modifies flow.  Likewise, vertically-integrated transport in the island passes indicates whether water volume exchange between the Mississippi Sound and Bight underwent non-negligible change.  Chapter II found temperatures to be fairly homogenous across the Mississippi Sound, so salinity gives a better representation on whether island loss permits more inflow of Mississippi Bight water into the Mississippi Sound.

In the Petit Bois Island removal under January steady state forcing conditions, bottom velocities over the removed western Dauphin Island rotated southward with magnitude changes of 2-3 cm/s.  Figure 4.15 shows differences for the January steady state Petit Bois Island removal bottom velocities minus bottom velocities in the January steady state control run.  Bottom velocities over the removed Petit Bois Island turned northeastward with speed changes of about 1 cm/s.  Additional shifts in bottom velocity occurred in the southeast and south-central Mississippi Bight as well as in the Chandeleur Sound.  In Figure 4.16, surface velocities differences pointed northward over the removed Petit Bois Island, northeastward in Petit Bois Island Pass, southeastward over the removed western Dauphin Island, and westward south of the two removed islands. Unlike with bottom velocities, regions throughout the Mississippi Bight experienced 1-5 cm/s surface current speed changes.  These modifications to circulations were concentrated in the southern Bight but appeared to extend southward from Petit Bois Island Pass and the removed islands.  Shifts in the direction of vertically-integrated transport, with magnitude changes exceeding $10^2$ $m^3/s$, was limited to Horn Island Pass and Petit Bois Island Pass.  Transport shifted southwestward in Horn Island Pass and northwestward in Petit Bois Island Pass.  Transport changes in the remaining passes had much smaller magnitudes.

Cross sections of salinity and currents in the passes as well as difference plots for the regions over the removed islands present small scale, 1-2 salinity change and <3 cm/s velocity change, alterations to exchange between the Mississippi Sound and Bight. While small, these alterations are still significant.  Salinity increased in the eastern Mississippi Sound with the removal of Petit Bois Island and western Dauphin Island under January steady state forcing.  In Figure 4.17, salinity increased by >1 from the surface to 3 m depths in Horn Island Pass.  Salinity likewise increased at the westernmost edge of Petit Bois Island Pass in the 2-3 m depth range, but salinity in the eastern half of the pass decreased by >1.  Flow into and out from the Mississippi Sound decreased by 1-3 cm/s in the existing passes, but island loss allowed flow over the removed islands down to 4 m depth.  This meant that although current speeds in the passes decreased relative to the control run, the number of exchange pathways increased.  Overall salinity increased by 0.3 across the entire Mississippi Sound, but salinity across all $\sigma$ layers immediately northward of the removed islands increased by 1-3.  Surrounding areas in the eastern Sound also saw increased salinity, but magnitudes of increase decreased with distance from the removed islands.

Removing West and East Ship Island under January steady state forcing conditions produced smaller magnitude and more localized changes to circulation than the Petit Bois Island removal run.  Bottom velocities rotated northeastward and speeds changed by about 4 cm/s over the removed West Ship Island as shown in Figure 4.18. Velocity changes also occurred by the Mississippi River bird foot delta and across the southern Mississippi Bight, but magnitude changes were less than 1 cm/s. As with the Petit Bois Island removal, higher magnitude surface velocity changes occurred in the vicinity of the removed islands, throughout the Chandeleur Sound, and across the southern Mississippi Bight, Figure 4.19. Surface velocities rotated southeast, with speed changes around 3 cm/s. Changes in the Chandeleur Sound and southern Bight ranged from 1-4 cm/s but lacked coherent directional change. As mentioned earlier, these near-boundary changes might be an artifact from using the boundary conditions of the control run. Similar to the Petit Bois Island removal, the Ship Island removal mostly affected transport in the passes on either side of the removed islands. Transport rotated east northeastward through Ship Island Pass and southwestward in Dog Keys Pass.

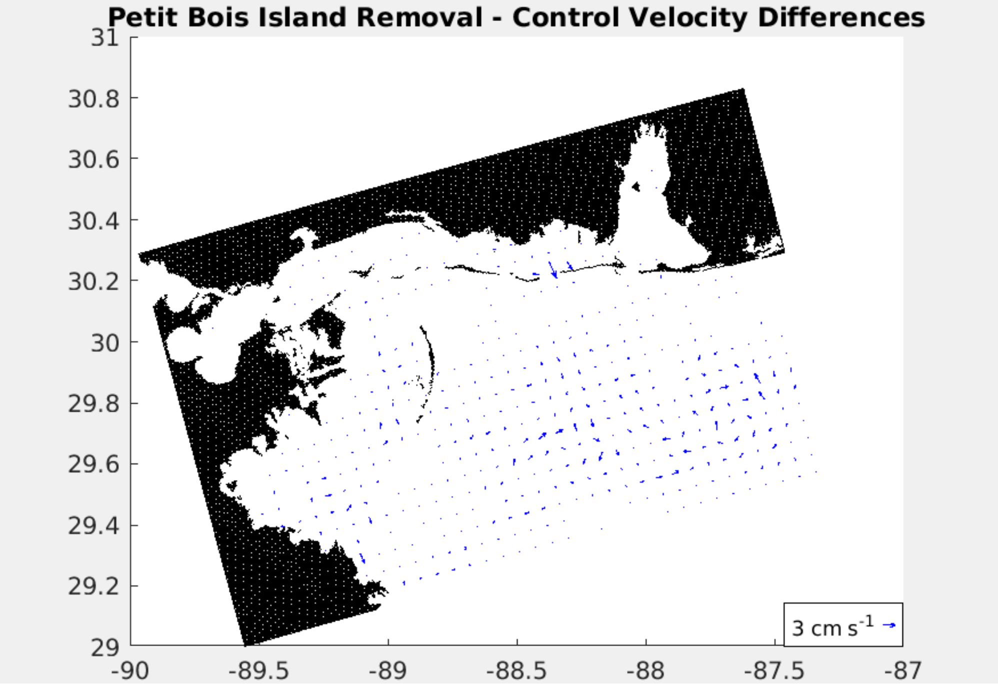

Figure 4.15 Bottom velocity differences of the January steady state Petit Bois Island removal run minus the control run

Velocities represent vector averages of the bottom 1.5 m across the model domain, and the velocity grid has been subsampled at 1/16 resolution to provide better visualization.

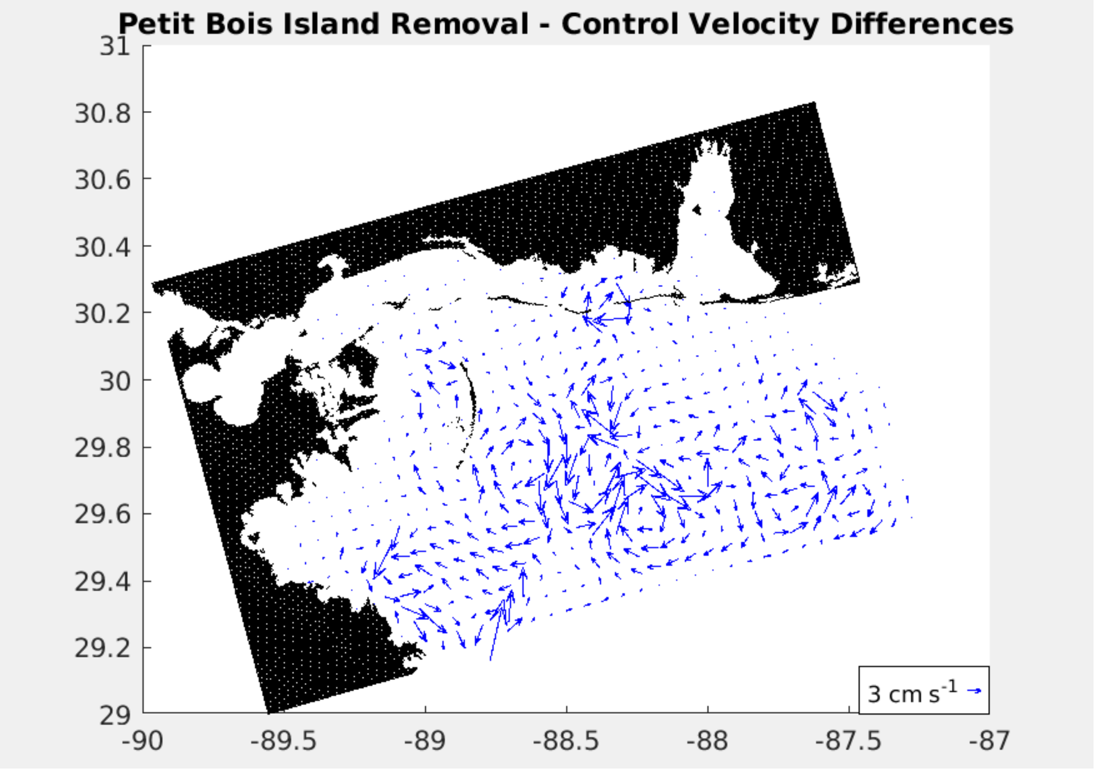

Figure 4.16 Surface velocity differences of the January steady state Petit Bois Island removal run minus the control run

Velocities represent vector averages of the surface 2.57 m across the model domain.  As with Figure 4.15, velocities at every 16th grid have been selectively plotted to better visualize flow patterns.

Island pass cross sections echo velocity and transport results; the January steady state Ship Island removal perturbed circulation less the Petit Bois Island removal. Salinity decreased in the 2-3 m depth range by <0.5 but increased in the 4-6 m depth range in the eastern edge of the pass by <0.5 (Figure 4.20).  Along the western edge of Dog Keys Pass, salinity increased up to 0.5 in the 2-3 m depth range and decreased by <0.2 at 4 m.  The remaining passes remained relatively unchanged.  As with the Petit Bois Island removal, velocity magnitudes saw an overall decrease in the existing passes, but island removal meant exchange occurred in the top 4 m of the water column where East and West Ship Island used to be.  This had the effect of increasing exchange between the Mississippi Sound and Bight, and salinity in the back-barrier region immediately north of the removed islands increased. Mississippi Sound salinity increased by 0.02, but the western Sound had locally higher salinity increases.

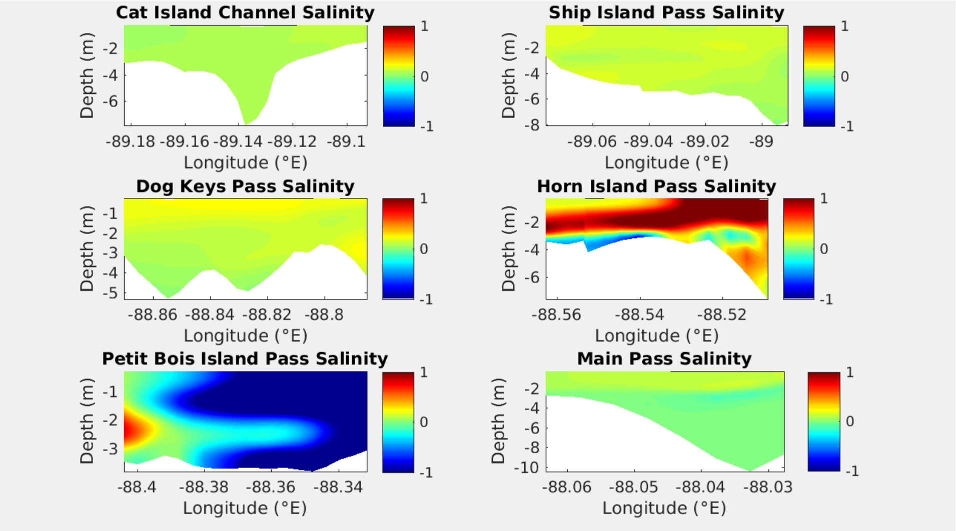

Figure 4.17 Salinity differences in the island passes for the January steady state Petit Bois Island removal run minus the control run

Across-pass grid points were indexed to extract salinity across all depths. Removal minus control salinity differences were calculated at each time step; the monthly mean of those differences is plotted. Red colors mean the removal run has higher salinity; blue means the control run salinity was higher.

In the January portion of the time varying forcing conditions for the Petit Bois Island removal, velocity changes ranging 1-4 cm/s were confined to the region around the removed islands. In Figure 4.21, bottom velocities shifted northwest over the removed Petit Bois Island and northeast to north over the removed western Dauphin Island. Velocities north of the removed islands shifted westward. At the surface in Figure 4.22, velocities rotated towards the west and southwest over the removed Petit Bois Island and southwest over the removed western Dauphin Island. Velocities changes pointed northward into Petit Bois Island Pass and mostly to the west north of the removed islands though flow immediately north of Petit Bois Island Pass turned to the east and northeast.

Transport changes greater than $10^2$ $m^3/s$ can be seen in Horn Island Pass where transport shifted to the southeast and in Petit Bois Island Pass where vertically-integrated transport differences pointed northwest.

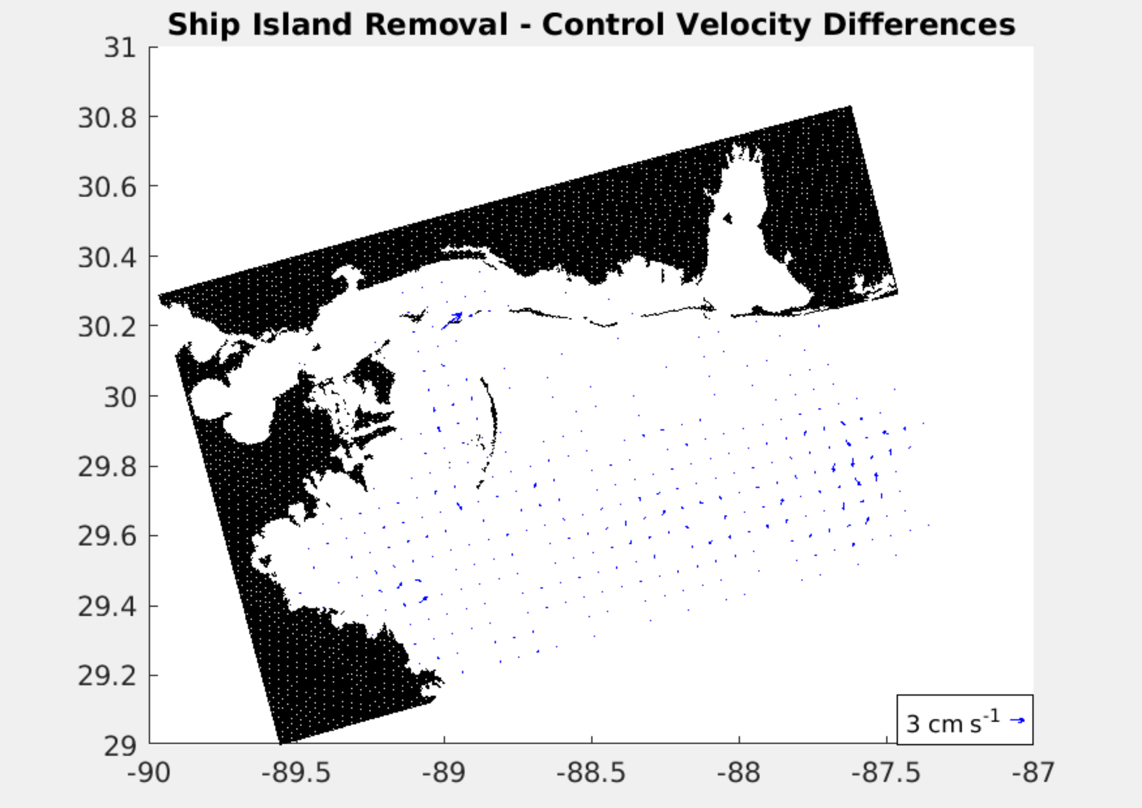

Figure 4.18 Bottom velocity differences of the January steady state Ship Island removal run minus the control run

Velocities represent vector averages of the bottom 1.5 m across the model domain.

Island pass cross sections and surface Hovmöller plots showed increased inflow pathways into the Mississippi Sound, but notable sections of the island chain still allowed periods of outflow during January. In Figure 4.23, the western half of Horn Island Pass saw freshening up to 0.5 in the top 2 m of water while the eastern edge of the pass increased in salinity by 0.8 down to 4 m. The top 2 m of Petit Bois Island Pass increased in salinity by >1 while the 2-3 m depth range increased by 0.5. The top 2 m of Main Pass decreased in salinity by as much as 0.5. Current speeds through existing island passes on either side of the removed island decreased in magnitude by a few cm/s, but island loss enabled flow over the subaqueous shoals. Figures 4.24 and 4.25 give two weeks of surface currents and surface salinity, from the Petit Bois Island removal run, for the stretch between Sand Island (West Petit Bois Island) and the eastern half of Dauphin Island. This covers the region where Petit Bois Island and the western half of Dauphin Island had been removed. Though currents alternated between inflow into the Sound and outflow from the Sound, surface water in the widened pass tended more frequently towards outflow while the eastern pass experienced diurnal reversals in current direction. With the widened pass, salinities increased.

During the January portion of the time varying Ship Island removal, bottom velocity differences turned southwest north of the removed West Ship Island, and velocity magnitudes changed by up to 4 cm/s, Figure 4.26. At the surface in Figure 4.27, velocity differences pointed southwest, with magnitude changes of 5 cm/s, over the removed West Ship Island and southeast to northeast south of the removed islands. Velocity changes elsewhere in the domain had magnitudes less than 1 cm/s. Vertically-integrated transport changes over $10^2$ $m^3/s$ included an east northeast shift in Ship Island Pass and a west northwest turn in Dog Keys Pass.

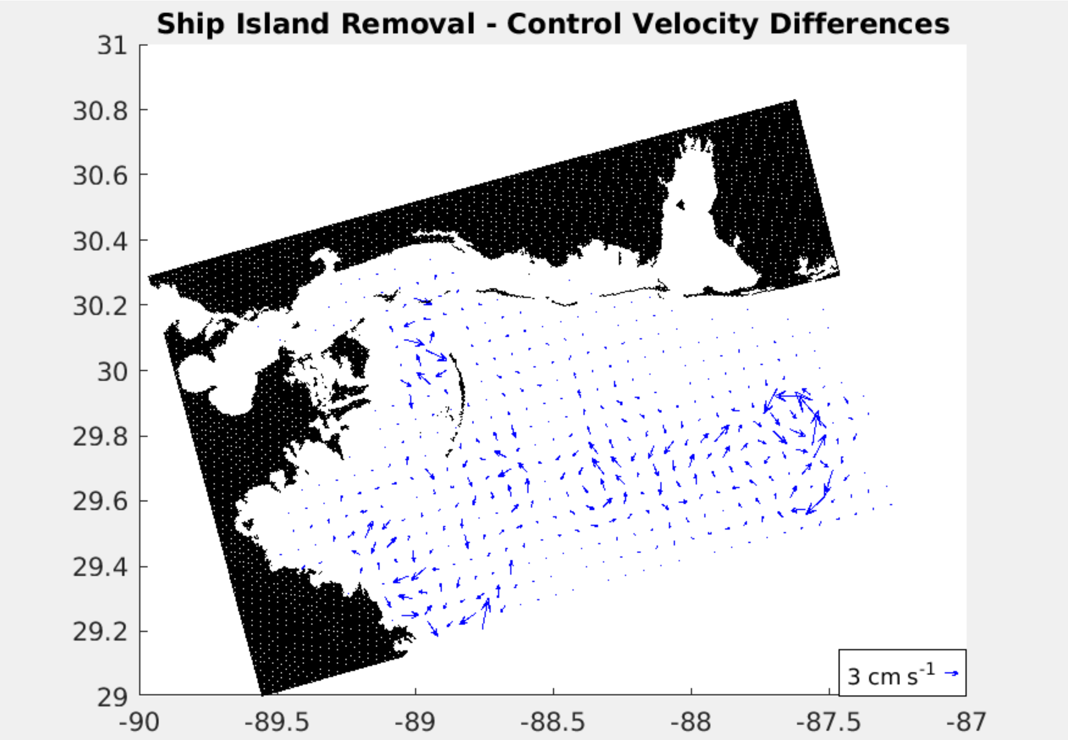

Figure 4.19 Surface velocity differences of the January steady state Ship Island removal run minus the control run

Velocities represent vector averages of the surface 2.57 m across the model domain.

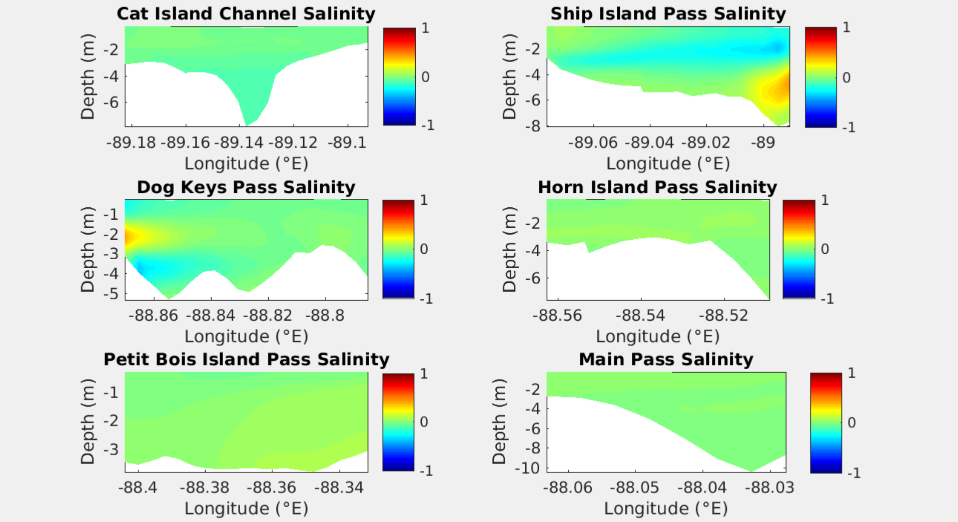

Figure 4.20 Salinity differences in the island passes for the January steady state Ship Island removal run minus the control run

Same design as Figure 4.17.

Mississippi Sound salinity increased by 0.1, but the eastern Sound north of the removed islands increased by 1-3. The remainder of the eastern Sound also saw a net increase in salinity, but magnitudes of change dropped sharply away from the removed islands. Saltwater intrusion occurred largely below the surface in the top few meters.

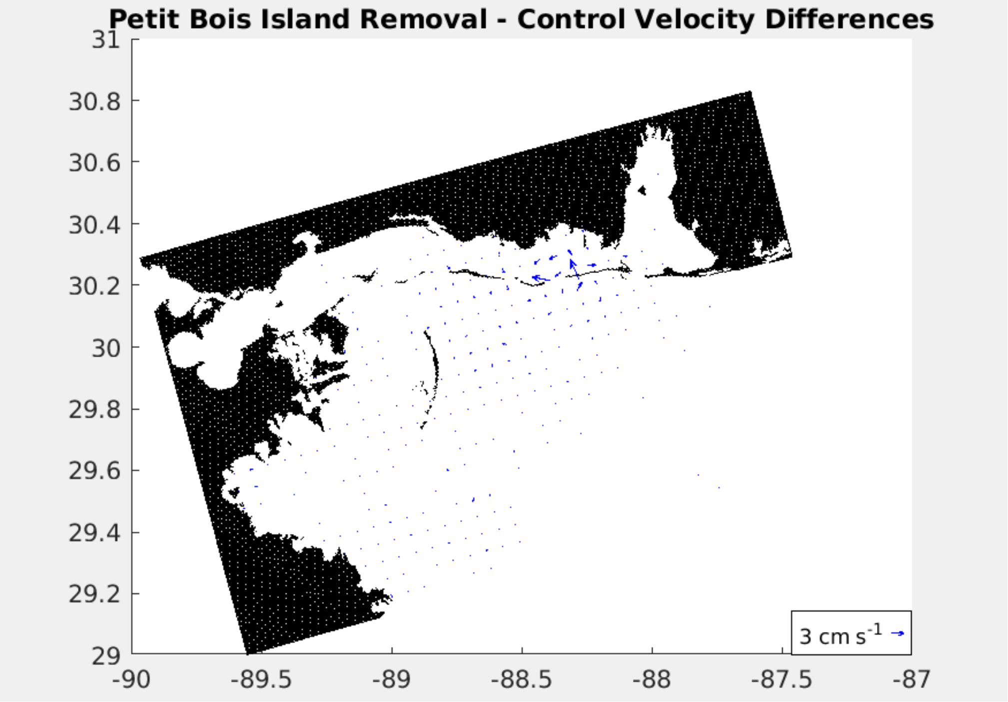

Figure 4.21 Bottom velocity differences of the time varying Petit Bois Island removal run minus the control run in January

Velocities represent vector averages of the bottom 1.5 m across the model domain.

Salinity decreased at the surface in Ship Island Pass but increased in Dog Keys Pass. In Figure 4.28, salinity changes in these two passes approached -1 and 1 respectively in January, but the other passes saw overall increases in salinity of <0.2. Looking across all depths, salinity decreased by about 0.3 in Ship Island Pass but increased by the same amount along the western edge of Dog Keys Pass. The other passes saw minimal changes of <0.1. Flow through the passes changed by <3 cm/s with velocity becoming more positive along the eastern edge of Ship Island Pass and more negative on the western edge of Dog Keys Pass. Disruption of the gravitational current corresponded to island loss since a new and wider pass was opened by transforming the island into a subaqueous shoal. Island removal also had the effect of allowing inflow pathways for higher salinity water where the islands once were. Figures 4.29 and 4.30 show Hovmöller plots for the first 2 weeks of January for surface currents and surface salinity from Cat Island to Horn Island; this includes the area where East and West Ship Island were removed. Currents alternate between northward into the Sound and southward out of the Sound, but the dominant direction at the surface is to the south. Velocities are lower than in the control run, but exchange happens across where the islands used to be. Salinity increased overall.

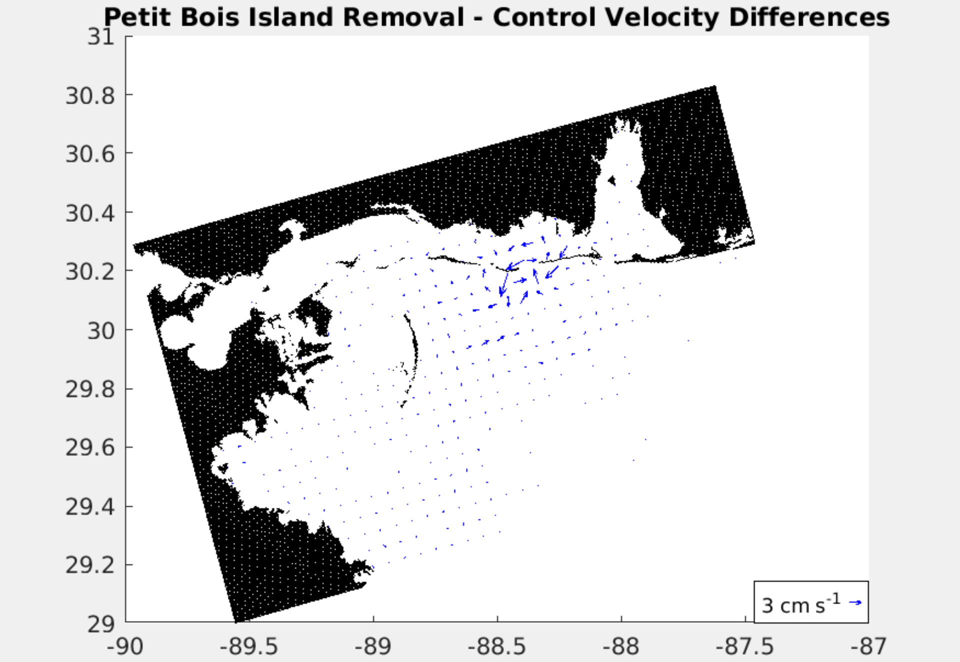

Figure 4.22 Surface velocity differences of the time varying Petit Bois Island removal run minus the control run in January

Velocities represent vector averages of the surface 2.57 m across the model domain.

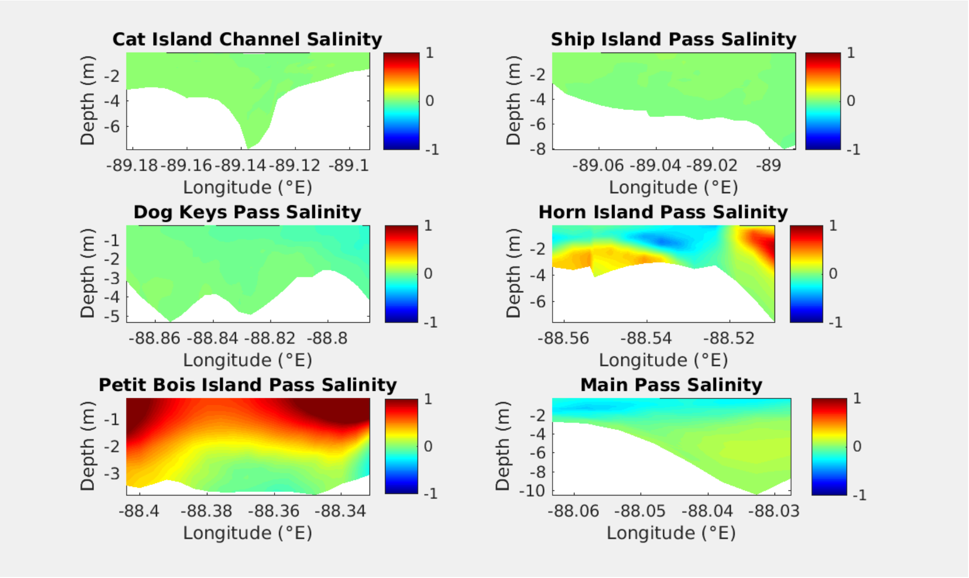

Figure 4.23 Salinity differences in the island passes for the January portion of the time varying Petit Bois Island removal run minus the control run

Same design as Figure 4.17.

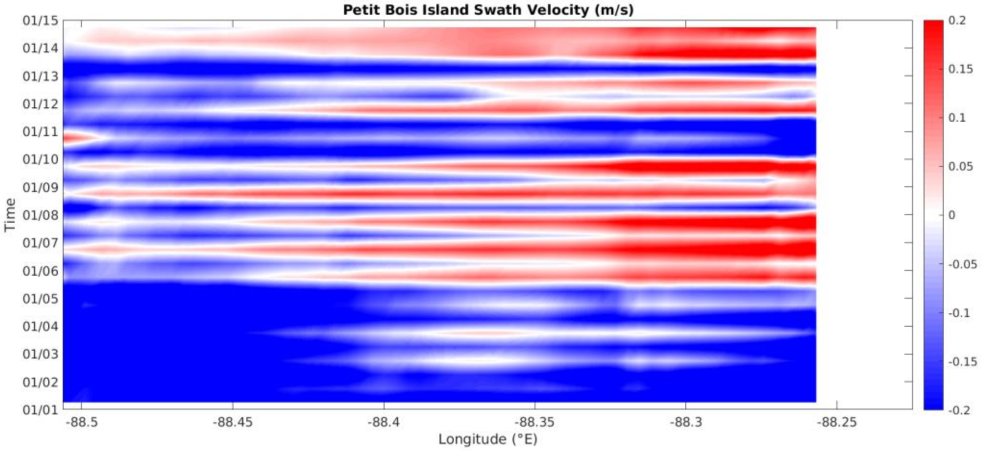

Figure 4.24 Surface meridional velocity Hovmöller diagram across the removed Petit Bois Island-western Dauphin Island complex for the January portion of the Petit Bois Island removal run

Horn Island Pass and Petit Bois Island Pass are included in the transect. Red denotes onshore flow; blue is offshore flow. For visual clarity, only the first two weeks of January are shown. Eastern Petit Bois Island remains as part of the land mask.

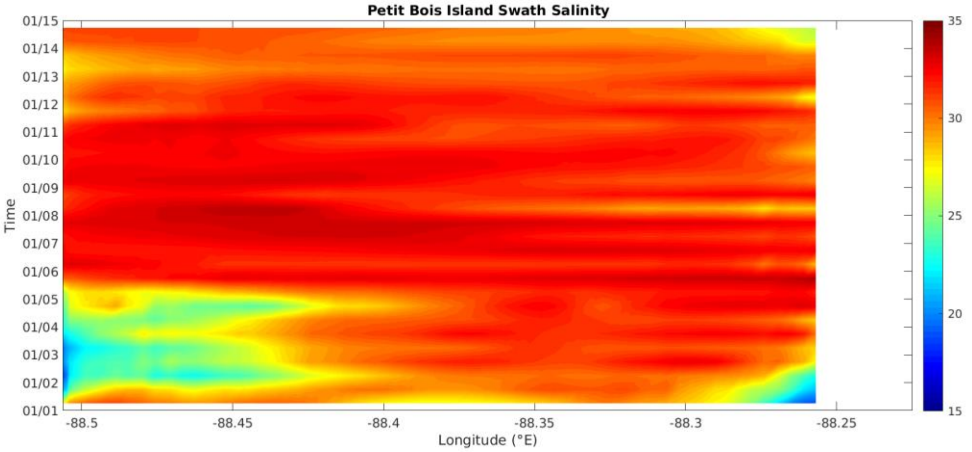

Figure 4.25 Surface salinity Hovmöller diagram across the removed Petit Bois Island-western Dauphin Island complex for the January portion of the Petit Bois Island removal run

Design follows Figure 4.24.

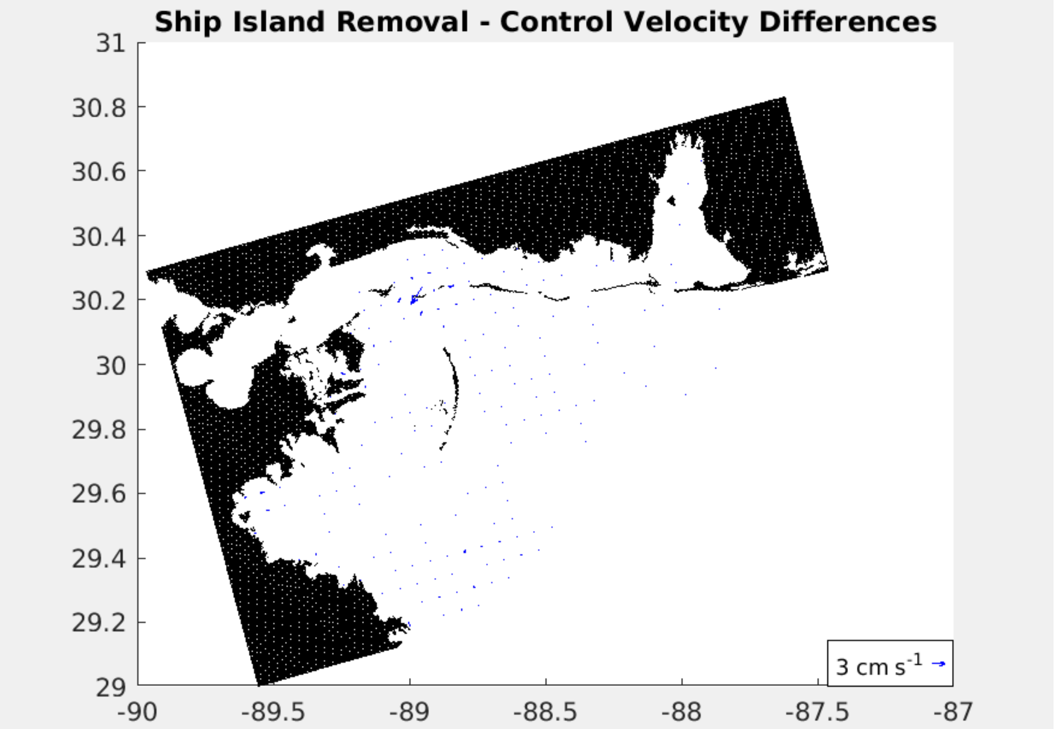

Figure 4.26 Bottom velocity differences of the time varying Ship Island removal run minus the control run in January

Velocities represent vector averages of the bottom 1.5 m across the model domain.

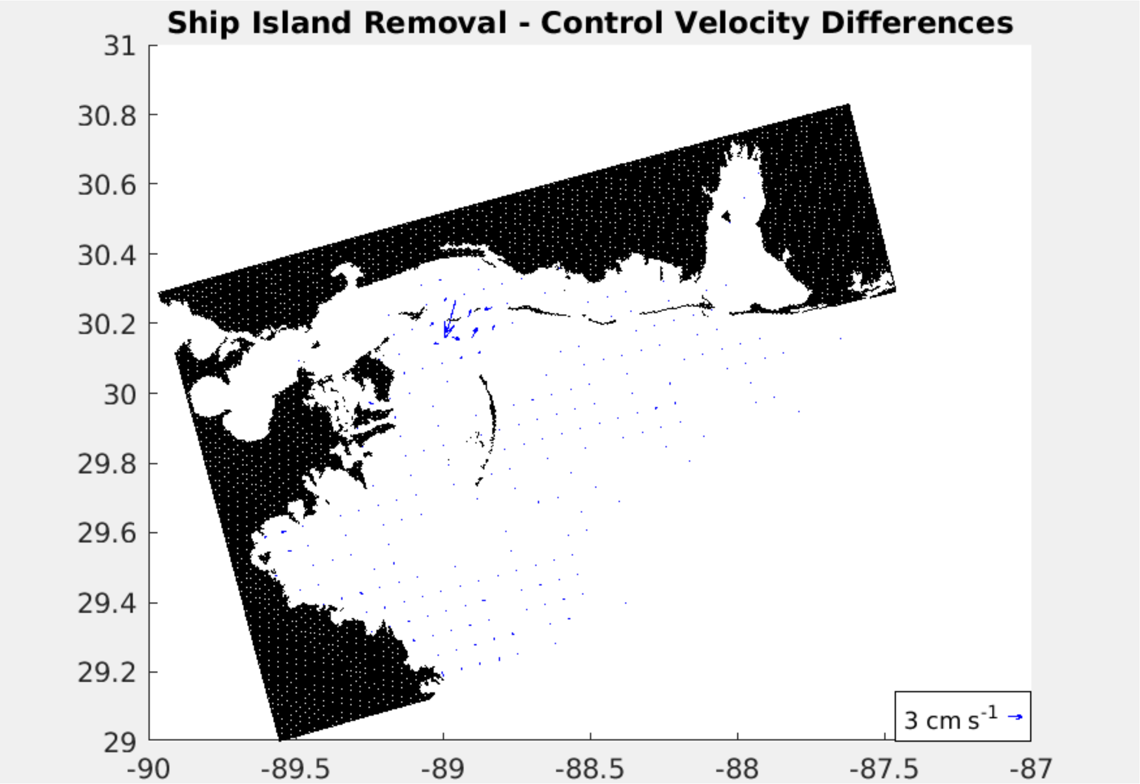

Figure 4.27 Surface velocity differences of the time varying Ship Island removal run minus the control run in January

Velocities represent vector averages of the surface 2.57 m across the model domain.

As with the other January runs, Mississippi Sound salinity increased when West and East Ship Island were removed, but higher salinity waters were mostly confined to the western Sound near the removed islands. The total salinity increase was 0.05, but near island salinity changes exceeded 2 with a sharp drop off with distance from the islands.

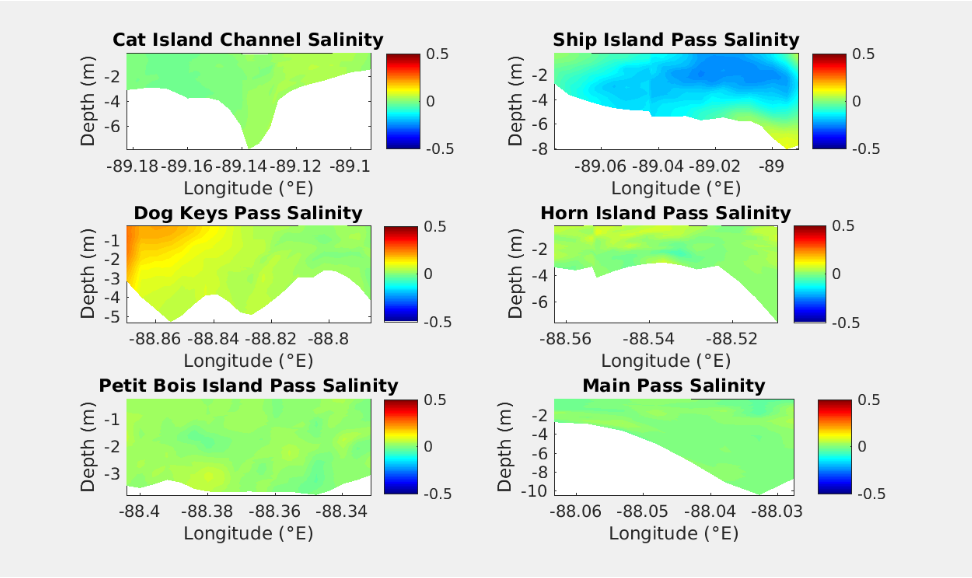

Figure 4.28 Salinity differences in the island passes for the January portion of the time varying Ship Island removal run minus the control run

Same design as Figure 4.17.

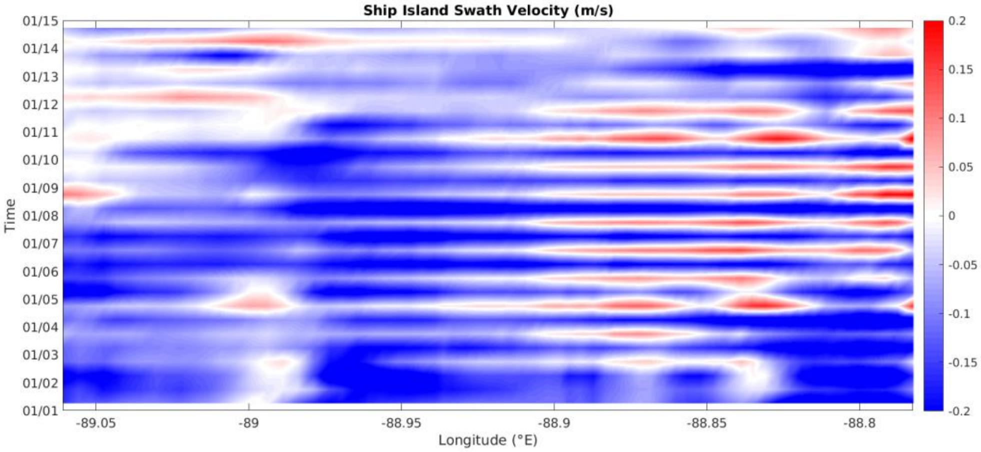

Figure 4.29 Surface meridional velocity Hovmöller diagram across the removed West Ship Island-East Ship Island complex for the January portion of the Ship Island removal run

Ship Island Pass, the gap between West and East Ship Island, and Dog Keys Pass are included in the transect. Red denotes onshore flow; blue is offshore flow. For visual clarity, only the first two weeks of January are shown.

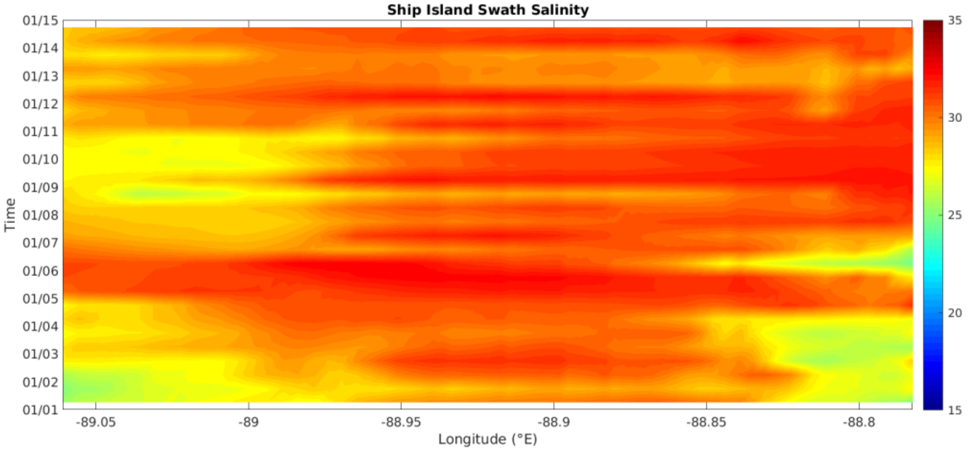

Figure 4.30 Surface salinity Hovmöller diagram across the removed West Ship Island-East Ship Island complex for the January portion of the Ship Island removal run

Same design as Figure 4.29.

Surface velocity changes were more confined to the region near the removed barrier islands in the time varying runs. The northeast trade winds dominate the winter months, so the January average steady state atmospheric file had strong and unchanging northeasterly winds. Some of the high magnitude surface velocity changes observed in the steady state removal runs in the southern Mississippi Bight may have been driven by persistent winds. With constant forcing, wind speed and direction never change, so time-averaged results will not show the smaller magnitude changes present when sub-daily, daily, and weekly shifts in wind velocities are present.

### 4.6.2 July Run Results

In the Petit Bois Island removal run using July steady state forcing, bottom current differences point northeast, with magnitude changes of 1 cm/s, and southeast, with magnitude changes of 2 cm/s, north of the removed western Dauphin Island. Velocity magnitudes change by 2 cm/s and point west northwest through Pass Aux Herons, Figure 4.31. In Figure 4.32, surface current speeds change about 1 cm/s and point southwest over the removed Petit Bois Island. Speeds change by 1 cm/s through Petit Bois Island Pass, and directions shift to the northeast. Velocity directional changes point southwest through the removed western Dauphin Island with speed changes falling between 3 cm/s and 4 cm/s. The longshore current south of western Dauphin Island shifted westward, with a magnitude adjustment of 5 cm/s. Additionally, current speeds in a cyclonic feature in the southeast Mississippi Bight changed by 1-5 cm/s. As with some of the January runs, circulation changes near the boundaries may not be attributable to island loss. In terms of vertically-integrated transport, transport shifted north northwest through Petit Bois Island Pass. Other pass transport changes had smaller magnitudes.

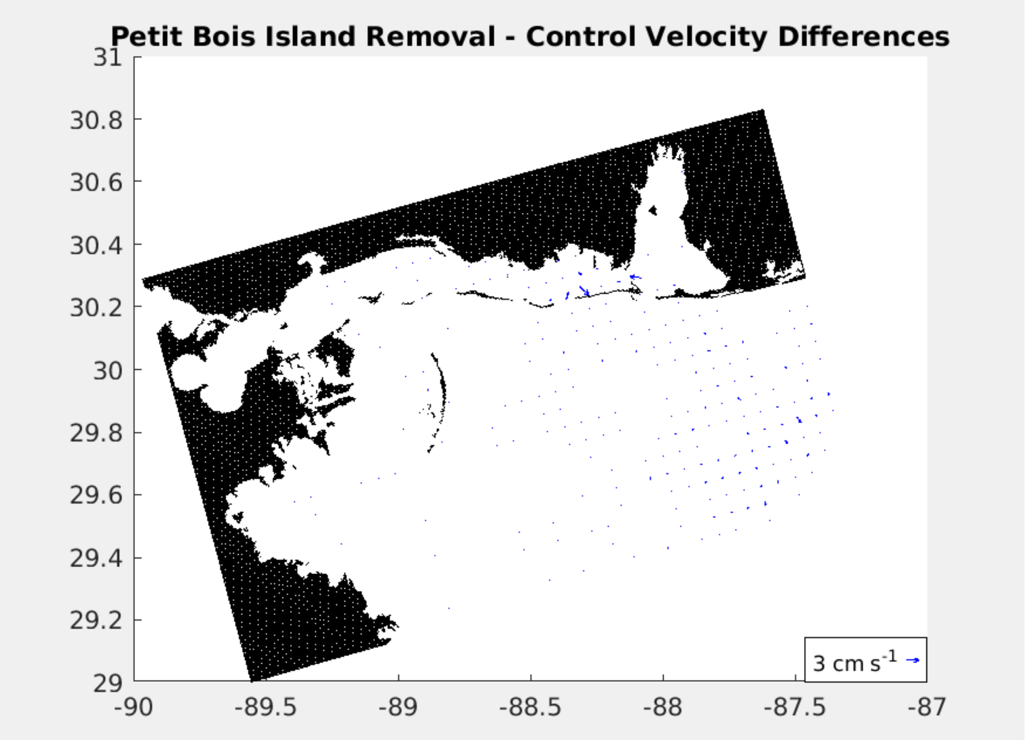

Figure 4.31 Bottom velocity differences of the July steady state Petit Bois Island removal run minus the control run

Velocities represent vector averages of the bottom 1.5 m across the model domain.

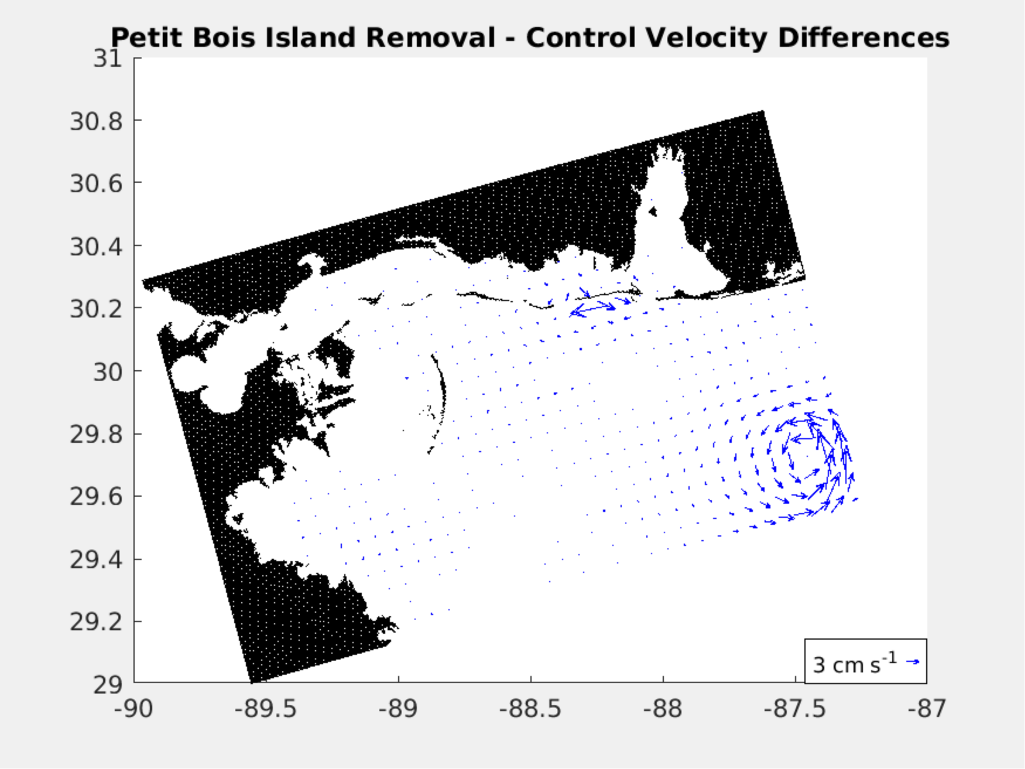

Figure 4.32 Surface velocity differences of the July steady state Petit Bois Island removal run minus the control run

Velocities represent vector averages of the surface 2.57 m across the model domain.

Salinity increased by more than 0.5 at all depths in Petit Bois Island Pass and increased by >1 in the bottom meter at 88.36°W and 88.4°W. The easternmost edge of Horn Island Pass also saw up to a 0.5 increase in salinity in the 2-5 m depth range (Figure 4.33). A slight, <0.3, increase in salinity could be seen in the 2-3 m depth range of Main Pass. Inflow through Horn Island Pass weakened by 4 cm/s at 4-6 m depths while average outflow weakened in Petit Bois Island Pass by several cm/s. Akin to the January steady state results, flow in the passes on either side of the removed islands weakened, but new flow enabled by the absence of the island's subaerial land caused a net inflow of

Mississippi Bight water into the Sound. Salinity in the Sound increased by 0.2, but higher increases were concentrated in the eastern Sound north of the removed islands.

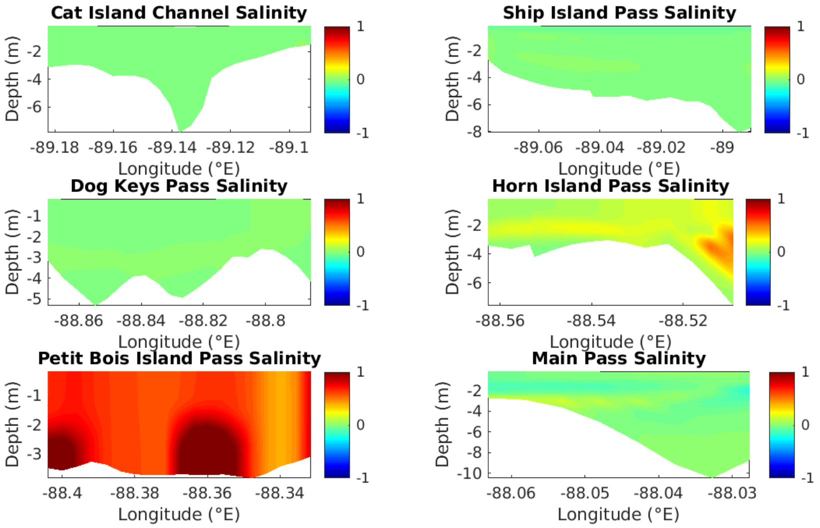

Figure 4.33 Salinity differences in the island passes for the July steady state Petit Bois Island removal run minus the control run

Same design as Figure 4.17.

The July steady state Ship Island removal mostly altered bottom currents in the vicinity of the removed islands. In Figure 4.34, bottom velocity changes pointed northeast, with speed changes of 5 cm/s, over the removed West Ship Island and northeast over the removed East Ship Island with velocity magnitudes changing by 2 cm/s. Likewise, most of the larger magnitude surface velocity changes occurred near the removed islands. With magnitude changes of 9 cm/s, a westward shift in surface velocity appeared over both components of the removed Ship Island, Figure 4.35. Current differences south of the Horn Island and the removed Ship Island have a fan pattern pointing south to southwest to west to northwest; speeds change by 1-2 cm/s. Transport changes through the island passes exceeding $10^2$ $m^3/s$ included a south southeast shift in Ship Island Pass and east southeast shift in Dog Keys Pass.

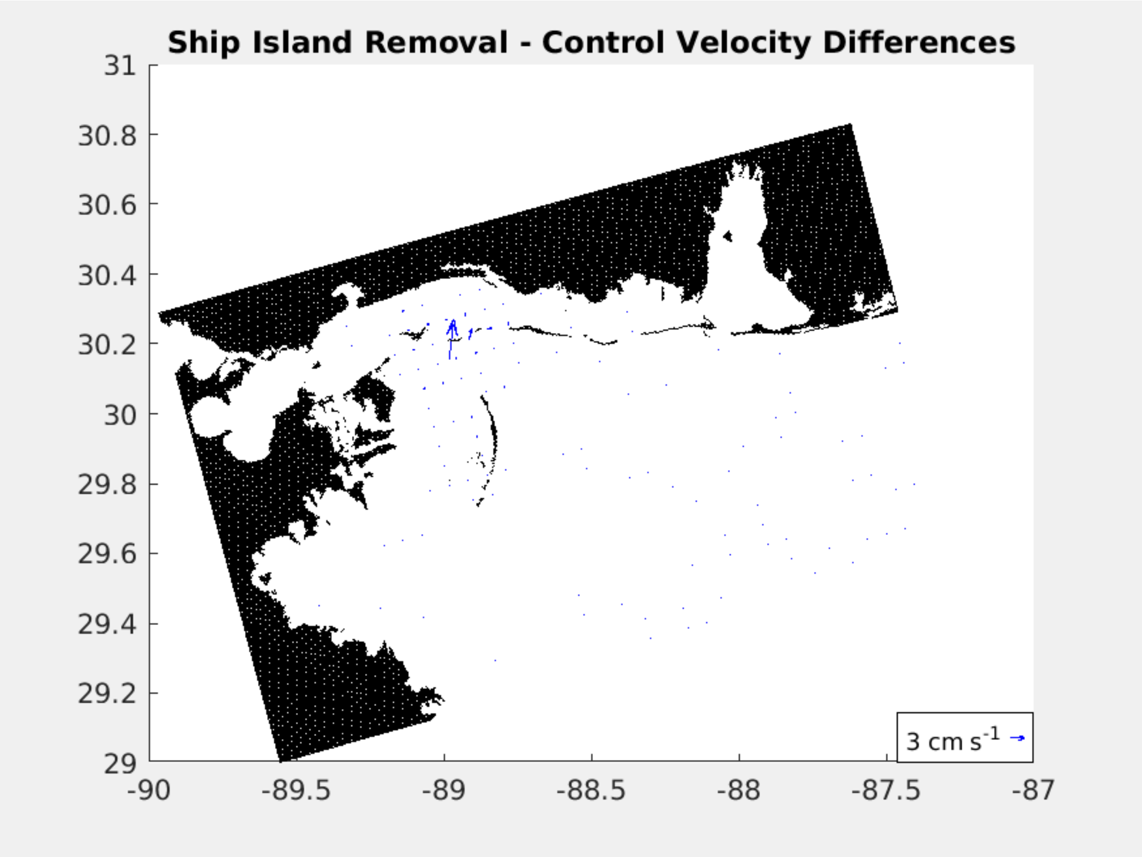

Figure 4.34 Bottom velocity differences of the July steady state Ship Island removal run minus the control run

Velocities represent vector averages of the bottom 1.5 m across the model domain.

Salinity on the eastern edge of Ship Island Pass increased by up to 1 in the 1-3 m depth range but decreased by the same amount at 4-6 m depths. In Figure 4.36, Dog Keys Pass freshened by 0.8 in the 2-4 m depth range. Salinity in the other passes remained mostly unchanged. Inflow through Ship Island Pass weakened by 5 cm/s in the mid-water column while outflow strengthened at 3 m depths by 1-2 cm/s. In keeping with the other removal runs, salinity increased across the Mississippi Sound by 0.07. Salinity increases disproportionately affected the western Sound north of the removed islands. The key change lay in the introduction of new wet cells where West and East

Ship Island were once located; this allowed higher salinity water to build up in the western Sound.

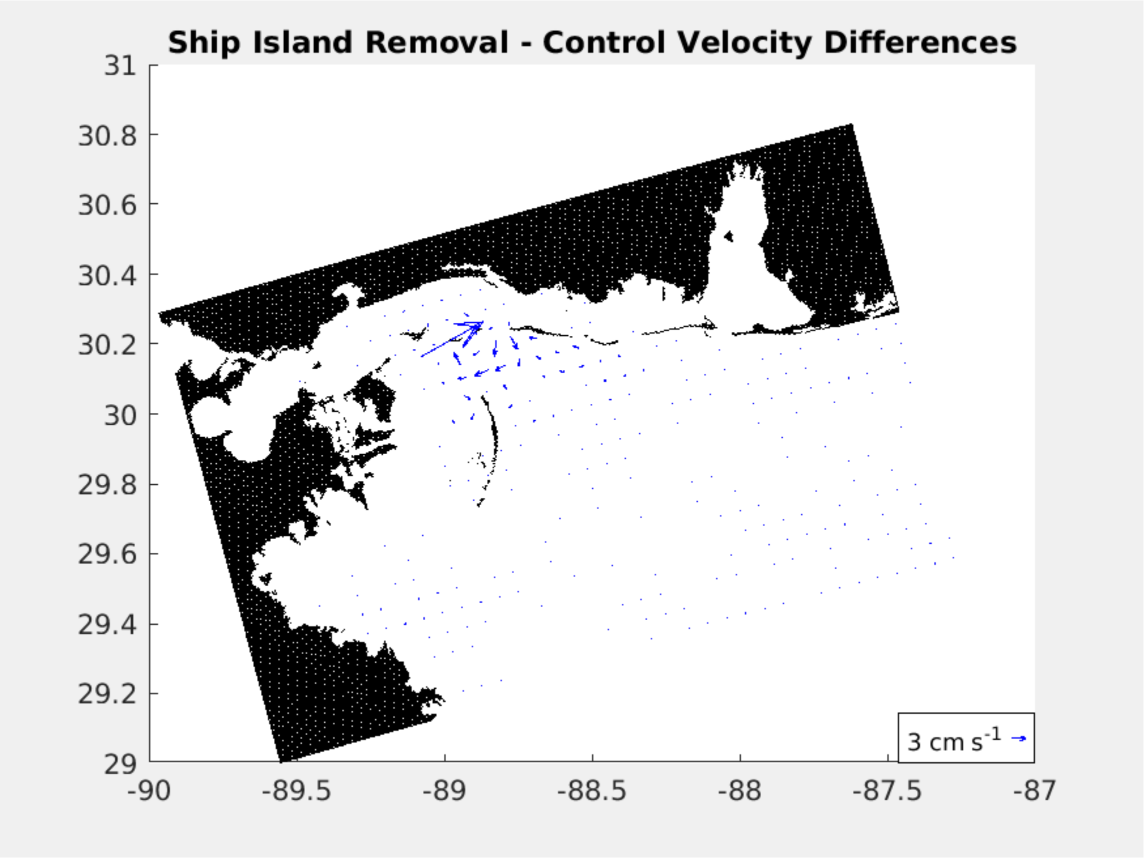

Figure 4.35 Surface velocity differences of the July steady state Ship Island removal run minus the control run

Velocities represent vector averages of the surface 2.57 m across the model domain.

Only minor speed and directional changes can be seen in the July portion of the Petit Bois Island removal time varying run. Shown in Figure 4.37, magnitude changes of 1 cm/s or less marked a northwest shift in current direction over the removed Petit Bois Island and southeast over the removed western Dauphin Island. At the surface, current differences include a speed change of 4 cm/s and a directional shift to the southeast and southwest over the removed western Dauphin Island, a 3-5 cm/s magnitude change and a rotation to the northwest and northeast in Petit Bois Island Pass, and a 2 cm/s speed change with a shift to the southwest and southeast over the removed Petit Bois Island, Figure 4.38. Additionally, current differences pointed to the east northeast toward the western edge of the removed Petit Bois Island. Speed changes elsewhere had magnitudes less than 1 cm/s. Vertically-integrated transport changes included a northeast shift in Horn Island Pass, a northwest rotation in Petit Bois Island Pass, and a northwest shift in Main Pass.

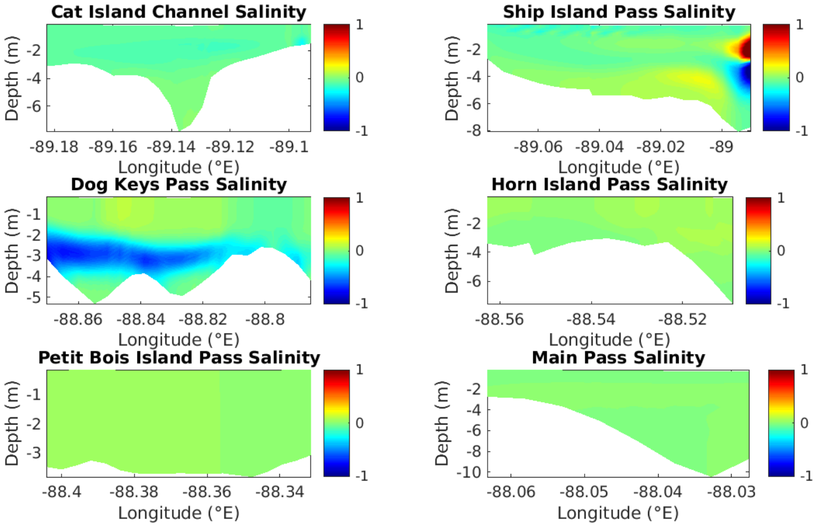

Figure 4.36 Salinity differences in the island passes for the July steady state Ship Island removal run minus the control run

Same design as Figure 4.17.

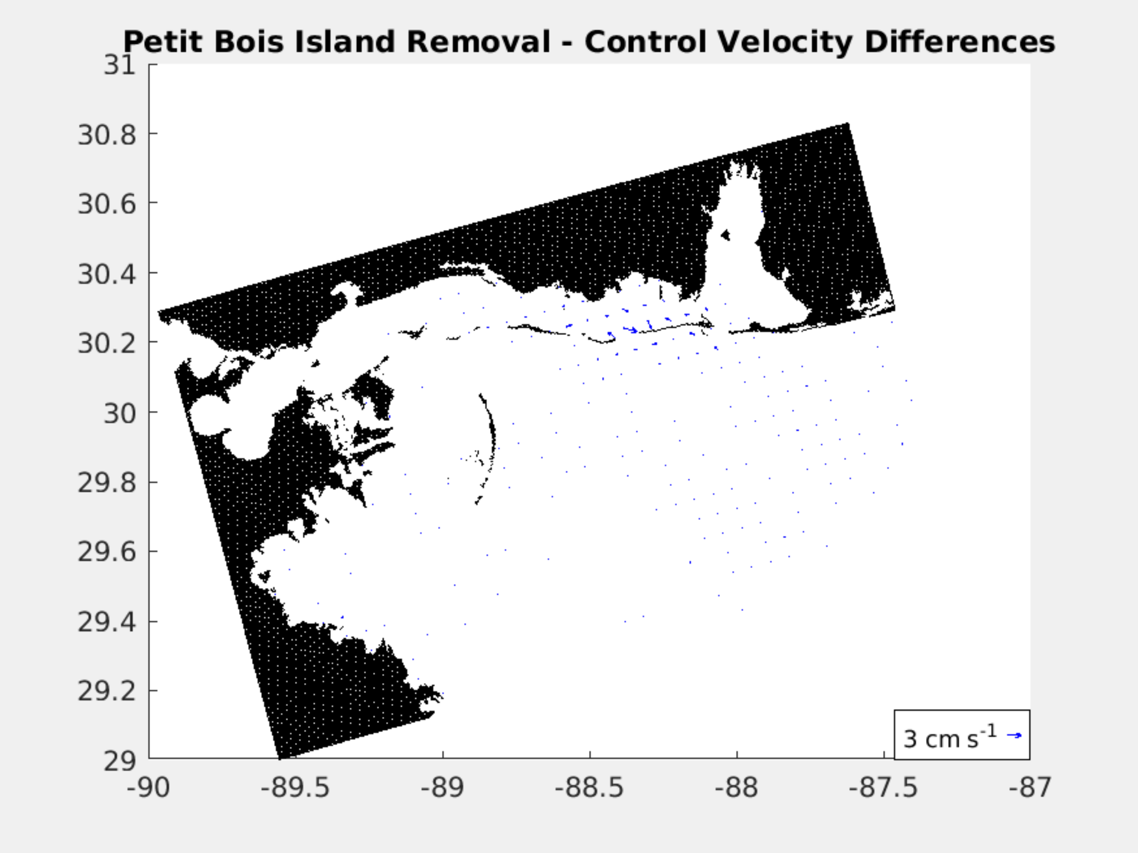

Figure 4.37 Bottom velocity differences of the time varying Petit Bois Island removal run minus the control run in July

Velocities represent vector averages of the bottom 1.5 m across the model domain.

Salinity increased by about 0.7 in the top 2 meters of the western side of Horn Island Pass and throughout the water column up to the top meter on the eastern side of the pass. By contrast, salinity decreased by up to 0.8 on the eastern side of Petit Bois Island Pass as seen in Figure 4.39. In the top half meter on the western side of the pass, salinity increased by as much as 0.5. Near bottom inflow in Horn Island Pass increased by 4 cm/s while outflow in Petit Bois Island Pass weakened by more than 5 cm/s. Salinity across the Sound increased by 0.1, but salinity increased in the eastern Sound near the removed islands by more than 2. Removing Petit Bois Island and western

Dauphin Island allowed tidal exchange across the remnant shoals of the islands. Diurnal cycling of surface inflow and outflow was present in the Hovmöller diagram in Figure 4.40, but island loss ultimately led to a net inflow of Mississippi Bight water at the surface. Subsurface inflow increased as well over the widened pass. Increases in salinity in the Sound accompanied the new dynamic (Figure 4.41).

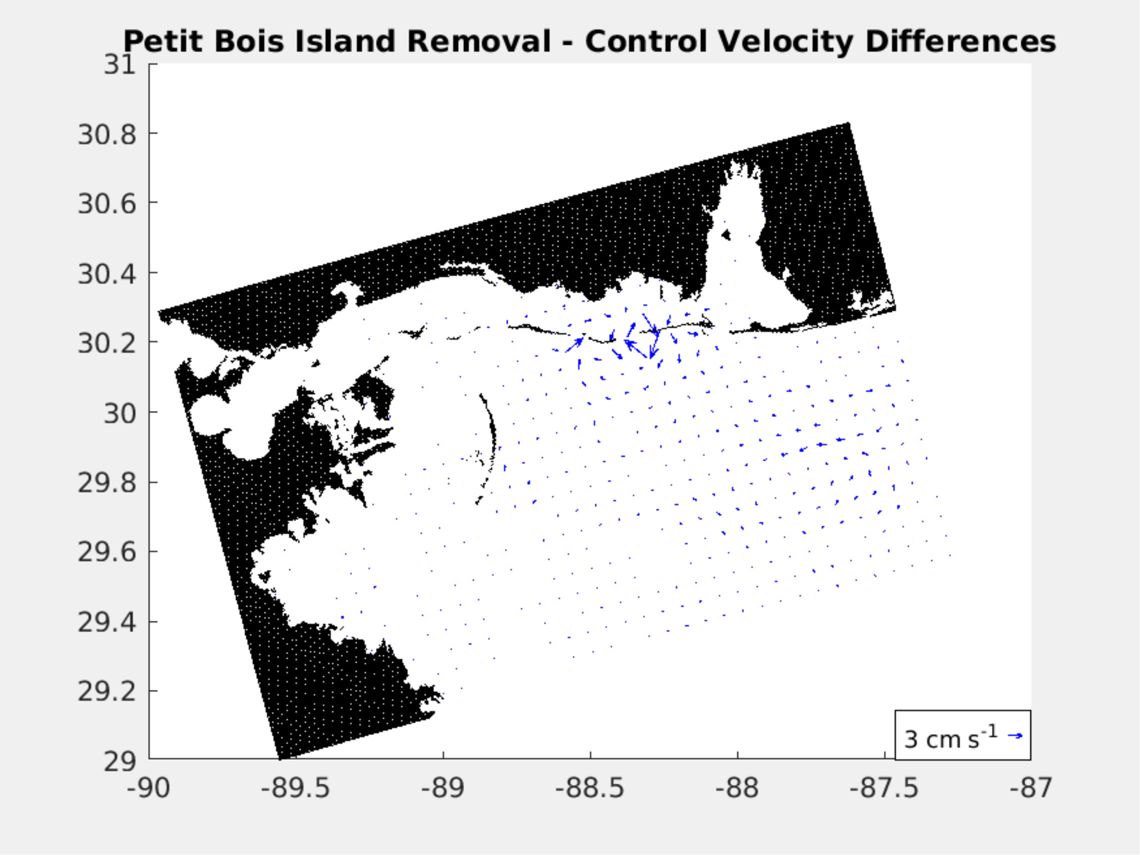

Figure 4.38 Surface velocity differences of the time varying Petit Bois Island removal run minus the control run in July

Velocities represent vector averages of the surface 2.57 m across the model domain.

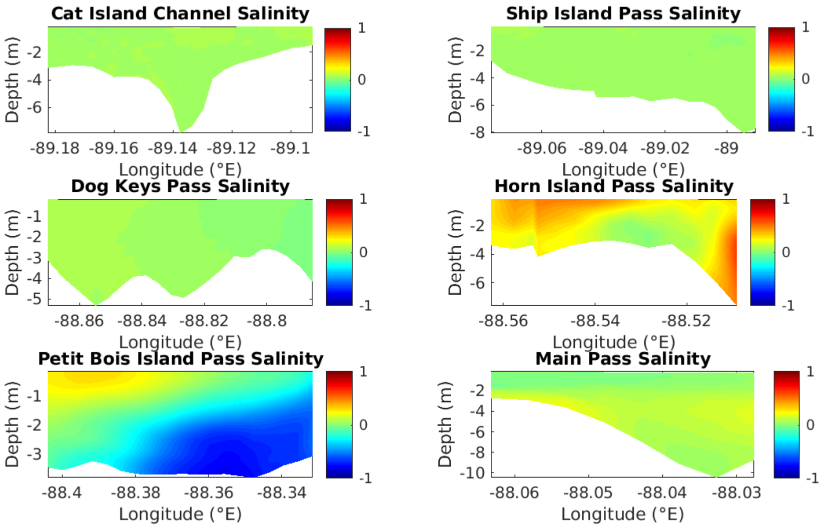

Figure 4.39 Salinity differences in the island passes for the July portion of the time varying Petit Bois Island removal run minus the control run

Same design as Figure 4.17.

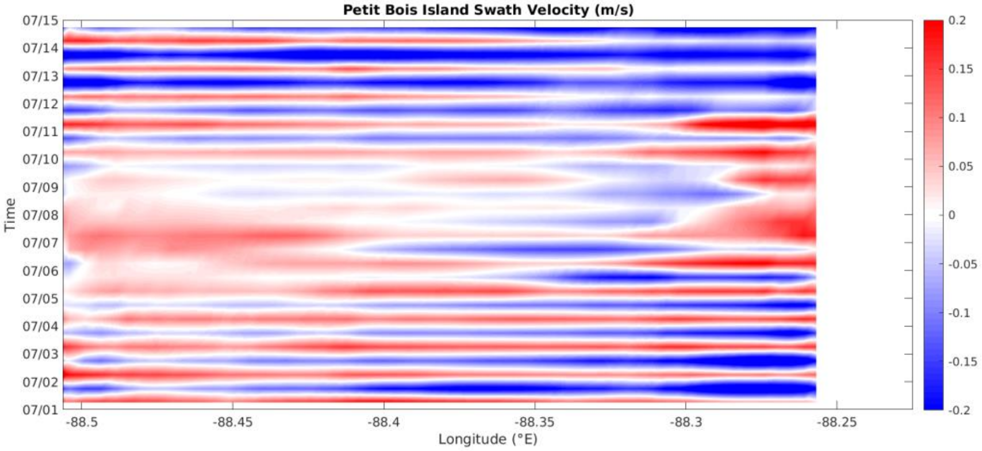

Figure 4.40 Surface meridional velocity Hovmöller diagram across the removed Petit Bois Island-western Dauphin Island complex for the July portion of the Petit Bois Island removal run

Horn Island Pass and Petit Bois Island Pass are included in the transect. Red denotes onshore flow; blue is offshore flow. For visual clarity, only the first two weeks of July are shown.

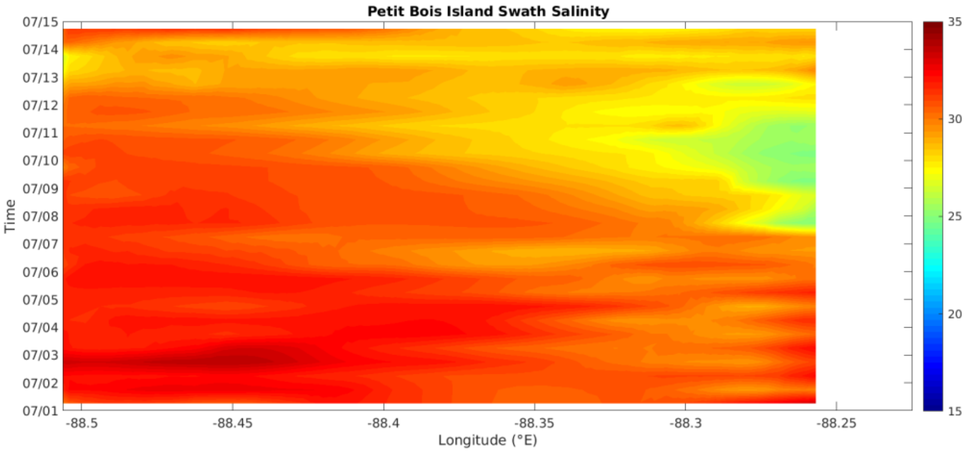

Figure 4.41 Surface salinity Hovmöller diagram across the removed Petit Bois Island-western Dauphin Island complex for the July portion of the Petit Bois Island removal run

Same design as Figure 4.40.

Bottom current changes in the July portion of the Ship Island removal look similar to those seen in the steady state run. Bottom velocity differences, shown in Figure 4.42, pointed to the northeast over the removed West Ship Island, with speed changes of 3 cm/s, and east northeast directional changes and accompanying 2 cm/s magnitude changes over the removed East Ship Island. Surface current differences include a shift to the east northeast over the removed West Ship Island, with magnitudes changing as much as 6 cm/s, and a 2 cm/s speed change in conjunction with a southwest directional shift over the removed East Ship Island, Figure 4.43. Transport changes exceeding $10^2$ $m^3/s$ saw an east southeast rotation in Ship Island Pass and south southeast turn in Dog Keys Pass.

Salinity in the eastern edge of Ship Island Pass increased by up to 0.5 from the seafloor to the top meter of water. By contrast, average salinity decreased in Dog Keys Pass; the largest decrease, about 0.5, was concentrated in the 1-2 m depth range (Figure 4.44). Inflow at depth in Ship Island Pass deepened by 2 m and shifted eastward. The magnitude of the northward velocity decreased in the Ship Island removal run relative to the control run. The weak inflow along the western side of Dogs Key Pass in the July control run gave way to nearly 0 cm/s average flow in the Ship Island removal. Looking at the surface Hovmöller diagram across the area where the islands had been removed, the net outflow seen during the July portion of the time varying run gave way to a net inflow of Mississippi Bight water (Figure 4.45). Figure 4.46 gives the same two week period in surface salinity, and increased salinity aligns with northward flowing currents. Mississippi Sound salinity increased by 0.04; the western Sound saw the largest salinity increase near the removed islands.

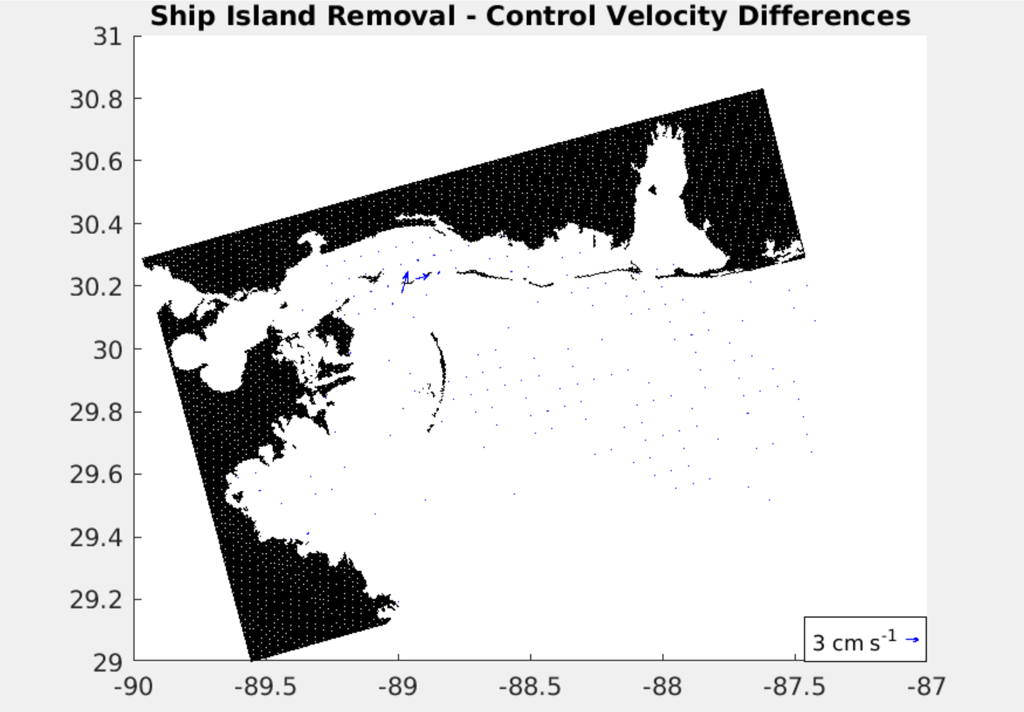

Figure 4.42 Bottom velocity differences of the time varying Ship Island removal run minus the control run in July

Velocities represent vector averages of the bottom 1.5 m across the model domain.

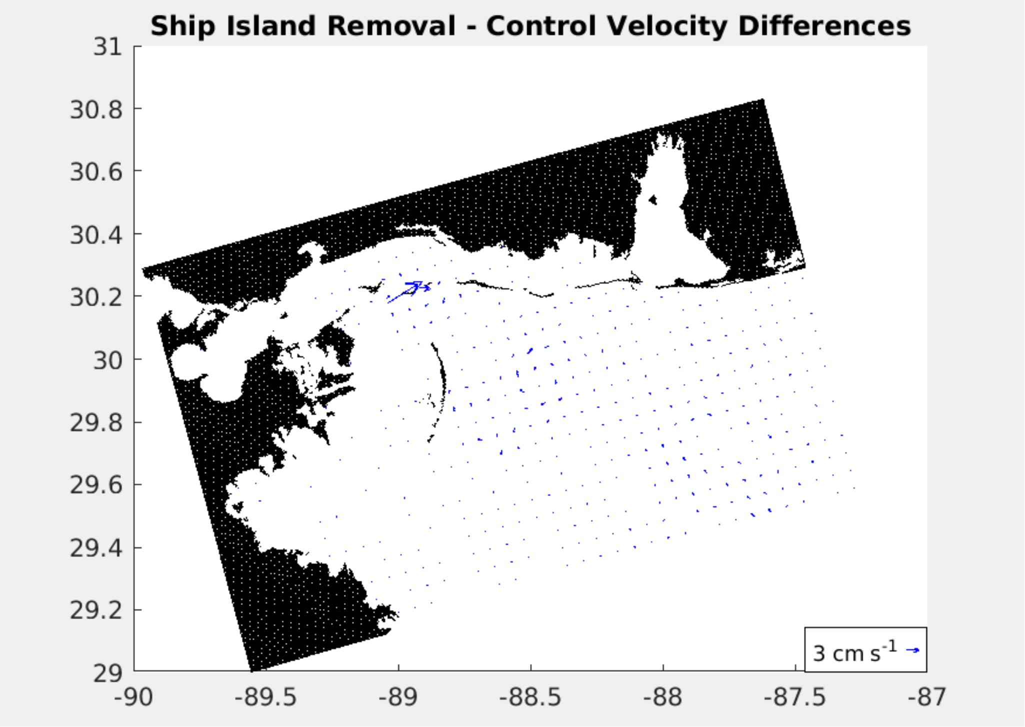

Figure 4.43 Surface velocity differences of the time varying Ship Island removal run minus the control run in July

Velocities represent vector averages of the surface 2.57 m across the model domain.

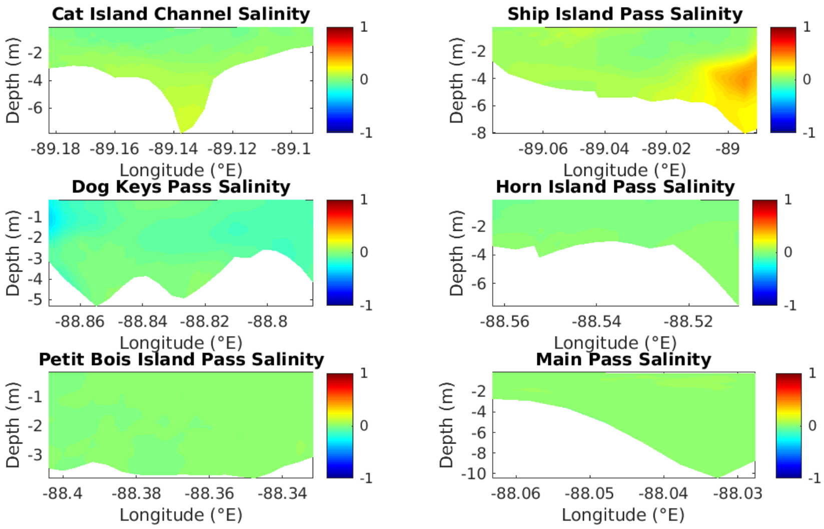

Figure 4.44 Salinity differences in the island passes for the July portion of the time varying Ship Island removal run minus the control run

Same design as Figure 4.17.

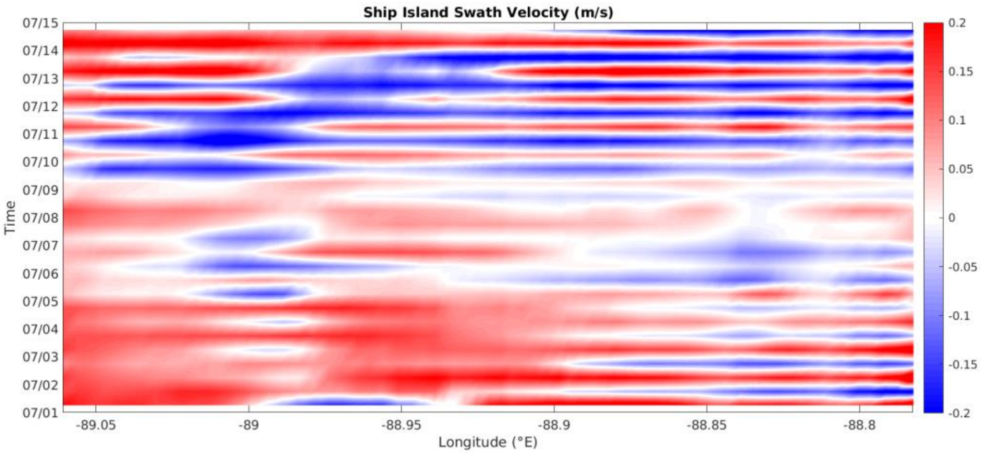

Figure 4.45 Surface meridional velocity Hovmöller diagram across the removed West Ship Island-East Ship Island complex for the July portion of the Ship Island removal run

Ship Island Pass, the gap between West and East Ship Island, and Dog Keys Pass are included in the transect. Red denotes onshore flow; blue is offshore flow. For visual clarity, only the first two weeks of July are shown.

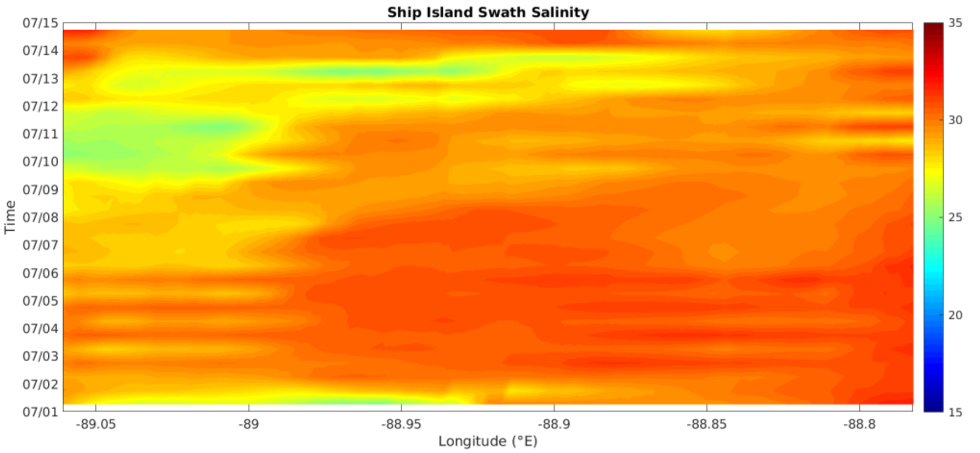

Figure 4.46 Surface salinity Hovmöller diagram across the removed West Ship Island-East Ship Island complex for the July portion of the Ship Island removal run

Same design as Figure 4.45.

### 4.6.3 Balancing Sea Surface Height

The horizontal momentum balance equations are given in (Eq. 4.6) and (Eq. 4.7) make up a portion of the primitive equations that drive the ROMS component of

ROMSmsb; momentum terms balance the horizontal pressure gradient term as well as the turbulent and viscous stress terms. Sea surface height differences are shown in Figures 4.47 through 4.50. Pressure gradient changes in general, and sea surface height changes in particular, match up to observed changes in velocity and salinity.

Sea surface height relative to a geopotential surface (free surface or ζ) in the island removal runs changed by less than 0.5 cm compared to the control runs. Under January steady state conditions, removing Petit Bois Island and western Dauphin Island increased sea surface height by almost 5 mm over the removed islands and by 1-3 mm south of the removed islands, as can be seen in the top plot of Figure 4.47. Sea surface decreased north of the removed barrier islands. This makes sense when compared to surface salinity which decreased south of the removed islands and increased north of the islands. Additionally, free surface decreased in the Mississippi Bight east of the Mississippi River bird foot delta, but regions to the north and south of the lowered sea surface saw increased sea surface height. In the middle plot of Figure 4.47, the Ship Island January steady state removal run lowered sea surface height over the removed islands, but free surface increased elsewhere in the western Mississippi Sound and northwestern Mississippi Bight. As in the Petit Bois Island removal, a portion of the Bight saw lowered sea surface extending east from the Mississippi River bird foot delta, but increased free surface occurred north and south of this section. Again, lowered surface height corresponded to increases in surface salinity. Removal minus control surface height differences were less than 2 mm in the Ship Island removal. Looking at the bottom plot in Figure 4.47, the main differences between the two removal runs were in the vicinity of the removed islands. Surface height changes in the Mississippi Bight looked qualitatively similar, but the Petit Bois Island removal displayed larger magnitude changes as wells as positional differences in the location of the lower and higher free surface areas.

Sea surface height differences in the time varying runs for January had magnitudes less than 2 mm. As with the January steady state run, the removal of West and East Ship Island produced both smaller magnitude changes and less widespread changes than the removal of Petit Bois Island and western Dauphin Island. The changes can be seen in the top plot of Figure 4.48. Surface heights decreased in the eastern Mississippi Sound, in Mobile Bay, and in part of the north-central Mississippi Bight. Removing Petit Bois Island increased surface height south of the removed islands as well as south of the barrier islands in the western half of the chain. In the middle plot of Figure 4.48, removing Ship Island raised the free surface to the southwest of the removed islands but lowered the free surface in the immediate vicinity of the removed islands. Reduced surface salinity matched up to increased surface height in the removal runs. The two removal runs differed in the western and eastern halves of the Sound (bottom plot of Figure 4.48).

The Petit Bois Island and Ship Island removal runs yielded qualitatively similar results under July steady state conditions. The area south and east of the removed islands showed an increase in sea surface height while the region north of the removed islands saw a decrease in surface height (Figure 4.49). As with the other removal runs, the Petit Bois Island removal scenario caused larger magnitude and wider spread changes in surface height. However, changes in both removal runs were less than 0.5 cm. The Petit

Bois Island removal run also had a decrease in the free surface in the southeastern Mississippi Bight that was not present in the Ship Island removal run.

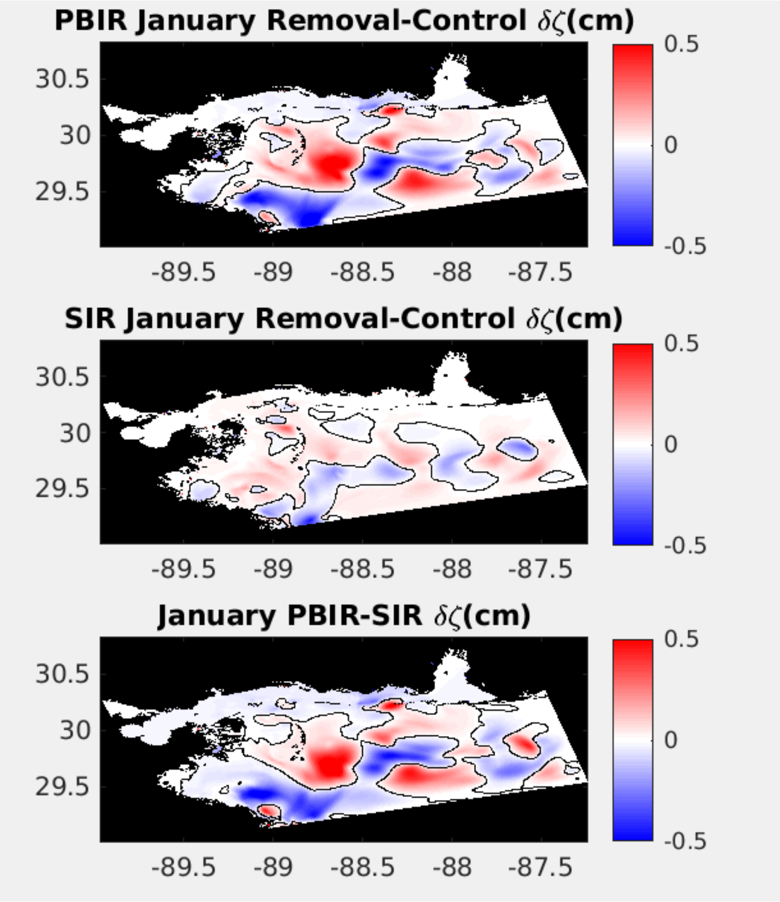

Figure 4.47 Sea surface height differences for January steady state runs

Red areas mean surface height in the removal run is higher; blue indicates surface height in the control run is higher. Top) Petit Bois Island removal (PBIR) run minus control run. Middle) Ship Island removal (SIR) run minus control run. Bottom) Petit Bois Island removal run minus Ship Island removal run.

Time varying results for July mimic those seen in the July steady state run. In both removal scenarios, sea surface height increased south and east of the removed islands while surface height decreased north and west of the removed islands (Figure 4.50). Changes in the free surface for the Ship Island removal were less than 1 mm. By contrast, increases and decreases in surface height had larger magnitudes in the time varying Petit Bois Island removal than the July steady state run. Additionally, in both removal runs, a small, <1 mm, increase could be seen east of the Mississippi River bird foot delta. Removing Ship Island produced little change in surface height while removing Petit Bois Island and western Dauphin Island modified surface height across the entire eastern Mississippi Sound, Mobile Bay, and the southeastern Mississippi Bight.

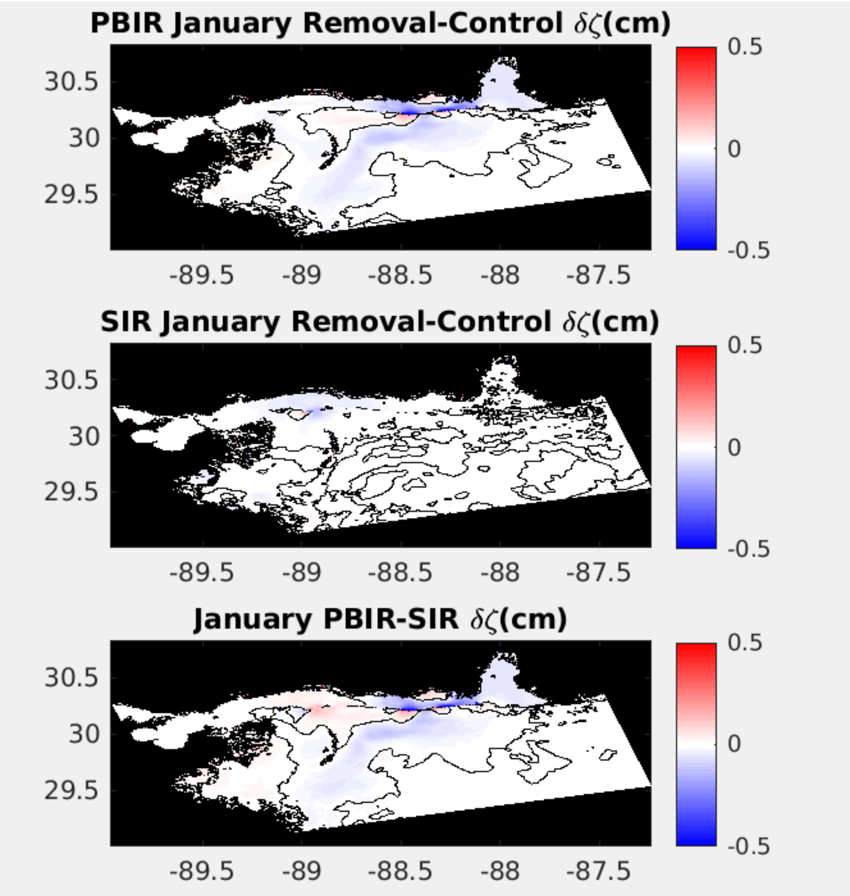

Figure 4.48 Sea surface height differences for the January portion of the time varying runs

Red areas mean surface height in the removal run is higher; blue indicates surface height in the control run is higher. Top) Petit Bois Island removal run minus control run. Middle) Ship Island removal run minus control run. Bottom) Petit Bois Island removal run minus Ship Island removal run.

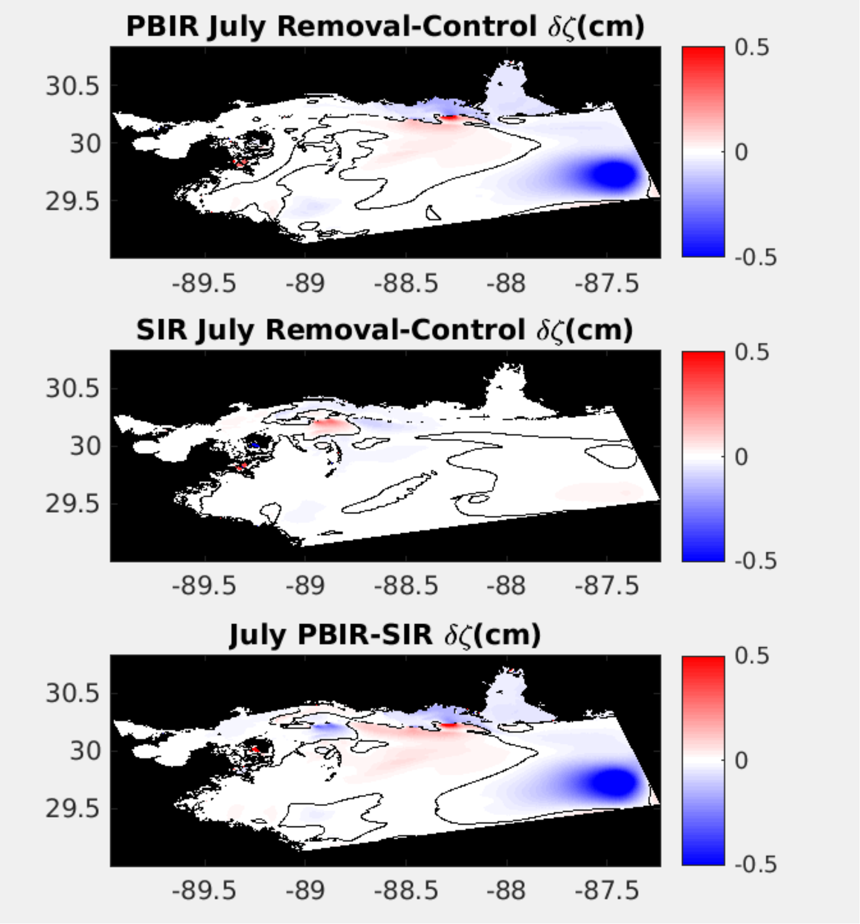

Figure 4.49 Sea surface height differences for the July steady state runs

Red areas mean surface height in the removal run is higher; blue indicates surface height in the control run is higher. Top) Petit Bois Island removal run minus control run. Middle) Ship Island removal run minus control run. Bottom) Petit Bois Island removal run minus Ship Island removal run.

For the most part, observed changes to sea surface can be tied to inverse changes in salinity. Salinity changes, in turn, can be linked to alterations in current patterns. Looking at the surface as well as throughout the water column, changes to the momentum components almost completely balance changes in the horizontal pressure gradient. Differences in the turbulent and viscous terms of the momentum balance equation tend to be 1-3 orders of magnitude smaller than the changes in momentum and horizontal pressure gradient terms. Changes in the turbulent and viscous terms only begin to have the same magnitudes as the other terms where the barrier islands were removed, near the Louisiana coast, and in isolated portions of the Mississippi Bight. These areas coincide with unexpectedly larger magnitude changes in velocity, salinity, and surface height. In future runs, island removal may need to be paired with alterations to model boundary conditions as some of the observed changes might result from model artifacts. However, this study aimed to minimize changes to ROMSmsb between the removal and control runs, so no changes to boundary conditions were made.

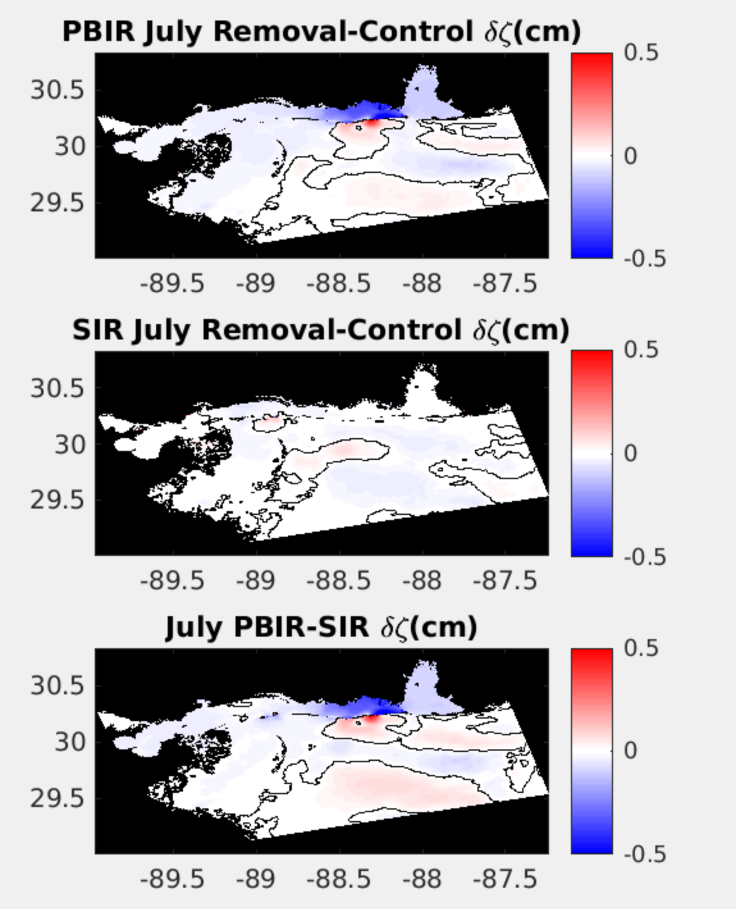

Figure 4.50 Sea surface height differences for the July portion of the time varying runs

Red areas mean surface height in the removal run is higher; blue indicates surface height in the control run is higher. Top) Petit Bois Island removal run minus control run. Middle) Ship Island removal run minus control run. Bottom) Petit Bois Island removal run minus Ship Island removal run.

## 4.7 Implications of Long Term Change

Key changes to circulation brought about by island loss include increased salinity in the Mississippi Sound and altered water exchange pathways between the Mississippi Bight and Mississippi Sound. Even considering the ongoing segmentation and westward migration of the barrier island chain, the Mississippi-Alabama barrier islands still serve to restrict flow into and out from the Mississippi Sound. Island passes share many circulation traits with inlets. Less dense, lower salinity flows out of the Sound at the surface, and a compensating higher density, higher salinity water flows into the Sound at depth. Additionally, water volume exchange between the Mississippi Sound and Bight is limited to the passes, and this keeps salinity lower in the Sound which in turn supports a number of species with salinity range preferences.

In both island removal scenarios, two islands were removed. Horn Island Pass lies to the west of Petit Bois Island and Sand Island while Petit Bois Island Pass separates Petit Bois Island and Dauphin Island. The two passes have lengths of 7 km and 6 km respectably, but the removal of Petit Bois Island and western Dauphin Island creates a 35 km break in the island chain. Ship Island Pass separates Cat Island and West Ship Island, and Dog Keys Pass separated East Ship Island and Horn Island. In ROMSmsb, a pass also existed between West and East Ship Island. These passes have lengths between 4 km and 9 km, so the Ship Island removal scenario transformed two islands in between three passes into a 28 km gap in the Mississippi-Alabama barrier island chain.

At first glance, modifications to salinity distributions and flow between the Mississippi Sound and Bight seem both localized and minimal. Salinity increases of more than 1 remain mostly confined to the island passes and areas immediately north of the removed islands. However, depending on the location of the removed island, half the Sound saw sustained increases in salinity. Also, since island loss more than tripled the length of the gap between the remaining barrier islands, flow looked more like open water exchange than narrow inlet-like exchange since flow was no longer constrained to narrow passes.

Changes in velocity, transport, and salinity were discussed in section 4.6, but changes in flushing time also bear examination. Results for calculated flushing time for each model run are given in (Table. 4.3). All times were rounded up to the nearest day. Flushing (or residence) time was shorter in the time varying control runs versus the steady state runs. The flushing time in the July steady state control run was almost 100 days longer than the January steady state control run flushing time while the July portion of the time varying run had a flushing time nearly 10 days shorter than its January counterpart. Removing Petit Bois Island and the western half of Dauphin Island reduced flushing time by 0.5 to 2 days while removing the two components of Ship Island increased flushing time by 2-10 days. This pattern held true except for the July portion of the time varying runs where removing Petit Bois Island increased flushing time by 22 days while removing Ship Island only increased flushing time by 2 days. Removing barrier islands increased the volume of the Mississippi Sound. Despite the increased volume, the Petit Bois Island removal runs tended to replenish water faster than the control runs while the Ship Island runs tended to take longer to flush the larger Mississippi Sound.

Within the model, the slight salinity increase would become the new norm with no additional increases, but under real world conditions, salinity would certainly continue to increase with time. The lack of subaerial land would diminish the barrier island chain’s ability to reduce storm impacts. Additionally, island loss would cause a substantial reduction in sediment supply down drift in the barrier island chain. Collectively, the changes brought about by island loss would be detrimental to the maintenance of flow and salinity in the Mississippi Sound, and flooding and storm damage would likely worsen during future tropical cyclones.

Table 4.3 Mississippi Sound Flushing Time

| Run | Flushing Time (Days) |
|---|---|
| Steady State January Control | 166 |
| Steady State January Petit Bois Island Removal | 166 |
| Steady State January Ship Island Removal | 168 |
| Time Varying January Control | 155 |
| Time Varying January Petit Bois Island Removal | 153 |
| Time Varying January Ship Island Removal | 165 |
| Steady State July Control | 254 |
| Steady State July Petit Bois Island Removal | 254 |
| Steady State July Ship Island Removal | 258 |
| Time Varying July Control | 146 |
| Time Varying July Petit Bois Island Removal | 168 |
| Time Varying Ship Island Removal | 148 |

# CHAPTER V – SUMMARY AND CONCLUSIONS

This project aimed to study the effect of barrier island loss on circulation within the Mississippi Bight and Mississippi Sound. To that end, analysis of multiple years of observational data provided a climatology for circulation across the calendar year and identified dominant periods of variability. Since the study region has a history of tropical cyclone strikes, hurricane seasons within the observational record were also studied to see how pulsed, non-periodic forcing events impacted the region. Finally, the ROMSmsb coastal ocean model enabled island removal scenarios.

## 5.1 General Summary of Observational Analysis

Circulation within the Mississippi Sound and Bight undergoes seasonal evolution that experiences temporary interruption by tropical cyclones that enter the Gulf of Mexico. The tropical cyclones can cause storm run up and occasional set down along the coast. The longshore current near the Mississippi-Alabama barrier islands reverses from a westward direction during cooler months to an eastward flow in summer months in conjunction with shifts in dominant wind direction. In agreement with previous studies, dominant forcing mechanisms include winds, tides, and riverine input. Mesoscale features, such as eddies, can also have prolonged impacts on circulation. Though changes in surface currents, bottom temperature, and bottom salinity can be seen in the monthly climatologies, higher frequency variations occur on time scales from a few hours to a few days.

The observational analysis shows the importance of dividing the Mississippi Bight and Sound into sub-regions for analysis since circulation characteristics change not only from the western Mississippi Sound to the eastern Sound but also throughout the

Mississippi Bight. Spatial variability can be attributed in part to the presence of the nearly perpendicular Louisiana and Mississippi-Alabama coasts, local rivers, Mobile Bay, the Mississippi River, and depth changes from the continental shelf to the De Soto Canyon (Hill et al., 2010; Ho et al., 1987).

Tropical cyclone analysis of storms that formed in or entered the Gulf of Mexico found only weak correlations between storm distance and approach direction to water level changes, current speeds and directions, and abrupt shifts in salinity and temperature. However, fluctuations in eddy kinetic energy suggest non-storm periods during hurricane seasons can alter circulation to the same degree as Gulf of Mexico storms. The 2014-2017 period used for this analysis did not contain any major hurricanes that made landfall within the study region. The absence of direct strike tropical cyclone data during the study period leaves uncertainty as to the relative magnitude of impacts from direct strike storms compared to that of storms located further away in the Gulf and non-storm periods. A longer record containing multiple direct strike hurricanes would likely disagree with the results presented for this four year study.

Finally, the barrier islands play a crucial role in limiting water exchange between the Mississippi Sound and Mississippi Bight, so their presence also plays a controlling role in circulation. This can be seen in bottom salinity distribution and surface velocity maps in both the western Mississippi Sound and Mississippi Bight.

### 5.2 Observed Versus Modeled Circulation

The CONCORDE Meteorological Analysis captured the land and sea breeze cycles reasonably well. The temperature gradient sign changed from negative (warmer ocean) to positive (warmer land) around mid-morning local time and back to negative around dusk.  Wind directional shifts showed transitions from onshore to offshore and back again.  While specifics did not always align with previous analysis by Hill et al. (2010), the differential heating and wind velocity rotation simulated a cycling land and sea breeze.

Since previous ROMSmsb validation efforts focused on the model-data agreement for towed and deployed equipment during the CONCORDE field campaigns as well as at buoys, this study examined model-data agreement for surface currents and bottom temperature and salinity used in the observational analysis.

Results of comparisons between HFR-derived surface currents and model currents were varied.  The region south of the eastern Mississippi Sound had the best overall agreement for both zonal and meridional velocities.  However, portions of the domain had negative correlations and high root mean square errors.  This occurred east of the Chandeleur Islands near the western limit of the HFR coverage and along the open boundaries of the model domain. The best and worst areas for model-data agreement aligned with the most and least reliable HFR grid points respectively.

ROMSmsb salinities in the western Mississippi Sound tended to be 4-8 higher than observations.  This result was not unexpected as a known salinity bias exists in NCOM which supplies boundary inputs to ROMSmsb.  Lack of riverine input in ROMSmsb from Lake Ponchartrain may be a contributing factor as well.  Temperature model-data agreement had high correlation coefficients, similar standard deviations, and low root mean square error.

## 5.3 Study Region Response to Island Removal

Ultimately island loss led to two major changes. To illustrate these changes, Figure 5.1 shows a conceptualized cross section of the barrier island chain before (top panel) and after (bottom panel) island removal. First, transforming the subaerial islands to subaqueous shoals allow water exchange between the Mississippi Sound and Mississippi Bight. This meant that while current speeds within existing island passes decreased throughout the water column, water could flow over the length of the removed islands as well as in the passes. Mean transport changes within the passes stayed under $10^3$ $m^3/s$, but mean velocity magnitudes and directions rotated near the removed islands, and speeds changed by as much as 10 cm/s. Second, island loss under some of the removal scenarios led to decreased salinity in parts of the Mississippi Sound, but the net effect of island loss was to permit a larger amount of higher salinity into the Mississippi Sound. The half of the Sound that contained the removed islands saw larger salinity increases than the remainder of the Sound.

In a real world scenario, the larger gap in the island chain combined with new localized velocity changes would lead to ongoing increases in salinity and would likely make the northern Gulf of Mexico susceptible to worse damage in the event of future tropical cyclones. The missing islands would not provide much storm resistance, and their absence would increase sediment starvation along the chain. The barrier islands would be less resilient after future hurricanes, and storm surge could more readily affect the coast.

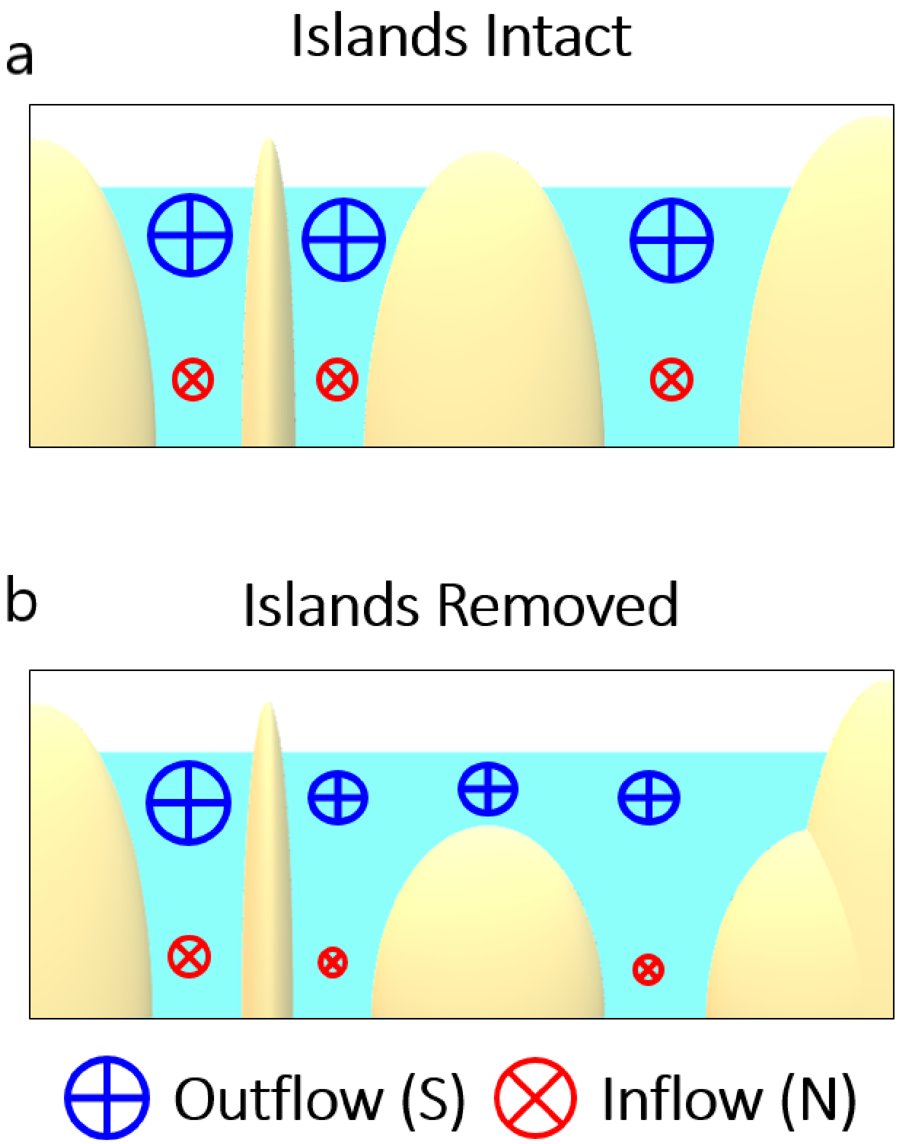

Figure 5.1 Conceptual drawing of island removal changes

Using the Petit Bois Island-western Dauphin Island removal scenario as an example, the top plot shows the vertical profile of the eastern half of the barrier island chain in its current configuration. Outflow occurs near the surface while inflow happens at depth. When one island and half of another island are transformed into subaqueous shoals, water can flow over the top of the shoals. Gravitational circulation in the passes weakens.

### 5.4 Future Work

The model results presented in this study represent one instance of each scenario, and the observational data provide a sub-decadal view of circulation in the Mississippi

Sound and Mississippi Bight. The 2014-2017 period has only one direct strike tropical cyclone, and only some of the observations captured the storm period. The climatology and variability analysis would benefit from a longer record. Model results would be improved if ensembles could be run for each scenario to allow the calculation of statistics. Sensitivity analysis should also be done. Additional model runs that remove only parts of islands or multiple islands within the chain would strengthen or contradict the results from this study.

The natural evolution of this project would model a future configuration of the Mississippi-Alabama barrier islands and Louisiana-Mississippi-Alabama coast with a more fully-developed version of ROMSmsb. This study occurred in time with the development of the sediment transport module of ROMSmsb, during comparison of different atmospheric forcing products, and development of the oceanic component of ROMSmsb. Future runs would benefit from the inclusion of the waves and sediment modules as part of a barrier island modification experiment.

A predictive island chain scenario would necessarily have to balance land loss with planned restoration efforts and maintenance of shipping channels. The coastline would have to be moved landward, and North and South Chandeleur Island modification would have to accompany the Mississippi-Alabama barrier island chain modification. Potential iterative adjustments could include: 1) widening the passes, 2) adding westward drift, and 3) creating a landward curvature of the islands. Simulated storm breaches could also be included. As this study proves, however, any of those changes in isolation can cause unexpected shifts in circulation in the Mississippi Bight.

Island removal simulations in this study do provide a useful step in simulating coastal change in the northern Gulf of Mexico using a coastal ocean model. The study sought to identify the role barrier islands played in circulation within the Mississippi Sound and Bight. Though island loss in isolation is improbable, the island removal scenarios provided a valuable first step in modeling coastal and barrier island change in the northern Gulf of Mexico.

# REFERENCES

Avila, L. A. (2017). National Hurricane Center Tropical Cyclone Report: Hurricane Katia. Miami: National Hurricane Center.

Beckman, A., & Haidvogel, D. B. (1993). Numerical simulation of flow around a tall isolated seamount. Journal of Physical Oceanography 23, 1736-1753.

Berg, R. (2015). National Hurricane Center Tropical Cyclone Report: Tropical Storm Bill. Miami: National Hurricane Center.

Berg, R. (2017). National Hurricane Center Tropical Cyclone Report: Hurricane Hermine. Miami: National Hurricane Center.

Berg, R. (2018). National Hurricane Center Tropical Cyclone Report: Tropical Storm Cindy. Miami: National Hurricane Center.

Beven, J. L. (2015). National Hurricane Center Tropical Cyclone Report: Tropical Storm Dolly. Miami: National Hurricane Center.

Beven, J. L. (2016). National Hurricane Center Tropical Cyclone Report: Tropical Storm Danielle. Miami: National Hurricane Center.

Beven, J. L. (2018). National Hurricane Center Tropical Cyclone Report: Hurricane Franklin. Miami: National Hurricane Center.

Beven, J. L., & Berg, R. (2018). National Hurricane Center Tropical Cyclone Report: Hurricane Nate. Miami: National Hurricane Center.

Bjerknes, V. (1914, 01). Meteorology as an exact science. Monthly Weather Review, pp. 11-14.

Blake, E. S., & Zelinsky, D. A. (2018). National Hurricane Center Tropical Cyclone Report: Hurricane Harvey. Miami: National Hurricane Center.

Bregy, J. C., Wallace, D. J., Minzoni, R. T., & Cruz, V. J. (2018). 2500-year paleotempestological record of intense storms for the northern Gulf of Mexico, United States. Marine Geology 396, 26-42.

Bryan, K., & Cox, M. D. (1967). A numerical investigation of the oceanic general circulation. Tellus 19(1), 54-80.

Bureau of Safety and Environmental Enforcement. (2018, 8 27). Offshore Statistics by Water Depth. Retrieved from BSEE Data Center: www.data.bsee.gov

Cangialosi, J. P. (2014). National Hurricane Center Tropical Cyclone Report: Tropical Storm Hanna. Miami: National Hurricane Center.

Cangialosi, J. P., Latto, A. S., & Berg, R. (2018). National Hurricane Center Tropical Cyclone Report: Hurricane Irma. Miami: National Hurricane Center.

Chang, Y. L., & Oey, L. Y. (2013). Coupled response of the trade wind, SST gradient, and SST in the Caribbean Sea, and the potential impact on Loop Current's interannual variability. Journal of Physical Oceanography 43, 1325-1344.

Chapman, D. C. (1985). Numerical treatment of cross-shelf open boundaries in a barotropic coastal ocean model. Journal of Physical Oceanography 15, 1060-1075.

Charney, J. G., Fjortoft, R., & von Neumann, J. (1950). Numerical integration of the barotropic vorticity equation. Tellus 2(4), 237-254.

Cipriani, L. E., & Stone, G. W. (2001). Net longshore transport and textural changes in beach sediments along the southwest Alabama and Mississippi barrier islands, U.S.A. Journal of Coastal Research 17(2), 443-458.

Coleman, J. M., Roberts, H. H., & Stone, G. W. (1998). Mississippi River Delta: an overview. Journal of Coastal Research 14(3), 698-716.

Conzelmann, C., Couvillion, B., Enwright, N., Hunnicutt, C., Meyers, M., Osland, M. J., & Wang, H. (2018). Alabama Barrier Island Restoration Assessment at Dauphin Island. Retrieved from Wetland and Aquatic Research Center: https://www.usgs.gov/centers/wetland-and-aquatic-research-center-warc/science/alabama-barrier-island-restoration?qt-science_center_objects=0#qt-science_center_objects

Courtier, A. (1938). Marées. Paris: Service Hydrographique de la Marine.

Cox, H. J. (1916). Cold waves. In A. J. Henry, E. H. Bowie, H. J. Cox, & H. C. Frankenfield, Weather Forecasting in the United States (pp. 143-167). U.S. Government Printing Office.

Dai, A., & Deser, C. (1999). Diurnal and semidiurnal variations in global wind and divergence fields. Journal of Geophysical Research 104, 31109-13125.

Dolan, G., & Wallace, D. J. (2012). Policy and management hazards along the Upper Texas coast. Ocean and Coastal Management 59, 77-82.

Eisemann, E. R., Wallace, D. J., Buijsman, M. C., & Pierce, T. (2018). Response of a vulnerable barrier island to multi-year storm impacts: LiDAR-data-inferred morphodynamic changes on Ship Island, Mississippi, USA. Geomorphology 313, 58-71.

Eleuterius, C. K. (1977). Location of the Mississippi Sound oyster reefs as related to salinity bottom waters during 1973-1975. Gulf Research Reports 6(1), 17-23.

Eleuterius, C. K., & Baugez, S. L. (1979). Mississippi sound: a Hydrographic and Climate Atlas. Ocean Springs: Blossom Printing.

Fitzpatrick, P., & Lau, Y. H. (2018). CONCORDE Meteorological Analysis (CMA) Data Guide. Stennis Space Center: Mississippi State University.

Flather, R. A. (1976). Tidal model of the north-west European continental shelf. Memoires Societe Royale de Sciences de Liege, 141-164.

Frigo, M., & Johnson, S. G. (1998). FFTW: an adaptive software architecture for the FFT. Proceedings of the Internal Conference on Acoustics, Speech, and Signal Processing 3, 1381-1384.

Fritz, H. M., Blount, C., Singleton, J., Fuggle, A., McAdoo, B. G., Moore, A., . . . Tate, B. (2007). Hurricane Katrina storm surge distribution and field observations of the Mississippi Barrier Islands. Estuarine Coastal and Shelf Science 74, 12-20.

Gal, N. (2018). Holocene Formation and Evolution of Horn Island, Mississippi, USA. Master's Theses, 603. Retrieved from https://aquila.usm.edu/masters_theses/603

Greer, A. T., Shiller, A. M., Hofmann, E. E., Wiggert, J. D., Warner, S. J., Parra, S. M., . . . Graham, W. M. (2018). Functioning of coastal river-dominated ecosystems and implications for oil spill response: From observations to mechanisms and models. Oceanography 31(3).

Hill, C. M., Fitzpatrick, P. J., Corbin, J. H., Lau, Y. H., & Bhate, S. K. (2010). Summertime precipitation regimes associated with the sea breeze and land breeze in southern Mississippi and eastern Louisiana. Weather and Forecasting 25, 1755-1779.

Ho, F. P., Su, J. C., Hanevich, K. L., Smith, R. J., & Richards, F. (1987). Hurricane Climatology for the Atlantic and Gulf Coasts of the United States. Silver Spring, MD: National Oceanic and Atmospheric Administration.

Hollis, R. (2018). Late Quaternary Evolution and Stratigraphic Framework Influence on Coastal Systems along the North-Central Gulf of Mexico, USA. Master's Theses, 598. Retrieved from https:///quila.usm.edu/masters_theses/598

Howden, S. D., Barrick, D., & Anguilar, H. (2011). Applications of high frequency radar for emergency in the coastal ocean: Utilization of the Central Gulf of Mexico Ocean Observing System during the Deepwater Horizon oil spill and vessel tracking. Proceedings of SPIE 8030. Orlando.

Howden, S., & Kern, A. (2013). Circulation on the continental shelf within the Mississippi Bight. Proceedings of SPIE 8724: Ocean Sensing and Monitoring (pp. OC1-OC9). Baltimore, Maryland: Society of Photographic Instrumentation Engineers.

Jeter Jr, G. W., & Carter, G. A. (2016). Habitat change on Horn Island, Mississippi, 1940-2010, determined from textural features in panchromatic vertical aerial imagery. Geocarto International 31(9), 985-994.

Johnson, D. R. (2008). Ocean surface current climatology in the northern Gulf of Mexico. Ocean Springs, Mississippi: Gulf Coast Research Laboratory.

Kaplan, D., Cook, M., & Atwater, D. (2007). HFR_Progs. Retrieved from High Frequency Radar Program Suite: https://github.com/rowg/hfrprogs

Kara, A. B., Barron, C. N., Martin, P. J., Smedstad, L. F., & Rhodes, R. C. (2006). Validation of interannual simulations from the 1/8 degree global Navy Coastal Ocean Model (NCOM). Ocean Modelling 11, 376-398.

Kjerfve, B. (1983). Analysis and Synthesis of Oceanic Conditions in Mississippi Sound, April thru October 1980. Mobile: US Army Corps of Engineers.

Landsea, C. W., Anderson, C., Charles, N., Clark, G., Dunion, J., Fernandez-Partagas, J., . . . Zimmer, M. (2004). The Atlantic hurricane database re-analysis project: Documentation for the 11851-1910 alterations and additions to the HURDAT database. In R. J. Murname, & K.-B. Liu, Hurricanes and Typhoons: Past, Present and Future (pp. 177-221). New York: Columbia University Press.

Lipa, B., & Barrick, D. (1983). Least-squares methods for the extraction of surface currents from CODAR cross-loop data: Application at ARSL at ARSLOE, IEEE. Journal of Ocean Engineering 84, 226-253.

Louisiana Water Data Support Team. (2019, 09 10). USGS 07381331 GIWW at Houma, LA. Retrieved from National Water Information System: Web Interface: https://waterdata.usgs.gov/la/nwis/uv

Lucas, K. L., & Carter, G. A. (2013). Change in distribution and composition of vegetated

habitats on Horn Island, Mississippi, northern Gulf of Mexico, in the initial five years following Hurricane Katrina. Geomorphology 199, 129-137.

Lundquist, J. D., & Cayan, D. R. (2002). Seasonal and spatial patterns in diurnal cycles in streamflow in the western United States. Journal of Hydrometeorology 3(5), 591-603.

Marchesiello, P. J., McWilliams, J. C., & Shchepetkin, A. F. (2001). Open boundary conditions for long-term integration of regional ocean models. Ocean Modelling 3, 1-20.

Martin, P. J., Barron, C. N., Smedstad, L. F., Campbell, T. J., Wallcraft, A. J., Rhodes, R.

C., & Carroll, S. N. (2009). User's manual for the Navy Coastal Ocean Model (NCOM) version 4.0. Stennis Space Center, Mississippi: Naval Research Laboratory.

Martin, P. J., Barron, C. N., Smedstad, L. F., Wallcraft, A. J., Rhodes, R. C., Campbell, T. J., . . . Carroll, S. N. (2008). Software design description for the Navy Coastal Ocean Model (NCOM) version 4.0. Stennis Space Center, Mississippi: Naval Research Laboratory.

McDougall, T. J., & Barker, P. M. (2011). Getting started with TEOS-10 and the Gibbs Seawater (GSW) Oceanographic Toolbox. SCOR/IAPSO WG127.

MDMR. (2009). 2009 Comprehensive Annual Report Fiscal Year Ended June 30, 2009. Biloxi: Mississippi Department of Marine Resources.

Mesinger, F., DiMego, G., Kalnay, E., Mitchell, K., Shafran, P. C., Ebisuzaki, W., . . . Shi, W. (2006). North American Regional Reanalyses. Bulletin of the American Meteorological Society, 343-360.

Mississippi Department of Environmental Quality. (2016). Round Island Marsh Restoration Project Begins. Retrieved from MDEQ Office of Restoration: www.restore.ms/round-island-marsh-restoration-project-begins-2/

Moore, A. M., Arango, H. G., Broquet, G., Powell, B. S., Weaver, A. T., & Zavala-Garay, J. (2011). The Regional Ocean Modeling System (ROMS) 4-dimensional variational data assimilation systems: Part I - System overview and formulation. Progress in Oceanography 91(1), 34-49.

Moore, A. M., Arango, H. G., Miller, A. J., Cornuelle, B. D., Di Lorenzo, E., & Neilson,

D. J. (2004). A comprehensive ocean prediction and analysis system based on the tangent linear and adjoint components of a regional ocean model. Ocean Modelling 7, 227-258.

Morton, R. A. (2007). Historical changes in the Mississippi-Alabama barrier islands and the roles of extreme storms, sea level, and human activities. St. Petersburg: US Geological Survey.

NOAA. (2001). NCEI 3 arc-second Coastal Relief Model Development. Retrieved from National Geophysical Data Center: https://www.ngdc.noaa.gov/mgg/coastal/model.html

NOAA Fisheries. (2018, 7). Shrimp Statistics. Retrieved from Office of Science and Technology: https://www.st.nmfs.noaa.gov/st1/market_news/doc45.txt

O'Brien, S. J., Wiggert, J. D., & Dodd, D. W. (2014). A circa 2011 bathymetric dynamic digital elevation model for the northern Gulf of Mexico. Gulf of Mexico Oil Spill and Ecosystem Science. Mobile, Alabama: Gulf of Mexico Oil Spill and Ecosystem Science.

Odezulu, C. I., Lorenzo-Trueba, J., Wallace, D. J., & Anderson, J. B. (2018). Follets Island: A case of unprecedented change and transition from rollover to subaqueous shoals. In L. J. Moore, & A. B. Murray, Barrier Dynamics and Response to Changing Climate (pp. 147-174). Springer.

Ohlman, J., & Niiler, P. (2005). Circulation over in the continental shelf in the northern Gulf of Mexico. Progress in Oceanography 64(1), 45-81.

Otvos, E. G. (1970). Development and migration of barrier islands, northern Gulf of Mexico. Geological Society of America Bulletin 81, 241-246.

Otvos, E. G. (1981). Barrier island formation through nearshore aggradation – Stratigraphic and field evidence. Marine Geology 43(3-4), 195-243.

Otvos, E. G., & Carter, G. A. (2008). Hurricane degradation - barrier island development cycles, northeastern Gulf of Mexico: Landform evolution and island chain history. Journal of Coastal Research 24(2), 463-478.

Otvos, E. G., & Carter, G. A. (2013). Regressive and transgressive barrier islands on the north-central Gulf Coast - Contrasts in evolution, sediment delivery, and island vulnerability. Geomorphology 198, 1-19.

Paduan, J. D., & Graber, H. C. (1997). Introduction to high-frequency radar: Reality and myth. Oceanography 10(2), 36-39.

Palmen, E. H. (1948). On the formation and structure of tropical cyclones. Geophysica 3, 26-38.

Pan, C., Dinniman, M. S., Fitzpatrick, P. J., Lau, Y. H., Cambazoglu, M., Parra, S., . . . Wiggert, J. (2017). Exploring the circulation dynamics of Mississippi Sound and Bight using the CONCORDE Synthesis Model. American Geophysical Union Fall Meeting. New Orleans.

Pasch, R. J., & Penny, A. B. (2017). National Hurricane Center Tropical Cyclone Report: Tropical Storm Colin. Miami: National Hurricane Center.

Pasch, R. J., Latto, A. S., & Cangialosi, J. P. (2018). National Hurricane Center Tropical Cyclone Report: Tropical Storm Emily. Miami: National Hurricane Center.

Pendleton, E. A., Barras, J. A., Williams, S. J., & Twichell, D. C. (2010). Coastal vulnerability assessment of the northern Gulf of Mexico to sea-level rise and coastal change. Reston, Virginia: US Geological Survey.

Perez, M. (2019, 2 18). Camille Cut is no more: a look at new changes to the barrier islands of the Mississippi Coast. SunHerald, p. n.p.

Reigner, I. C. (1966). A method of estimating streamflow loss by evapotranspiration from the riparian zone. Forest Science 12(2), 130-139.

Richardson, L. F. (1922). Weather Prediction by Numeric Process. Cambridge, England: Cambridge University Press.

Roberts, H. H., Huh, O. K., Hsu, S. A., Rouse, L. J., & Rickman, D. A. (1989). Winter storms impacts on the Chenier Plain coast of southwestern Louisiana. Transactions - Gulf Coast Association of Geological Societies XXXIX, 515-522.

Rogers, J. C., & Rohli, R. V. (1991). Florida citrus freezes and polar anticyclones in the Great Plains. Journal of Climate 4, 1103-1113.

Rosati, J. D., & Stone, G. W. (2009). Geomorphologic evolution of barrier islands along the northern U.S. Gulf of Mexico and implication for engineering design in barrier restoration. Journal of Coastal Research 25(1), 8-22.

Sallenger, A., Wright, W., Lillycrop, J., Howd, P., Stockdon, H., Guy, K., & Morgan, K. (2007). Extreme changes to barrier islands along the central Gulf of Mexico during Hurricane Katrina. US Geological Survey Circular 1306, 113-118.

Shchepetkin, A. F., & McWilliams, J. C. (2003). A method for computing horizontal pressure-gradient force in an oceanic model with a nonaligned vertical coordinate. Journal of Geophysical Research 108(C3), 3090.

Shchepetkin, A. F., & McWilliams, J. C. (2005). The Regional Ocean Modeling System: A split-explicit, free surface, topography following coordinate ocean model. Ocean Modelling 9, 347-404.

Shcherbina, A. (2014). editmask.m. The ROMS/TOMS Group.

Sikiric, M. D., Janekovic, I., & Kuzmic, M. (2009). A new approach to bathymetry smoothing in sigma-coordinate ocean models. Ocean Modelling 29, 128-136.

Song, Y., & Haidvogel, D. B. (1994). A semi-implicit ocean circulation model generalized topography-following coordinate system. Journal of Computational Physics 115, 228-244.

Stewart, R. H., & Joy, J. W. (1974). HF radio measurements of surface currents. Deep Sea Research and Oceanographic Abstracts, 1039-1049.

Stewart, S. R. (2017). National Hurricane Center Tropical Cyclone Report: Hurricane Earl. Miami: National Hurricane Center.

Taylor, K. E. (2001). Summarizing multiple aspects of model performance in a single diagram. Journal of Geophysical Research 106, 7183-192.

Twichell, D. C., Flocks, J. G., Pendleton, E. A., & Baldwin, W. E. (2013). Geologic controls on regional and local erosion rates of three northern Gulf of Mexico barrier-island systems. Journal of Coastal Research Special Issue 63, 32-45.

Umlauf, L., & Burchard, H. (2003). A generic length-scale equation for geophysical turbulence models. Journal of Marine Research 61, 235-265.

US Army Corps of Engineers. (2016). Tonnage for Selected U.S. Ports in 2016. Retrieved from Waterborne Commerce Statistics Center: https://www.iwr.usace.army.mil/about/technical-centers/wcsc-waterborne-commerce-statistics-center/

US Department of the Interior & US Geological Survey. (2016). Mississippi Coastal

Improvement Plan (MsCIP). Retrieved from United States Geological Survey in the Gulf of Mexico: https://gom.usgs.gov/web/Projects/View/4

Warner, J. C., Armstrong, B., He, R., & Zambon, J. B. (2010). Development of a Coupled Ocean-Atmosphere-Wave-Sediment Transport (COAWST) modeling system. Ocean Modelling 35(3), 230-244.

Warner, J. C., Sherwood, C. R., Arango, H. G., & Signell, R. P. (2005). Performance of four turbulence closure models implemented using a generic length scale method. Ocean Modelling 8, 81-113.

Warner, J. C., Sherwood, C. R., Signell, R. P., Harris, C., & Arango, H. G. (2008). Development of a three-dimensional, regional, coupled wave, current, and sediment-transport model. Computers and Geosciences 34, 1284-1306.

Watson, D. F. (1992). Contouring: A Guide to the Analysis and Display of Spatial Data. Tarrytown, New York: Pergamon Press.

Wei, E., Zhang, A., Yang, Z., Chen, Y., Kelley, J. G., Aikman, F., & Cao, D. (2014). NOAA's nested Northern Gulf of Mexico Operational Forecast Systems development. Journal of Marine Science and Engineering 2(1), 1-17.

Wicht, C. L. (1941). Diurnal fluctuations in Jonkershoek streams due to evaporation and transpiration. Journal of the South African Forestry Association 7(1), 34-49.

Wilkin, J., & Hedstrom, K. S. (1998). User's Manual for an Orthogonal Curvilinear Grid-generation Package. Rutger's University.